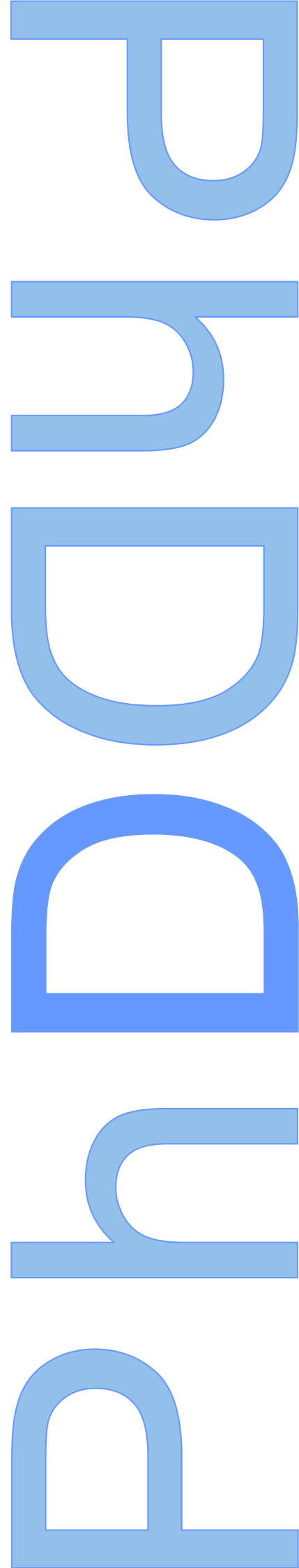
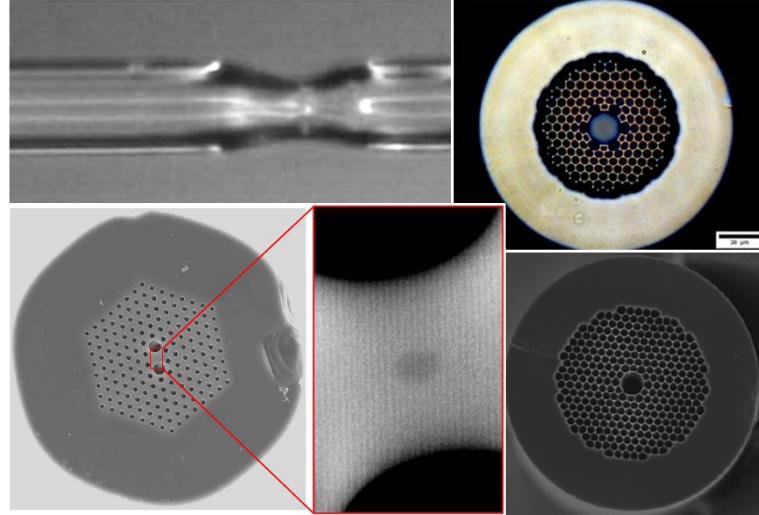


# Optical Sensing: Fiber Structures and Interrogation Techniques

Joel Pedro Carvalho







# Optical Sensing: Fiber Structures and Interrogation Techniques

Joel Pedro Carvalho

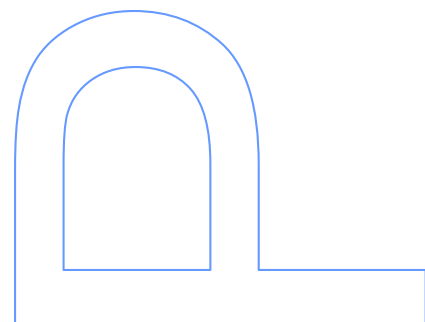
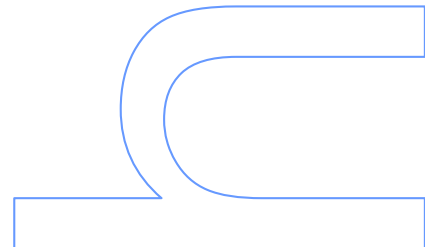
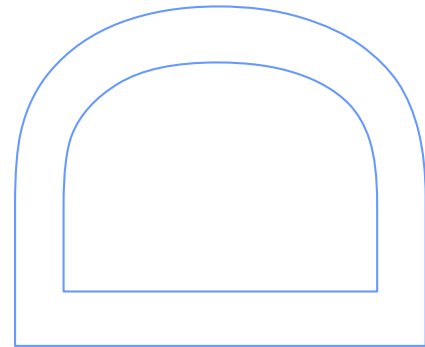
PhD in Physics  
Physics and Astronomy Department  
2013

**Supervisor**

José Luís Santos, Full Professor, FCUP

**Co-Supervisor**

José Manuel Baptista, Associate Professor, University of Madeira





## Dedication

*To my wife  
Raquel*

*For where your treasure is, there your heart will be also.  
(Matthew 6:21)*



## Acknowledgments

First I would like to thank Prof. José Luís Santos for giving me the opportunity, in 2005, to make research directly with him at INESC Porto, at the Optoelectronics and Electronic Systems Unit. I would also like to acknowledge his guidance, advices and suggestions as my PhD supervisor. Prof. José Luís Santos will always be a person whom I will remember with remarkable appreciation.

Thank you Prof. José Manuel Baptista for your enthusiasm every time I have to write something related with my work plan, your intensive reinforcement callings, and interest in the laboratorial developments.

I also would like to thank Dr. Orlando Frazão for his ideas, the motivation provided, his ‘optic feelings’, optimism and encouragement.

I cannot forget Prof. Paulo Marques’ positive ‘*bocas*’ and the friendship of Ireneu Dias.

I have to thank the INESC Porto - Optoelectronics and Electronic Systems Unit big family which I have been working with since February 2002, and the good working atmosphere we had together. Thank you Diana Viegas, Susana Silva, Paula Tafulo, Paulo Caldas, Luís Coelho, Ricardo Silva, Filipe Magalhães, Pedro Jorge, Carlos Gouveia, Sérgio Mendonça, Manuel Marques and of course Luísa Mendonça.

I would also to acknowledge for the financial support provided by:

- The 6<sup>th</sup> Framework Programme through the European Project NextGenPCF – Next Generation Photonic Crystal Fibers (IST 34918);
- The Portuguese Foundation for Science and Technology for the grant SFRH/BD/30850/2006;
- The European COST Action 299 – FIDES;
- The project *Estudo e Desenvolvimento de Sensores Ópticos para Monitorização Remota de Parâmetros Ambientais* (FCT/CAPES 4.4.1.00)

- The project AMBISENSE – *Monitorização Remota de Parâmetros Ambientais Através de Sensores de Fibra Óptica* (CNPq 61/2008; FCT 411.00)

Finally, I want to thank my lovely and sweet wife Raquel, for her love, support and patience all these years. I am sorry for the quality time I took away from you.

Many and truly thanks to all of you!

Sincerely yours,

*Joel Pedro Carvalho*



## **Abstract**

Optical fiber based sensing technology has been the target of increasing interest in the research and development of useful applications. The circumstance of the optical fiber being simultaneously a sensing element and communication channel, as well as its immunity to electromagnetic interferences, allow the development of different kinds of sensing solutions, for measurement of physical, chemical and/or other environmental relevant parameters.

The following work fits within a broad field that goes from the optical fiber based sensing head concept and its development, to the optoelectronic interrogation techniques applied to quantify in an adequate way the measurements. Standard and microstructured optical fibers were used as the basis of the developed sensing heads.

Multi-parameter measurement is a vital topic because, in general, it allows the reduction of the complexity, size and cost of the sensing system, and it also provides parameter discrimination, in situations where cross-sensitivity is a major issue. Mature structures like fiber Bragg gratings were combined in standard and microstructured fiber sensing heads to perform simultaneous measurement of strain and temperature. Sensing capabilities of physical parameters with long period gratings and rocking filters designed in highly birefringent microstructured fibers were also studied.

During the last decade, optical fiber based gas sensing attracted considerable attention. Hollow-core microstructured fibers brought the advantage of easy alignment with the communication channel – due to its similar size – and a much longer interaction length due to the air filled core. An interrogation system relying on the wavelength modulation spectroscopy technique was developed and tested to quantify small concentrations of methane in the ppm order. A versatile compact and portable system for methane detection with multipoint sensing capabilities was then built.

The multimode operation of short lengths of microstructured fibers brings the possibility of building intermodal interferometers with potentially interesting characteristics to perform optical fiber sensing. Firstly, using hollow-core microstructured fibers and secondly, using highly birefringent microstructured fibers, sensing structures were developed, and tested, to measure strain, temperature and curvature.

Considering that the associated photodetection, amplification and processing of the information obtained from the optical based sensing heads are in most cases in the static or quasi-static regime, the measurand readout resolution can be substantially affected by the  $1/f$  noise of the electronics. So, an interrogation approach compatible with signal photodetection and amplification at higher frequencies was studied and implemented: the so called electrical dynamic interrogation. Such an approach was also tested in a multiplexed sensing system.

Since the sensing head in a real scenario usually is located far away – a few kilometers – from the signal processing machinery, it makes sense to speak in remote detection, relevant in many situations, particularly in environmental monitoring. In this domain, an *in situ* optical source for remote sensing was developed. An optical fiber based intensity sensor for multiparameter measurements was also proposed. Finally, a Raman amplified system for remote sensing was simulated and tested.

In all cases, the fundamental objective was to research and develop optical fiber based sensing structures and interrogation approaches looking for the buildup of sensing systems with the potential of being implemented in several areas, mainly in the context of environmental monitoring.

## Resumo

A tecnologia dos sensores baseados em fibra óptica tem sido alvo de crescente interesse na investigação e no desenvolvimento de um vasto conjunto de aplicações. A circunstância da fibra óptica ser, simultaneamente, um elemento sensor e um canal de comunicação, bem como a sua imunidade às interferências electromagnéticas, permite o desenvolvimento de diferentes tipos de soluções sensoras para a medição de parâmetros físicos, químicos e outros de relevância em contextos diversos, nomeadamente no domínio ambiental.

O presente trabalho situa-se numa ampla área que vai desde o conceito de uma cabeça sensora baseada em fibra óptica e do desenvolvimento dessa estrutura, até as técnicas de interrogação optoelectrónica aplicadas para quantificar de uma forma adequada as medições. Fibras ópticas do tipo convencional e microestruturadas foram utilizadas como base das estruturas sensoras desenvolvidas.

A medição multi-parâmetro é um tópico importante porque, em geral, permite minimizar o tamanho, complexidade e custo do sistema de detecção, e também possibilita a discriminação de parâmetros físicos em situações em que a sensibilidade cruzada é uma questão importante. Estruturas como redes de Bragg foram combinadas em fibras ópticas do tipo convencional e microestruturadas, formando cabeças sensoras capazes de efectuar a medição simultânea de deformação e temperatura. As capacidades de detecção de parâmetros físicos de redes de período longo e de *rocking filters* implementados em fibras microestruturadas de elevada birrefringência também foram estudadas.

Durante a última década, o desenvolvimento de sensores de gás baseados em fibra óptica atraiu considerável atenção. As fibras ópticas microestruturadas de núcleo oco trouxeram a vantagem de facilitar o alinhamento com o canal de comunicação – com dimensões semelhantes de secção recta – e também por proporcionarem um muito maior comprimento de interacção devido ao núcleo destas fibras ser preenchido com ar. Um sistema de interrogação baseado na técnica de espectroscopia por modulação de comprimento de onda foi desenvolvido e testado para a detecção de pequenas

concentrações de metano - na ordem de *ppm*. Para a detecção de metano, com capacidade de medição multiponto, foi construído um sistema compacto e versátil.

A operação multimodo em pequenos comprimentos de fibra microestruturada traz a possibilidade de construir interferómetros intermodais com características potencialmente interessantes para realizar sensores em fibra óptica. Esta abordagem foi investigada recorrendo primeiro a fibras microestruturadas de núcleo oco e, posteriormente, a fibras microestruturadas altamente birrefringentes, tendo sido desenvolvidas e testadas estruturas sensoras para medição de deformação, temperatura e curvatura.

Considerando que a fotodetecção, amplificação e processamento da informação proveniente das cabeças sensoras baseadas em fibra óptica são, na maioria dos casos, efectuadas em regime DC ou quase-DC, a resolução de leitura do mensurando pode ser substancialmente afectada pelo ruído  $1/f$  da electrónica. Assim, uma abordagem usando um tipo de interrogação compatível com a fotodetecção do sinal e respectiva amplificação a frequências mais elevadas foi estudado e implementado: a chamada interrogação eléctrica dinâmica. Esta metodologia foi também testada num sistema projectado para a multiplexagem de sensores em fibra óptica.

Considerando que em muitas situações de aplicação a cabeça sensora pode situar-se a distâncias de quilómetros do bloco de detecção e processamento, procurou-se o desenvolvimento de um sistema de sensorização com a fonte óptica localizada *in situ*. Também foi proposto um sensor de intensidade em fibra óptica para medição multiparâmetros. Finalmente, um sistema de amplificação Raman para detecção remota foi simulado e testado.

Em todos os casos, foi objetivo fundamental investigar e desenvolver estruturas sensoras em fibra óptica bem como técnicas de interrogação que permitissem o desenvolvimento de sistemas de detecção com potencial de serem implementados em várias áreas, principalmente no contexto da monitorização de parâmetros ambientais.

## Table of Contents

Dedication .....	iii
Acknowledgments.....	v
Abstract .....	vii
Resumo .....	ix
Table of Contents .....	xi
List of Figures .....	xv
List of Tables .....	xxiii
Chapter 1 – Introduction .....	1
1.1 Background and Thesis Motivation .....	1
1.2 Thesis Structure .....	1
1.3 Contributions.....	2
1.4 List of publications .....	3
Patents .....	3
Papers in Journals .....	3
Papers published in international conferences .....	5
Papers published in national conferences .....	7
Chapter 2 – Optical Fiber Sensing .....	9
2.1 Introduction.....	9
2.2 Optical Fiber Sensors .....	9
2.3 Fiber Bragg Gratings.....	10
2.4 Long Period Gratings .....	14
2.4.1 Optical Fiber Rocking Filters.....	17
2.5 Microstructured Optical Fibers .....	18
2.6 Summary .....	20
Chapter 3 – Optical Sensing with Microstructured Optical Fibers.....	21
3.1 Introduction.....	21
3.2 Microstructured Fiber Splicing .....	22
3.2.1 Microstructured Fiber Characteristics.....	23
3.2.2 Experimental Results .....	23
3.3 Coupling Losses Evaluation in Hollow Core Microstrutured Fibers.....	26
3.3.1 Modelling.....	28
3.4 Strain and Temperature Measurements with Microstructured Fibers.....	34
3.4.1 MOF Bragg Grating Structure .....	34
3.4.2 MOF and SMF Bragg Gratings Combined Structure .....	39
3.5 Long Period Gratings and Rocking Filters in Hi-Bi MOFs.....	42
3.5.1 LPG Characterization and Sensing Properties .....	44
3.5.2 Rocking Filter Characterization and Sensing Properties .....	48
3.6 Spectral Characterization of a Hollow-Core MOF for Sensing Applications ...	52
3.7 Summary .....	60
Chapter 4 – Gas Sensing with Hollow-Core Microstructured Optical Fibers .....	63
4.1 Introduction.....	63
4.2 Gas sensing with Optical Fibers .....	64
4.2.1 Gas Sensing with Photonic Crystal Fibers.....	66
4.2.2 Other Gas Species Sensing with Optical Fibers .....	67
4.3 HC-MOF Based Sensing System.....	68
4.3.1 Diffusion Time.....	69

4.4 Hollow core MOF based sensing head .....	72
4.5 Wavelength Modulation Spectroscopy .....	74
4.3.1 Interrogation Technique Implementation Scheme .....	76
4.4 Results .....	79
4.4.1 Methane Gas Diffusion Time Measurements .....	79
4.4.2 Methane Detection Limit Quantification .....	81
4.4.3 Measurement Portable Unit for Methane Detection .....	82
4.5 Summary .....	83
Chapter 5 – Fiber Sensing with Modal Interferometry .....	85
5.1 Introduction .....	85
5.2 Modal Interferometry for Optical Sensing .....	85
5.3 Modal Interferometers in Hollow-Core Microstructured Fibers .....	86
5.3.1 Sensing Principle .....	87
5.3.2 Experimental Setup .....	90
5.3.3 Results .....	91
5.4 Modal interferometers in Hi-Bi microstructured fibers .....	97
5.4.1 Sensor Fabrication and Operation Principle .....	98
5.4.2 Experimental Results and Discussion .....	105
5.5 Summary .....	111
Chapter 6 – Dynamic Interrogation of Fiber Optic Sensors .....	113
6.1 Introduction .....	113
6.2 Electrical Dynamic Interrogation .....	114
6.3 Dynamic Interrogation for Refractive Index Measurements .....	116
6.3.1 Results for the Refractive Index Measurement .....	120
6.4 Dynamic Interrogation for Curvature Measurements .....	123
6.4.1 Results for Curvature Measurement .....	126
6.5 Distributed Feedback Lasers Based Dynamic interrogation .....	129
6.5.1 Experimental Setup for the DFB Laser Based Dynamic Interrogation ....	130
6.5.2 Results for the DFB Laser Based Multiplexed Interrogation Scheme .....	133
6.6 Summary .....	135
Chapter 7 – Optical Fiber Sensing Configurations for Remote Sensing .....	137
7.1 Introduction .....	137
7.2 In-situ Optical Source for Remote Sensing Purposes .....	138
7.2.1 In Situ Optical Source for Remote Sensing .....	139
7.2.2 Standard Remote Sensing Approach .....	140
7.2.3 Results and Discussion .....	141
7.3 Remote Sensing of Refractive Index with an OTDR .....	145
7.3.1 Sensing Scheme for Refractive Index Measurements .....	146
7.3.2 Multiplexing Sensing Scheme for Refractive Index and Temperature Measurements .....	150
7.4 Remote LPG Sensor with Electrical Interrogation Assisted by Raman Amplification .....	152
7.4.1 CW Raman Amplification Applied to Remote Sensing .....	153
7.4.2 Validation of the Numerical Modeling Results .....	158
7.4.3 Numerical Analysis .....	159
7.4.4 Experimental Analysis .....	161
7.5 Summary .....	168
Chapter 8 – Conclusions and further work .....	171
Appendix 1 .....	175
Methane Detection with Non-PCF Based Solutions .....	175

Methane Measurements with the U-bench .....	175
Methane Measurements with a Developed Open-Path Gas-Cell.....	177
Appendix 2.....	181
Interferometric Optical Fiber Inclinator with Dynamic FBG Based Interrogation .....	181
Principle and Discussion.....	182
Conclusions.....	190
Appendix 3.....	193
Sistema de Interrogação Remoto com Fonte Óptica Acoplada à Cabeça Sensora (Portuguese Patent: 105244) .....	193
Bibliography .....	197





## List of Figures

Figure 1 - Reflection and transmission spectrum of the very first fiber Bragg grating [3].	11
Figure 2 - Schematic of a Fiber Bragg Grating operation principle	12
Figure 3 - Transmission spectrum over a broad wavelength range shows the various cladding modes to which the fundamental guided mode couples. [10]	14
Figure 4 - Percentage of power converted from one principal axes to the orthogonal axis for: (a) 170 cm fiber length and (b) 100 cm fiber length, according to [16, 17].	18
Figure 5 - SEM of the first Photonic Crystal Fiber [20].	19
Figure 6 - Cross-sectional SEM images of the MOF (NL 2. 3 1555) from Crystal Fiber A/S.	23
Figure 7 - a) Result of the Fujikura's splice machine automatic jointing of the fibers (the 25 $\mu\text{m}$ gap between both fibers is seen). Now the MOF is fixed and the SMF-28 <sup>TM</sup> is moved on; b) Result of manual alignment (After this, the electric arc is discharged).	24
Figure 8 - Evaluation of arc duration time with a constant current power.	25
Figure 9 - Visualization of the SMF-28 <sup>TM</sup> /MOF splice in the Fujikura's FSM-40S screen.	26
Figure 10 - Hollow-core microstructured fibers from BlazePhotonics:	27
Figure 11 - Transmission spectra for a 7-cell HC-MOF (HC-1550-02) and a 19-cell HC-MOF core fiber (HC19-1550-01), both designed for operation at 1.55 $\mu\text{m}$ .	27
Figure 12 - Coupling between two fibers separated by distance $d$	28
Figure 13 - a) Mode of 7-cell HC-MOF; b) Mode of 19-cell HC-MOF; c) Averaged mode of 7-cell HC-MOF; d) Averaged mode of 19-cell HC-MOF.	29
Figure 14 - Radially average of mode profiles for SMF, 7-cell HC-MOF, and 19-cell HC-MOF	29
Figure 15 - a) Coupling coefficients, SMF $\rightarrow$ 7-cell HC-MOF, SMF $\rightarrow$ 19-cell HC-MOF; b) Coupling coefficients, 19 cell HC-MOF $\rightarrow$ 19-cell HC-MOF.	30
Figure 16 - Setup used for the experimental evaluation of the coupling loss between: a) SMF and HC-MOF; b) to portions of HC-MOF.	31
Figure 17 - Excess loss dependence on axial displacement: (a) between a SMF and 19-cell HC-MOFs, and between two 19-cell HC-MOFs; (b) between a SMF and 7-cell HC-MOF, and between two 7-cell HC-MOFs.	31
Figure 18 - Excess loss dependence on lateral displacement: (a) between a SMF and 19-cell HC-MOF and between a SMF and a 7-cell HC-MOF; (b) between a SMF and 19-cell HC-MOFs, and between two 19-cell HC-MOFs.	32
Figure 19 - Experimental results obtained for estimation of losses in light coupling between SMF and 19-cell HC-MOF in different cases.	33
Figure 20 - Photographs of the different splices between SMF and 19-cell HC-MOF showed in Figure 19.	33
Figure 21 - Optical spectra of the FBG written in the NL 2.3 1555 fiber.	35
Figure 22 - Experimental apparatus for the strain and temperature measurements.	35
Figure 23 - Strain response of the fast and slow axis signatures of the grating in the microstructured fiber.	36
Figure 24 - Temperature response of the fast and slow axis signatures of the grating in the microstructured fiber.	37

Figure 25 - Temperature-independent strain behavior of the sensor consisting of a Bragg Grating written in a MOF: a) $T = 20^{\circ}\text{C}$ and b) $\varepsilon = 0 \mu\text{ε}$ .....	38
Figure 26 - Sensor output as determined by equations (3.4) and (3.5) for an applied strain at a constant temperature and the temperature variation at a constant strain.....	39
Figure 27 - Strain response of the sensing head made with the MOF and SMF gratings.....	40
Figure 28 - Temperature response of the sensing head made with the MOF and SMF gratings.....	41
Figure 29 - Sensor output as determined by equations (3.6) and (3.7).....	42
Figure 30 - SEM image of the highly birefringent MOF used for fabrication of the LPGs. ....	43
Figure 31 - Setup for LPG and rocking filter inscription using a CO <sub>2</sub> laser. ....	44
Figure 32 - LPG transmission spectrum after 25 exposition points separated by 650 $\mu\text{m}$ . ....	45
Figure 33 - Location of the LPG resonance pair corresponding to different polarization modes in the Hi Bi MOF in the wavelength region near 670 nm.....	45
Figure 34 - Variation of the resonance wavelength versus temperature for: a) pair of resonances around 670nm region: b) pair of resonances around 960 nm region.....	46
Figure 35 - Variation of the LPG resonance power loss as a function of hydrostatic pressure (resonance pair in $\sim 670\text{nm}$ region).....	47
Figure 36 - Rocking filter (with a period $\Lambda=8 \text{ mm}$ and 13 coupling points) transmission spectra for the two eigen-polarization components of the fiber. The solid line and dotted line correspond to the polarization component parallel (guided mode) and orthogonal, respectively, to the input polarization state. ....	48
Figure 37 - Rocking filter resonant wavelength as function of temperature for: a) second resonance at $\sim 1004\text{nm}$ ; b) third resonance at $\sim 1265\text{nm}$ ; c) fourth resonance at $\sim 1493\text{nm}$ . ....	49
Figure 38 - Rocking filter resonant wavelength as function of pressure for: a) second resonance at $\sim 1004\text{nm}$ ; b) third resonance at $\sim 1265\text{nm}$ ; c) forth resonance at $\sim 1493\text{nm}$ .....	50
Figure 39 - Spectrum shift of the $\sim 1493 \text{ nm}$ resonance for different hydrostatic pressure values. ....	51
Figure 40 - Dependence of the rocking filter second wavelength resonance with applied strain.....	51
Figure 41 - Transmission spectrum of the HC-MOF fiber considered for characterization of measurand-induced effects on the PBG edge. ....	53
Figure 42 - Optical microscope image of the cross section of the selected microstructured optical fiber.....	53
Figure 43 - Experimental setup for the characterization of the measurand-induced shift of the edge of the spectral bandgap; also shown is the configuration that was used to apply torsion and curvature to the HC-MOF.....	55
Figure 44 - Effect of applied strain to the HC-MOF on (a) the spectral position of the PBG lower wavelength edge, (b) the loss variation at wavelength 1509nm located in the PBG edge, (c) the loss variation at wavelength 1525nm located in the PBG passband region.....	56
Figure 45 - Effect of temperature variation on (a) the spectral position of the PBG lower wavelength edge, (b) the loss variation at wavelength 1508nm located in the PBG edge, (c) the transmission versus temperature at wavelength 1525nm located in the PBG passband region. ....	57

Figure 46 - Effect of curvature variation on (a) the spectral position of the PBG lower wavelength edge, (b) the loss variation at wavelength 1508nm located in the PBG edge, (c) the transmission versus temperature at wavelength 1525nm located in the PBG passband region. ....	58
Figure 47 - Effect of twist applied to the HC-MOF on (a) the spectral position of the PBG lower wavelength edge, (b) the loss variation at wavelength 1507nm located in the PBG edge, (c) the transmission versus twist at wavelength 1525nm located in the PBG passband region. ....	59
Figure 48 - Optical microscope image of a 7-cell HC-MOF. ....	68
Figure 49 - Spectral 7-cell HC-MOF transmission at its operation bandwidth. ....	69
Figure 50 - Time-dependence of the average relative methane concentration inside different lengths of HC-MOF with two open ends (a) and a single open end (b). ....	71
Figure 51 - (a) Project of the sensing head with periodic openings in the MOF fiber; (b) Butt-coupling of HC-MOF pieces using standard zirconium ferrules connected with a standard zirconium mating sleeve. ....	72
Figure 52 - (a) photo of HC-MOF and the ferrule when they are not still in the same plane; (b) photo of the HC-MOF transversely and axially aligned with ferrule; (c) detailed photo of the HC-MOF aligned with the ferrule. ....	73
Figure 53 - Multi-segment sensing head containing 4 segments of HC-MOF. ....	73
Figure 54 - Wavelength modulation converted to amplitude modulation in Wavelength Modulation Spectroscopy; ....	74
Figure 55 - Spectral contents of the optical signal: <i>left</i> ) laser unmodulated; <i>middle</i> ) laser modulated with no absorption; <i>right</i> ) laser modulated with absorption. ....	75
Figure 56 - Absorption line of an acetylene gas cell (a) and amplitude of the output signals at the dithering frequency (b) and at double of this frequency (c) ....	76
Figure 57 - Layout of the developed interrogation system based on Wavelength Modulated Spectroscopy. ....	77
Figure 58 - Gas chamber for test of the sensing system: (top) computer generated pictures; (bottom) photographs of the implemented gas chamber (the U-benches shown on the right were used to test the WMS interrogation technique). ....	78
Figure 59 - (a) Setup used to measure the diffusion time of gas inside the HC-MOF based sensing head; (b) illustration of the joint between SMF and HC-MOF. ....	80
Figure 60 - Experimental results for the diffusion time of 5% of CH <sub>4</sub> inside a HC-MOF with a length of 13.7 cm (two open ends). The theoretical expected value (241 s) is shown by the vertical dashed line, while the experimentally obtained was 248 s. ....	80
Figure 61 - System response for a methane concentration change. ....	81
Figure 62 - (a) Diagram of the gas measurement unit prototype; (b) photo of the portable measurement unit; (c) response for three different methane gas concentrations. The fluctuations that the different plateau exhibit are due to the effect of the pressure of the gas being injected into the chamber which causes a broadening effect on the absorption peaks. ....	83
Figure 63 - (a) Cross section photograph of a 7 cell HC-MOF and (b) normalized spectral transmission of ~1 m of this fiber spliced to a SMF28 illuminating fiber (the oscillations at lower wavelengths are artifacts due to the normalization) ....	87
Figure 64 - (a) Visualization of the SMF-28/HC-MOF splice in the Fujikura's SM-40 screen; (b) Channeled spectrum of the interferometric sensing head. ....	89
Figure 65 - Experimental setup for initial characterization of the modal interferometer. ....	90

Figure 66 - Wavelength responses of the sensing head for variations of applied (a) strain and (b) temperature. ....	92
Figure 67 - Scheme of the experimental setup for phase reading with white light interferometry. ....	94
Figure 68 - Phase changes induced by strain and temperature variations applied to the sensing head, respectively. ....	95
Figure 69 - Phase response of the sensing head implemented with HC-MOF fiber for a step change in (a) strain and (b) temperature, respectively ....	96
Figure 70 - SEM image of the birefringent MOF with boron doped inclusion in the center of the core (darker spot) used for fabrication of the intermodal interferometer. ....	99
Figure 71 - Field distribution calculated for the fundamental (a) and the first order mode (b) at $\lambda = 1.55 \mu\text{m}$ . Spectral dependence of the effective indices in the fiber with boron doped inclusion for the fundamental and the first order modes and the effective index change introduced by the inclusion (c). ....	100
Figure 72 - (a) Schematic configuration of the proposed intermodal interferometric sensor and the (b) microscope image of the microstructured fiber with the interferometer formed by two tapered regions. ....	101
Figure 73 - The interference spectrum at the output of an in-fiber Mach-Zehnder intermodal interferometer fabricated in the microstructured fiber. ....	103
Figure 74 - Calculated (solid line) and measured (dots) difference in group effective indices of the $\text{LP}_{01}$ and $\text{LP}_{11}$ modes averaged with respect to polarization. ....	104
Figure 75 - (a) Calculated group modal birefringence of the $\text{LP}_{01}$ (solid line) and $\text{LP}_{11}$ (dashed line) modes in the investigated fiber with boron doped inclusion and (b) comparison of the calculated (solid line) and measured (dots) birefringence. ....	105
Figure 76 - Experimental setup for strain and temperature measurements. ....	106
Figure 77 - (a) Transmission characteristic registered in the full spectral range for selected values of applied strain and (b) variation of the modulation depth and displacement of the third fringe in response to applied strain. ....	106
Figure 78 - (a) Displacement of the third interference fringe against applied strain and (b) change in its visibility. ....	109
Figure 79 - Displacement of the third interference fringe against temperature (a) and change of its visibility (b). ....	110
Figure 80 - $P_{out}(\lambda)/P_0$ in a typical LPG spectrum and $(dP_{out}/d\lambda)/P_0$ versus wavelength ....	115
Figure 81 - Experimental setup for different configurations: a) for 1.5 meters with and without EDF amplifier; b) for 5 km with and without EDF amplifier; c) for 50 km with and without Raman amplifier. ....	117
Figure 82 - Optical spectra of the FBGs and LPG in air and immersed in water. ....	118
Figure 83 - Noise level of the electronics at low frequencies. ....	119
Figure 84 - Electrical spectra when modulating FBG1 and FBG2 with $f_1 = 620 \text{ Hz}$ and $f_2 = 740 \text{ Hz}$ , respectively, for the LPG immersed in solutions with different refractive indexes. ....	119
Figure 85 - System output versus refractive index for the case of not using and using EDFA amplification. Fiber length to the sensing head: 1.5 m. ....	120
Figure 86 - System output versus refractive index for the case of not using and using EDFA amplification. Fiber length to the sensing head: 5 km. ....	121
Figure 87 - System output versus refractive index for the case of not using and using Raman amplification. Fiber length to the sensing head: 50 km. ....	121

Figure 88 - System output for a refractive index step variation for the different configurations: a) sensing head located 1.5 meters away with an EDF amplifier; b) sensing head located 5 km away with EDF amplifier; c) sensing head located 50 km away with Raman Amplification. ....	122
Figure 89 - Experimental setup to test the LPG dynamic interrogation method for curvature measurement purposes .....	124
Figure 90 - Optical spectra of the FBGs and LPG, both written in a Corning® SMF-28e® fiber. ....	125
Figure 91 - Optical (a) and electrical (b) spectra of the output signal for the LPG with a curvature radius of 5.81 m and 1.85 m, respectively (the spectral position of the FBG <sub>1</sub> and FBG <sub>2</sub> resonances are sinewave modulated with frequencies $f_1 = 900\text{Hz}$ and $f_2 = 1040\text{Hz}$ , respectively). The inset of (b) shows the system electrical noise level at low frequencies. ....	126
Figure 92 - System output <i>versus</i> radius of curvature .....	127
Figure 93 - System output signal for step changes of the LPG curvature. ....	127
Figure 94 - Electrical dynamic interrogation approach of a LPG based multiplexed scheme.....	128
Figure 95 - $P_{out}(\lambda)/P_0$ , $(dP_{out}/d\lambda)/P_0$ and $(d^2P_{out}/d\lambda^2)/P_0$ <i>versus</i> wavelength. ....	130
Figure 96 - Experimental setup of the multiplexing layout for measuring refractive index variations using the electrical dynamic interrogation approach.....	131
Figure 97 - Optical reflection spectra of the LPGs multiplexing scheme for refractive index measurement. Spectrum of both structures immersed in distilled water (solid line); optical response of the multiplexed LPGs in air (dashed line).....	131
Figure 98 - Electrical spectra of the multiplexed scheme, being (in red) $\omega_1$ and $\omega_2$ , the first and second harmonic of the DFB Laser modulation frequency ( $f_1$ ), and (in blue) $\omega_1$ and $\omega_2$ , the first and second harmonic of the DFB Laser modulation frequency ( $f_2$ ). ....	132
Figure 99 - System output <i>versus</i> refractive index variations for each LPG: LPG <sub>1</sub> (in blue); LPG <sub>2</sub> (in red). ....	133
Figure 100 - Step response for induced refractive index variations of the aqueous solution of NaCl (a) of LPG <sub>1</sub> and (b) of LPG <sub>2</sub> .....	134
Figure 101 - Experimental setup for the new LPG-sensor layout. ....	140
Figure 102 - Experimental setup for the standard LPG-sensor layout.....	141
Figure 103 - Optical spectra recorded by the OSA at point A of configurations depicted in Figure 101 and Figure 102 when: (a) the LPG is not present; (b) after the insertion of the LPG.....	142
Figure 104 - Relative spectral positions of the LPG/FBGs and associated optical powers for the cases (no strain applied to the LPG): (a) local source configuration; (b) remote source configuration. ....	143
Figure 105 - Variation of $P_{proc}$ <i>versus</i> strain for the two configurations studied. ....	144
Figure 106 - Experimental setup of the LPG based sensing head for refractive index measurements.....	146
Figure 107 - OTDR multiwavelength laser and LPG spectrum at (a) 1310 nm and (b) 1550 nm ranges. ....	147
Figure 108 - Detail of the OTDR obtained traces for different refractive index values, ....	147
Figure 109 - Comparison of an LPG ( $\Lambda=395\mu\text{m}$ ) attenuation observed in the 1310 nm and 1550 nm ranges of the OTDR as function of refractive index variation.....	148

Figure 110 - LPG ( $\Lambda=395\mu\text{m}$ ) based sensing head attenuation, obtained from the setup depicted in Figure 1, for the 1550nm OTDR range, as function of the refractive index variations with and without optical amplification.....	149
Figure 111 - Experimental setup of the implemented multiplexing scheme for refractive index and temperature measurements based in two LPGs. ....	150
Figure 112 - OTDR multiwavelength laser for the 1550 nm range superimposed with (in red) LPG at 1546 nm ( $\Lambda=397\mu\text{m}$ ) used for refractive index measurement, and (in blue) LPG at 1552 nm ( $\Lambda=398\mu\text{m}$ ) used for temperature discrimination. ....	150
Figure 113 - LPGs based sensing head attenuation, obtained from the setup depicted in Figure 111, for the 1550nm OTDR range as function of (a) the refractive index (LPG at 1546nm) and (b) temperature (LPG at 1552nm) variations.....	151
Figure 114 - Boundary conditions in co-propagating Raman amplifier applied in telecommunications systems.....	155
Figure 115 - Co-propagating Raman amplifier remote LPG system. ....	156
Figure 116 - Counter-propagating Raman amplifier remote LPG system.....	156
Figure 117 - Raman amplifier remote LPG system using two optical fibers. ....	157
Figure 118 - Experimental (symbols) and simulated optical spectrum (straight line) for a pump power of (a) 800 mW and (b) 1 W. ....	158
Figure 119 - Optical spectrum at the receiver for the different setups calculated by the numerical modeling. ....	160
Figure 120 - Mirrored LPG transfer function measured at 300 K written in a single mode fiber (SMF 28). ....	162
Figure 121 - (a) Remote temperature optical fiber sensor system with one optical fiber with co-propagating pump setup. (b) Remote temperature optical fiber sensor system with two optical fibers with the total pump power coupled to the feed optical fiber.	163
Figure 122 - Spectrum of the signal processed by the LPG with resonance wavelength at 1544 nm measured at the input port of the interrogation unit for the two setups; it is also shown the transfer function of the FBGs at the interrogation unit. ....	164
Figure 123 - Electrical power spectrum of the signal received at the ESA for the temperature of 36.2C, 39.5C, 44.50C and 49.00C, respectively. ....	166
Figure 124 - $P_{proc}$ parameter as a function of temperature for the setup depicted at Fig. 2 (laser pump at 1455.1 nm and launched power of 1.5 W).....	167
Figure 125 - Detail of the U-bench for methane measurements inside the gas chamber. ....	175
Figure 126 - Experimental setup of the detection scheme using the U-bench as a sensing head. ....	176
Figure 127 - System response for three methane concentration changes. ....	176
Figure 128 - Graphical representation of the open path gas cell and expanded view revealing the different components of which it is made up. ....	177
Figure 129 - Detail of 80 mm open path sensing head inside the gas chamber.....	177
Figure 130 - Experimental setup of the detection scheme using the developed reflective open-path gas-cell. ....	178
Figure 131 - Measured amplitude of the second harmonic for four different methane concentrations. ....	178
Figure 132 - Schematic representation of the fiber-taper Michelson interferometer.	182
Figure 133 - Optical spectrum of the optical inclinometer based on tapered optical fiber and a 21 cm cavity length (obtained at zero tilt angle) ....	183
Figure 134 - Behavior of the optical inclinometer for the angular range between 0 and 15 degrees with steps of 1 degree. (a) response of fringe visibility; (b) response of peak wavelength position.....	184

Figure 135 - Plots of the angular coefficient and correlation coefficient ( $R^2$ ) referring to the changes observed in optical power as a function of wavelength obtained for tilt variations between 3 and 6 degrees. The wavelengths with higher sensitivity and linearity are 1549.2 nm ( $R^2 = 0.994$ ) and 1550.3 nm ( $R^2 = 0.982$ ) and are signaled by the vertical lines. ....	185
Figure 136 - Interferometric fringes and spectral locations of the interrogation FBGs represented by vertical lines.....	186
Figure 137 - Normalized response of the sensor obtained through simulations.....	187
Figure 138 - Normalized response of the inclinometer optical for the range of 10 to 14 degrees. ....	188
Figure 139 - Setup of the Interferometric optical fiber inclinometer with dynamic FBG based interrogation .....	189
Figure 140 - Normalized output of the electric interrogation system as a function of inclination angle of fiber-taper Michelson interferometer for 3.5° to 5.5°.....	190





## List of Tables

Table 1 - Geometrical parameters of the highly birefringent MOF .....	43
Table 2 - Theoretical diffusion times to obtain 90% average methane concentration in the core of HC-MOF fibers for different lengths.....	71
Table 3 - Geometrical parameters of the highly birefringent MOF .....	98
Table 4 - refractive index resolutions obtained with the dynamic interrogation technique for the studied configurations.....	123
Table 5 - Refractive index resolutions obtained for the traces depicted in Figure 110. ....	149
Table 6 - Resolutions obtained for the traces depicted in Figure 113 .....	152



# **Chapter 1 – Introduction**

---

## **1.1 Background and Thesis Motivation**

Optical fiber technology progress provided the availability of a wide range of new optical fiber devices and components that permit the revisitation of previous concepts and developments, enabling novel and important advances in the optical fiber sensing area. Optical fiber intrinsic advantages, such as low weight and size, and electromagnetic immunity, will continue to be the motivation to develop fiber sensing structures and adequate interrogation techniques for such devices.

Over the past 40 years, the development of optical sources and lightwave amplifiers, the appearance of fiber devices such as fiber Bragg gratings, long period gratings, modal interferometers and the advent of the revolutionary microstructured optical fibers, attracted much interest among researchers due to their special properties and potential applications. Hybrid structures have also been introduced to form new fiber optical devices that can enhance the capabilities to sense strain, temperature, curvature, twist, and several other physical, chemical or environmental parameters in gases and liquids.

The multiplexing capability is a clear asset of the optical fiber sensing technology, which is rooted in the fact that the optical fiber is simultaneously a sensing element and a communication channel, which means that a dedicated telemetry channel is not required – a unique feature of this technology. Therefore, it is feasible to conceive and develop large optical fiber sensing systems for local or remote monitoring.

## **1.2 Thesis Structure**

This thesis is divided in eight chapters as follows:

- Chapter 1 gives a brief overview of the thesis content and the contributions achieved within its topics.
- Chapter 2 presents a general state of the art in the optical fiber sensors filed.
- Chapter 3 highlights a few developments in optical sensing with microstructured fibers.
- Chapter 4 describes briefly the state of the art in optical fiber sensors for gas detection and then some research achievements for methane detection with hollow-core microstructured fibers are presented.
- Chapter 5 explains how modal interferometry could be used in the fiber sensing technology.
- Chapter 6 describes the principle of operation of a new concept for measuring quasi-static parameters, the electrical dynamic interrogation.
- Chapter 7 presents some optical fiber based configurations for remote sensing of physical parameters.
- Chapter 8 concludes the thesis with a discussion of the obtained results. Future work suggestions are also given.

### 1.3 Contributions

The main contributions of this research work may be summarized as follows:

1. Low loss splicing in a microstructured optical fiber (MOF)
2. Low Splicing and coupling losses in hollow-core (HC) MOF fibers
3. Strain and temperature measurements using fiber Bragg gratings (FBG) in MOF
4. Long Period gratings (LPG) and rocking filters written with a CO<sub>2</sub> Laser in a highly birefringent (Hi-Bi) MOF
5. Spectral characterization of MOFs for sensing applications
6. Gas sensing with MOFs
7. Methane detection based in wavelength modulation spectroscopy (WMS) and HC-MOFs
8. Remote system for detection of low levels of methane based on WMS
9. Modal interferometer based on hollow-core MOF for strain and temperature measurements

10. Intermodal interferometer for sensing applications fabricated in a Hi-Bi MOF
11. LPGs dynamic interrogation with modulated FBGs and optical amplification for refractive index detection
12. Dynamic interrogation using a LPG sensing head for curvature measurements
13. Interferometric optical fiber inclinometer with dynamic FBG based interrogation.
14. LPG remote fiber sensor with an *in situ* optical source
15. Remote sensing of refractive index with an optical time-domain reflectometer (OTDR)
16. Remote LPG sensor with Raman amplification for temperature detection

#### 1.4 List of publications

The contributions of this research work have led to the following patent and publications, in peer-review journals, associated, totally or partially, with research reported in this thesis:

##### Patents

O. Frazão, D. Viegas, L. Coelho, J. P. Carvalho, “Sistema de Interrogação Remoto com Fonte Óptica Acoplada à Cabeça Sensora”, PT105244, Pedido de patente registado no Instituto Nacional da Propriedade Industrial, 2010.

##### Papers in Journals

Thiago V. N. Coelho, Joel P. Carvalho, José L. Santos, Maria José Pontes and Ariel Guerreiro, “A Remote Long-Period Grating Sensor with Electrical Interrogation assisted by Raman Amplification”, accepted for publication in Optics & Laser Technology.

J. P. Carvalho, A. Anuszkiewicz, G. Statkiewicz-Barabach, J. M. Baptista, O. Frazão, P. Mergo, J. L. Santos, W. Urbanczyk, “Long Period Gratings and Rocking Filters Written with a CO<sub>2</sub> Laser in Highly-Birefringent Boron-Doped Photonic Crystal Fibres for Sensing Applications”, Opt Commun. 2012; 285(3):264-8.

J. P. Carvalho, L. Coelho, M. J. Pontes, A. P. Barbero, M. A. Martinez, R. M. Ribeiro, J. Weyl, J. M. Baptista, M. T. R. Giraldo, I. Dias, J. L. Santos, O. Frazão, “Long Period Gratings Dynamic Interrogation with Modulated Fibre Bragg Gratings and Optical Amplification”, IEEE Sensors Journal, Vol. 12 , No. 1, pp. 179 – 183, January 2012.

G. Statkiewicz-Barabach, J. P. Carvalho, O. Frazão, J. Olszewski, P. Mergo, J. L. Santos, W. Urbanczyk, “Intermodal interferometer for strain and temperature sensing fabricated in birefringent boron doped microstructured fiber”, Applied Optics, Vol. 50, Issue 21, pp. 3742-3749, DOI:10.1364/AO.50.003742, 2011.

J. P. Carvalho, L. Coelho, J. M. Baptista, J. L. Santos, O. Frazão, “Dynamic Interrogation for Optical Fibre Sensors based on Long Period Gratings”, Measurement and Science Technology, 22 065201, DOI:10.1088/0957-0233/22/6/065201, IOP, 2011.

Diana Viegas, Joel P. Carvalho, Luís Coelho, José L. Santos, Francisco M. Araújo, and Orlando Frazão, “Long Period Grating Fibre Sensor with In Situ Optical Source for Remote Sensing”, IEEE Photonics Technology Letters, Vol. 22, No. 20, October 15, 2010.

J. P. Carvalho, F. Magalhães, O. Frazão, J. L. Santos, F. M. Araújo and L. A. Ferreira, “Splicing and Coupling Losses in Hollow-Core Photonic Crystal Glass Fibers”, Solid State Phenomena, Trans Tech Publications, Volume 161 (2010) Glass Science and its Applications, pp. 43-50, 2010.

S. Hashem Aref, Rodrigo Amezcua-Correa, Joel P. Carvalho, Orlando Frazão, José L. Santos, Francisco M. Araújo, Hamid Latifi, Faramarz Farahi, Luis A. Ferreira, and Jonathan C. Knight, “Spectral characterization of a photonic bandgap fiber for sensing applications”, Applied Optics, Vol. 49, Issue 10, pp. 1870-1875, 2010.

S. H. Aref, R. Amezcua-Correa, J. P. Carvalho, O. Frazão, P. Caldas, J. L. Santos, F. M. Araújo, H. Latifi, F. Farahi, L. A. Ferreira, and J. C. Knight , “Modal interferometer based on hollow-core photonic crystal fiber for strain and temperature measurement”, Optics Express, Vol. 17, Issue 21, pp. 18669-18675, 2009.

J. P. Carvalho, H. Lehmann, H. Bartelt, F. Magalhães, R. Amezcua-Correa, J. L. Santos, J. Van Roosbroeck, F. M. Araújo, L.A. Ferreira, J. C. Knight, “Remote System for Detection of Low-Levels of Methane based on Photonic Crystal Fibres

and Wavelength Modulation Spectroscopy”, Journal of Sensors, Volume 2009, Article ID 398403, 10 pages, Hindawi Publishing Corporation, 2009.

### **Papers published in international conferences**

C. R. da Silveira, J. P. Carvalho, M. T. R. Giraldi, P. A. S. Jorge, J. Weyl, "Sensor de temperatura baseado em fibra monomodo padrão com afunilamento", MOMAG 2012, 5-8th August, João Pessoa-Paraíba, Brazil, 2012

T. V. N. Coelho, J. P. Carvalho, M. J. Pontes, José L. Santos, "Impacto da Amplificação Raman em sistemas sensores remotos baseados em grades de difração", MOMAG 2012, 5-8th August, João Pessoa-Paraíba, Brazil, 2012

T. V. N. Coelho, J. P. Carvalho, M. J. Pontes, A. Guerreiro, José L. Santos, "DFB laser-based electrical dynamic interrogation for optical fiber sensors", SPIE Photonics Europe, 16-19th April, Brussels, Belgium, 2012

J. P. Carvalho, O. Frazão, J. M. Baptista, J. L. Santos, A. P. Barbero, "DFB laser-based electrical dynamic interrogation for optical fiber sensors", SPIE Photonics Europe, 16-19th April, Brussels, Belgium, 2012

J. P. Carvalho, C. Gouveia, J. L. Santos, P. A. S. Jorge, J. M. Baptista, "Optical time-domain reflectometer-based multiplexed sensing scheme for environmental sensing", SPIE Photonics Europe, 16-19th April, Brussels, Belgium, 2012

J. P. Carvalho, T. V. N. Coelho, M. J. Pontes, A. Guerreiro, J. L. Santos, "Dynamically Interrogated Remote Long-Period Grating Fiber Sensor with Raman Amplification", MAP-Fis PhD Research Conference January 20th, Braga, Portugal, 2012

J. P. Carvalho, C. Gouveia, P. A. S. Jorge, D. Chamorro, M. A. Martinez, M. T. R. Giraldi, A. P. Barbero, J. M. Baptista, "Refractive Index Remote Sensing based in an Optical Time-Domain Reflectometer", ICO-22 — 22nd General Congress of the International Commission for Optics, August 15-19, Puebla – Mexico, 2011

C. R. da Silveira, J. P. Carvalho, P. A. S. Jorge, J. W. A. Costa, M. T. R. Giraldi, J. L. Santos, E. L. Carvalho Júnior, D. O. Figueredo, O. Frazão, "Interferometric optical fiber inclinometer with dynamic FBG based interrogation", AOP'2011, International

Conference on Applications of Optics and Photonics, July 3-7, Universidade do Minho, Braga – Portugal, 2011

J. P. Carvalho, C. Gouveia, P. A. S. Jorge, D. Chamorro, M. A. Martinez, M. T. R. Giraldi, A. P. Barbero, J. M. Baptista, “Intermodal interferometric sensor based in a birefringent boron-doped microstructured fiber”, AOP’2011, International Conference on Applications of Optics and Photonics, July 3-7, Universidade do Minho, Braga – Portugal, 2011

G. Statkiewicz-Barabach, J. P. Carvalho, O. Frazão, J. Olszewski, P. Mergo, J. L. Santos, W. Urbanczyk, “Intermodal interferometric sensor based in a birefringent boron-doped microstructured fiber”, AOP’2011, International Conference on Applications of Optics and Photonics, July 3-7, Universidade do Minho, Braga – Portugal, 2011

J. P. Carvalho, L. Coelho, O. Frazão, J. L. Santos, “Electrical Dynamic Interrogation System for Long Period Gratings”, WSEAS International Conferences - SENSIG’10, 3-5 November, Faro, Algarve, Portugal, 2010

D. Viegas, J. P. Carvalho, L. Coelho, J. L. Santos, L. A. Ferreira, F. M. Araújo, O. Frazão, “Fibre Optic Remote Sensing Based on Long Period Gratings with In Situ Optical Source”, EWOFS 2010 – 4th Workshop on Optical Fiber Sensors, 8-10th September, Porto, Portugal, 2010

J. P. Carvalho, L. Coelho, L. Correia, O. Frazão, P. A. S. Jorge, J. M. Baptista, I. Dias, J. L. Santos, J. Weyl, M. J. Pontes, M. A. Martinez, A. P. Barbero, R. M. Ribeiro, A. J. G. Abelém, M. T. R. Giraldi, “Dynamic Interrogation of Long Period Gratings with Modulated Fibre Bragg Gratings”, EWOFS 2010 – 4th Workshop on Optical Fiber Sensors, 8-10th September, Porto, Portugal, 2010

J. P. Carvalho, G. Statkiewicz-Barabach, A. Anuszkiewicz, J. M. Baptista, O. Frazão, J. Wojcik, J. L. Santos, W. Urbanczyk, “Sensing characteristics of long period gratings and rocking filters based on highly birefringent boron doped photonic crystal fiber and fabricated by a CO<sub>2</sub> laser”, SPIE Photonics Europe, 12-16th April, Brussels, Belgium, 2010

S. H. Aref, R. Amezcua-Correa, J. P. Carvalho, O. Frazão, P. Caldas, J. L. Santos, F. M. Araújo, H. Latifi, F. Farahi, L. A. Ferreira, J. C. Knigh, “Sensing Characteristics of Hollow-Core Photonic Crystal Fibre Modal Interferometers”, OFS-



20 - Twentieth International Conference on Optical Fibre Sensors, 5-9 October, Edinburgh, Scotland, 2009

F. Magalhães, J. P. Carvalho, J. L. Santos, F. M. Araújo, L. A. Ferreira, "Development of an Optoelectronics gas monitoring unit based in wavelength modulation spectroscopy", IRF'2009 – 3rd International Conference on Integrity, Reliability & Failure, FEUP, 20-24 July, Porto, 2009

F. Magalhães, J. P. Carvalho, L. A. Ferreira, F. M. Araújo, J. L. Santos, "Methane detection system based on wavelength modulation spectroscopy and hollow-core fibres", IEEE Sensors 2008, 26th-29th October, Lecce – Italy, 2008

M. B. Marques, F. Magalhães, J. P. Carvalho, O. Frazão, F. M. Araújo, J. L. Santos, L. A. Ferreira, "Recent Advances on Optical Sensing Using Photonic Crystal Fibers", WSOF – 1st Workshop on Specialty Optical Fibers, 20-22 August, SP Brazil, 2008

J. P. Carvalho, F. Magalhães, O. V. Ivanov, O. Frazão, F. M. Araújo, L. A. Ferreira, J. L. Santos, "Evaluation of coupling losses in hollow-core photonic crystal fibres", aceite para apresentação em formato poster no Third European Workshop on Optical Fibre Sensors, EWOFs 2007, 4th-6th July, Napoli, Italy, session III, poster 85, 2007

### **Papers published in national conferences**

J. P. Carvalho, O. Frazão, J. L. Santos, "Long Period Gratings Dynamic Electrical Interrogation Scheme", SEON 2010 – VIII Symposium on Enabling Optical Networks and Sensors, FEUP - Porto, June 25th, 2010

D. Viegas, J. P. Carvalho, L. Coelho, J. L. Santos, F. M. Araújo, O. Frazão, "Novel in situ optical source scheme for remote sensing", Física 2010 – 17ª Conferência Nacional de Física, UTAD – Vila Real, 1-3 September, 2010

J. P. Carvalho, F. Magalhães, F. M. Araújo, J. L. Santos, L. A. Ferreira, "Optoelectronic sensing system based on wavelength modulation spectroscopy for methane detection", SEON 2009 – VII Symposium on Enabling Optical Networks and Sensors, Lisbon, June 26th, 2009

S. H. Aref, J. P. Carvalho, R. Amezcua-Correa, O. Frazão, P. Caldas, J. L. Santos, F. M. Araújo, H. Latifi, F. Farahi, L. A. Ferreira, J. C. Knight, "Sensing

Characteristics of Modal Interferometers based on HC-PCF”, SEON 2009 – VII Symposium on Enabling Optical Networks and Sensors, Lisbon, June 26th, 2009

F. Magalhães, J. P. Carvalho, O. Frazão, F. M. Araújo, J. L. Santos, L. A. Ferreira, “Sistema de Detecção de Metano baseado em Espectroscopia por Modulação de Comprimento de Onda e em Fibras Ópticas Microestruturadas de Núcleo Oco”, Quartas Jornadas de Engenharia de Electrónica e Telecomunicações e de Computadores, JETC’08, 20-21 November, ISEL, Lisboa, 2008

F. Magalhães, J. P. Carvalho, L. A. Ferreira, F. M. Araújo, J. L. Santos, “Gas detection system based on wavelength modulation spectroscopy and hollow-core fibres”, Física 2008, 3 th-6th September, Lisbon – Portugal, 2008

J. P. Carvalho, F. Magalhães, J. L. Santos, F. M. Araújo, L. A. Ferreira, “Optoelectronic methane detection system based in wavelength modulation spectroscopy and a hollow-core fibre”, SEON 2008 – VI Symposium on Enabling Optical Networks and Sensors, Porto, June 20th, 2008

F. Magalhães, J. P. Carvalho, J. L. Santos, F. M. Araújo, L. A. Ferreira, “Implementation of a compact interrogation system for remote detection of methane”, SEON 2007 – V Symposium on Enabling Optical Networks and Sensors, Aveiro, June 29th, 2007

J. P. Carvalho, F. Magalhães, O. Frazão, J. L. Santos, F. M. Araújo, L. A. Ferreira, “Hollow-core photonic crystal fibres for gas sensing applications”, aceite para apresentação oral no SEON 2007 – V Symposium on Enabling Optical Networks and Sensors, Aveiro, June 29th, 2007

## **Chapter 2 – Optical Fiber Sensing**

---

### **2.1 Introduction**

Optical fiber technologies have suffered a huge growth. The increase of research on the optical fiber sensors area arouse firstly from the optical communications technology, but nowadays the research and development come from the real need of sensing functionality in a large spectrum of situations and applications.

In this chapter the field of optical fiber sensors will be briefly described, with special attention for technologies such as: fiber Bragg gratings, long period gratings, microstructured fibers and modal interferometers. Finally, particular emphasis is given to the interrogation techniques available to read optical fiber based sensing heads.

### **2.2 Optical Fiber Sensors**

Optical fiber sensors for different applications have been developed in a huge variety. According to the measurand modulation, optical fiber sensors can be divided in the following categories [1]: intensity, phase, polarization and wavelength. The light modulation must always be processed, independently of the type of the sensor employed, into an optical intensity signal at the optical receiver, which additionally performs an optical-electrical conversion.

In intensity sensors, the magnitude to be measured modifies the optical intensity transmitted by the fiber. This type of sensors can be used in a wide spectrum of applications, since they use very simple optical components and are technically and economically competitive with commercial products based in other sensing technologies.

Phase sensors are based on a change of the phase of the light which is propagated along the fiber. Usually phase modulation must be converted into an intensity modulation before detection. This may be accomplished by means of an optical interferometer. This type of sensor requires coherent light sources and single mode fibers. Usually, the sensitivity of these sensors is higher than the one achieved with the intensity sensors.

Polarimetric sensors are based on the modulation of the polarization of the light. An example is current measurement based on the Faraday Effect. Moreover, polarization effects can also be linked to phase measurements as polarimetric interferometers.

Wavelength or spectroscopy sensors are based on the modulation of the light spectrum.

The presented optical fiber sensors categories do not cover all fiber based sensing systems. Distributed sensors are usually based on Rayleigh, Raman or Brillouin scattering effects of the light inside the fibers [2]. In such distributed sensors, a single measurand can be monitored continuously over the fiber light path. They are effectively used in applications where monitoring a single measurand is required at a large number of points, or continuously over the path of the fiber.

The following sections will focus on topics related with the sensors that have been targetted in this thesis.

## **2.3 Fiber Bragg Gratings**

Bragg gratings inside optical fibers were first formed in 1978 by irradiating a silica fiber for a few minutes with an intense argon-ion laser beam [3]. The grating period was fixed by the argon-ion laser wavelength, and the grating reflected light only within a narrow region around that wavelength. The mechanism behind the grating formation can be understood as follows. The 4% reflection occurring at the two fiber air interfaces creates a standing-wave pattern, such that the laser light is absorbed only in the bright regions. If the glass structures changes in such a way that the refractive

index increases permanently in the bright regions, an index grating is formed. The reflection and transmission spectrum of such device is depicted in Figure 1.

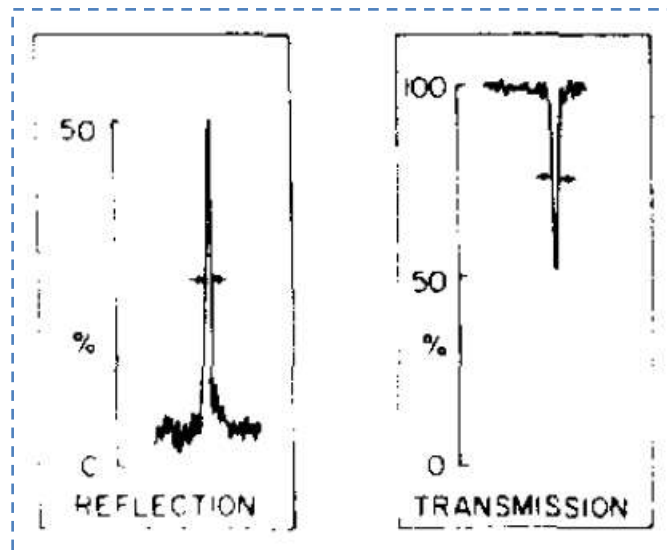


**Figure 1 - Reflection and transmission spectrum of the very first fiber Bragg grating [3].**

Curiously it was only from 1989 onwards that fiber Bragg gratings (FBGs) became a topic of intense investigation, mostly due to the observation of second-harmonic generation in photosensitive fibers. In that year, a paper presented a side-exposed holographic technique that was used to make FBGs with controllable period [4]. This technique was quickly adopted to produce fiber gratings in the third telecommunications window, near 1500 nm [5]. During the early 90s considerable work was done in order to understand the physical mechanism behind the photosensitivity of fibers and to develop techniques that made possible large changes in the fiber's refractive index [6, 7]. By 1995, FBGs became commercially available.

In its simplest form, a fiber Bragg grating consists of a periodic modulation of the refractive index of the core of a single-mode optical fiber. Light guided along the core of an optical fiber will be scattered by each grating plane; if the Bragg condition is not satisfied, the reflected light from each of the subsequent planes becomes progressively out of phase and will eventually cancel out. When the Bragg condition is satisfied, the contributions of reflected light from each grating plane add constructively in the backward direction, to form a back-reflected peak with a centre wavelength defined by the grating parameters. The FBG's principle of operation is schematically described in Figure 2 [8].

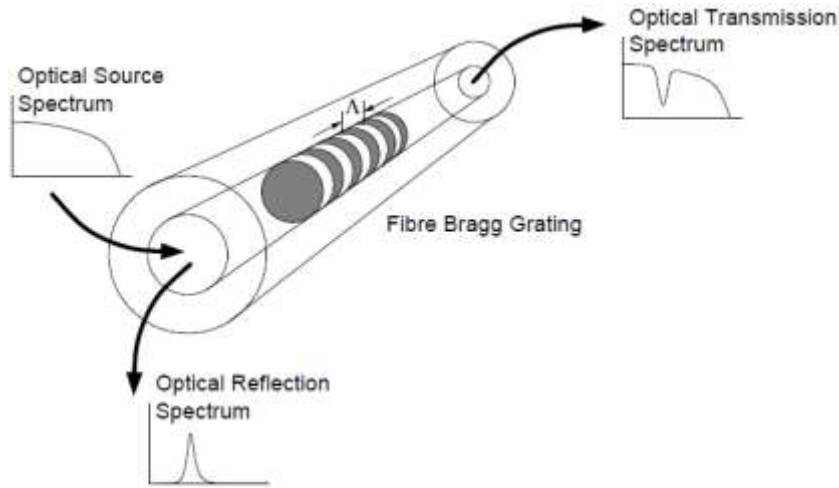


**Figure 2 - Schematic of a Fiber Bragg Grating operation principle and spectral response.**

In fiber Bragg gratings, the reflected wavelength is given by the following equation:

$$\lambda_B = 2n_{eff}\Lambda \quad (2.1)$$

where  $n_0$  is the refractive index of the fiber core and  $\Lambda$  is the modulation period of the grating [9].

The Bragg relationship in its differential form is given by

$$\Delta\lambda_B = \lambda_B \left( \frac{\Delta n_0}{n_0} + \frac{\Delta\Lambda}{\Lambda} \right) \quad (2.2)$$

This equation states that any measurable quantity applied to the grating that causes a refractive index change or period change, induces a deviation in the resonant wavelength. This is one of the key features of these devices.

Fiber Bragg gratings can be fabricated with extremely low loss (0.1 dB) and a high wavelength accuracy is easily achieved ( $\pm 0.05$  nm). In the case of apodized FBGs [9] high adjacent crosstalk suppression (40 dB) can be obtained, as well as flat tops.

The sensitivity of the gratings with temperature is a consequence of thermal expansion of the silica matrix and thermal dependence of the refractive index. Thus, for a temperature deviation  $\Delta T$ , the correspondent deviation in wavelength is given by

$$\Delta\lambda_B = \lambda_B \left( \frac{1}{\Lambda} \frac{\partial \Lambda}{\partial T} + \frac{1}{n_{eff}} \frac{\partial n_{eff}}{\partial T} \right) \Delta T = \lambda_B (\alpha + \xi) \Delta T \quad (2.3)$$

where  $\alpha$  and  $\xi$  are respectively, the thermal expansion coefficient and the thermo-optical coefficient [10]. In the case of silica, the thermal expansion coefficient has an absolute value of  $0.55 \times 10^{-6} \text{ }^\circ\text{C}^{-1}$  and the thermo-optical coefficient a value of  $6.7 \times 10^{-6} \text{ }^\circ\text{C}^{-1}$ . This means that, the change in the reflected wavelength as a result of temperature variations is dominated by the change in the refractive index. On the other hand, mechanical stress sensitivity comes simultaneously from deformation of the silica matrix and alteration of the refractive index due to the photo-elastic effect. The resulting change in the resonant wavelength through mechanical strain, for a longitudinal deformation  $\Delta\varepsilon$ , is given by

$$\Delta\lambda_B = \lambda_B \left( \frac{1}{\Lambda} \frac{\partial \Lambda}{\partial \varepsilon} + \frac{1}{n_{eff}} \frac{\partial n_{eff}}{\partial \varepsilon} \right) \Delta\varepsilon = \lambda_B (1 - p_e) \Delta\varepsilon \quad (2.4)$$

where  $p_e$  represents the photo-elastic constant of the fiber's material [10]. For a fiber with a germanium doped core, where the typical refractive index is  $n_{eff} = 1.465$ , the effective photoelastic constant is  $p_e = 0.22$ . Using these parameters, the expected sensitivity of an FBG at 1550 nm is  $1.2 \text{ pm}/\mu\varepsilon$ .

The temperature coefficient of a FBG is typically  $1.25 \times 10^{-2} \text{ nm}/^\circ\text{C}$  due to the variation in fiber length with temperature. However, it is possible to compensate for this change by packaging the grating with a material that has a negative thermal expansion coefficient. These passively temperature-compensated gratings have temperature coefficients around  $0.07 \times 10^{-2} \text{ nm}/^\circ\text{C}$ . This fact implies a very small 0.07 nm center wavelength shift over an operating temperature range of  $100^\circ\text{C}$ , which

means that they can be operated without any active temperature control. The previously mentioned properties make fiber gratings very useful devices for optical sensing systems applications.

## 2.4 Long Period Gratings

Long-period gratings (LPGs) are fiber structures where the light guided in the core is coupled to several cladding modes at specific resonant wavelengths, as can be seen in Figure 3 [11]. Such type of fiber gratings are optically passive devices which share the intrinsic characteristics of conventional optical fiber sensors, such as electrically passive operation, immunity to electromagnetic interference and multiplexing capability, and show some specific characteristics such as low back reflection and low insertion loss. The low back reflection characteristic occurs because such devices operate in transmission, owing to the coupling of the fundamental guided mode to co-directional cladding modes.

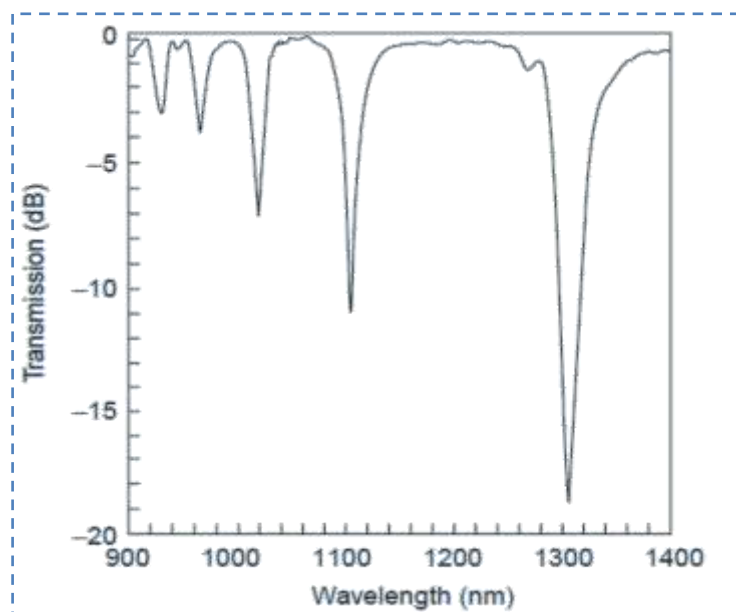


**Figure 3 - Transmission spectrum over a broad wavelength range shows the various cladding modes to which the fundamental guided mode couples [11].**

The coupling between forward modes occurs when the phase matching vector is short, which corresponds to a refractive index spatial modulation periodicity of 100  $\mu\text{m}$  to 10 mm [1], which means an advantage in terms of fabrication when compared with fiber Bragg gratings.



The LPG operation principle is based on the coupling of the fundamental mode to the co-propagating cladding modes and is given by the following expression

$$\beta_{01} - \beta_{cl}^n = \frac{2\pi}{\Lambda} \quad (2.5)$$

where  $\Lambda$  is the grating periodicity required to couple the fundamental mode,  $\beta_{01}$ , to the  $n^{\text{th}}$ -cladding mode  $\beta_{cl}^n$ . As the propagation constant  $\beta$ , is given by

$$\beta = \frac{2\pi n_{eff}}{\lambda} \quad (2.6)$$

the *phase matching* condition can also be described by

$$\lambda_n = (n_{01} - n_{cl}^n)\Lambda \quad (2.7)$$

where  $\lambda_n$  is the resonance wavelength between the fundamental guided mode and the  $n^{\text{th}}$ -cladding mode, and  $n_{01}$  and  $n_{cl}^n$  are, respectively, the effective refractive index of the  $LP_{01}$  mode and the  $n^{\text{th}}$ -cladding mode. Knowing the effective refractive index of the propagating core and cladding modes it is possible to infer the resonance wavelength for each specific grating period [12].

Because LPGs deal with radiation that propagates in the cladding region, its resonance loss band is sensitive to changes in the fiber structure induced by different physical parameters, namely torsion, transverse load and, in particular, when bending is applied to the section of the fiber containing the grating. They are also prone to changes in the surrounding medium, mainly to changes in its refractive index [13]. The LPG devices are also sensitive to strain and their temperature sensitivity can be substantial.

Differentiating equation (2.7) as a function of temperature the following expression is obtained

$$\frac{d\lambda_n}{dT} = \left( \frac{d}{dT} (n_{01} - n_{cl}^n) \right) \Lambda + (n_{01} - n_{cl}^n) \frac{d\Lambda}{dT}. \quad (2.8)$$

The first term represents the thermo-optical effects (the material contribution) and the second term the variation introduced by the LPG period (the waveguide contribution). The LPG response to temperature changes goes from 0.0007 nm/°C to 2.25 nm/°C [14]. Temperature sensitivity in LPG depends mostly on the material contribution term, so the optical fiber type and the resonance mode chosen are the relevant parameters.

Differentiating equation (2.7) as a function of the applied axial strain the following expression is obtained

$$\frac{d\lambda_n}{d\varepsilon} = \left( \frac{d}{d\varepsilon} (n_{01} - n_{cl}^n) \right) \Lambda + \Lambda \frac{d\lambda_n}{d\Lambda}. \quad (2.9)$$

Once more it is clear the material and waveguide contribution in both terms of the expression. The first term describes the period changes introduced by the elastic deformation of the fiber, and the second one the variation introduced in the fiber refractive index due to the applied strain (photo-elastic effect) [12]. The typical wavelength response to the applied axial strain is linear but its sensitivity strongly depends on the order of the excited cladding mode and it could change between the 19.42 nm/%ε and 0.32 nm/%ε [15].

Therefore, LPGs are tunable band-rejection filters that find a wide range of applications as optical fiber sensors [16].

### 2.4.1 Optical Fiber Rocking Filters

An optical fiber rocking filter is a special type of a long period grating which resonantly couples the fundamental polarization modes launched in the principal axes of a single mode birefringent fiber [17, 18]. Typically, the coupling effect is achieved by periodic mechanical twist of the birefringent fiber. If the distance between successive twist points equals the fiber beat length, resonant coupling between orthogonally polarized modes occurs.

From coupled-mode theory [19], the transfer of power between two polarization eigenmodes by periodic perturbation may be analyzed. When only one polarization mode is excited at the start of the interaction region, the fraction of power coupled to the other mode is given by

$$P(z) = (kz)^2 \operatorname{sinc}^2(z\sqrt{k^2 + \delta^2}) \quad (2.10)$$

where  $z$  is the interaction length,  $k$  is the coupling constant, and  $2\delta=\Delta\beta$  is the detuning parameter of the grating, given by

$$\Delta\beta = \beta_x - \beta_y - \frac{2\pi}{\Lambda} \quad (2.11)$$

where  $\beta_x$  and  $\beta_y$  are the propagation constants of the two polarization eigenmodes, and  $L$  is the perturbation length. Complete power transfer can occur only when  $\Delta\beta = 0$ . This is the longitudinal phase-matching condition and is equivalent to matching the spatial period of perturbation  $L$  to beat length  $L_b$  between the two polarization eigenmodes. At this point the input polarization is rotated by  $\pi/2$ , from which it follows that

$$kL = \frac{\pi}{2} \quad (2.12)$$

where  $L$  is the length at which maximum conversion occurs. The bandwidth for maximum conversion is directly related to the number of periods (or the total length) and the angle of rotation, thus, broader bandwidths can be obtained by use of higher twist angles and shorter total lengths [17, 18], as can be seen on Figure 4.

In the sensing field, similarly to what happens with LPGs, rocking filters have proved to be effective sensing elements of different measurands [20].

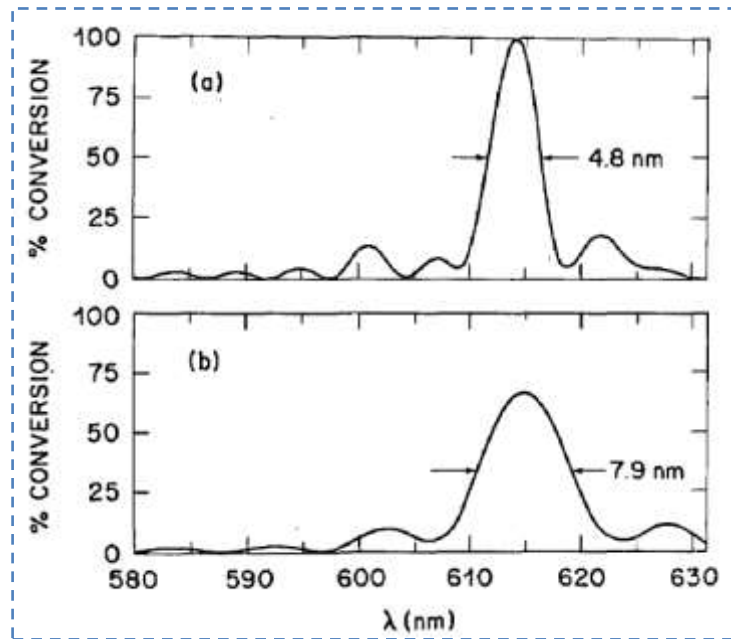


**Figure 4 - Percentage of power converted from one principal axes to the orthogonal axis for: (a) 170 cm fiber length and (b) 100 cm fiber length, according to [17, 18].**

## 2.5 Microstructured Optical Fibers

Since the first publication in 1996 of a microstructured optical fiber (MOF) called photonic crystal fiber (PCF) [21], the optical fiber community has studied the optical properties and fabrication of these new classes of fibers. The different fiber structures with a lattice of air holes running along the fiber length, provide a large variety of novel MOF. A commonly accepted classification of MOF divides the fibers into two main classes: index-guiding and photonic bandgap [22, 23].

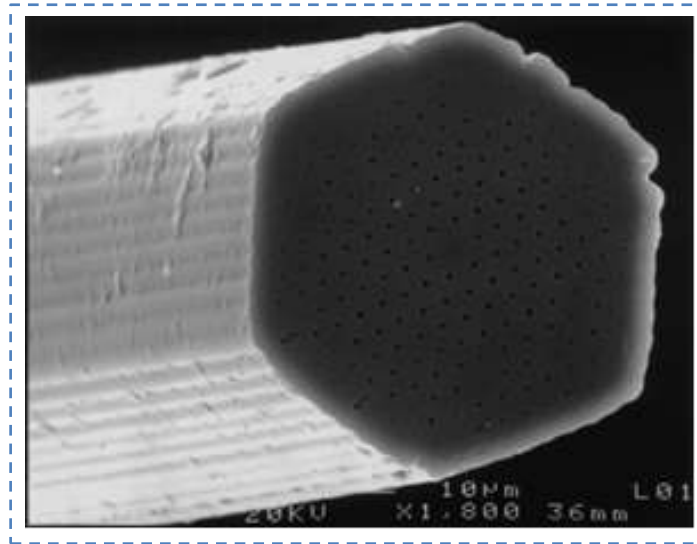


**Figure 5 - Scanning electron microscope (SEM) image of the first Photonic Crystal Fiber [21].**

With index guiding MOF and in optical sensing, *Monro et al.* [24] presented a review that includes a range of applications in which MOF offer new alternatives for sensing applications. On the other hand, *Fini* [25] presented an interesting work in optical sensing of gases and liquids using MOF, reporting improved designs for sensing applications, including detailed simulations of guidance properties.

Photonic bandgap fibers rely on an entirely new mechanism for transmitting light. Light is trapped in the core not by total internal reflection, but by a photonic bandgap (PBG) in the cladding that acts like an insulator for light. This new kind of optical fiber propagation was demonstrated in 1995 by *Birks et al.* [26]. The PBG cladding is made with hundreds of periodically spaced air holes in a silica matrix, typically arranged in a honey combed-like pattern. Because light guidance is no longer dependent on the core's effective index, it becomes possible to create fibers that guide light in an empty or gas-filled core that can be used for optical sensing. Two papers published in *Science* presented the first bandgap guiding fiber in which light is trapped in a ring of glass around a central hole [27], and the first hollow-core photonic bandgap fiber consisting of a triangular lattice of holes from which seven capillaries were removed to form an hollow-core [28].

With the possibility of filling the air holes of MOF with gas, with large interaction lengths, new ways to monitor or detect gases are possible.

Fiber Bragg gratings written in germanium-doped microstructured fibers with reduced cladding mode losses were demonstrated by Eggleton *et al.* [29], showing high potential for sensing. In the same line, Monro *et al.* [24] reported that, in certain conditions, long period gratings written in MOF were insensitive to the external environment. Also, Dobb *et al.* [30] presented a temperature insensitive sensing head based on a long period grating written in a photonic crystal fiber with the capability of measure strain and/or bending. Similarly to what happens with LPGs, rocking filters were also developed in MOFs and have proved, like stated by Kakarantzas *et al.* [17, 31] and by Statkiewicz-Barabach *et al.* [32], to be effective sensing elements of different mesurands.

## 2.6 Summary

The area of optical fiber sensing can be classified considering its measurand modulation as presented in section 2.2. Sections 2.3 to 2.5 briefly described some of the technologies that will be discussed and were object of research in the following chapters.

## Chapter 3 – Optical Sensing with Microstructured Optical Fibers

---

### 3.1 Introduction

Microstructured optical fiber (MOF) technology has recently attracted much interest among researchers because of its special properties and potential applications in novel fiber devices. The optical properties of such fibers may vary in a dramatic manner depending on its geometry, inter-hole spacing, hole size and hole lattice arrangement. Although they have peculiar characteristics, an important issue on the practical application of such fibers is their connection with single mode fibers (SMF) with a low loss. Section 3.2 presents the study of a splicing technique developed to achieve low loss in a splice between a MOF and a SMF.

Further, an evaluation of the coupling losses in a hollow-core MOF is presented in section 3.3. A study of the dependence such losses on lateral and axial gap misalignment between SMF and two different types of HC-MOFs, and the applicability of the splicing technique described in section 3.2, will be also shown.

Multi-parameter measurement/discrimination has been a subject of intensive worldwide research and microstructured optical fibers offer new implementation possibilities for the measurand discrimination concept. In section 3.4 two sensing configurations are proposed, aiming for such functionality, but with different characteristics. One of them, based on a single Bragg grating inscription in a microstructured optical fiber, permits us to obtain a temperature-independent strain measurement; the other, supported by a structure formed by two Bragg gratings, one written in a microstructured fiber and the other on a standard SMF fiber, allows us to perform simultaneous measurement of these parameters.

Long period gratings (LPGs) can also be written in microstructured fibers. Due to the MOFs particular design, interesting behaviours can be observed in the attenuation

band spectrum profile of the LPG when it is subjected to a physical parameter. Rocking filters are a special type of LPGs that can also be drawn in highly birefringent fibers. In section 3.5 the spectral characteristics and sensing capabilities of two different kinds of optical filters, LPGs and rocking filters, are compared. Both elements were fabricated by the CO<sub>2</sub> laser inscription method in a highly birefringent photonic crystal fiber.

Several microstructured fibers have a periodic structure layout in the fiber cladding that induces a photonic bandgap (PBG) behaviour. The cladding of the fiber acts as a periodic crystal that forbids propagation of light in specific wavelength ranges. Light with wavelengths in these bandgaps can be confined inside the air core and propagates along it. The spectral shift of the PBG edge of a HC-MOF induced by physical measurands, such as strain, temperature, curvature, and twist, is characterized in section 3.6.

### 3.2 Microstructured Fiber Splicing

Good splicing of microstructured fibers to standard SMF is vital in order to enhance their potential use in communication and sensing systems [33]. Furthermore, the splicing of fibers with different glass materials is difficult, due to the different coefficients of thermal expansion and melting temperatures of the two fibers.

In 1999, Bennett [34] reported a splice loss of 1.5 dB using a conventional fusion splicer between a holey fiber and a SMF-28<sup>TM</sup> (Corning). An alternative method has been proposed in 2003 by Chong [35], using a CO<sub>2</sub> laser, and a splice loss in the range of 1.3-2.8 dB was obtained. This technique is used in order to avoid holes collapsing and condensation trapping inside the microstructured fiber during the splicing process. Also in 2003, Bourliaguet [36] described a simple method that can be used to splice microstructured optical fibers, relying only on commercial electric-arc splicers [37-39]. The results were presented in terms of fusion losses and tensile strength. A range between 0.6 and 0.9 dB fusion losses were obtained for 0.40 or 0.45 second arc durations, respectively.



### 3.2.1 Microstructured Fiber Characteristics

In the following study a simple method to fuse a MOF fiber with a SMF-28™ is presented, which achieved, to the best of our knowledge the lowest splice loss reported to date with these fibers.

The highly nonlinear photonic crystal fiber used in these experiments has been supplied by Crystal Fiber A/S (NL 2.3 1555) [40]. This MOF has a core diameter of 2.3  $\mu\text{m}$ , a cladding diameter of 125  $\mu\text{m}$  and a numerical aperture of  $\sim 0.5$ . An effective area of 7  $\mu\text{m}^2$ , losses of 60 dB/km at 1550 nm and a non-linear coefficient  $\gamma$  of 18  $\text{W}^{-1}\text{km}^{-1}$  are specified. The average pitch-to-hole size ratio is  $d/\Lambda = 0.5$  and the pitch  $\Lambda$  (period of hole structure in cladding) is 1.6  $\mu\text{m}$ . According to [41], it exhibits single-mode operation at the third window of optical communications since it has a  $\lambda/\Lambda$  ratio of  $\sim 0.975$ . The fiber had a length of 9 meters. Figure 6 shows the cross-sectional SEM image of the microstructured fiber. This type of microstructured fibers can be applied in wavelength conversion setups, Raman and parametric amplification schemes, and also for signal regeneration or pulse compression.

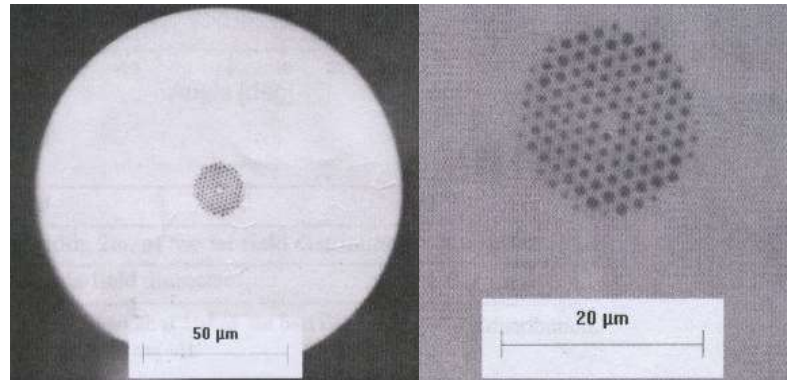


**Figure 6 - Cross-sectional SEM images of the MOF (NL 2.3 1555) from Crystal Fiber A/S.**

### 3.2.2 Experimental Results

The splice technique reported here relies on butting the fibers and then, the electric arc discharge being applied over the SMF region. This requires the electric arc fusion splicer to be operated in manual mode to control the region of the SMF (core diameter

and numerical aperture are respectively  $8.2\ \mu\text{m}$  and  $0.4$ ) where the electric arc should be applied. During the splicing process the results for the losses were obtained, using the well-known cutback technique, by injecting light into the SMF from a tuneable laser source (TL200C from Thorlabs, Inc.) operating with a wavelength peak of  $1550\ \text{nm}$ . The procedure is described as follows.

First, the fibers were automatically positioned at a distance of  $25\ \mu\text{m}$  of each other (the region where the arc usually happens) as seen in Figure 7 (a). From this moment on all the fusion process was manually operated. The microstructured fiber position was kept fixed and the SMF was moved against the microstructured fiber, using the translation stage of the splice machine. The two fibers were aligned and butted, while the fiber losses of this alignment were quantified. After optimization of the alignment, a minimum loss of  $5\ \text{dB}$  was measured. This  $5\ \text{dB}$  value was achieved when both fibers were aligned without any matching.

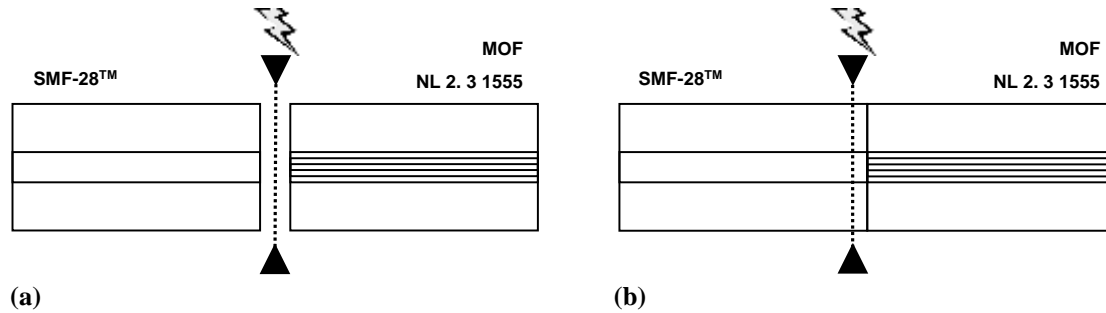


**Figure 7 - a) Result of the Fujikura's splice machine automatic jointing of the fibers (the  $25\ \mu\text{m}$  gap between both fibers is seen). Now the MOF is fixed and the SMF-28™ is moved on; b) Result of manual alignment (After this, the electric arc is discharged).**

Next, the splicing process was carried out by applying the electric arc near the top of the SMF fiber that has been butted to the microstructured fiber, as shown in Figure 7 (b). Then Fujikura's internal units for the electric arc current (given in bits in the fusion machine display) were chosen to achieve an appropriate splice. Starting, a low electric arc discharge of  $13.675\ \text{mA}$  (5 bit value in Fujikura's internal units) was applied. Usually, in a conventional splice between two SMF fibers, a current of  $\sim 14.2\ \text{mA}$  (20 bit value in Fujikura's internal units) is used. The current choice was made through several tests, namely with 5, 10, 15 and 20 bits. Comparing all current tests, it was verified that with the 5 bit value (and also a  $\sim 14.2\ \text{mA}$  current), a significant decrease of the splice loss, of about  $1\ \text{dB}$ , was achieved. All the other

parameters that the splice machine uses (overlap, gap, prefuse, etc), had remained the same as those normally used for standard single mode fiber. Since the microstructured fiber consists of air holes across the fiber cross-section, the electric arc required to melt the MOF is expected to be smaller than the required for the SMF. In order to protect the MOF properties and the hole-arrangement profile, lower discharge currents had been used and the electric arc was mainly applied over the SMF.

The dependence of the splice loss with arc duration was also investigated. The results given are presented in terms of arc duration time for a constant current power. In this experiment the arc duration time was first set at 2000 ms (time used for SMF fibers splicing) and was gradually decreased until the final value corresponding to 200 ms was reached. The time step of the splice machine is set to 100 ms and the measurement results are shown in Figure 8.

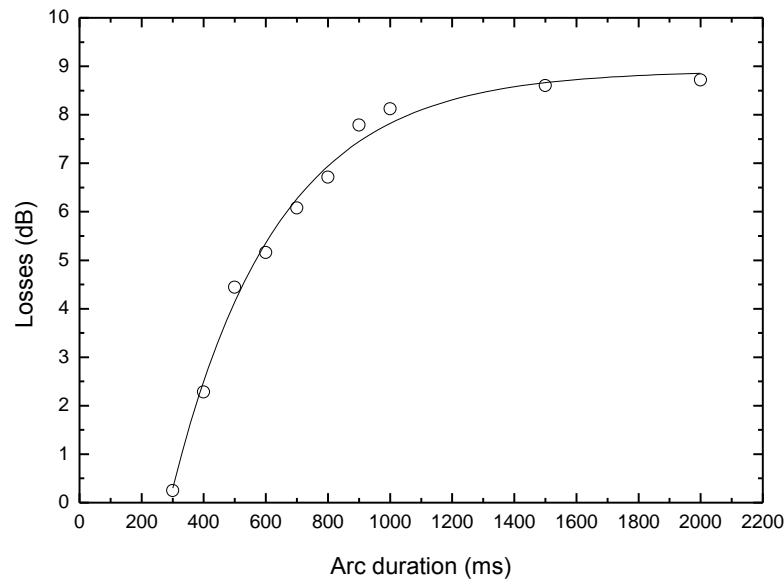


**Figure 8 - Evaluation of losses as a function of arc duration, with a constant current power.**

The optimized loss of the splice was achieved for an arc duration of 300 ms, where a minimum loss value of 0.25 dB was obtained. Up to this value all the splices passed the Fujikura's tension test (corresponding to 200 gr). For an arc duration of 200 ms, the loss value was 3.8 dB, and it was verified that the two fibers were not well fused.

This result indicates that both fibers are not really spliced, i.e., the arc duration time is too small to obtain the glass fusion temperature.

Figure 9 shows the splice (X and Y directions) between the MOF and SMF. Several splice attempts were carried out and the measured loss obtained for 300 ms and 13.7 mA was in the range of 0.25-0.6 dB. These results are in good agreement with the Crystal Fiber's NL-2.3-1555 specifications (with splice loss at 1550 nm < 0.65 dB).

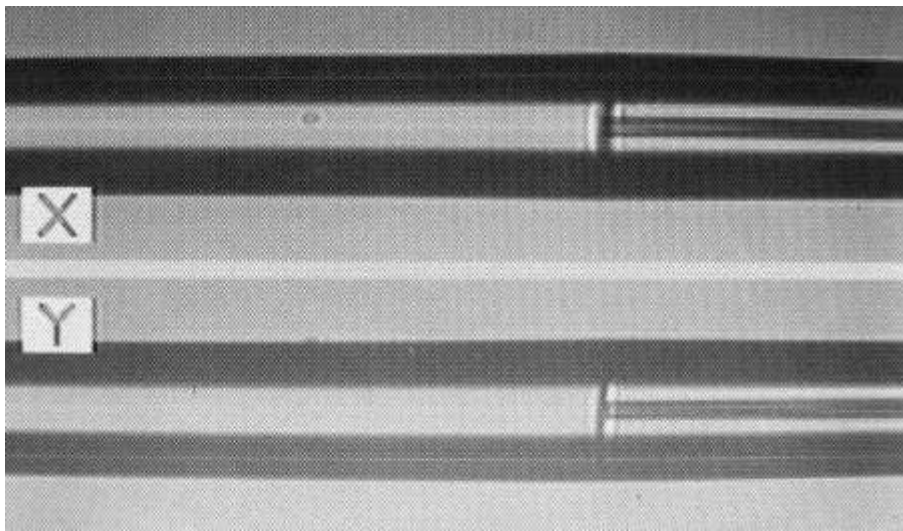


**Figure 9 - Visualization of the SMF-28<sup>TM</sup>/MOF splice in the Fujikura's FSM-40S screen.**

Some tests were also performed by varying the applied discharge current in 0.1 mA steps, keeping the arc duration constant at 300 ms. A splice loss in the range of 0.25-3.3 dB was obtained for electrical arc discharge currents of 4 to 10 bits (in Fujikura's internal units). A statistical study was also conducted that shows that the average value for the splice loss between the microstructured fiber and the SMF was 0.4 dB.

### 3.3 Coupling Losses Evaluation in Hollow Core Microstrutured Fibers

As observed in the previous section, to be practically useful in optical sensing systems, microstructured fibers must be connected to standard single mode fibers (SMF), which remains a rather delicate process. The splice losses between

hollow-core microstructured fibers have been studied in the last years by several groups [42-44].

In order to allow the use of microstructured hollow core fibers in gas sensing, a study of the splicing and coupling losses was performed for two different types of HC-MOFs, 19-cell and 7-cell HC-MOF, shown in Figure 10.

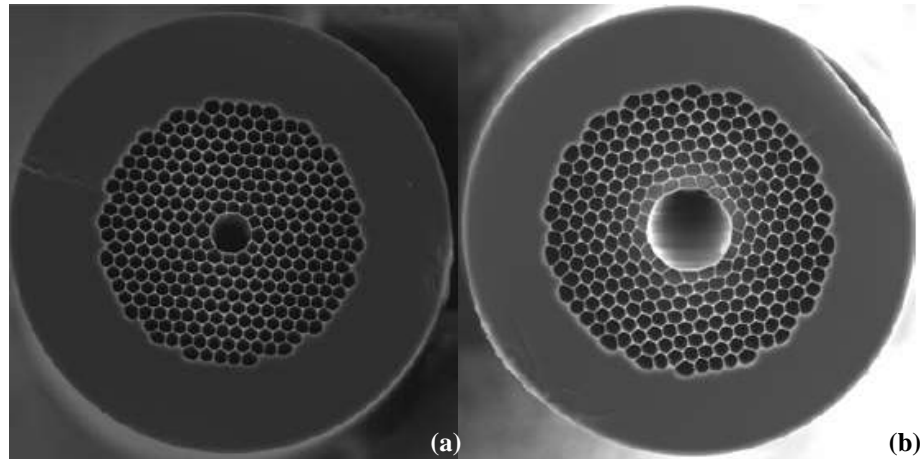


**Figure 10 - Hollow-core microstructured fibers from BlazePhotonics:**  
a) 7-cell HC-MOF (HC-1550-02); b) 19-cell HC-MOF (HC19-1550-01).

Such fibers were designed to guide light in the 1.55  $\mu\text{m}$  window and its operation bandwidth can be observed in Figure 11.

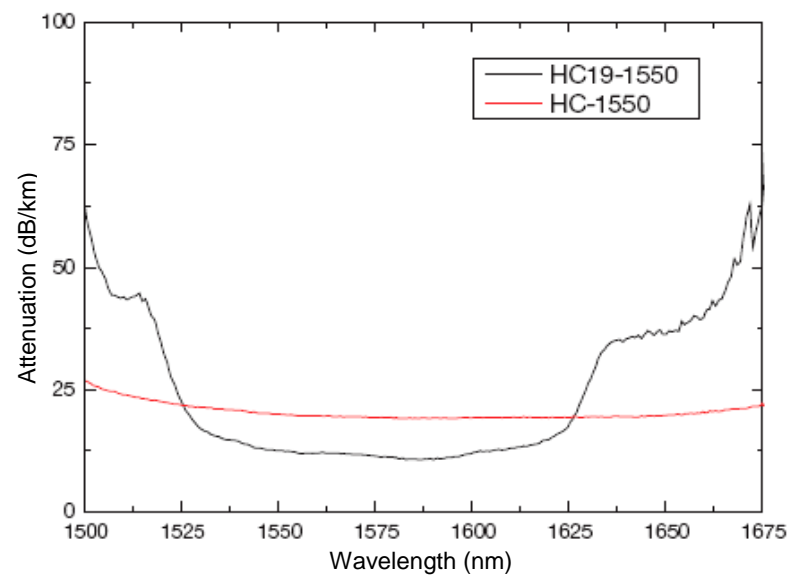


**Figure 11 - Transmission spectra for a 7-cell HC-MOF (HC-1550-02) and a 19-cell HC-MOF core fiber (HC19-1550-01), both designed for operation at 1.55  $\mu\text{m}$ .**

### 3.3.1 Modelling

A brief modelling analysis and experimental measurements were made in order to allow the multiple-coupling gaps loss assessment in these types of fibers. The coupling coefficient between fiber 1 and fiber 2 can be determined from their mode profiles given by the equation (3.1):

$$C_{12} = \frac{\int E_1 E_2^* dS}{\sqrt{\int |E_1|^2 dS \int |E_2|^2 dS}} \quad (3.1)$$

If the fibers are separated by a distance  $d$ , as depicted in Figure 12, the mode field of one fiber has to propagate to the cut-end of the other fiber, as described in equation (3.2).

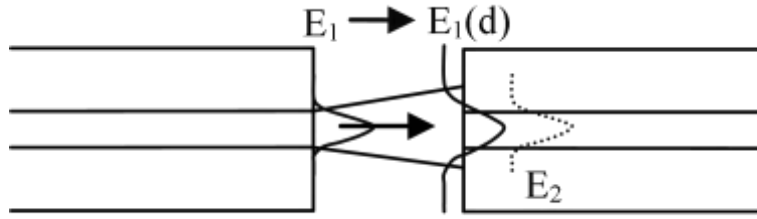


**Figure 12 - Coupling between two fibers separated by distance  $d$ .**

$$C_{12} = \frac{\int E_1(d) E_2^*(0) dS}{\sqrt{\int |E_1|^2 dS \int |E_2|^2 dS}} \quad (3.2)$$

The mode field of the SMF can be easily computed. The mode fields of 7-cell HC-MOF and 19-cell HC-MOF are presented in Figure 13 (a) and (b), respectively.

The modes of HC-MOF are not radially symmetric, therefore to simplify the analysis field amplitudes of HC-MOF modes were radially averaged. The side lobes around the central spot of the 19-cell HC-MOF are small and have alternating amplitude signs. The light transmitted by these side lobes strongly diverge and will miss the second fiber core. Also, the side lobes of the first fiber are very probably misaligned with the side lobes of the mode of the second fiber.

The estimation of the portion of light propagating in the side holes of a 19-cell HC-MOF is 1.8%. Therefore, it was assumed that the light in the side lobes of 19-cell HC-MOF is effectively lost and not coupled to the other fiber. The average mode profiles of 7-cell HC-MOF, and 19-cell HC-MOF are shown in Figure 13 (c) and (d).

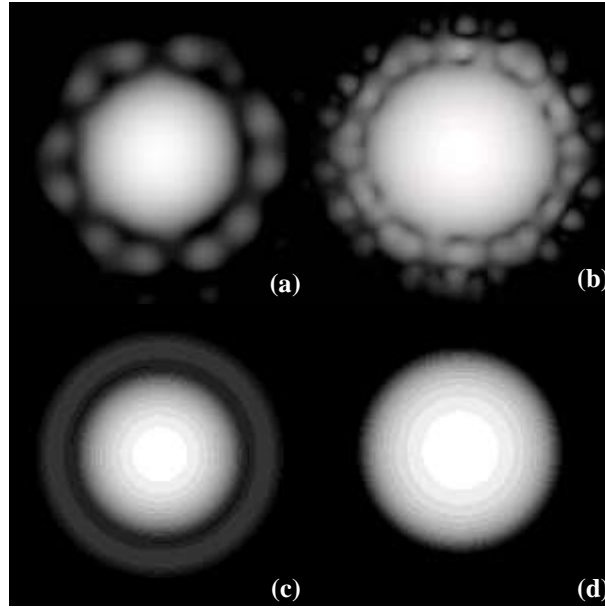


**Figure 13 - a) Mode of 7-cell HC-MOF; b) Mode of 19-cell HC-MOF; c) Averaged mode of 7-cell HC-MOF; d) Averaged mode of 19-cell HC-MOF.**

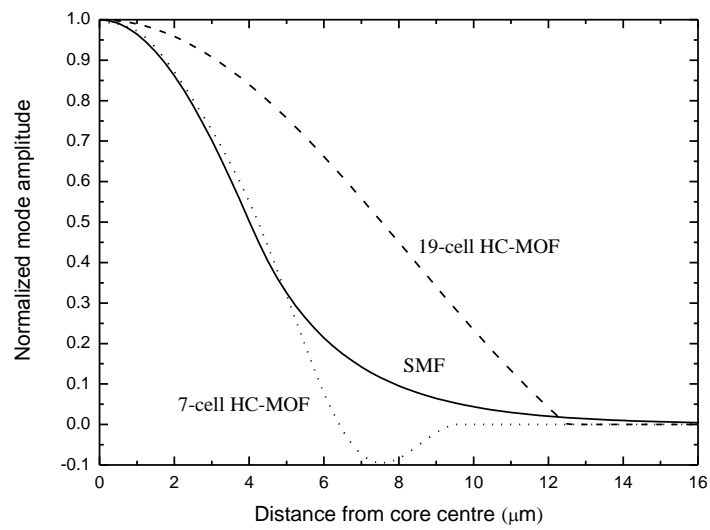


**Figure 14 - Radial average of the mode profiles for SMF, 7-cell HC-MOF, and 19-cell HC-MOF**

The mode profile of the left end fiber of Figure 12 (assuming it is centre-symmetrical) was used, and simulated how it propagates in the free space between the two fibers by decomposing the beam into space Fourier components. The coupling coefficients SMF  $\rightarrow$  7-cell HC-MOF, SMF  $\rightarrow$  19-cell HC-MOF, and 19-cell HC-MOF  $\rightarrow$  19-cell HC-MOF, were then calculated according to equation (3.2).

The decomposition of the mode profiles of SMF, 7-cell HC-MOF, and 19-cell HC-MOF showed that more than 95% of the beam is in the zero-order Gaussian beam (Figure 14). The major difference between the fibers under analysis is then the mode field diameter. Therefore, it is a good approximation to consider that the beams have Gaussian profiles. The coupling coefficient between two Gaussian beams radiated from two fibers at distance  $d$  can be found from equation (3.2) and is defined as follows,

$$|C_{12}|^2 = \frac{4}{2 + \frac{z_2}{z_1} + \frac{z_1}{z_2} + \frac{d^2}{z_1 z_2}} \quad (3.3)$$

where  $z_i = \pi w_i^2 / \lambda$  and  $w_i$  are the beam waists. In Figure 15 computed results from this equation can be found.

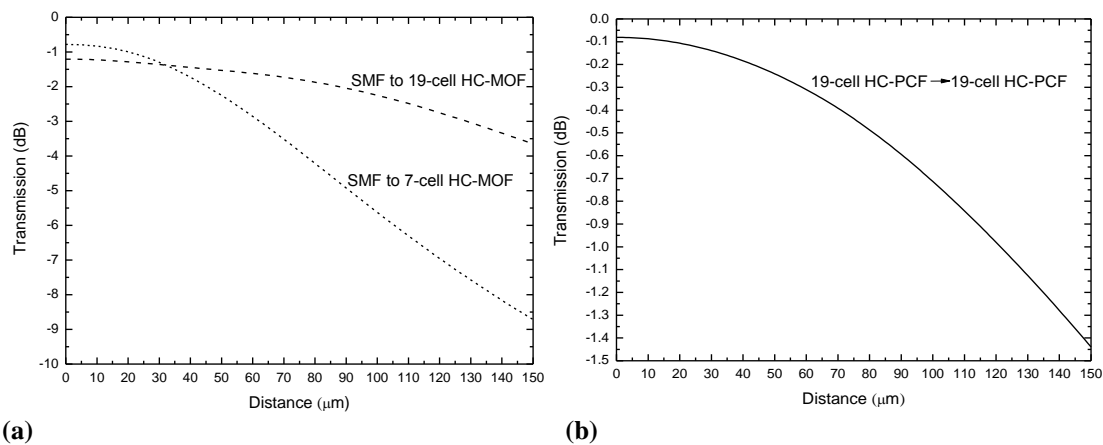
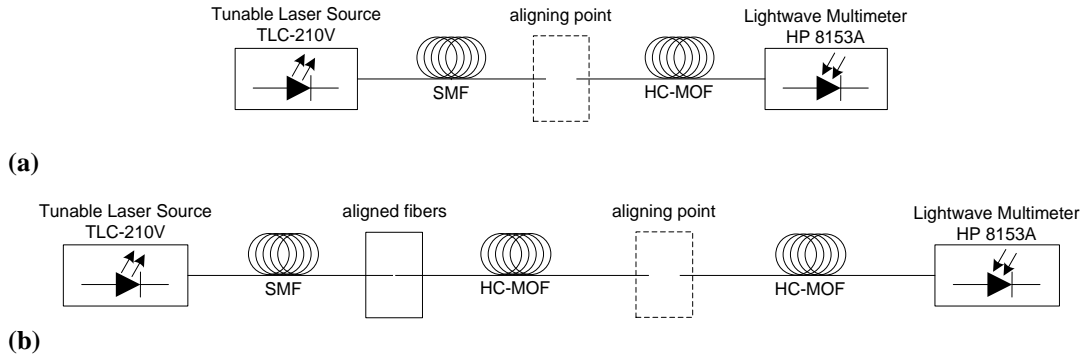


**Figure 15 - a) Coupling coefficients, SMF  $\rightarrow$  7-cell HC-MOF, SMF  $\rightarrow$  19-cell HC-MOF; b) Coupling coefficients, 19 cell HC-MOF  $\rightarrow$  19-cell HC-MOF.**

For evaluating gap coupling loss between a SMF and a HC-MOF, and also between two HC-MOFs, several measurements were made to evaluate the dependence on

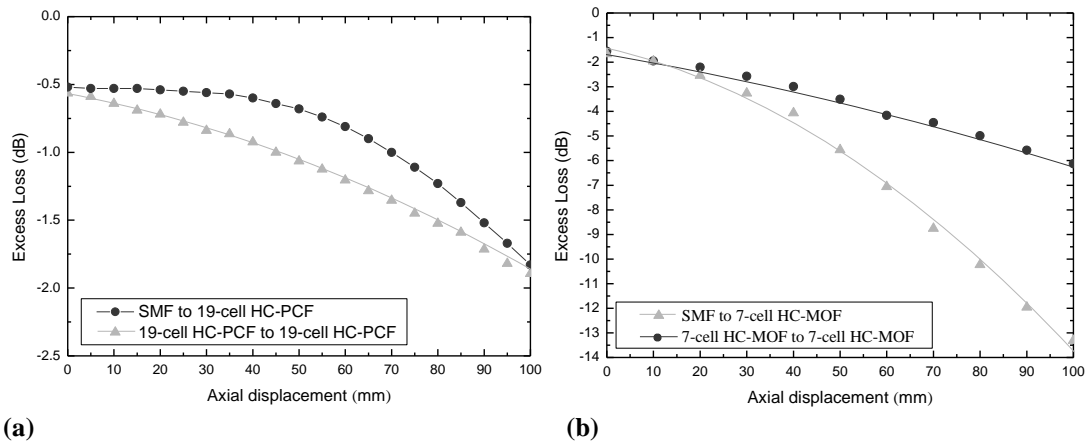


lateral and axial gap misalignment. A tuneable laser with 10 mW of maximum power was used as optical power source. The alignment between different fibers was achieved through a system with an axial step resolution of 5  $\mu\text{m}$  and a horizontal/vertical step resolution of 0.1  $\mu\text{m}$ . Light detection was made through a large area detector for the 1.55  $\mu\text{m}$  wavelength region. The experimental setup used for the measurements is the one depicted in Figure 16.



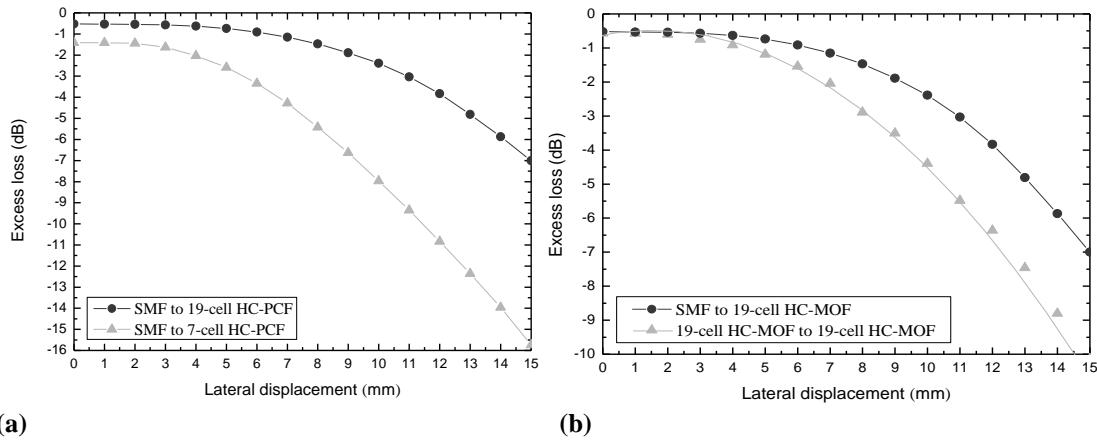
**Figure 16 - Setup used for the experimental evaluation of the coupling loss between:**  
**a) SMF and HC-MOF; b) two portions of HC-MOF**

Figure 17 shows the obtained results for axial displacement between SMF and HC-MOFs, and between two HC-MOFs of the same type. The excess loss values presented are referenced to minimal loss corresponding to direct fiber connection between the laser and the photodetector. The obtained results show that for similar axial displacements, the 19-cell HC-MOF has much lower loss dependence than the 7-cell HC-MOF, as can be seen on Figure 17 (b).



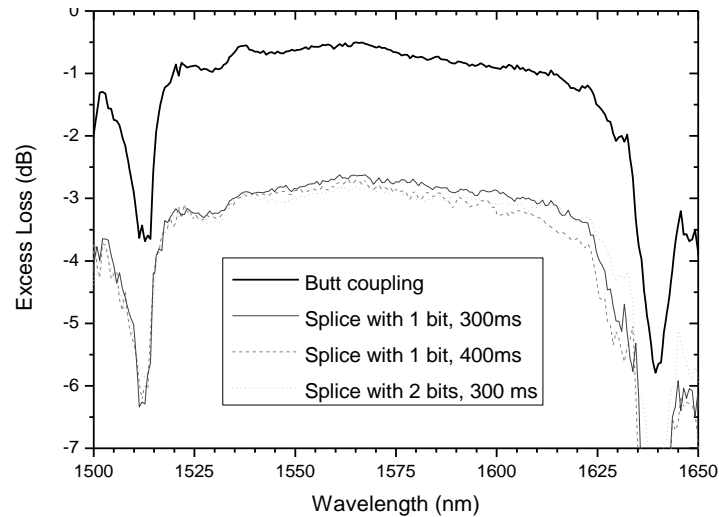
**Figure 17 - Excess loss dependence on axial displacement: (a) between a SMF and 19-cell HC-MOFs, and between two 19-cell HC-MOFs; (b) between a SMF and 7-cell HC-MOF, and between two 7-cell HC-MOFs.**

Figure 18 (a) shows the obtained results for lateral displacement between SMF and HC-MOFs. Figure 18 (b) shows the results for lateral displacement between two 19-cell HC-MOFs. During these measurements, the fibers were kept in close proximity. The presented results confirm the previous tendency; the 19-cell HC-MOF loss coupling has much lower dependence on lateral displacement both with SMF and with another 19-cell HC-MOF. The coupling losses in the 7-cell HC-MOF have always a larger dependence either on lateral or axial gap misalignment. This behaviour was expected due to the higher mode field diameter of the 19-cell HC-MOF when compared to both the SMF fiber and the 7-cell HC-MOF which are quite similar. These results indicate that 19-cell HC-MOF is less susceptible to misalignments induced during multiple-coupling gaps implementation or during system operation due to environmental effects.



**Figure 18 - Excess loss dependence on lateral displacement: (a) between a SMF and 19-cell HC-MOF and between a SMF and a 7-cell HC-MOF; (b) between a SMF and 19-cell HC-MOFs, and between two 19-cell HC-MOFs.**

Furthermore, spectral measurements were performed for evaluating splicing losses at different conditions between SMF and 19-cell HC-MOF. Obtained results are presented in Figure 19. From the previous experiments it was concluded that for an arc current around 13.5 mA, the ideal electric discharge time is around the 300-400 ms, using the splicing technique described in section 3.2 [45].



**Figure 19 - Experimental results obtained for estimation of losses in light coupling between SMF and 19-cell HC-MOF in different cases.**

A simple analysis of splice losses between 19-cell HC-MOF and SMF showed that the lowest insertion loss attainable is  $\sim 2$  dB. The use of these splicing parameters allows reproducible splice losses to be attained.

In Figure 20 photographs of splices obtained under different conditions are presented. The physical shapes of the different splices do not significantly affect the splice losses between SMF and HC-MOFs. Nevertheless, even using optimum splice parameters the coupling efficiency is always lower when compared with straight butt-coupling.

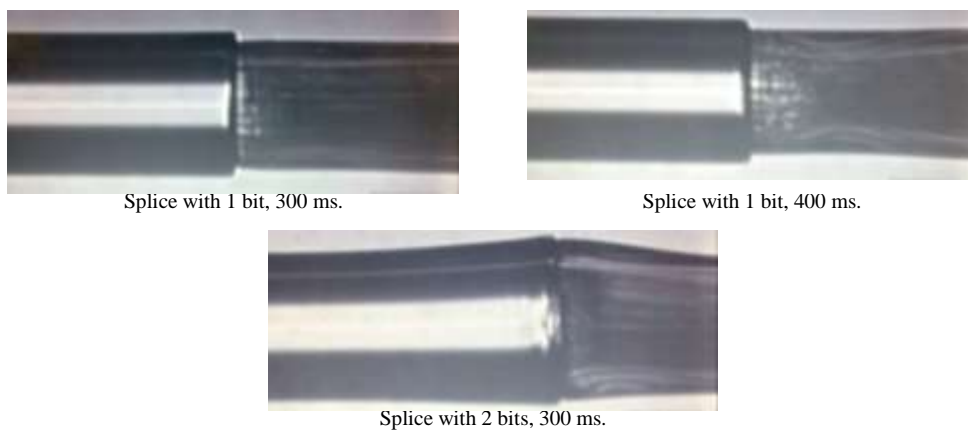


**Figure 20 - Photographs of the different splices between SMF and 19-cell HC-MOF.**

### 3.4 Strain and Temperature Measurements with Microstructured Fibers

The use of microstructured fibers can be an alternative solution not only for gas sensing, but also for the deployment of sensors for simultaneous measurement of various multi-parameters. The following study is a contribution along this line. Two sensing configurations are proposed aiming for such functionality, one based on a single Bragg grating inscription on a microstructured optical fiber, and another on a structure formed by two Bragg gratings, one written in a microstructured fiber and a second on a standard SMF fiber. The characteristics of these configurations are experimentally determined and their relative performance compared.

#### 3.4.1 MOF Bragg Grating Structure

Using the phase mask technique with a KrF<sub>2</sub> Excimer laser ( $\lambda_{UV} = 248$  nm), a 10 mm long FBG was fabricated on a microstructured optical fiber supplied by Crystal Fiber A/S (NL 2.3 1555) [40]. This fiber, shown in Figure 21, had a germanium-doped core with 2.3  $\mu\text{m}$  diameter and a 125  $\mu\text{m}$  cladding diameter. An effective core area of 5  $\mu\text{m}^2$  and a loss of 60 dB/km at 1550 nm were specified. The average pitch-to-hole size ratio was  $d/\Lambda=0.5$  and the pitch period of the hole structure in the cladding was  $\Lambda=1.6$   $\mu\text{m}$ . According to the literature [41], this fiber is single-mode in the third telecommunication window. The microstructured region is slightly elliptical (2.8 %), and therefore there is birefringence that turns out into the polarization maintaining properties of this fiber.

This birefringence is evident from the optical spectrum of the MOF grating structure that can be observed in Figure 21. The two resonance peaks have wavelengths of  $\lambda_{\text{fast}} = 1508.43$  nm (fast axis) and  $\lambda_{\text{slow}} = 1508.61$  nm (slow axis). From the difference between these two values (0.18 nm) a birefringence of  $1.59 \times 10^{-4}$  @ 1508 nm can be calculated, in good agreement with reported values in literature for this type of fiber [40].

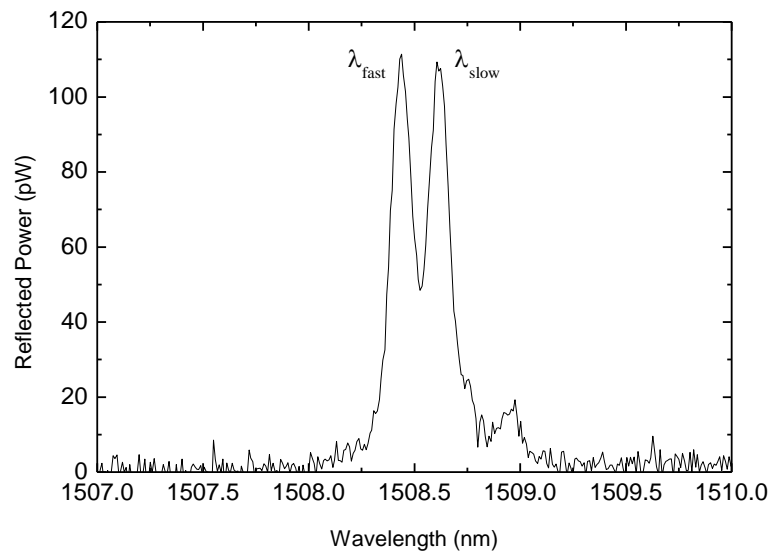


**Figure 21 - Optical spectrum of the FBG written in the NL 2.3 1555 fiber.**

The experimental setup is showed in Figure 22. A broadband optical source (BBOS) was used to illuminate the sensing head and the Bragg wavelength shifts were recorded using an optical spectrum analyser (OSA) with a standard resolution of 0.05 nm. A LabView platform was utilized for monitoring, processing and storage of the data in a personal computer. The sensing head was bonded to a translation stage (TS) with a displacement resolution of 1  $\mu\text{m}$  and placed in a tubular furnace, which permits the temperature of the sensing head to be set with an error smaller than 0.1  $^{\circ}\text{C}$ .

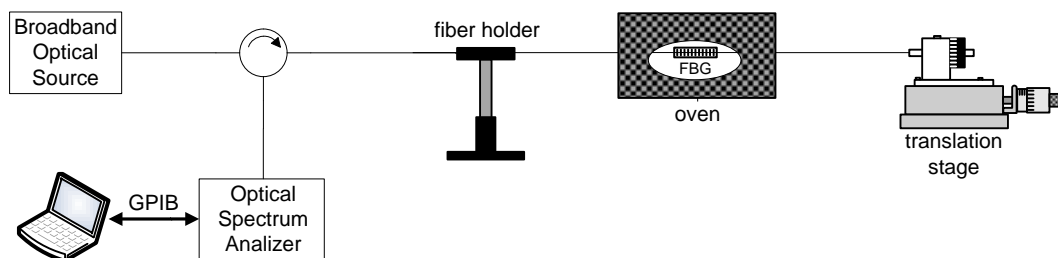


**Figure 22 - Experimental apparatus for strain and temperature measurements**

The lead and return fiber is a standard SMF-28<sup>TM</sup> optical fiber. This was spliced to the MOF using a conventional splice machine and following the technique described in section 3.2, resulting in a splice loss of  $\sim 0.3$  dB.

The response to temperature and strain of the MOF Bragg grating was determined separately. Figure 23 shows the experimental results obtained when the temperature is fixed to 20 °C and strain was varied. It can be noticed a difference of ~ 3.2 % between the strain coefficients of the two resonance peaks. This difference is attributed to the slightly elliptical geometry of the air hole region of the MOF.

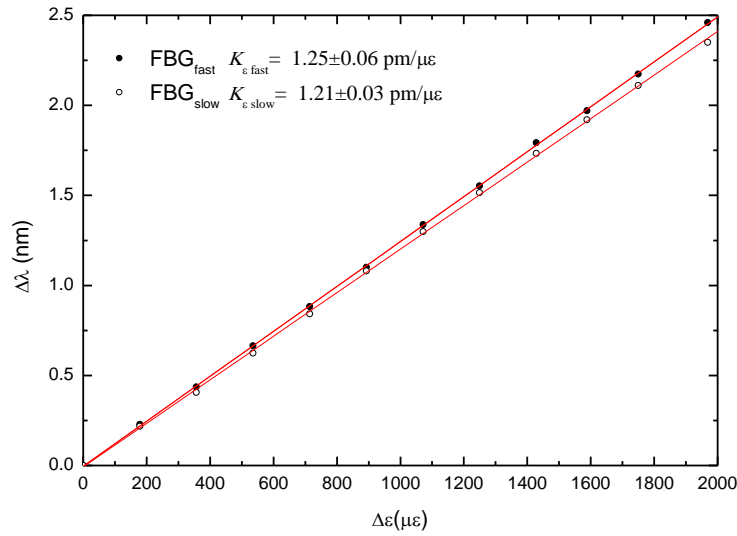


**Figure 23 - Strain response of the fast and slow axis signatures of the grating in the microstructured fiber.**

On the other hand, Figure 24 shows the results obtained when the temperature changed from 20 °C to 120 °C at constant strain. In this case, the difference in the temperature sensitivity of the two FBG resonant peaks is negligible (smaller than 1%). Considering the MOF does not have frozen stress regions, this temperature behaviour was expectable. It is interesting to note that in standard stress based Hi-Bi fibers the strain and temperature dependences are opposite, i.e., the strain sensitivities are similar and the temperature sensitivities are different [46].

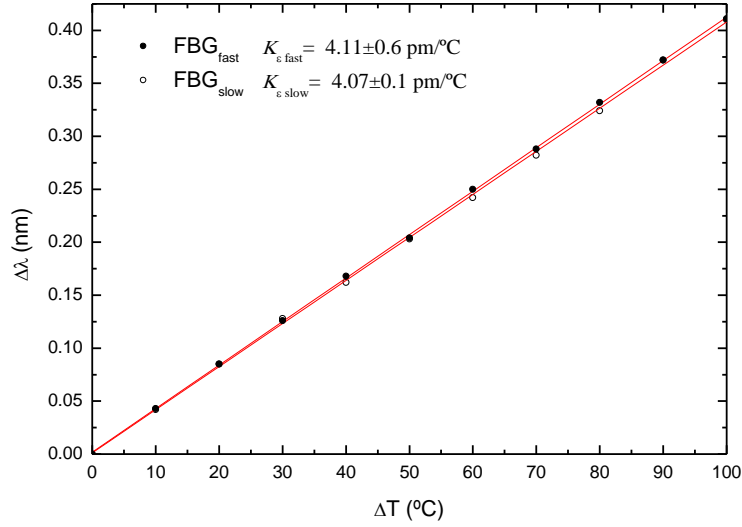


**Figure 24 - Temperature response of the fast and slow axis signatures of the grating in the microstructured fiber.**

In view of the different strain sensitivities of the fast and slow axis signatures of the grating written in the MOF fiber, it is theoretically possible to measure simultaneously strain and temperature using the following matrix equation [47]

$$\begin{bmatrix} \Delta T \\ \Delta \varepsilon \end{bmatrix} = \frac{1}{D} \begin{bmatrix} K_{\varepsilon \text{ slow}} & -K_{\varepsilon \text{ fast}} \\ -K_{T \text{ slow}} & K_{T \text{ fast}} \end{bmatrix} \begin{bmatrix} \Delta \lambda_{\text{fast}} \\ \Delta \lambda_{\text{slow}} \end{bmatrix} \quad (3.4)$$

where  $D = K_{T \text{ fast}} K_{\varepsilon \text{ slow}} - K_{\varepsilon \text{ fast}} K_{T \text{ slow}}$ . From the coefficients given in Figure 23 and Figure 24, equation (3.4) turns out to be

$$\begin{bmatrix} \Delta T \\ \Delta \varepsilon \end{bmatrix} = -\frac{1}{0.117} \begin{bmatrix} 1.21 & -1.25 \\ -4.07 & 4.11 \end{bmatrix} \begin{bmatrix} \Delta \lambda_{\text{fast}} \\ \Delta \lambda_{\text{slow}} \end{bmatrix} \quad (3.5)$$

This configuration based in two resonant peaks can be used as a temperature independent strain sensor due to the different strain sensitivities. Figure 25 shows the immunity of the sensing head to temperature and also the response of the sensing head to the applied strain. This result was obtained when the system output is given by

$(\lambda_{\text{slow}} - \lambda_{\text{fast}})$ . A strain resolution of  $\pm 7 \mu\epsilon$  over a total measurement range of  $2000 \mu\epsilon$  has been achieved.

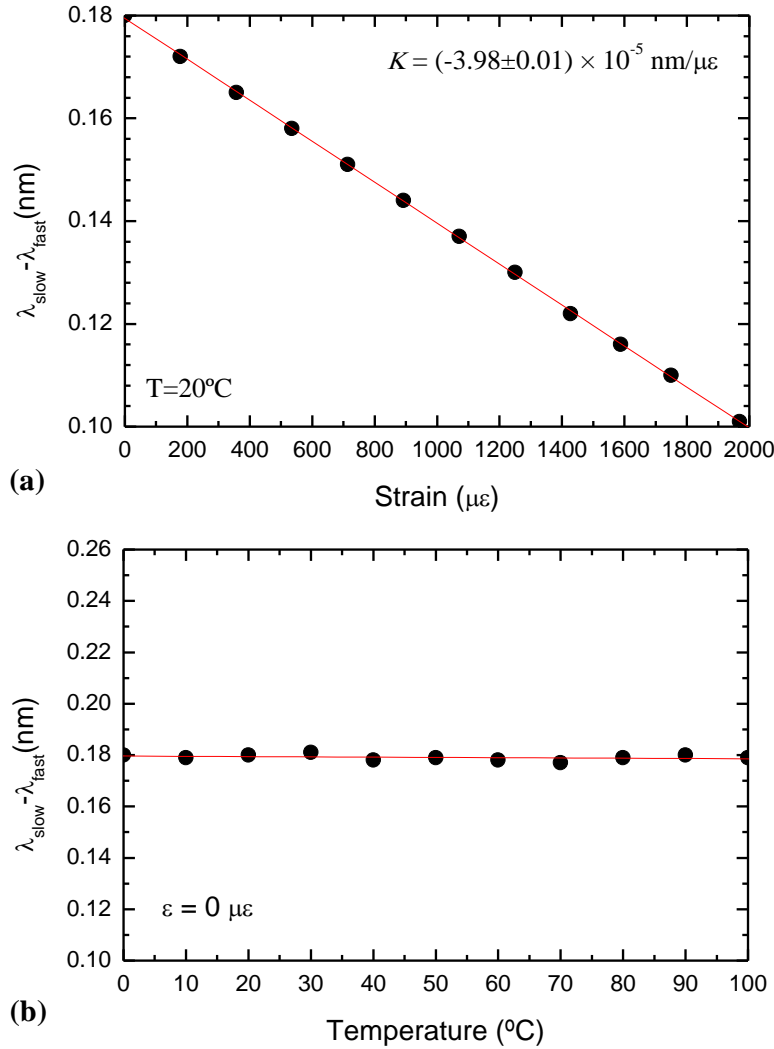


**Figure 25 - Temperature-independent strain behavior of the sensor consisting of a Bragg Grating written in a MOF: a)  $T = 20^\circ\text{C}$  and b)  $\epsilon = 0 \mu\epsilon$ .**

The performance of this sensing configuration was experimentally determined by undertaking strain variations in a range of  $2000 \mu\epsilon$  at a fixed temperature ( $50^\circ\text{C}$ ) and the other way around, i.e., temperature variations in a range of  $100^\circ\text{C}$  for a specific applied strain ( $\Delta\epsilon = 1000 \mu\epsilon$ ). The results are expressed in Figure 26, from where the maximum errors relative to the applied values can be seen.



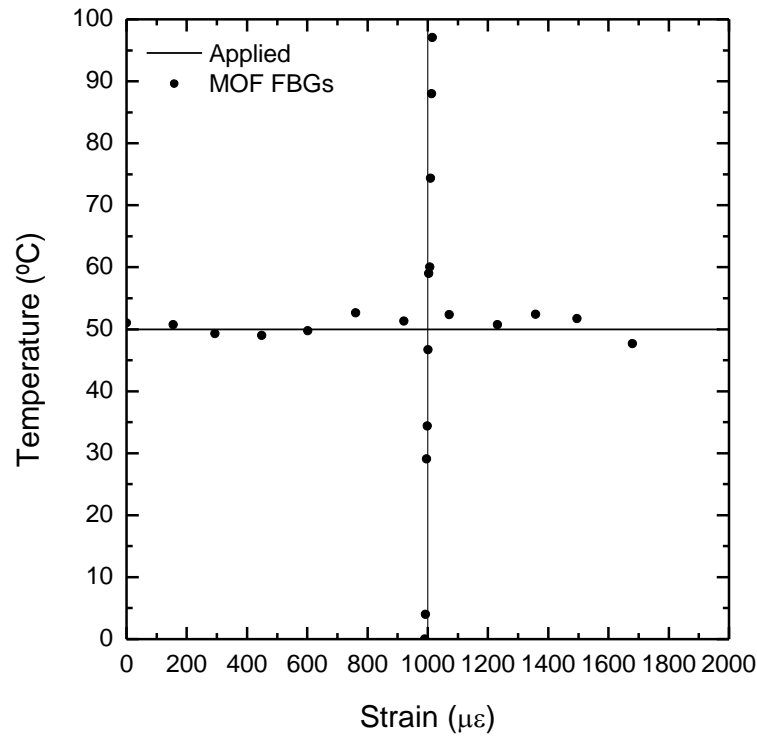


**Figure 26 - Sensor output as determined by equations (3.4) and (3.5) for an applied strain at a constant temperature and the temperature variation at a constant strain.**

The resolutions achieved were  $\pm 2.3^{\circ}\text{C}$  and  $\pm 18.5 \mu\epsilon$  for temperature and strain, respectively, which are typical values for simultaneous measurement schemes relying on the two signatures of a Hi-Bi grating.

It is worthwhile to emphasize the simplicity of this structure, where only one FBG writing step is required and the problem of the losses appearing in the splice junctions of different fibers are avoided when the WDM multiplexing of several sensing heads is considered.

### 3.4.2 MOF and SMF Bragg Gratings Combined Structure

In order to achieve simultaneous measurement of temperature and strain a second configuration was studied. It consisted of a sensing head implemented around the splice region between a standard SMF and a microstructured fiber. FBGs were written in each side of the splice using the phase mask technique described previously,

resulting in a separation of 10 mm (being the total length of the sensing head  $< 30\text{mm}$ ). The same phase mask was used in both cases, resulting in Bragg wavelengths of 1556 nm for the SMF and 1508 nm for the MOF ( $\lambda_{\text{fast}}$ ). This indicates a difference between the effective refractive indices of the fiber modes ( $\Delta n_{\text{eff}}$ ) of  $4.26 \times 10^{-2}$ .

Figure 27 and Figure 28 show the responses of the two gratings of the sensing head to variations of strain and temperature. It can be observed that the measurand sensitivities are substantially different for these gratings, particularly concerning temperature, where the difference between the sensitivity coefficients reaches  $\sim 60\%$ . The large volume of the holes, which are filled with air, has a determinant effect on the thermo-optic coefficient of the MOF, decreasing the temperature sensitivity of the FBG written in this type of fiber [48]. On the other hand, the strain coefficient of the MOF grating is  $\sim 9.6\%$  larger than the one relative to the SMF grating. This result is a consequence of the reduction of the Young modulus in the microstructured fiber due to the presence of holes [49].

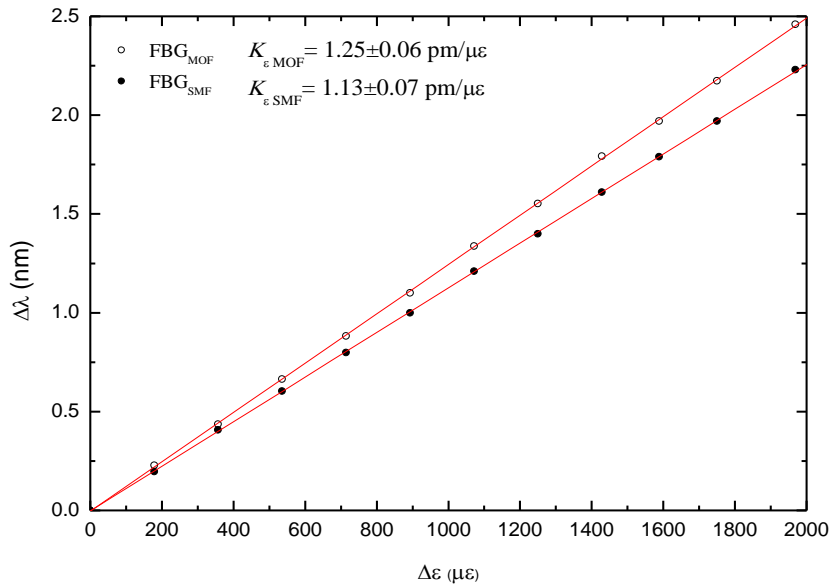


**Figure 27 - Strain response of the sensing head made with the MOF and SMF gratings.**

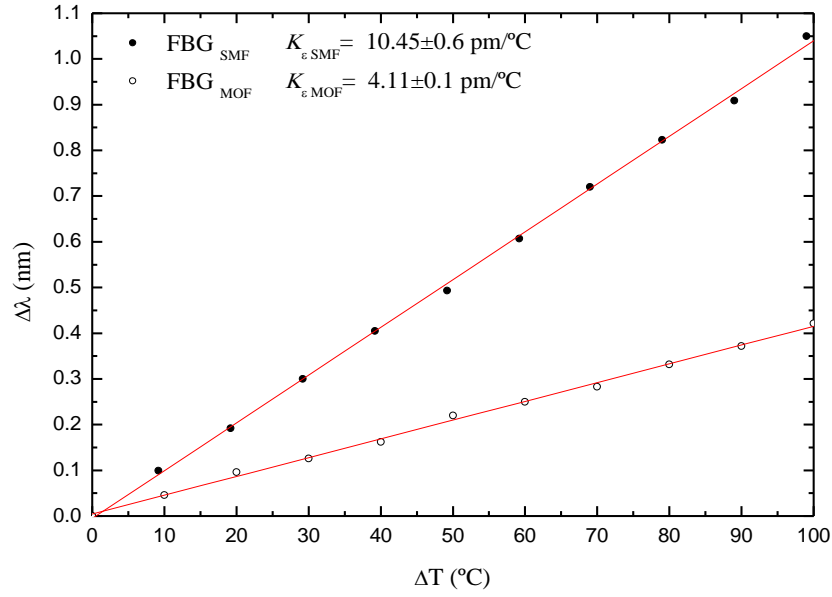


**Figure 28 - Temperature response of the sensing head made with the MOF and SMF gratings.**

In view of the different strain and temperature sensitivities of the two gratings, it is feasible to measure these parameters simultaneously using the following matrix equation

$$\begin{bmatrix} \Delta T \\ \Delta \varepsilon \end{bmatrix} = -\frac{1}{D} \begin{bmatrix} K_{\varepsilon \text{ SMF}} & -K_{\varepsilon \text{ MOF}} \\ K_{T \text{ SMF}} & K_{T \text{ MOF}} \end{bmatrix} \begin{bmatrix} \Delta \lambda_{\text{MOF}} \\ \Delta \lambda_{\text{SMF}} \end{bmatrix} \quad (3.6)$$

where  $D = K_{T \text{ MOF}} K_{\varepsilon \text{ SMF}} - K_{\varepsilon \text{ MOF}} K_{T \text{ SMF}}$ . The limitation of most methods reported for simultaneous measurement of pairs of quasi-static parameters arises from a small value of the matrix determinant, which makes it highly sensitive to noise [50]. The proposed MOF/SMF–FBG configuration is substantially immune to this problem because the difference in the sensitivity slopes of the two gratings is large. From these values, given in Figure 27 and in Figure 28, equation (3.6) becomes

$$\begin{bmatrix} \Delta T \\ \Delta \varepsilon \end{bmatrix} = -\frac{1}{8.46} \begin{bmatrix} 1.13 & -1.25 \\ -10.48 & 4.11 \end{bmatrix} \begin{bmatrix} \Delta \lambda_{\text{MOF}} \\ \Delta \lambda_{\text{SMF}} \end{bmatrix} \quad (3.7)$$

The performance of this simultaneous measurement configuration was experimentally determined using the same method described for the first proposed

structure. The results are expressed in Figure 29, where maximum errors relative to the applied values appear.

From these results, resolutions of  $\pm 1.5$  °C and  $\pm 10.7$   $\mu\epsilon$  were determined for temperature and strain measurements, respectively. The main factor that determines these values is the reduced optical power available from the broadband optical source in the spectral region where the resonance of the MOF grating (1508 nm) appears. Therefore, this performance can be improved either by increasing this power or by using more sensitive FBG interrogation techniques [51].

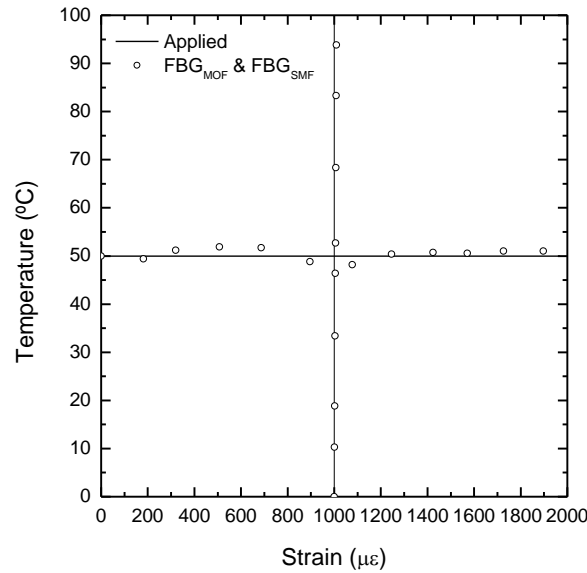


**Figure 29 - Sensor output as determined by equations (3.6) and (3.7).**

### 3.5 Long Period Gratings and Rocking Filters in Hi-Bi MOFs

The spectral characteristics and sensing capabilities of two different kinds of optical filters, LPGs and rocking filters, make them very interesting for optical fiber sensors applications. In this section is demonstrated the possibility of fabricating both kinds of gratings with a CO<sub>2</sub> laser inscription method in a highly birefringent photonic crystal fiber. Further, the sensing capabilities of both structures were also studied regarding temperature, strain and hydrostatic pressure sensitivities by interrogating the wavelength shifts at different resonances.

For fabrication of the LPGs and rocking filters, an highly birefringent (Hi-Bi) MOF produced by the Department of Optical Fiber Technology – from the University of Marie-Curie Skłodowska (UMCS) in Lublin, Poland – was used. The birefringence in this fiber is induced by two holes located symmetrically with respect to the core. The cross-section of the fiber obtained in the scanning electron microscope (SEM) is shown in Figure 30.



**Figure 30 - SEM image of the highly birefringent MOF used for fabrication of the LPGs.**

From this image, the geometrical parameters were determined and gathered in Table 1, where  $A_F$  is the pitch distance,  $D$  the diameter of the large holes,  $d$  the diameter of the cladding holes and  $\phi$  the external diameter of the cladding.

**Table 1 - Geometrical parameters of the highly birefringent MOF**

$A_F$ [ $\mu\text{m}$ ]	$D$ [ $\mu\text{m}$ ]	$d$ [ $\mu\text{m}$ ]	$\phi$ [ $\mu\text{m}$ ]
3.76	4.6	1.63	127

To fabricate the gratings in the Hi-Bi MOF presented in Figure 30 the point-by-point  $\text{CO}_2$  laser based inscription system shown in Figure 31 was used.

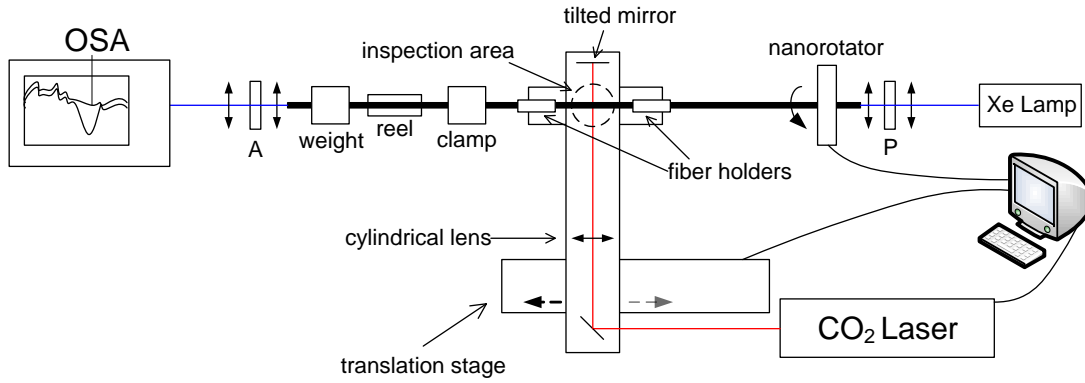


**Figure 31 - Setup for LPG and rocking filter inscription using a CO<sub>2</sub> laser.**

During the gratings fabrication process, the fiber was illuminated using a broadband Xe-lamp and the grating growth was monitored using an ANDO AQ6317B optical spectrum analyzer (OSA).

In the case of the LPG fabrication, the polarizers ‘P’ and ‘A’ could be discarded, as well as the nanorotator. For the rocking filter formation, the nanorotator allows the Hi-Bi MOF principal axes to be pre-twisted with a constant angle. After that, the fiber twist is partially released by heating the fiber at one point with the CO<sub>2</sub> laser beam. The polarizers ‘P’ and ‘A’ permit to excite at the fiber input and attenuate at the fiber output the desired polarization modes, respectively.

### 3.5.1 LPG Characterization and Sensing Properties

The investigated LPG contained 25 coupling points fabricated in the Hi-Bi MOF using the CO<sub>2</sub> laser based system. The grating, with a period of 650  $\mu\text{m}$  and a total length of 15.6 mm, was then optically characterized. Its transmission spectrum, shown in Figure 32, features three pronounced pairs of attenuation bands centered at 670 nm, 960 nm and 1450 nm, respectively.

When the two polarizers are rotated it is possible to check if the nature of the resonances is due to the polarizing properties of the Hi-Bi MOF. As can be seen in Figure 33, the two observed peaks in the first pair of resonances are polarization sensitive, which proves they arise due to coupling between the fundamental polarization modes and the cladding modes located in the fiber microstructure. The

same behavior was observed for the second pair of resonances located around 950 nm. On the other hand, the third pair of resonances arising around 1450 nm was not polarization sensitive. It is believed that the two observed peaks correspond to resonances of different order, each of them having negligible split versus polarization. This effect can be attributed to very small birefringence difference between the fundamental mode and the cladding mode producing the resonant coupling.

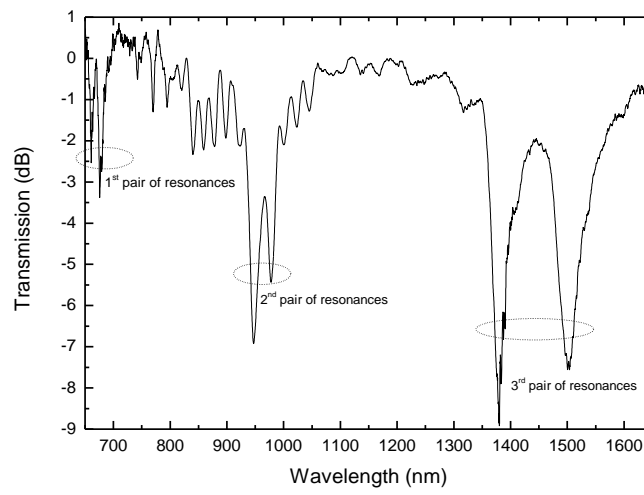


**Figure 32 - LPG transmission spectrum after 25 exposition points separated by 650  $\mu\text{m}$ .**

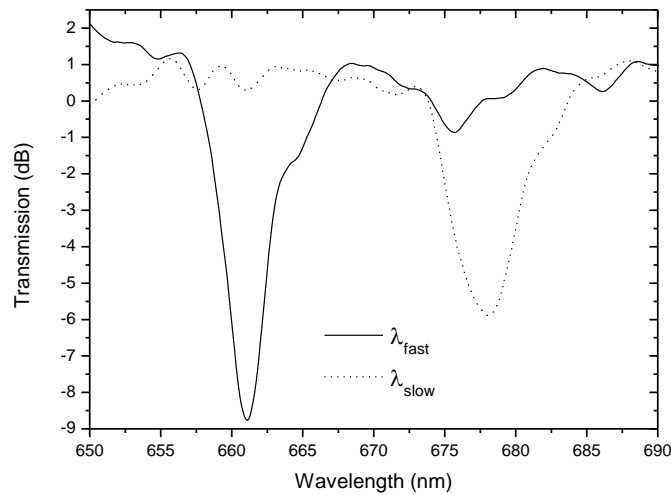
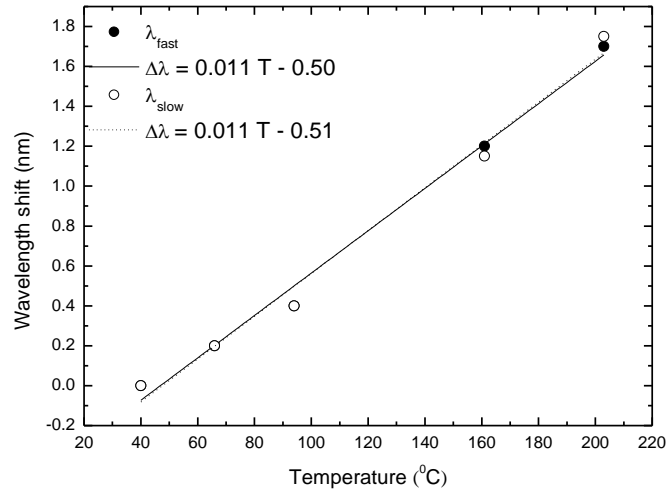


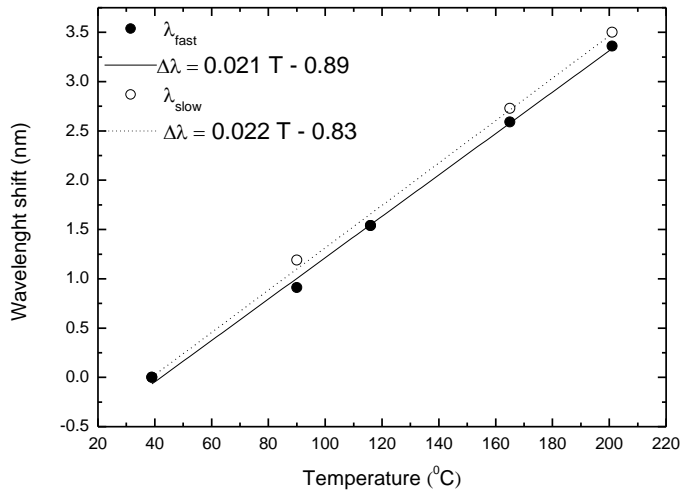
**Figure 33 - Location of the LPG resonance pair corresponding to different polarization modes in the Hi-Bi MOF in the wavelength region near 670 nm.**

Concerning the LPG sensing properties, the device was submitted to temperature changes and characterized. The third pair of resonances was insensitive to temperature in terms of its wavelength dependence, but the same did not happen for the 670 nm and ~960 nm resonances, as the data in Figure 34 shows.

A similar linear response for the two peaks in each resonance pair can be observed. The data indicates that the sensitivities are ~11 pm/°C for the first pair of resonances and ~21 pm/°C for the second one.



(a)



(b)

**Figure 34 - Variation of the resonance wavelength versus temperature for: a) pair of resonances around 670nm region: b) pair of resonances around 960 nm region.**



Regarding the hydrostatic pressure sensitivity, a wavelength dependence of the three pairs of resonances against pressure change was not observed. Although, for the first pair of resonances, at the 670 nm region, an amplitude variation for the optical transmission spectrum of the two attenuation depths was detected, as can be seen in Figure 35. It is important to point out that these measurements were taken while monitoring a constant optical source power.

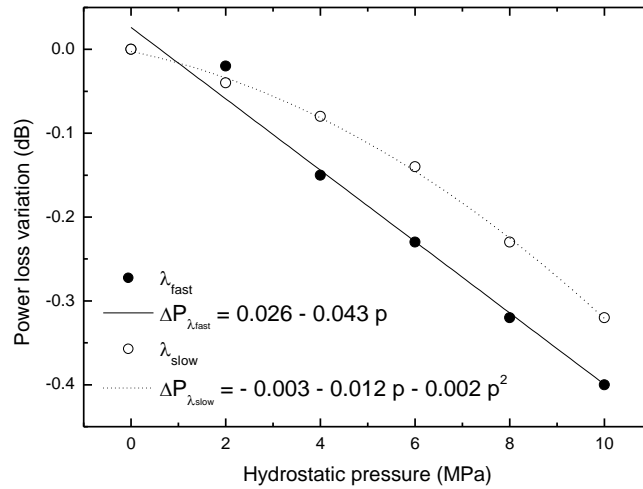


**Figure 35 - Variation of the LPG resonance power loss as a function of hydrostatic pressure (resonance pair in ~ 670nm region).**

The results presented were obtained, in a constant temperature measurement, using a coupler after the optical source which allowed the monitoring of the Xe lamp power. Such a basic optical referencing scheme permitted to obtain the normalized results presented in Figure 35. As can be seen, the two resonances at ~ 670 nm ( $\lambda_{fast}$  and  $\lambda_{slow}$ ) show different behaviors, with the peak loss associated with  $\lambda_{fast}$  showing a linear response with hydrostatic pressure, while for the one relative to  $\lambda_{slow}$  the dependence is parabolic.

It was not possible to obtain results for the strain sensitivity with this LPG because it broke with the application of strain. Unfortunately, this is one of the impairments of the structures developed with a CO<sub>2</sub> laser since the exposure of the fiber to the laser beam increases tremendously its fragility.

These results indicate that LPGs fabricated with CO<sub>2</sub> lasers show a moderate sensitivity to temperature, between 11 pm/°C and 22 pm/°C. The spectral response of the LPG to hydrostatic pressure presented no change, but a small increase of optical peak loss against pressure for the first pair of resonances was noticed.

### 3.5.2 Rocking Filter Characterization and Sensing Properties

The developed rocking filter was formed after 13 beam exposures, physically separated by 8 mm, being the rocking angle 30° and the twisted length ~100 μm. The transmission spectra of the guided mode, as well as, of the orthogonal mode are shown in Figure 36, where it is evident four pronounced resonances centered at ~700 nm, ~1000 nm, ~1300 nm and ~1500 nm, respectively.

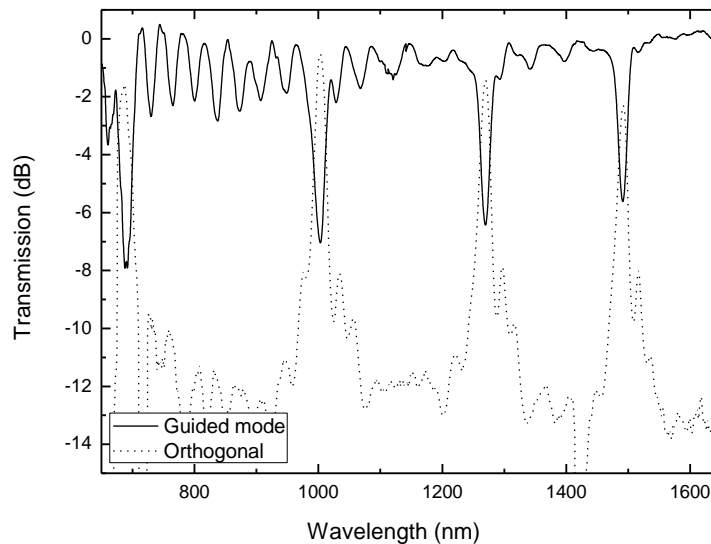
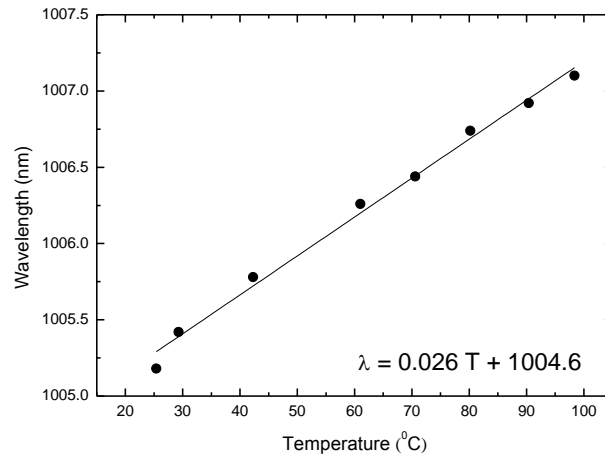
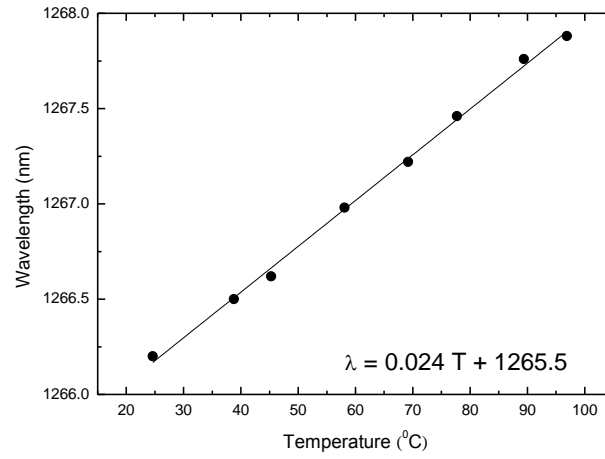


**Figure 36 - Rocking filter (with a period  $\Lambda=8$  mm and 13 coupling points) transmission spectra for the two eigen-polarization components of the fiber. The solid line and dotted line correspond to the polarization component parallel (guided mode) and orthogonal, respectively, to the input polarization state.**

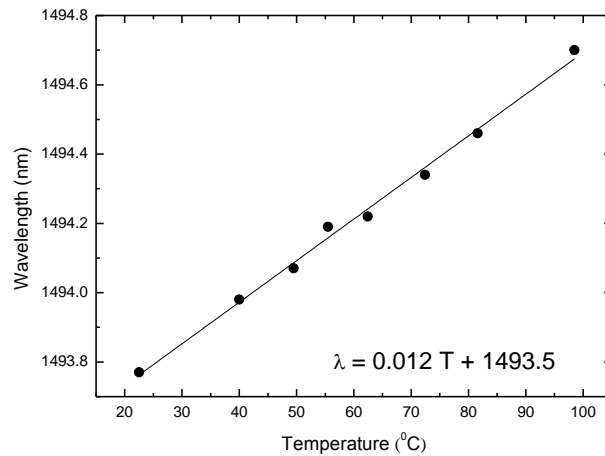
Considering the sensitivity of the resonant wavelengths to temperature, the behavior of the second, third and fourth resonances were studied. The expected linear behavior of  $\Delta\lambda$  with temperature can be confirmed by the data in Figure 37.



(a)



(b)



(c)

**Figure 37 - Rocking filter resonant wavelength as function of temperature for: a) second resonance at ~1004nm; b) third resonance at ~1265nm; c) fourth resonance at ~1493nm.**

From the previous figure, it should be pointed out that the rocking filter sensitivity is decreasing for longer wavelengths. As can be observed, for the fourth resonance a

sensitivity value of 12 pm/°C was achieved, which is more than a factor of two smaller than the one associated with the second resonance (~26 pm/°C).

The sensitivity of the resonance wavelengths of the fabricated rocking filter was also tested to hydrostatic pressure measurement. The obtained results are shown in Figure 38.

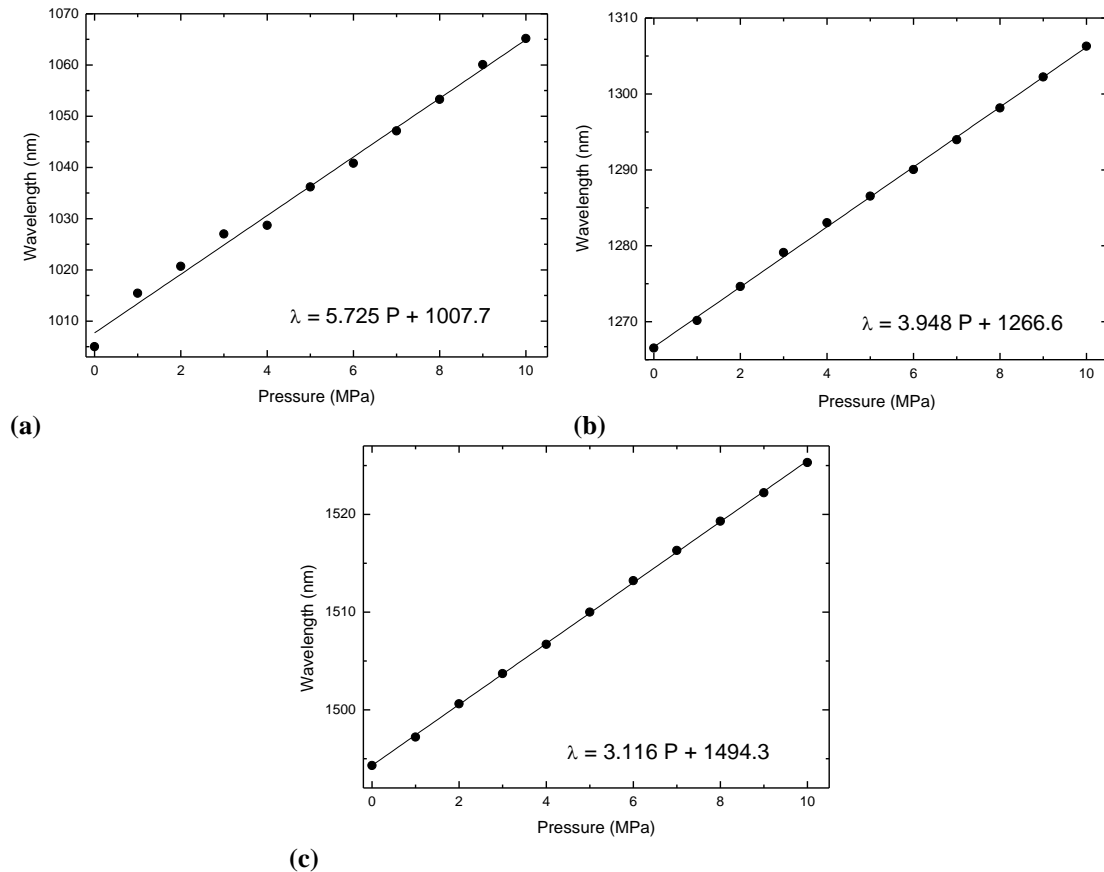


**Figure 38 - Rocking filter resonant wavelength as function of pressure for: a) second resonance at ~1004nm; b) third resonance at ~1265nm; c) fourth resonance at ~1493nm.**

The sensitivity of the rocking filter to hydrostatic pressure ranges from 5.7 nm/MPa down to 3.1 nm/MPa (for the second and the fourth resonance wavelengths, respectively). Again, the rocking filter sensitivity is decreasing for longer wavelengths. Figure 39 shows the evolution of the fourth resonance of the rocking filter for different values of applied pressure.

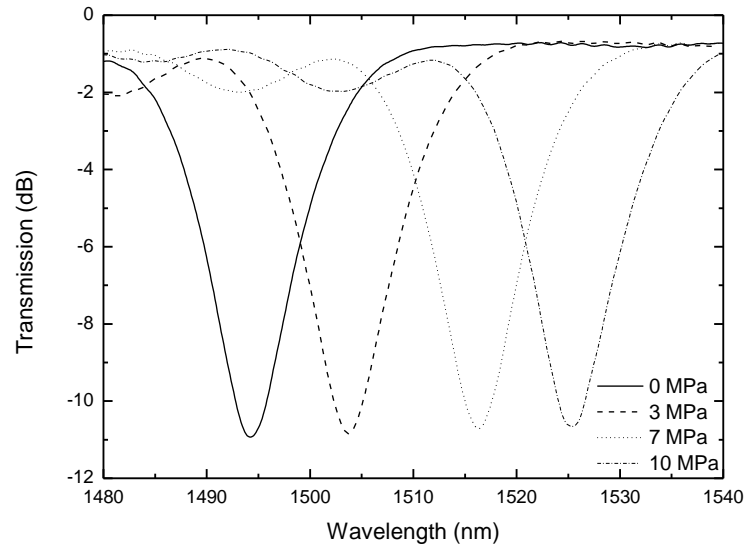


**Figure 39 - Spectrum shift of the ~1493 nm resonance for different hydrostatic pressure values.**

As can be observed, beyond the spectral shift, its shape does not change with hydrostatic pressure, a positive feature of this fiber device, when considering the implementation of a simple interrogation system [52].

Finally, it was tried to quantify the rocking filter strain sensitivity. Due to the fragility of this Hi-Bi MOF based structure, strain was measured only until the application of 300  $\mu\epsilon$ . From Figure 40, a linear dependence could be observed with a coefficient of  $\sim 0.95$  pm/ $\mu\epsilon$ .

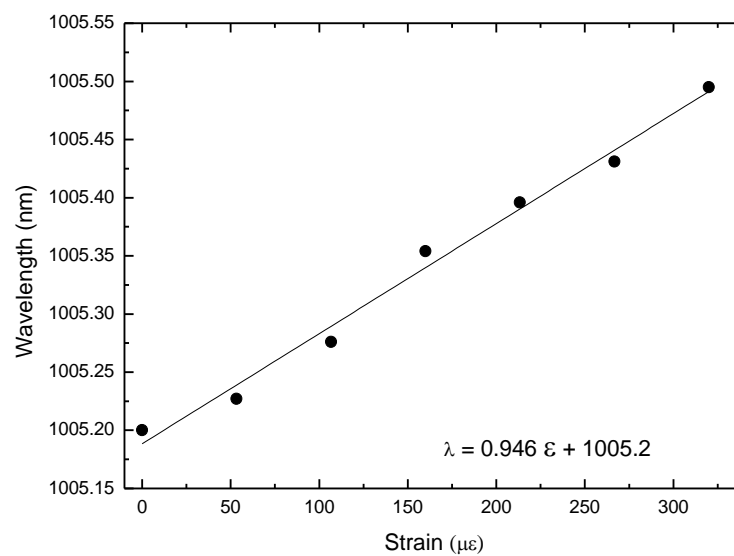


**Figure 40 - Dependence of the rocking filter second wavelength resonance with applied strain.**

The results obtained indicate it is feasible to fabricate rocking filters in highly birefringent MOFs using a CO<sub>2</sub> laser, showing several resonances. Measurements of the sensing characteristics of these devices indicate that their sensitivity to temperature is moderate (between 12 to 26 pm/°C), while the sensitivity to hydrostatic pressure is higher (between 3.1 and 5.7 nm/MPa). The obtained value for sensitivity to strain is low (0.946 pm/μ $\epsilon$ ), being noticeable that the fiber becomes very fragile after CO<sub>2</sub> laser beam exposition. As a consequence of such results, the ratio of the pressure sensitivity to the temperature sensitivity is high and in the range of 220-260 °C/MPa. These results make the rocking filter an adequate solution for hydrostatic pressure measurement with relatively small cross-sensitivity to temperature.

### **3.6 Spectral Characterization of a Hollow-Core MOF for Sensing Applications**

Several sensing applications with MOFs require fibers with different index contrasts between the high and the low refractive-index regions of the photonic crystal cladding of the fiber. For a hollow core fiber, of the type presented in Figure 10, a characterization of the spectral shift of the photonic bandgap (PBG) edge of a HC-MOF, induced by physical measurands such as strain, temperature, curvature, and twist, is presented.

To characterize the measurand-induced spectral shift of the PBG edge, a section of HC-MOF was spliced directly between two lengths of SMF. For this purpose a bandgap fiber that was designed and fabricated at the University of Bath was considered. The bandgap of this fiber, shown in Figure 41, is a seven-cell HC-MOF with a core diameter of ~15 μm and an outside diameter of ~125 μm, with a PBG edge at wavelengths around 1540 nm. A cross section view of this fiber is shown in Figure 42.

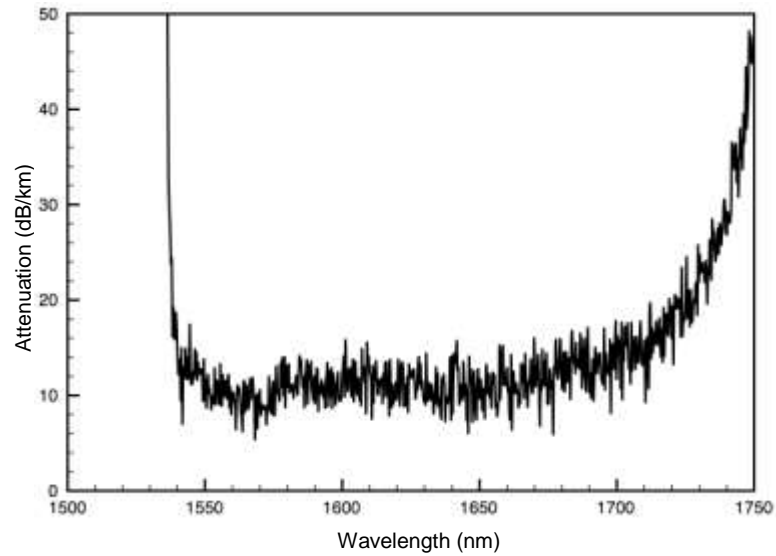


**Figure 41 - Transmission spectrum of the HC-MOF fiber considered for characterization of measurand-induced effects on the PBG edge.**

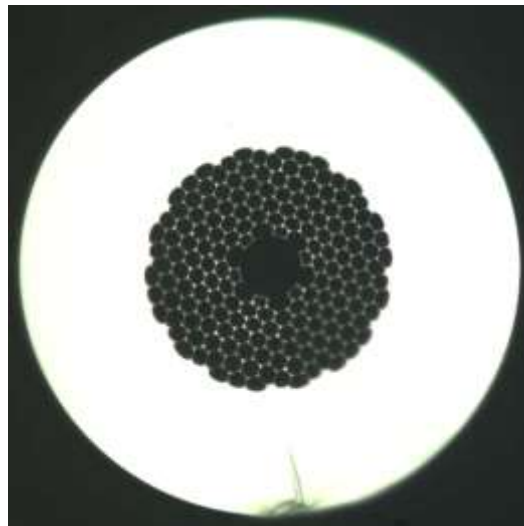


**Figure 42 - Optical microscope image of the cross section of the selected microstructured optical fiber.**

It has been observed that the loss pattern of PBG fibers in the PBG edge region is a function of the fiber length, particularly when small lengths are considered, i.e., after light propagation along 100–200 m of MOF the spectral features of the bandgap essentially stabilize. This process involves the shift of the low-wavelength edge to longer wavelengths (together with the disappearance of spectral transmission oscillations located to the left of the bandgap), and the shift of the high-wavelength edge to lower wavelengths [53]. Therefore, a bandgap spectrum narrowing was observed with a longer fiber length. Studies indicate that this effect in the bandgap low-wavelength region is dominated by the loss via coupling to fiber surface modes

[54]. The mechanism by which light is leaked out can be either by intrinsic loss of the surface mode or by coupling of the latter to a continuum of leaky modes. On the long-wavelength side of the bandgap, the shift of the edge is owed to the fact that the fundamental mode is no longer supported and higher-order modes propagate, which show higher losses and therefore disappear after some propagation length, which permits the appearance of an effective bandgap edge.

Focusing on the wavelength region close to the low wavelength edge of the bandgap, coupling to fiber surface modes in practical HC-MOF is promoted by tunneling mechanisms [55]. The light in this region is less well confined and, therefore, it is natural to deduce that the action on the fiber by some physical parameters should be accompanied by a relatively strong loss in the fiber. The motivation for this research was to verify this hypothesis and to quantify the effect of physical measurands on the fiber. Indeed, some previous results already pointed out this path [56-58]. As indicated above, the description of the edge shift of a PBG which is due to changes in the refractive-index contrast of the HC-MOF is simply evaluated by using the refractive-index scaling law, which is based on the scalar waveguide approximation [56, 57]. Based on these findings, Antonopoulos and his co-workers reported an experimental demonstration of the frequency shift of the PBG edge that is due to refractive-index scaling using D<sub>2</sub>O-filled HC-MOFs [56]. Also, Sun and Chan [58] reported the use of PBG fibers as a refractive-index sensor and described its behavior based again on refractive-index scaling laws. In general, it can be expected that some physical measurands can change the PBG property of a HC-MOF due to changes in refractive-index contrast and geometric effects, therefore inducing a PBG spectral shift.

The experimental setup used is shown in Figure 43. The light source used was an Er-doped fiber with amplified spontaneous emission power, central wavelength, and full width at half-maximum of 1.8 mW, 1550 nm, and 60 nm, respectively. The output transmission spectrum was observed with an optical spectrum analyzer (OSA). By means of a conventional fusion splicer (Fujikura SM40), the HC-MOF was spliced at both ends to SMFs. All the splicing was done manually, and the optimum parameters were obtained after some attempts to achieve minimum fusion loss. This resulted in 0 bit (bit is Fujikura's internal unit that is used for arc current) and 400 ms for the



power and arc time duration, respectively, and a typical splice loss of 1.5 dB. The length of the HC fiber was  $\sim 28$  cm. To investigate the strain effect on the spectral position of the bandgap edge, two micropositioners were used to fix the SMF fibers and to apply strain. With regard to the effect of temperature, the HC-MOF was placed inside a vessel of heated water and the measurements were taken during the cooling period.

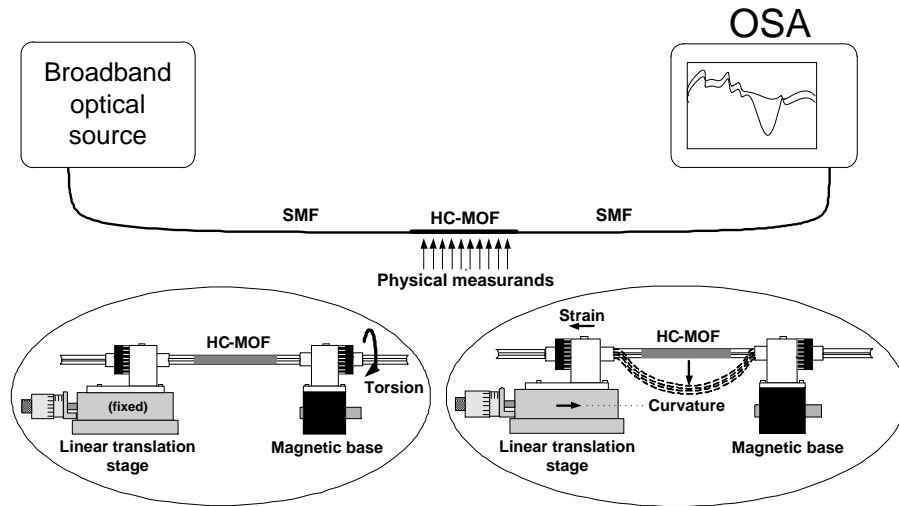


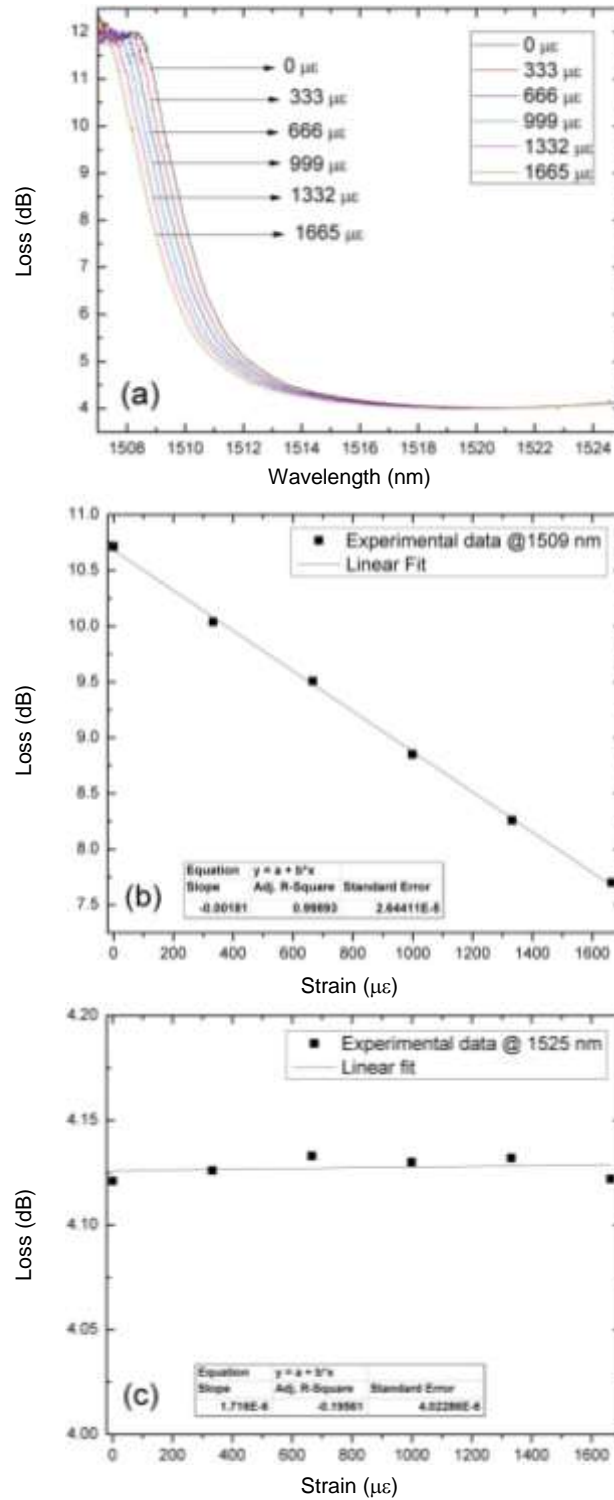
**Figure 43 - Experimental setup for the characterization of the measurand-induced shift of the edge of the spectral bandgap; also shown is the configuration that was used to apply torsion and curvature to the HC-MOF.**

To apply torsion to the HC-MOF, one of the holding stages could be rotated while the other was stationary. By moving longitudinally one holder relative to the other, curvature could also be applied to the HC-MOF.

When strain is applied to the HC-MOF, it was observed a spectral shift of the PBG edge, as indicated in Figure 44, which shows the shift of the PBG edge [Figure 44 (a)], the variation of the transmission in one wavelength in the edge (located approximately at the middle of the edge) [Figure 44 (b)], and the transmission at a wavelength located in the PBG passband [Figure 44 (c)]. These results indicate a blueshift of the PBG edge with the increase of strain (with a slope of approximately  $-0.7 \text{ pm}/\mu\epsilon$ ).

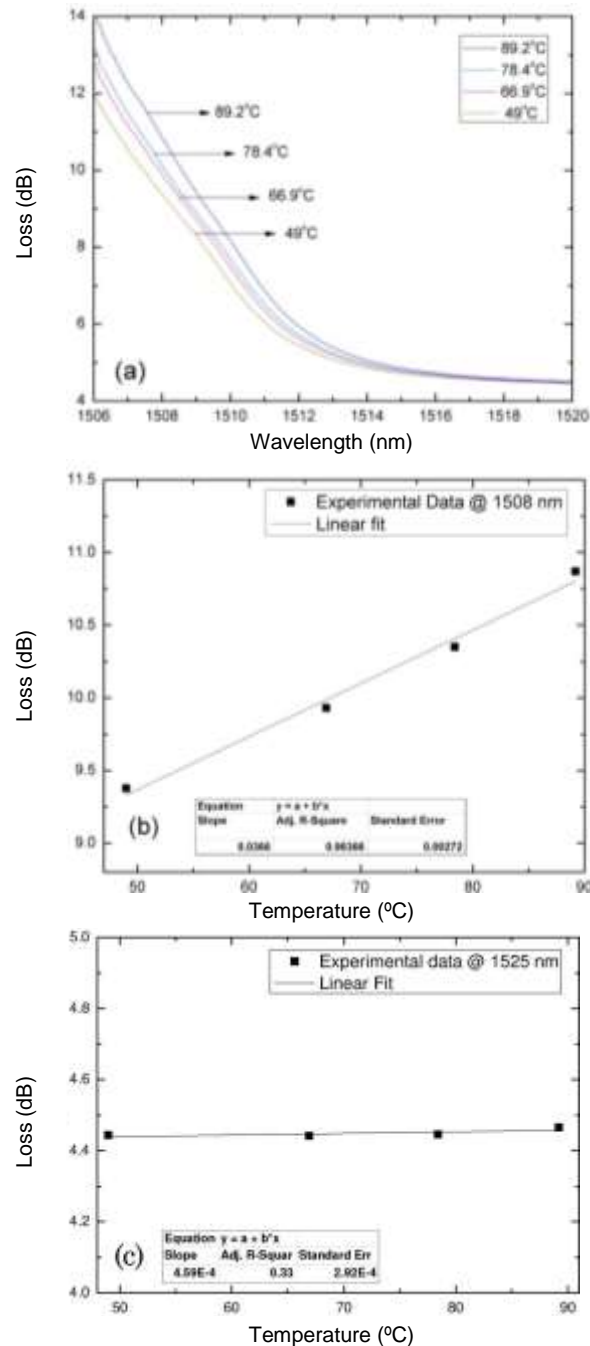
For wavelengths located approximately in the middle of the edge, Figure 44 (b) shows that the loss dependence on a logarithmic scale with strain associated with the

PBG edge shift is fairly linear, with a slope of  $-0.0018 \text{ dB}/\mu\epsilon$ . As expected, within the passband of the bandgap, the transmission is independent of applied strain.



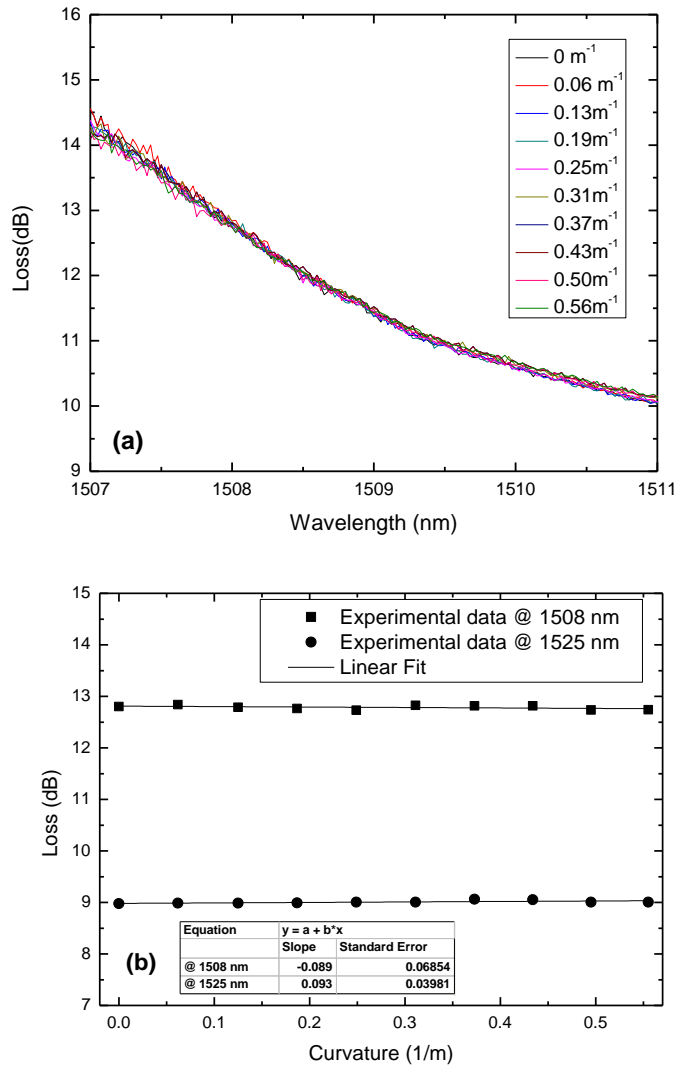
**Figure 44 - Effect of applied strain to the HC-MOF on (a) the spectral position of the PBG lower wavelength edge, (b) the loss variation at the wavelength of 1509 nm, located in the PBG edge, (c) the loss variation at the wavelength of 1525 nm, located in the PBG passband region.**

Figure 45 shows the results relative to variations of temperature [Figure 45 (a), edge shift; Figure 45 (b), transmission at approximately the middle of the edge]. Different from what happens in the case of strain, now a temperature increase results in a redshift of the PBG edge with a slope of  $\sim 29 \text{ nm}/^\circ\text{C}$ .



**Figure 45 - Effect of temperature variation on (a) the spectral position of the PBG lower wavelength edge, (b) the loss variation at the wavelength of 1508 nm, located in the PBG edge, (c) the transmission versus temperature at the wavelength of 1525 nm, located in the PBG passband region.**

The results obtained when curvature was applied to the HC-MOF are shown in Figure 46. It is clear that this parameter does not affect the PBG.



**Figure 46 - Effect of curvature variation on (a) the spectral position of the PBG lower wavelength edge, (b) the loss variation versus curvature, at the wavelengths of 1508 nm, located in the PBG edge, and at the wavelength of 1525 nm, located in the PBG passband region.**

Figure 47 shows the data relative to the application of twist to the HC-MOF. A redshift was observed at the PBG edge that was fairly symmetric considering the clockwise or counterclockwise twist orientations.

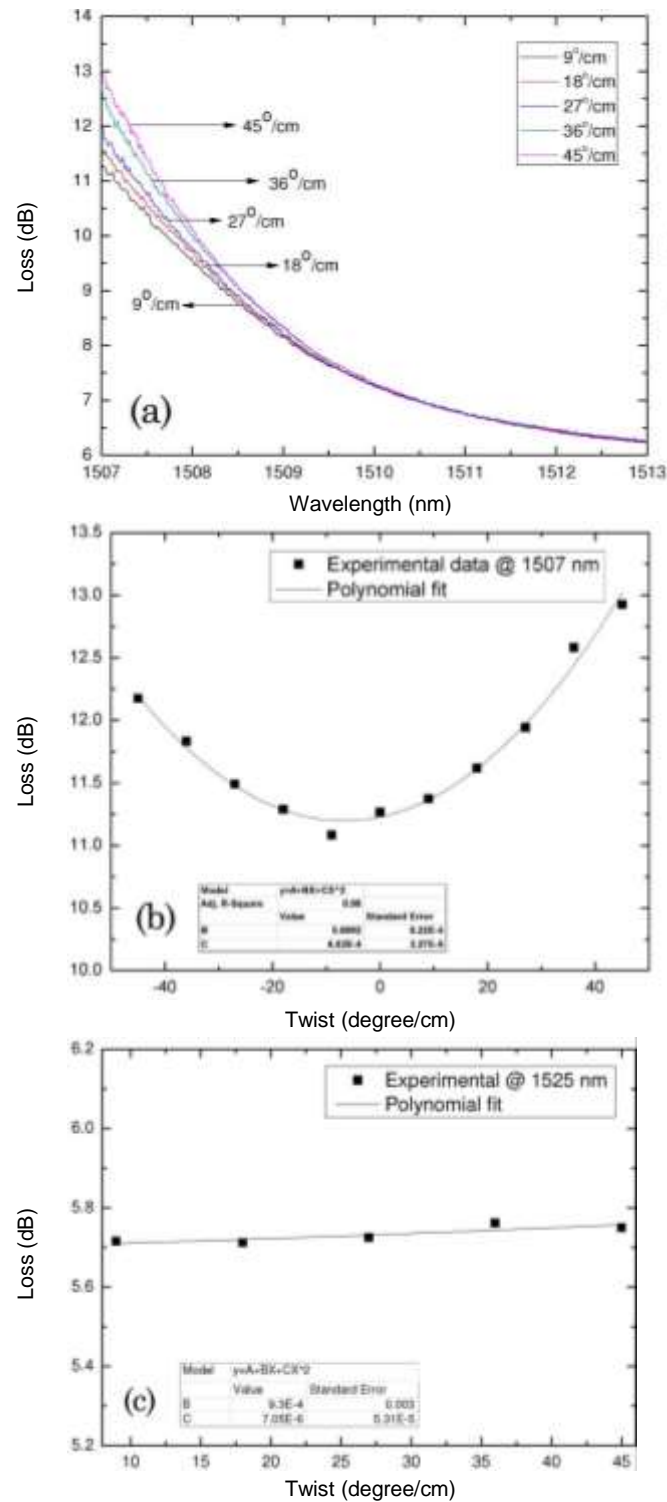


**Figure 47 - Effect of twist applied to the HC-MOF on (a) the spectral position of the PBG lower wavelength edge, (b) the loss variation at the wavelength of 1507 nm located in the PBG edge, (c) the transmission versus twist at the wavelength of 1525 nm located in the PBG passband region.**

The PBG process is a complex phenomenon, and the interpretation of the changes induced in the fiber transmission by strain, temperature, and twist requires a theoretical study of the problem and its computational simulation. However, the

results obtained indicate that the measurand-induced shift of the PBG edge of hollow-core fibers can be used as the basis for sensing configurations supported by this type of fiber. Figure 41 shows that the edge slope can be large, which is favorable for high sensitivity readout. Compensation for optical power fluctuations can be obtained if a second wavelength in the PBG passband, where its transmission is essentially independent of the measurand value, is taken into consideration.

The obtained results show it is feasible to apply HC-MOFs as sensing elements based on the measurand-induced PBG edge shift. But it is also feasible to apply these fibers for the optical demodulation of signals coming from other sensing heads, where the tunability of the PBG edge provides additional flexibility. An example of this role is within the context of fiber Bragg grating (FBG) interrogation [1, 59]. Indeed, when dealing with FBG sensors, the conversion of the measurand-induced wavelength modulation into an optical intensity modulation can be performed when the light that returns from the FBG propagates through a length of HC-MOF located in the control region, with the tuning of the PBG edge to the optimum sensitivity position achieved by application of strain to this fiber. Certainly, many other possibilities can be thought of, but the most relevant factor to point out is the dual functionality of HC-MOF, i.e., the freedom to use this type of fiber as a sensing or as a processing element. This characteristic can be advantageous in several fiber optic sensing applications, and a systematic study of its potential is currently under way.

### 3.7 Summary

The development of systems based on MOFs cannot be viewed as an insuperable barrier due to the fusion-splice losses between these fibers and the standard ones. The results reported in section 3.2 suggest that the SMF/MOF fusion can be done with very good results and high reproducibility. The obtained results are within the range of 0.25–0.6 dB for 300 ms arc duration and 13.7 mA discharge current. In spite of being very challenging, the splicing process can easily be achieved using standard fusion splicers. A technique has been presented whereby a low-loss splice was achieved by applying an electric-arc discharge mainly on the SMF region. This avoids the collapsing of the air holes in the microstructured fiber, caused by the different

melting-point temperatures along the transversal direction of the MOF structure. With this technique, it was demonstrated that low splice loss can be achieved.

In section 3.3 an analysis of the coupling losses dependence on axial and lateral displacement between SMF and HC-MOF fibers was performed. It was found that 19-cell HC-MOF presents lower coupling losses than 7-cell HC-MOF. In coupling between HC-MOFs of the same type it was observed that loss dependence is higher for both axial and lateral misalignments. However, the obtained results are very encouraging towards the implementation of practical multiple coupling gap based gas sensing systems. A simple analysis of splice losses between 19-cell HC-MOF and SMF was also done, being the lowest insertion loss attainable  $\sim 2$  dB.

The design, fabrication and characterization of two sensing heads based on Bragg grating structures for strain/temperature discrimination have been presented in section 3.4. One of them relies on a single grating written in a microstructured optical fiber that exhibits Hi-Bi properties. Monitoring the difference between the two polarization-related resonance wavelengths, a temperature-independent strain measurement functionality was obtained, which provides a strain resolution of  $\pm 7 \mu\epsilon$ . The second sensing head is formed by two connected lengths of MOF and SMF fibers with gratings impressed. The temperature and strain sensitivities of the MOF-SMF gratings on this structure are substantially different, which permitted us to implement simultaneous measurements of these two parameters with resolutions of  $\pm 1.5^\circ\text{C}$  and  $\pm 10.7 \mu\epsilon$ , respectively.

In section 3.5, the possibility of LPGs and rocking filter fabrication with several resonances in a Hi-Bi MOF using a  $\text{CO}_2$  laser inscription technique was presented. The observed variations of resonant wavelengths depend on the type of filter (LPG or rocking) and on the type of measurand that interacts with the fiber device. The sensitivity of the LPG to temperature is low and varies between 11 and 22  $\text{pm}/^\circ\text{C}$ , being similar to that of the rocking filter (12–26  $\text{pm}/^\circ\text{C}$ ). These values are higher than those obtained with LPGs fabricated in endlessly single mode MOFs (that range from 2.0 to 6.0  $\text{pm}/^\circ\text{C}$  [30, 60–62]). Measurements also show that the wavelength sensitivity of the LPG is pressure independent, while it is high for the rocking filter (3.1–5.7  $\text{nm}/\text{MPa}$ ). This last result is far greater than the sensitivity of the LPG in

endlessly single mode MOF (0.1 nm/MPa [63]), as well as the sensitivity of a rocking filter in conventional elliptical core fibers (0.5 nm/MPa [64]). The fragility of CO<sub>2</sub> fabricated structures did not allow us to measure the sensitivity of the LPG to strain, but for the rocking filter the measured sensitivity was 0.946 pm/ $\mu\epsilon$ , which is lower than the sensitivity of the LPGs in endlessly single mode MOFs (2.0–2.5 pm/ $\mu\epsilon$  [30, 61, 62]). These sensitivity results make the rocking filter an adequate device for hydrostatic pressure measurements, in view of the small cross-sensitivity to temperature.

A measurand-induced spectral shift of the photonic bandgap edge of a hollow-core microstructured fiber was characterized in section 3.6. The physical measurands considered were strain, temperature, curvature, and twist. To increasing strain a blueshift was observed in the spectral position of the PBG edge, whereas a redshift appears for increase in temperature and twist. Curvature does not introduce a noticeable change in the bandgap edge. These characteristics indicate the feasibility of using this type of fiber for sensing as well as for optical signal processing.



## Chapter 4 – Gas Sensing with Hollow-Core Microstructured Optical Fibers

---

### 4.1 Introduction

Methane is an extremely explosive gas and one of the main constituents of natural gas, so its detection is a subject of major importance. The idea of sensing methane by laser absorption was first proposed in 1961 by Moore [65], and later demonstrated by Grant [66] in 1986 using a He-Ne laser. Although methane has a strong absorption line at 3.3  $\mu\text{m}$ , this wavelength region is not suited for optical fiber sensor applications due to the high losses in standard optical fibers and also since it is difficult to fabricate laser diodes operating at wavelengths higher than 2.2  $\mu\text{m}$  at room temperature.

In order to effectively use the currently available low loss optical fibers, remote detection in the near infrared, around 1.1-1.8  $\mu\text{m}$ , is desirable, where optical fibers have minimum transmission losses ( $<1$  dB/km). Methane has two absorption bands in this region, corresponding to wavelengths of 1.33  $\mu\text{m}$  and 1.65  $\mu\text{m}$ . It was found that the 1.65  $\mu\text{m}$  band of methane absorption is more suitable considering the lower loss of the optical fiber in this region, the fact that the absorption coefficients are larger and also the circumstance that the spectral widths are broader than those in the 1.33  $\mu\text{m}$  band [67].

Further in this chapter an optical fiber sensing system for detecting low-levels of methane will be described. The properties of hollow-core photonic crystal fibers are explored to have a sensing head with favourable characteristics for gas sensing, particularly in what concerns intrinsic readout sensitivity and gas diffusion time in the sensing structure. The sensor interrogation was performed by applying the *Wavelength Modulation Spectroscopy Technique*, and a portable measurement unit was developed with performance suitable for remote detection of low-levels of methane.

## 4.2 Gas sensing with Optical Fibers

Several authors have proposed many configurations using laser diodes, in particular, distributed feedback (DFB) lasers with almost monochromatic emission, having bandwidths much narrower than the individual gas absorption lines. These devices are a suitable solution for optical-based gas sensing since DFB laser technology has reached maturity due to its broad use in telecommunication systems, with the consequent large reduction of the associated costs.

In 1992, Uehara *et al.* [68] demonstrated high sensitivity real time remote detection of methane in air with a DFB operating at 1.65  $\mu\text{m}$  (transmission and reflection schemes). Silveira *et al.* [69] presented a methane optical sensor using a 1.31  $\mu\text{m}$  DFB laser and proposed a new type of signal processing technique based on amplitude modulation which provides auto-calibration.

The performance limitations of a fiber optic methane sensor using GRIN lenses in either transmission or reflective configurations were examined by Stewart *et al.* [70]. DFB lasers exhibit very long coherence lengths and, therefore, multi-reflections occurring within the gas cells and joints/connectors give rise to interference signals which produce harmonics in the output indistinguishable from the gas signals.

In 2000, Iseki *et al.* [71] developed a portable remote methane sensor based on frequency modulation using a DFB laser, where a dithering technique is employed and the first and second derivative of the absorption line are directly related with the gas concentration.

Chan *et al.* [72, 73] developed an optical remote sensing system for differential absorption measurement of various inflammable, explosive, and polluting substances, employing low loss optical fiber networks and near-infrared high radiant LEDs. The highly sensitive technique was achieved employing the power-balanced two-wavelength differential absorption method in the system, which enables direct detection of differential absorption signals for the specific molecule being monitored.

In 2003, Whitenett *et al.* [74] reported an alternative optical configuration for environmental monitoring applications, namely the utilization of cavity ring-down spectroscopy using an Erbium Doped Fiber Amplifier (EDFA). This configuration monitors the exponential decay of a light pulse inside a gas chamber that ideally exhibits very high finesse, causing therefore  $1/e$  ring-down time to be very long and very sensitive to small changes in the cavity loss, as induced, for example, by a gas absorber in the cavity.

Photo-acoustic spectroscopy (Kosterev *et al.* [75]) is another technique for detection of absorbing analytes and it relies on the photo-acoustic effect. In this interesting technique, the sample gas is confined in a chamber, where modulated (e.g., chopped) radiation enters, via a transparent window, and is absorbed by the active molecular species. The temperature of the gas thereby increases, leading to a periodic expansion and contraction of the gas volume, synchronous with the modulation frequency of the radiation. This, consequently, produces a pressure wave with amplitude (measured with simple microphones) related to the gas concentration.

Another approach, known as multipass transmission absorption spectroscopy, can be used, and consists of a chamber with mirrors at each end, filled with the targeted sample [76, 77]. The beam is folded back and forth through the cell, creating an extended, yet defined, optical path length in a confined space. Although it presents a high sensitivity, the slow system response to concentration fluctuations and the relatively high volume of the sample required constitute the major disadvantages of this technique.

Other approaches have also been implemented, exploring different types of fibers (e.g., D fiber) and effects, such as evanescent wave absorption (Culshaw *et al.* [78]). Their major obstacles, namely low sensitivity for short interaction lengths, spurious interference effects and degradation through surface contamination, were analysed (Stewart *et al.* [79]) and it was determined that the sensitivity of a D-fiber methane gas sensor could be improved by overcoating the flat surface of the fiber with a high index layer, reaching a detection limit lower than 5 ppm (Muhammad *et al.* [80]).

More recently, several authors proposed new methods for gas detection. Benounis *et al.* [81] demonstrated a new evanescent fiber sensor based on cryptophane molecules deposited on a PCS (polycarbosilane) fiber. Roy *et al.* [82] demonstrated a methane sensor based on the utilization of carbon tubes and nanofibers deposited by an electro-deposition technique.

A review of optical sensing methods for methane detection can be found in the work of Magalhães [83].

#### 4.2.1 Gas Sensing with Photonic Crystal Fibers

The holes in microstructured fibers open up new opportunities for exploiting the interaction of light with gases or liquids. With the possibility of filling the air holes of MOF with gas, with large interaction lengths, new ways to monitor or detect gas are possible. Evanescent field gas sensing in the holes of MOF (Monro *et al.* [84]) or in a fiber random hole structure (Pickrell *et al.* [85]) has been reported. Hoo *et al.* [86] demonstrated an absorption spectroscopy evanescent wave acetylene detection system based on a 75 cm length MOF sensing head. Another work of the same group presents the design and modelling of a MOF based structure for gas sensing with enhanced characteristics, relying on the amplifying effect associated with the use of the multi-coupling gaps (Hoo *et al.* [87]).

On the other hand, Ritari *et al.* [88] studied gas characteristics by monitoring the photonic bandgap parameters within hollow-core MOF. Methane detection at the 1670 nm band using hollow-core MOF has been reported (Cubillas *et al.* [89]). It is estimated a detection limit of 10 ppm/volume with the system configuration used in the experience. Cubillas *et al.* [90] also published a work that describes methane sensing with an hollow-core MOF at 1.3  $\mu\text{m}$ . Other authors studied the characteristics of gas sensing based on evanescent-wave absorption in solid-core by filling the cladding air holes (Cordeiro *et al.* [91, 92], Li *et al.* [93]). Side access to the holes of the MOF was demonstrated by Cordeiro *et al.* [92]. The method consists in inserting the liquid or gas to be sensed laterally to the fiber while the tips are optically monitored. An elegant solution to the problem of the long filling time of the gas inside

the fiber was proposed by van Brakel *et al.* [94], using femtosecond-laser drilling microchannels in both hollow and solid core MOFs.

#### 4.2.2 Other Gas Species Sensing with Optical Fibers

Hydrogen is one of the cleanest energy sources once it can easily be obtained from water via electrolysis or photolysis, and upon plain burning it turns into water, so it does not contribute to global warming, via production of CO<sub>2</sub>. Therefore, it has been used in many chemical processes in various fields: propellant in aerospace rockets, and fuel for fuel cells and explosion engines in automotive devices.

Control of H<sub>2</sub> concentration is of the utmost importance, which implies the development of accurate and robust sensors, with sensitivity to H<sub>2</sub> as low as ppb levels.

Over the last 30 years, a variety of configurations for hydrogen sensing have been attempted and successfully demonstrated. Many devices developed in that period have found a place in the market, due to the need of monitoring hydrogen-based systems, namely with regard to the inherent explosion risk. The need for local detection of hydrogen in hazardous atmospheres and/or at high temperatures has consistently led to the choice of optical fiber sensors. In fact, when compared with conventional sensors, optical fiber-based hydrogen ones possess as main advantage the fact that they are risk-free in potentially explosive environments. They also enable remote sensing and multipoint measurement, and are immune to electromagnetic interferences. So far, Palladium (*Pd*) has been the most common transducer used with the optical fiber, due to its high sensitivity to, and selectivity for molecular hydrogen.

To date, several hydrogen sensors have been described, based on distinct physicochemical principles: metal oxide semiconductor sensors [95], electrochemical sensors [96], thermoelectric sensors [97], surface acoustic wave sensors [98], and optical sensors [99], among others. The latter usually resort to optical fibers as a basis, and may in turn be classified according to their working principle: (a) interferometric-based; (b) intensity-based; or (c) fiber grating-based sensors.

Regardless of the technology used, one notices that the recovery time is still quite long (many seconds, and in some cases, minutes or hours); hence, further research investment is required to address this issue, to eventually be able to design and implement better configurations for hydrogen sensing.

A review of palladium-based fiber-optic sensing methods for hydrogen detection can be found in the work of Silva *et al.* [100].

### 4.3 HC-MOF Based Sensing System

Hollow-Core microstructured fibers (HC-MOF) are structures where the light is guided not by total internal reflection but by a photonic bandgap in the cladding that acts like an insulator for light. The HC-MOF cladding is made with hundreds of periodically spaced air holes in a silica matrix, typically arranged in a honey comb-like pattern. Figure 48 shows the cross section of the hollow-core fiber that was used in the experiments. As can be seen, the hollow-core is formed by the suppression of some of such periodically spaced honey comb-like air holes.

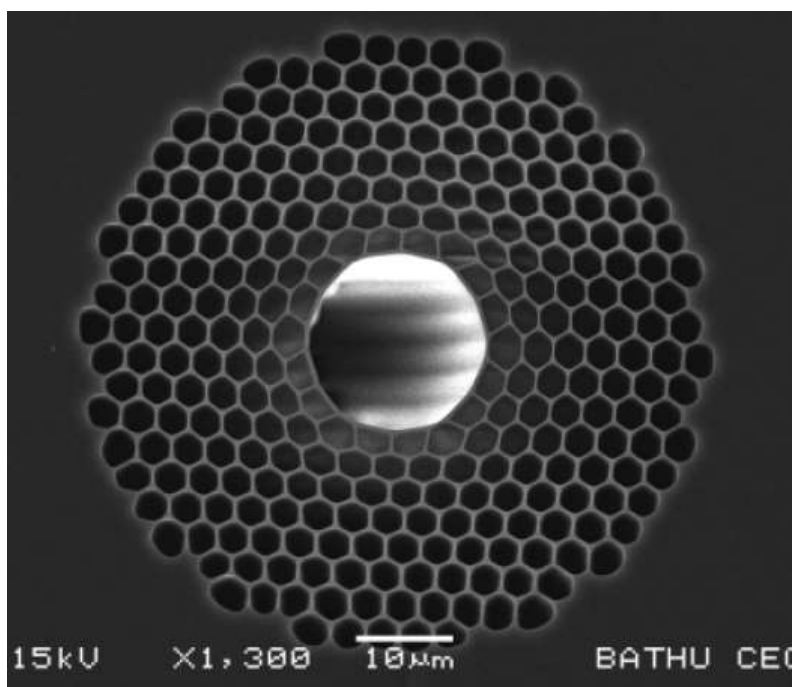
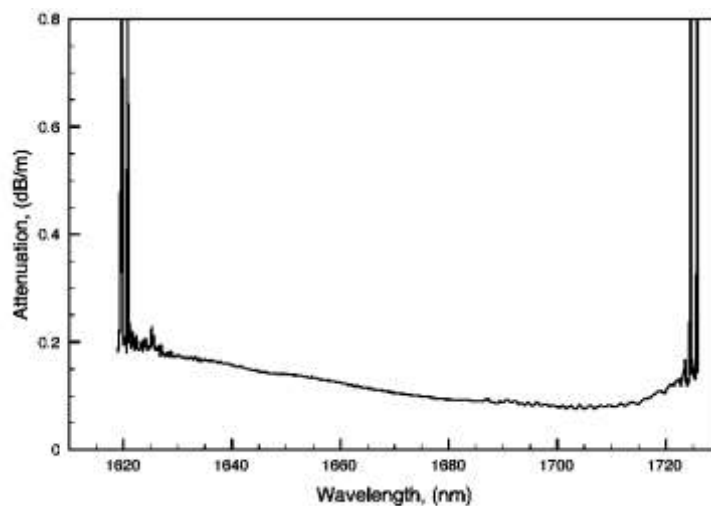


Figure 48 - Optical microscope image of a 7-cell HC-MOF.

These fibers exhibit a large potential concerning gas sensing, since long interaction lengths can be created when light and gas share a common path, therefore, enabling the development of HC-MOF gas sensing heads. This particular fiber is a 7-cell HC-MOF (due to the fact that 7 of those small structures were removed) with a core diameter of 16  $\mu\text{m}$ . To explore the 1.65  $\mu\text{m}$  absorption band of methane, the fiber was designed to have a well-defined bandgap in this spectral region. Also, more than 90% of the light propagates in the core, assuring a high field overlap with the gas and therefore enhanced detection sensitivity [101]. The transmission spectrum of this fiber in the region around 1.65  $\mu\text{m}$  is shown in Figure 49, obtained using a tuneable laser.



**Figure 49 - Spectral transmission of the 7-cell HC-MOF at its operational bandwidth.**

#### 4.3.1 Diffusion Time

A critical factor in sensing heads projected for the detection of dangerous gases is the measurement time. In most cases this is not limited by the intrinsic time constant of the optoelectronic components, but by the diffusion time of the gas into the measurement volume. This issue is particularly relevant when these volumes are reduced and accessed only through specific inputs, as is the case when MOF fibers are considered. Therefore, this problem was studied in detail in the context of this work.

We considered a HC-MOF fiber with one or two open ends, immersed in a methane atmosphere. Methane gradually penetrates the fiber by diffusion. The diffusion was characterized by the relative concentration of gas inside the fiber, averaged over the

fiber length. This concentration can be found by integration of local concentration that is obtained by solving the diffusion equation with the corresponding boundary conditions. The diffusion into a piece of MOF of length  $l$ , having two open ends, can then be described by [87, 102]

$$C(x, t) = C_0 \left[ 1 - \frac{4}{\pi} \sum_{j=1,3,5}^{\infty} \frac{1}{j} \sin\left(\frac{j\pi x}{l}\right) \exp\left[-\left(\frac{j\pi}{l}\right)^2 Dt\right] \right] \quad (4.1)$$

This formula gives the gas concentration  $C(x, t)$  as a function of the position  $x$  along the fiber and as a function of  $t$  relative to the time  $t = 0$ , which represents the moment when the gas concentration  $C_0$  was released at the open fiber ends. Here,  $D$  is the binary diffusion coefficient between the trace gas and air. Integrating this equation over the entire fiber length gives us the time-dependent average gas concentration  $C(t)$

$$C(t) = 1 - \frac{8}{\pi^2} \sum_{j=1,3,5}^{\infty} \frac{1}{j^2} \exp\left[-\left(\frac{j\pi}{l}\right)^2 D \cdot t\right]. \quad (4.2)$$

The diffusion coefficient for methane in nitrogen is  $0.22 \times 10^{-6} \text{ m}^2/\text{s}$  [103]. Using this value, the dependence of the average relative concentration on time for four fiber lengths (2, 6, 18, and 54 cm) was plotted. The result is shown in Figure 50 (a).

For the case of the fiber with one open end, the average relative methane concentration inside the fiber is obtained from equation (4.2) with  $l$  replaced by  $2l$ , resulting in the dependence given in Figure 50 (b). It should be mentioned that on these calculations surface effects were neglected, given the considerably large diameter of the core of the HC-MOF in comparison to the gas molecules size. Table 2 summarizes the results relative to the diffusion time of methane into the HC-MOF with one and two ends open.



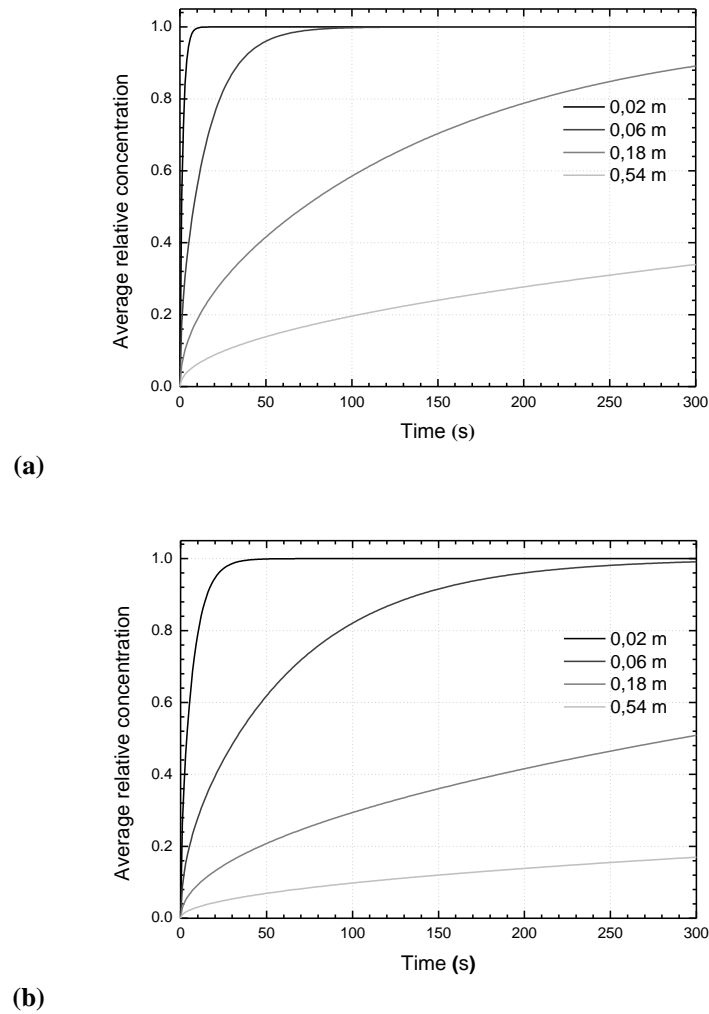


**Figure 50 - Time-dependence of the average relative methane concentration inside different lengths of HC-MOF with two open ends (a) and a single open end (b).**

**Table 2 - Theoretical diffusion times to obtain a 90% average methane concentration in the core of HC-MOF fibers for different lengths.**

$l$ (m)	<i>Two open ends</i>		<i>One open end</i>	
	$t$ (s)	$t$ (min)	$t$ (s)	$t$ (min)
0.02	4	0.07	16	0.27
0.06	34	0.57	136	2.27
0.18	305	5.08	1220	20.33
0.54	2745	45.75	10980	183

This analysis allows us to conclude that the length of the fiber used as the sensing head will directly affect the response time of the sensing system, limiting the time that gases may take to diffuse into the holes. As expected, with two open ends the gas diffusion inside the microstructured fibers happens significantly faster compared with the single open end configuration.

#### 4.4 Hollow core MOF based sensing head

To optimize the sensing head sensitivity without compromising the response time, a structure was devised where the introduction of periodic openings along the sensing head fiber was considered, as shown in Figure 51(a). The several hollow-core microstructured optical fiber (HC-MOF) pieces are connected through butt-couplings [101]. As previously stated, the length of each segment can be tuned to control the diffusion speed of the gas inside the sensor and hence the response time of the sensor. In turn, the number of segments determines the total fiber length and, therefore, dictates the sensitivity of the sensing head. Standard zirconium mating sleeves, as shown in Figure 51(b), were found suitable for this butt-coupling approach.

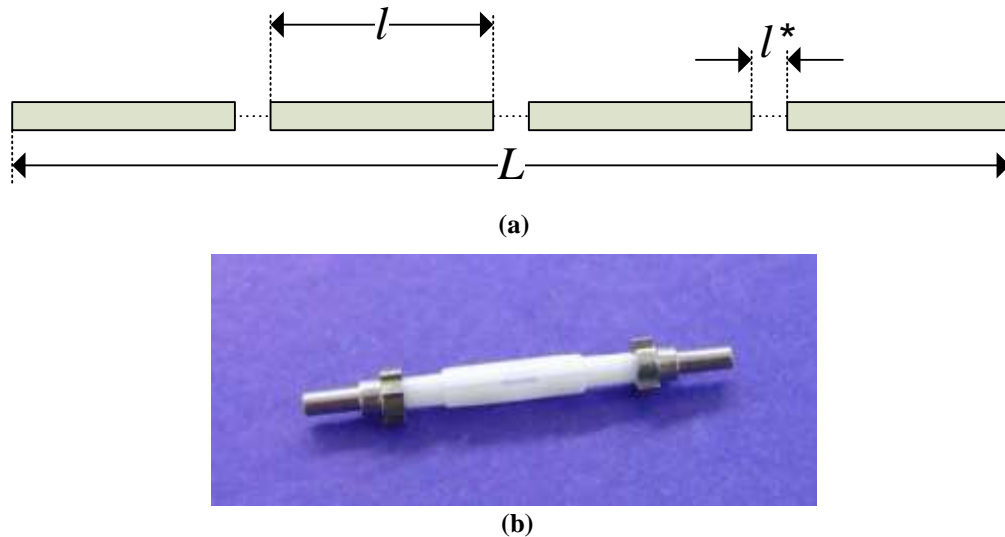


**Figure 51 - (a) Project of the sensing head with periodic openings in the MOF fiber; (b) Butt-coupling of HC-MOF pieces using standard zirconium ferrules connected with a standard zirconium mating sleeve.**

The HC-MOF inside the ferrules was aligned using nanometre resolution positioning stages as can be seen in Figure 52. The diameter of the sleeves is deliberately slightly smaller than the diameter of the ferrules. A slit along the length of the sleeve gives some extra flexibility to the inner diameter and allows the sleeve to act like a small spring (in the radial direction).

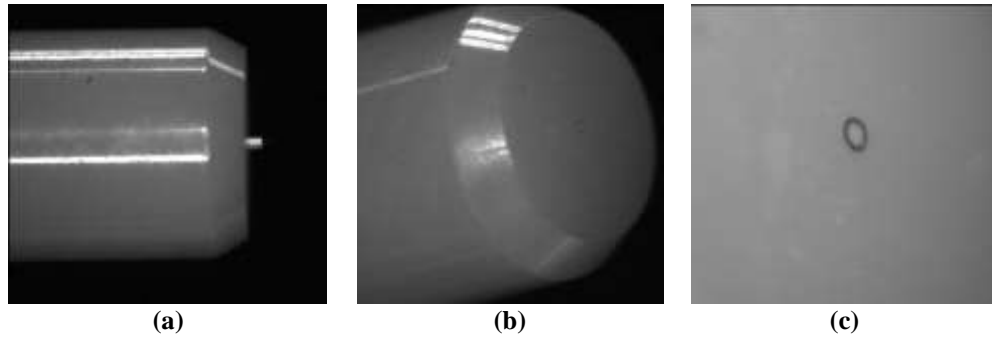


**Figure 52 - (a) photo of HC-MOF and the ferrule when they are not still in the same plane; (b) photo of the HC-MOF transversely and axially aligned with the ferrule; (c) detailed photo of the HC-MOF aligned with the ferrule.**

This mechanism ensures that the ferrules are clamped inside the sleeve, thus optimizing the alignment. Since this is the standard technology for aligning fiber connectors, the technology is well established and the components are relatively cheap. Furthermore, the slit in the sleeves is also well suited to allow gas in-diffusion through open gaps. Figure 53 shows a chain of different HC-MOF segments connected with this method.



**Figure 53 - Multi-segment sensing head containing 4 segments of HC-MOF.**

This multi-segment sensor was placed inside a silica tube that acts like a gas chamber which facilitates greatly the experimental test. The insertion loss of the sensing head is a consequence of the loss induced by each butt joint and can be quantified as presented in section (3.3), where the optical coupling was characterised in a 19-cell HC-MOF with a core diameter, and thus a guided mode behaviour, quite similar to the 7-cell HC-MOF fiber used here. Typically, it was found that the loss in each butt-joint was smaller than 1 dB.

With adequate sensing head packaging, that involves fiber wrapping the several butt-joints segments, which is possible due to the geometrical flexibility of the optical fiber, the volume increase when the number of butt-joint segments increases can follow a slow grow.

## 4.5 Wavelength Modulation Spectroscopy

The ability to have sensitive detection of methane with the previously described sensing head requires the consideration of a high performance interrogation approach. Therefore, the technique of Wavelength Modulated Spectroscopy (WMS) was selected, in view of its favourable characteristics (Silver *et al.* [104]). In WMS, the source wavelength is slowly modulated, sweeping the entire absorption peak and an higher frequency signal (dithering) is superimposed on this signal. As the emission source wavelength slowly scans through the gas absorption line, the wavelength modulation becomes an amplitude modulation, presenting its highest amplitude as it passes in the highest slope points of the absorption peak, as presented in Figure 54.

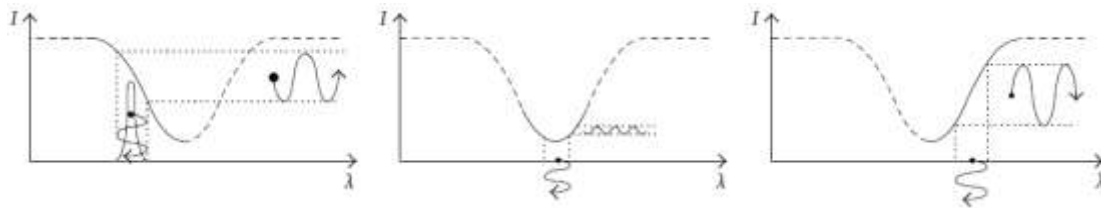


**Figure 54 - Wavelength modulation converted to amplitude modulation in Wavelength Modulation Spectroscopy.**

As the schemes in this figure indicate, this interrogation method requires that the optical source should have a linewidth significantly smaller than the absorption line of the gas species to be monitored. Considering that the detection bandwidth is shifted to higher frequencies where the laser intensity noise is reduced towards the shot noise, the signal-to-noise ratio is substantially increased, which means a better measurement resolution. This concept is similar to that of data encoding in the side bands of a radio transmission carrier wave. Figure 55 shows the spectral output of a frequency modulated laser, where it can be seen the carrier frequency  $\omega_c$  and the side-band frequencies  $\omega_c \pm \Omega$ . Therefore, when the laser slowly scans through the absorption line, the amount of light absorbed, which by the Lambert-Beer Law [105] is proportional to the gas concentration, is “written” into the side bands. Schematically, this is represented in Figure 55 as a decrease in the amplitude of the side bands. Consequently, the absorption information can be retrieved by means of a lock-in amplifier, where a voltage output proportional to gas concentration can be generated.

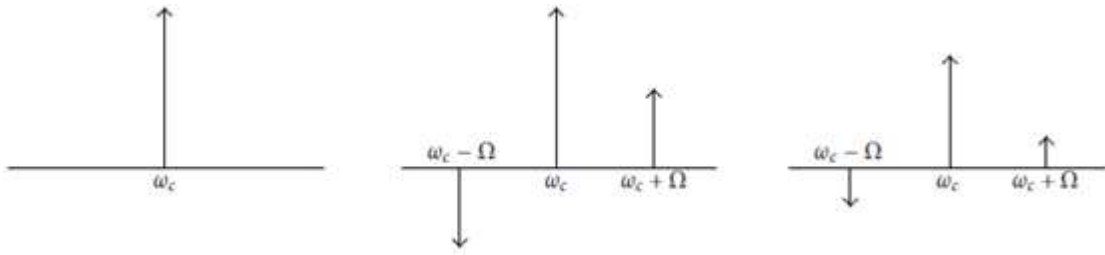


**Figure 55 - Spectral contents of the optical signal: *left*) laser unmodulated; *middle*) laser modulated with no absorption; *right*) laser modulated with absorption.**

Some features of this interrogation technique can be better appreciated observing the curves shown in Figure 56. They are relative to acetylene, the gas that was used in the system development phase because it shows an absorption band around 1530 nm (Figure 56 (a); the acetylene strongest absorption peak in the P branch of the  $\nu_1 + \nu_3$  band [106]), a highly convenient spectral position considering the large range of optical fiber components that can be used in view of its location in the third optical communications spectral window.

The interaction between acetylene (pressure ~200 Torr, ~100 % concentration) and the optical field happened in a U-bench with 30 mm length. The laser source used for these experiments was an Avanex-1905 LMI DFB laser optimized for operation at 1530 nm. With the lock-in amplifier locked at the dithering frequency, the output signal is the first derivative of the gas absorption line, and it equals zero when the source wavelength is centred in the absorption peak (Figure 56 (b)).

The lock-in amplifier output for the second harmonic is the derivative trace of the output at the dithering frequency, and reaches a maximum at the peak absorption wavelength (Figure 56 (c)).

Disabling the slow modulation and stabilizing the source emission wavelength at the absorption peak, the dithering gives rise to a transmitted signal with a frequency that is twice the dithering one and with an amplitude that depends on the gas concentration.

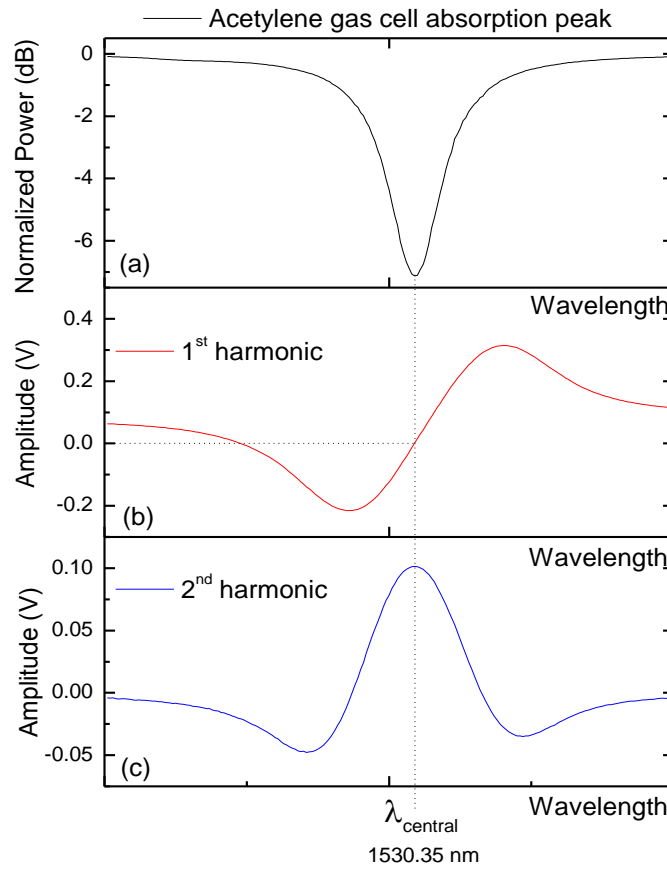


**Figure 56 - Absorption line of an acetylene gas cell (a) and amplitude of the output signals at the dithering frequency (b) and at double of this frequency (c)**

This detection method thus converts a frequency modulation into an amplitude modulation. The measured signal will contain both an AC and a DC component. Fluctuations of the optical power (from the source, fiber bends, etc.) will commonly modify the AC and DC components of the signal, so the ratio of the AC component with the DC component remains fairly unaltered, and therefore only affected by the gas concentration. This insensitivity to optical power fluctuations is one of the main advantages of the WMS method.

#### 4.3.1 Interrogation Technique Implementation Scheme

Figure 57 shows the detailed scheme of the optoelectronic detection technique based in WMS. Ideally, an optical source suited for the WMS method shall have the following properties: high power (assures good signal-to-noise ratios and allows

sensor multiplexing); narrow line width (in comparison with the line width of the methane absorption lines), which is also important to enhance the signal-to-noise ratio; and tuneable emission wavelength. Distributed Feedback Lasers meet all these demands at an affordable cost. A DFB diode can be tuned in wavelength by changing either the temperature or the operating current. While current-tuning is favourable for rapid modulation tasks, thermal tuning has the advantage of providing extremely large mode-hop free tuning ranges.

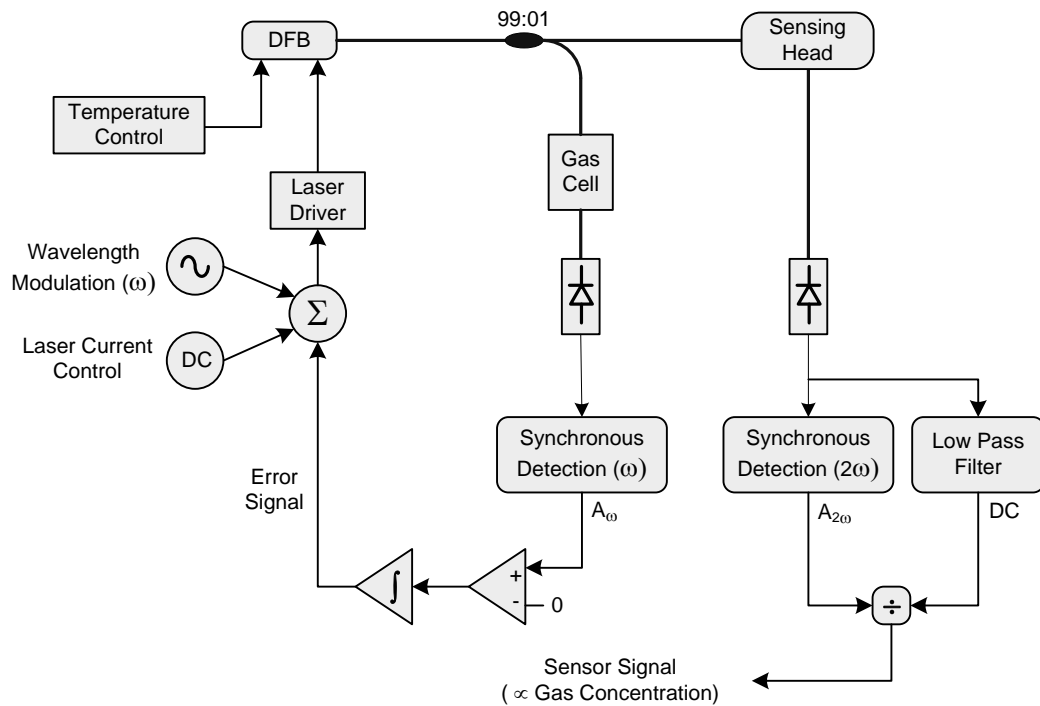


**Figure 57 - Layout of the developed interrogation system based on Wavelength Modulated Spectroscopy.**

In the configuration presented in the figure, the wavelength of the DFB optical source is modulated with a frequency  $\omega$  by means of current tuning. The light is then guided through a directional coupler. Part of the light is sent to a reference gas cell whereas the remaining portion of light is sent to a sensing head. The reference cell is used to keep the laser wavelength locked to the gas absorption line. Monitoring of the light from the reference cell happens with a lock-in amplifier working at the modulation frequency and the resulting signal is feedback to the laser driver. The light coming from the sensor is analysed for two components. The DC component is filtered out using a low-pass filter and the doubled frequency amplitude modulated

signal is isolated using synchronous detection at  $2\omega$ . The information for gas concentration is obtained from the ratio

$$S = \frac{A_{2\omega}}{DC} \quad (4.3)$$

where  $A_{2\omega}$  is the amplitude of the signal synchronously detected at  $2\omega$  and  $DC$  the continuous level. This relation yields the absorbance and hence the gas concentration. The resulting signal, as previously stated, should be independent of optical power fluctuations.

In order to enable the variation of the gas concentrations and to test the implemented setup with the HC-MOF based sensing heads, a gas chamber was developed (Figure 58). The chamber was hermetically sealed and had one gas input and output, as well as a pressure manometer and an optical feedthrough to allow the entrance of fibers. Inside of this chamber there were also two U-benches with different path lengths (30 mm and 6.8 mm, respectively) which were used for testing purposes before the final implementation of the MOF based sensing head.

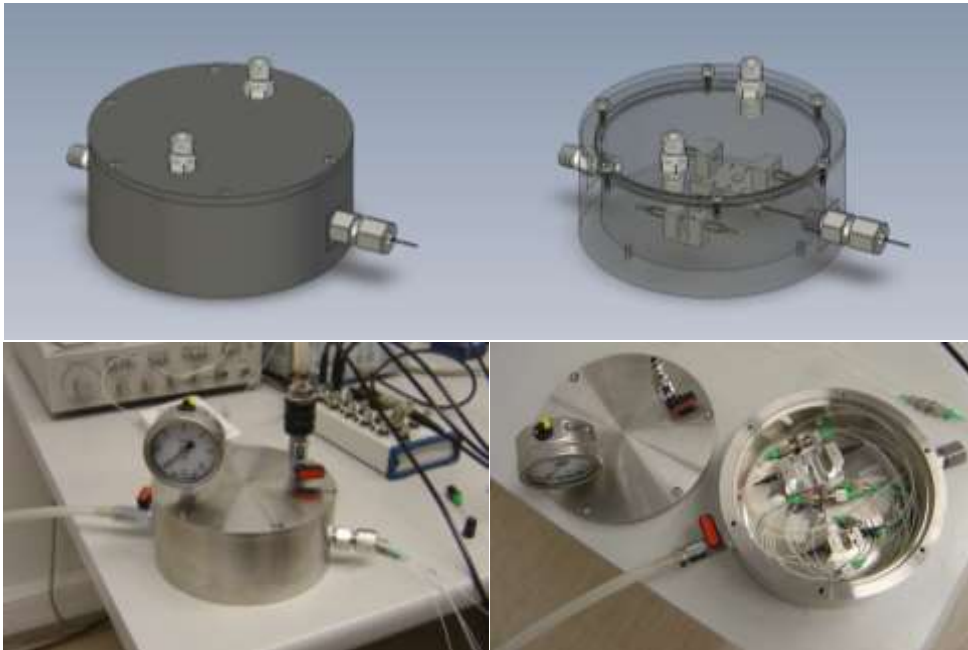


**Figure 58 - Gas chamber for testing the sensing system: (top) computer generated pictures; (bottom) photographs of the implemented gas chamber (the U-benches shown on the right were used to test the WMS interrogation technique).**



A LabVIEW<sup>®</sup> application was developed to control all the signal generation, acquisition as well as all the single processing stages. With a standard computer and a DAQ board a virtual instrumentation workbench was implemented, with the objective of performing the system integration of a portable and customizable solution for remote detection of gas species.

## 4.4 Results

In this section the results for the gas diffusion time in the HC-MOF based sensing head are shown. Further the detection limit of the developed WMS interrogation system for methane gas quantification is presented. Finally a prototype of a portable unit for methane detection is presented as a result of the applied research in this field.

### 4.4.1 Methane Gas Diffusion Time Measurements

The experimental arrangement implemented to test the gas diffusion time into the HC-MOF is shown in Figure 59 (a). Standard SMF transmitted light to the HC-MOF and guided it to the detection unit. After injection of gas into the chamber (a mixture of 5% of methane and 95% of nitrogen), the decay of transmitted light with time caused by the absorbance of the gas inside the HC-MOF was registered. The length of the HC-MOF sensing head was 13.7 cm. The optical source, a NEL DFB laser optimized to work at 1666 nm, was emitting at the strongest methane absorption line in the Q branch of the  $2\nu_3$  band (Rothman *et al.* [107]). The frequency of the dithering signal that modulated the DFB was 500 Hz. To allow gas diffusion, the gap between the input and output SMF and the HC-MOF was guaranteed by the use of angled ferrules (FC/APC) in the side of the standard fibers (Figure 59 (b)). These ferrules, exhibiting an angle of  $8^\circ$ , were chosen because they do not permit Fresnel (silica-air interface) back reflections to be guided.

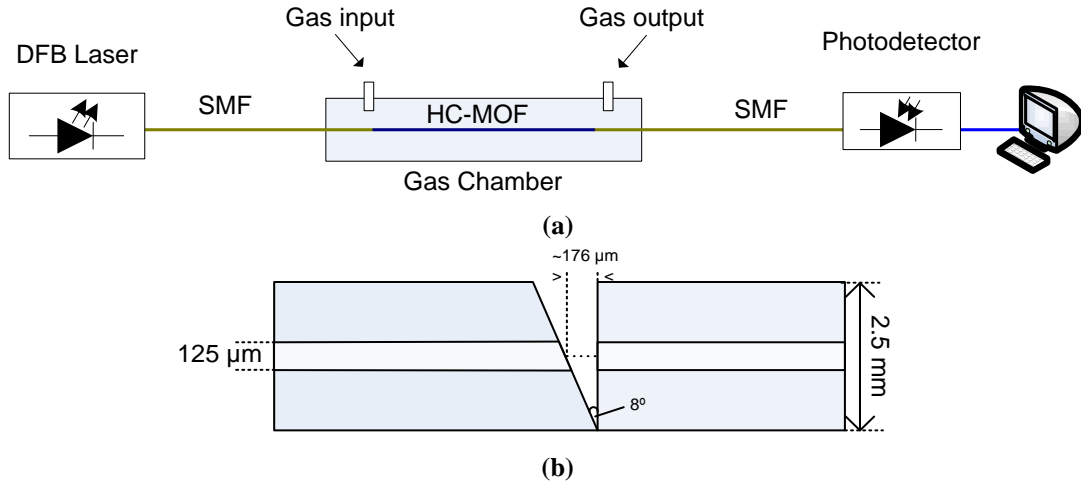


**Figure 59 - (a) Setup used to measure the diffusion time of gas inside the HC-MOF based sensing head; (b) illustration of the joint between SMF and HC-MOF.**

The obtained results for methane diffusion inside the HC-MOF are presented in Figure 60. It can be observed that the time taken to achieve 95 % of the steady-state was about 248 s, while the theoretically predicted value obtained from equation (4.2) was about 241 s, thus leading to a relative error of ~2.8 %. This agreement therefore confirms the reliability of the adopted model.

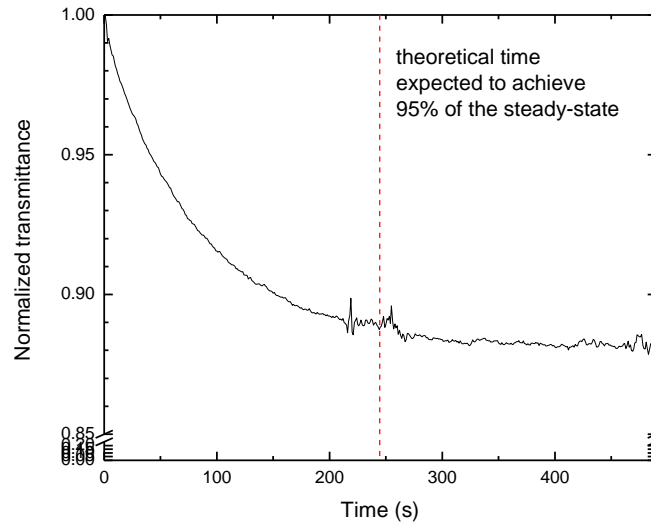


**Figure 60 - Experimental results for the diffusion time of 5% of CH<sub>4</sub> inside a HC-MOF with a length of 13.7 cm (two open ends). The theoretical expected value (241 s) is shown by the vertical dashed line, while the experimentally obtained was 248 s.**

#### 4.4.2 Methane Detection Limit Quantification

After implementing the WMS based experimental setup described in Figure 57, to interrogate the developed HC-MOF sensing head, the detection limit of the methane sensing head can be estimated from the signal-to-noise ratio ( $SNR$ ) of the demodulated signal. The  $S$  parameter defined by equation (4.3) obtained at 1000 Hz ( $2\omega$ ) shows a linear signal-to-noise ratio ( $S/N$ ) of 316 which corresponds to a methane concentration of 5 %, or 50000 ppm.

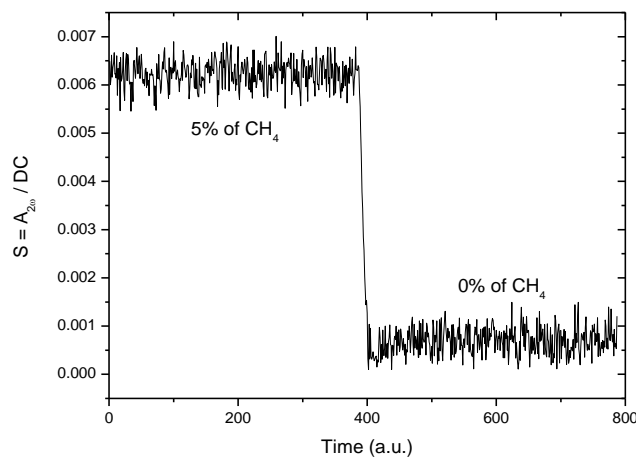


**Figure 61 - System response for a methane concentration change**

In terms of a voltage signal, the  $SNR$  can be written to be

$$SNR = 20 \log \left( \frac{S}{N} \right) \quad (4.4)$$

where  $S$  is the signal and  $N$  is the noise level. This gives rise to an  $SNR$  of 68.8 dB. The noise level yields,

$$N = S \times 10^{-\frac{SNR}{20}} \quad (4.5)$$

Therefore, the sensing head with 13.7 cm length and opened in both sides, whose gas diffusion time was plotted in Figure 60, permits a methane detection limit of 158 ppm.

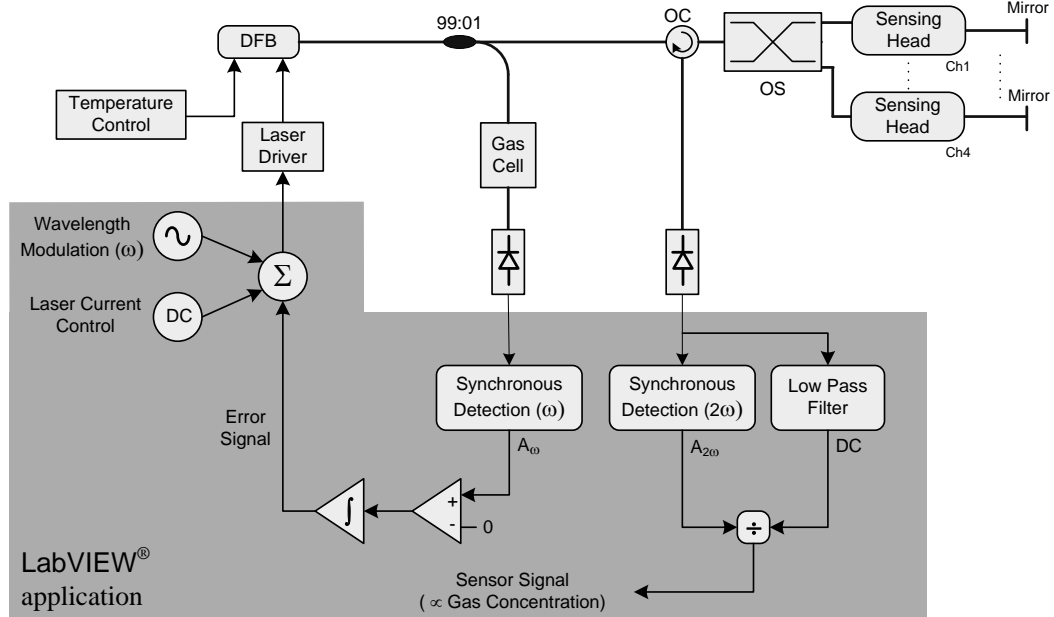
If more segments are considered in the sensing head, as shown in Figure 53, the detection limit shall improve proportionally to the increase of the light interaction length with the gas. However, the presence of a deleterious effect, associated with superficial modes at the boundary of the fiber hollow core was noticed. These modes induce interference effects that reduce the signal-to-noise ratio. Research is going on aiming to overcome this problem. Additional results for methane detection with non-MOF-based solutions can be found in Appendix 1.

#### **4.4.3 Measurement Portable Unit for Methane Detection**

Looking for a field application of the R&D described above, an optoelectronic portable measurement unit was developed to measure gas concentration with HC-MOF based sensors, in straight cooperation with FiberSensing, a world leader Portuguese company in the development and production of optical fiber based advanced monitoring systems.

The portable unit integrates a computer (motherboard, memory, hard-disk, touch-screen, etc.), an optoelectronic board and optical switching capability for multiplexing four remote photonic crystal fiber sensing heads.

A LabVIEW<sup>®</sup> application was developed to control the measurement unit system and present a graphical interface to the user. A diagram of the implemented system is presented in Figure 62 (a), while Figure 62 (b) shows a photo of the equipment. Figure 62 (c) gives a unit screen plot representing the system response to a change of methane concentration in the sensing head.



(a)



(b)



(c)

**Figure 62 - (a) Diagram of the gas measurement unit prototype; (b) photo of the portable measurement unit; (c) response for three different methane gas concentrations. The fluctuations that the different plateau exhibit are due to the effect of the pressure of the gas being injected into the chamber which causes a broadening effect on the absorption peaks.**

## 4.5 Summary

In this chapter was reported the development of an optical fiber sensing system for detection of low-levels of methane, based on a sensing concept that explores the favourable characteristics for gas sensing of hollow-core photonic crystal fibers, together with the Wavelength Modulation Spectroscopy interrogation technique.

Concerning remote gas detection, optical fiber based sensing heads and more specifically MOF fibers extend the detection and measurement capabilities of sensing small gas sample volumes in the vicinities of pipelines, landfills and mining sites, where the increase of gas concentration can naturally occur and consequently reach explosive limits. Additionally, the development of hollow-core MOF based gas sensing systems enable the direct interaction of light with gases, which consequently results in an intrinsically explosion safe solution since the risk of electrical spark ignition does not exist.

A MOF sensing head structure was designed that is compatible with sensitive methane detection (158 ppm) and has an acceptable measurement time (248 s), which is related with the gas diffusion time into the measurement volume. The results obtained confirm the potential of this sensing approach, and aiming at field applications, a portable measurement unit was developed that has the capacity to simultaneously interrogate four remote sensing heads.

Monitoring of multiple sensing points is an effective advantage of the presented system and the qualitative monitoring of small changes in gas concentrations (at the ppm level) was proved to be possible.

## Chapter 5 – Fiber Sensing with Modal Interferometry

---

### 5.1 Introduction

Optical fiber sensors based in intermodal interference between core and cladding modes have been proposed in recent years and tested for various applications. Such interferometric sensors have several advantages over other sensing concepts, including small size, high sensitivity and resolution, fast response time and low cost. Different solutions to obtain all-fiber intermodal interference in microstructured optical fibers are reported in published literature. In section 5.2 a brief review of such technology is presented.

Sections 5.3 and 5.4 will describe two different sensors based on the modal interference concept using, respectively, a hollow core microstructured optical fiber and a highly birefringent microstructured optical fiber.

### 5.2 Modal Interferometry for Optical Sensing

Microstructured optical fibers based on new hybrid structures have been introduced to form fiber modal interferometers [108-113]. For example, in a single mode – multimode – single mode fiber structure it was examined the effect of modal interference on the performance of a microbend sensor [114], as well as when considering strain [115, 116] and temperature [116, 117] measurement. Another interesting configuration was based on the series combination of single mode – two mode – single mode fiber sections, which generates a transmission interference pattern with high extinction ratio [118].

This type of interferometers has also been explored in the general context of microstructured optical fibers (MOF). Indeed, a configuration based on tapering an index-guiding MOF was suggested for refractive index sensing, in-line variable

attenuator and strain sensor, where the complete collapse of the air holes around the fiber core originates a region of solid unclad multimode fiber [110, 119, 120]. Another approach to implement modal interferometry is by doing a lateral offset in the SMF-MOF splice point, to excite higher order modes in the index-guiding fiber [108, 111, 121].

A recently reported technique is based on the partial collapse of the air hole at a limited region of a MOF to couple light to higher modes, and it was used for strain measurement in conditions of very high temperature in view of the thermal characteristics of fused silica fibers [121]. Also, a modal Mach-Zehnder structure in a hollow-core fiber with standard single-mode input and output fibers was proposed and characterized for high-temperature sensing [122].

### **5.3 Modal Interferometers in Hollow-Core Microstructured Fibers**

HC-MOF are made with hundreds of periodically spaced air holes in a silica matrix, typically arranged in a triangular lattice, using the photonic band gap concept to propagate light inside the air-core. These fibers are usually multi-mode waveguides supporting, besides the fundamental core mode, higher order core modes, cladding modes and surface modes [103, 104]. However, the attenuation of the different types of modes varies substantially and after propagation along an extended length of fiber only the fundamental core mode subsists. The multimode operation of short lengths of HC-MOFs creates the possibility of building up modal interferometers, with characteristics potentially interesting to perform optical fiber sensing.

In this section a fiber optic modal interferometer based on an HC-MOF was studied and its characteristics for strain and temperature sensing were investigated, as well as for curvature. The readout of the interferometric phase was achieved combining white light addressing with pseudo-heterodyne signal processing.



### 5.3.1 Sensing Principle

The sensor was fabricated using a piece of HC-MOF directly spliced between two lengths of single mode fiber (SMF-28<sup>TM</sup>). A 7-cell HC-MOF with a low-loss transmission band centered at 1550 nm and a core diameter of  $\sim 16 \mu\text{m}$  was used. Figure 63 (a) shows an optical microscope image of this fiber. The transmission characteristics, in the light injection conditions in which the experiments were performed, are depicted in Figure 63 (b).

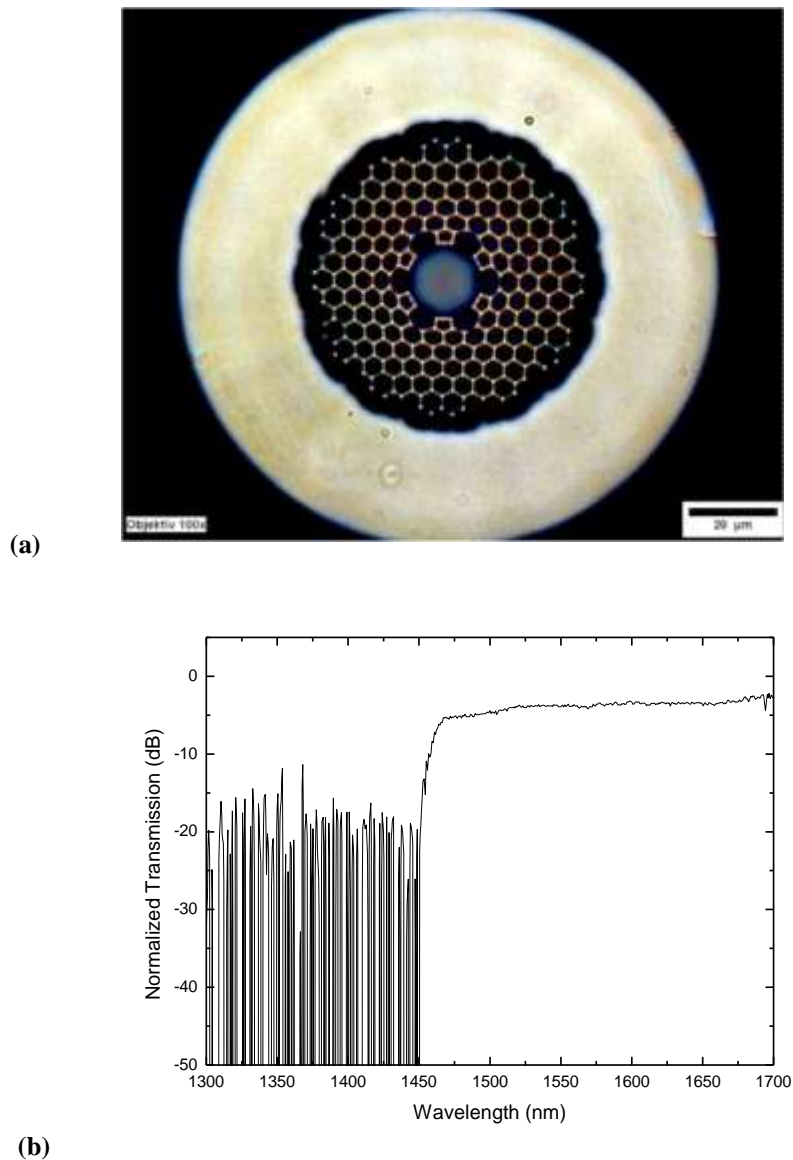


**Figure 63 - (a) Cross section photograph of a 7 cell HC-MOF and (b) normalized spectral transmission of  $\sim 1$  m of this fiber spliced to a SMF28 illuminating fiber (the oscillations at lower wavelengths are artifacts due to the normalization).**

The developed sensing head uses the effect of modal interference at the exit of the HC-MOF to achieve the measurement functionality. Indeed, when light travels through the single mode fiber and is injected into the HC-MOF, the fundamental core mode and other modes are excited. After propagation of these modes in the HC-MOF, they are recombined at the entrance of the output single mode fiber. This simple configuration is similar to an all-fiber Mach-Zehnder modal interferometer, with two coupling points in series, different from what is most usual when considering in-line fiber interferometers, which show a Fabry-Perot structure.

Therefore, when light is injected into the input single mode fiber, we expect to observe interference fringes at the output single mode fiber. It should be noticed that the fringes are not related to the collapse of air channels of the HC-MOF, like tapering in the fusion splice point and/or broadening of fundamental mode in this region, as reported in literature [123].

In order to confirm this, some experiments were carried out to check if the fringes still appear with butt coupling instead of fusion splicing. The results obtained showed that the formation of the interference fringes is independent of the coupling method, but the amplitude of the effect is dependent on the coupling conditions. Indeed, it was also found that the amplitude of the fringes (interference visibility) can be substantially reduced by proper adjustment of the input SMF and the HC-MOF in the junction region, which actually is not necessarily the condition for optimum power coupling.

The analysis of the obtained results points out to the important role of the HC-MOF cladding modes in the operation of this modal interferometer, but further theoretical and experimental studies are required for a detailed understanding of the exact type of modes involved in this interferometric structure.

Figure 64 (a) shows the splice structure (in the X and Y directions) between the SMF-28 and HC-MOF fibers, as well as the observed output channeled spectrum for a piece of HC-MOF with a length of 27.8 cm.

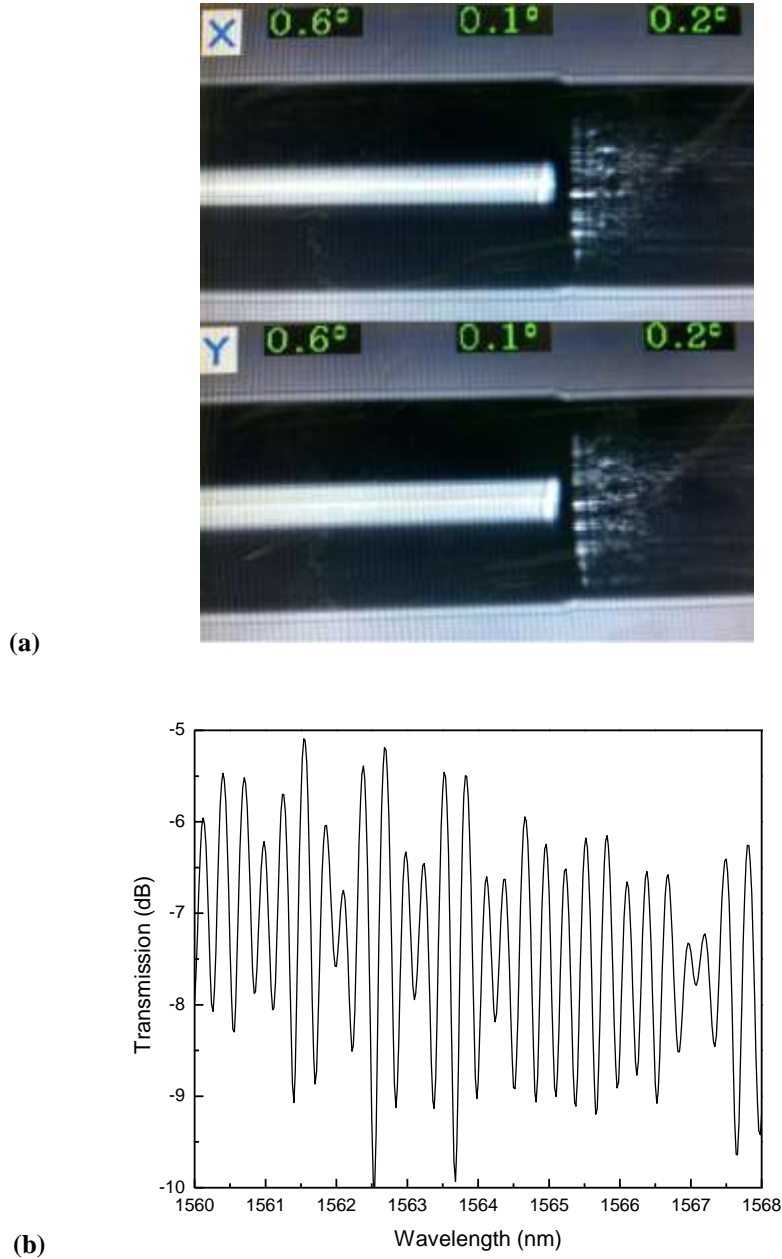


**Figure 64 - (a) Visualization of the SMF-28/HC-MOF splice in the Fujikura's SM-40 screen; (b) Channeled spectrum of the interferometric sensing head.**

It can be observed that besides the typical two-wave interferometric behavior, there is also fringe amplitude modulation, indicating the presence of more than two modes interference. The refractive index difference associated with the observed fringe periodicity in the figure can be calculated by means of the relation

$$n_{eff}^{FM} - n_{eff}^{other\ modes} = \frac{\lambda_1 \lambda_2}{L(\lambda_1 - \lambda_2)} \quad (5.1)$$

Here  $n_{eff}^{FM}$  and  $n_{eff}^{other\ modes}$  are, respectively, the effective refractive index of the fundamental core mode and the average value of the effective refractive indexes of the other modes predominantly excited in the experiment performed. Also,  $\lambda_1$  and  $\lambda_2$  are the wavelengths corresponding to two adjacent intensity maxima and  $L$  is the length of HC-MOF. It was found that the value of  $\Delta n_{eff} = n_{eff}^{FM} - n_{eff}^{other\ modes}$  is 0.016, independently of  $L$ .

### 5.3.2 Experimental Setup

The initial experimental set up is shown in Figure 65. A superluminescent Er-doped fiber ASE (amplified spontaneous emission) source, operating at 1550 nm, with a FWHM (full width at half maximum) of 60 nm and output power of 1.8 mW was used to illuminate the concatenated fibers.

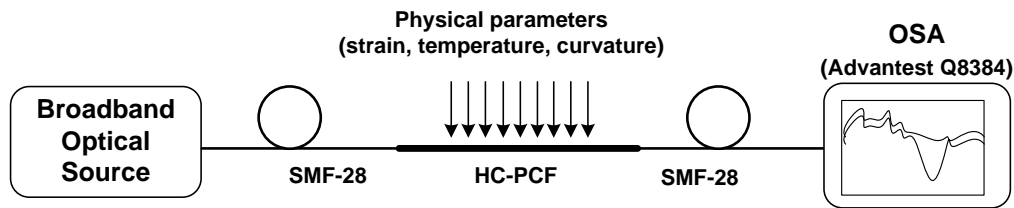


**Figure 65 - Experimental setup for initial characterization of the modal interferometer.**

The HC-MOF was spliced in both ends to single mode fibers applying general procedures described previously in sections 3.2 and 3.3. The standard splicing machine Fujikura FSM 40-S was used and a splice loss of ~1.5 dB was achieved. In order to evaluate the dependence of the fringe visibility with the HC-MOF length, sensing heads with lengths of 5.1 cm, 11.6 cm, 21.4 cm and 58.8 cm were fabricated and the associated channelled spectra analyzed.

For the first three lengths the visibility was around 50%, but when the longer fiber length was considered the visibility showed a substantial decrease to ~36%. This behavior is compatible with a visibility reduction due to power loss in the higher order

modes, originated by the weak propagation guidance of these modes in the longer fiber.

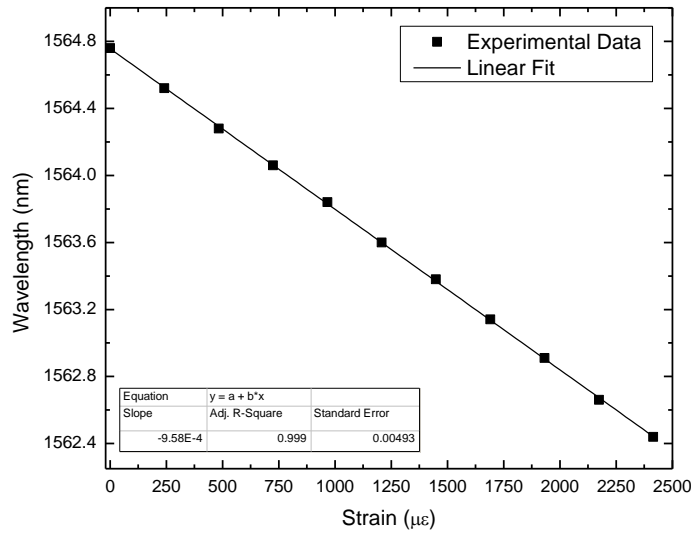
In order to investigate the strain, temperature and curvature characteristics of the sensing head, two micro-positioners were used to fix the SMF fibers and to apply strain and curvature to the HC-MOF. For temperature characterization a furnace was used. The length of the HC-MOF was ~28 cm and the fringe visibility was found to be ~55%.

### 5.3.3 Results

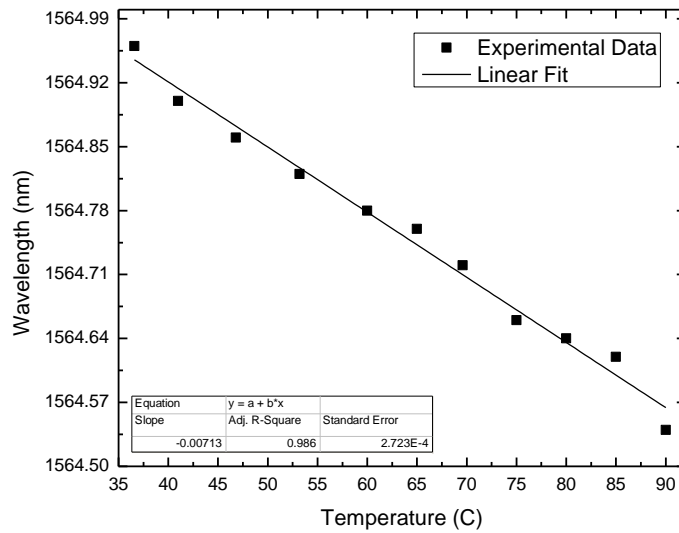
Figure 66 shows the strain and temperature wavelength responses of the sensing head, obtained by monitoring the shift of the channeled spectrum under the measurand action. The interferometric fringes were linearly shifted toward shorter wavelengths with the increase of strain or temperature, with slopes of  $-0.96 \text{ pm}/\mu\epsilon$  and  $-7.1 \text{ pm}/^\circ\text{C}$ , respectively.

These sensitivity values can be compared with those of a conventional single mode-multimode-single mode structure, which are  $-2.3 \text{ pm}/\mu\epsilon$  and  $-15 \text{ pm}/^\circ\text{C}$  [115, 117]. Concerning curvature, no measurable sensitivity was noticed, which is indeed an expectable result. The core of the fiber follows the fiber neutral line and, therefore, the optical path of the core mode is essentially curvature independent.

On the other hand, the cladding modes integrate along the propagation positive and negative variations in their optical path, induced by the presence of curvature in the fiber, which means the net effect shall be residual. Therefore, this argument points out to an insensitivity of the sensing head to curvature.



(a)



(b)

**Figure 66 - Wavelength responses of the sensing head for variations of applied (a) strain and (b) temperature.**

The blue shift of the channeled spectrum associated with the increase of temperature and strain can be understood with the following argument. Considering temperature, the thermal expansion implies a longer propagation length for the cladding modes when the temperature increases, but is similar to the longer propagation length of the core mode, i.e., an increase in temperature shall originate for this type of fiber, and in view of the differential operation of the interferometer, a residual shift of the channeled spectrum due to the thermal expansion effect. The same does not happen when the thermo-optic effect is considered. The experimental

results indicate its contribution is associated with the decrease of the absolute value of  $\Delta n_{eff}$ .

To understand this, it should be considered what happens with the core mode and cladding modes involved in the modal interferometer operation when temperature increases. Because the core mode propagates essentially in air, its effective refractive index is close to one and residually sensitive to temperature variations. Therefore, the variation of  $\Delta n_{eff}$  is essentially associated with the temperature behaviour of the cladding modes. These modes have a substantial fraction of their optical field that propagates in silica. It is known that silica has a positive thermo-optic coefficient, therefore considering only this effect the effective refractive index of these modes would increase with temperature, leading to a larger absolute value of  $\Delta n_{eff}$  and, consequently, to a red shift of the channeled spectrum, contrary to what is observed. However, the situation is more complex because the optical field of these cladding modes propagates also in the air of the core/cladding holes, and the thermal expansion can induce changes in the mode fraction that propagates in the silica and in the air, with a net effect that leads to a decrease with temperature of the effective modal refractive index. Certainly this is a complex phenomenon that needs further theoretical/experimental studies for its detailed understanding.

Concerning strain, the experimental results indicate that the contribution to the variation of  $\Delta n_{eff}$  associated with the elasto-optic effect is dominant relatively to the direct expansion effect. This is understandable, considering that the refractive index of silica decreases with strain, with the consequence that the effective refractive index of the cladding modes decreases with the increase of strain. Having in mind that the effective index of the core mode is essentially unaffected by strain, the net effect is a reduction of the absolute value of  $\Delta n_{eff}$  originating a blue shift of the channeled spectrum with the increase of applied strain.

To measure the phase changes in the fiber modal interferometer, a second interferometer was built to implement coherence reading [124]. Figure 67 shows the setup implemented.

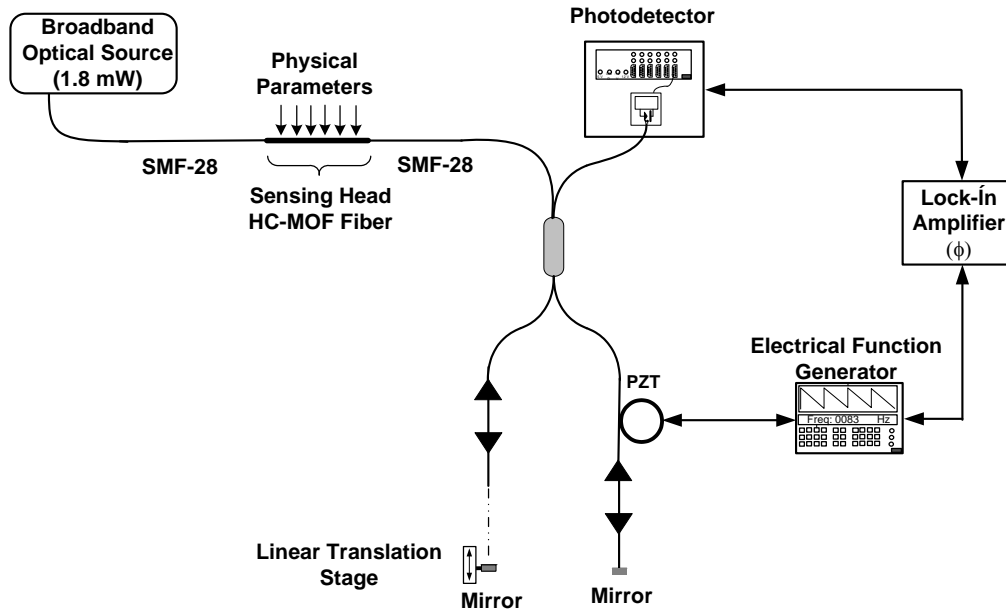


**Figure 67 - Scheme of the experimental setup for phase reading with white light interferometry.**

The second interferometer is a conventional fiber Michelson interferometer with an open air path in one of its arms, which is adjusted to match the optical path difference of the sensing interferometer. The fiber in the other arm of this interferometer is wrapped around a ringshaped piezoelectric transducer that is modulated with an electrical sawtooth waveform, whose amplitude is adjusted to obtain a signal at the photodetection suitable for pseudo-heterodyne processing. After adequate electronic filtering, this signal has the form of an electric carrier (90 Hz) with a phase that mirrors the optical phase of the tandem interferometric system. This pseudo-heterodyne processing technique is known to provide sensitive interferometric phase reading [125].

Figure 68 shows the phase changes associated with strain and temperature variations applied to the sensing head, now with  $L \approx 32$  cm and with an interferometric visibility of  $\sim 49$  %. Following the behavior represented in Figure 66, the sensitivity is constant in the measurement range considered, with values of  $0.76$   $^{\circ}/\mu\epsilon$  and  $8.1$   $^{\circ}/^{\circ}\text{C}$  for strain and temperature, respectively.



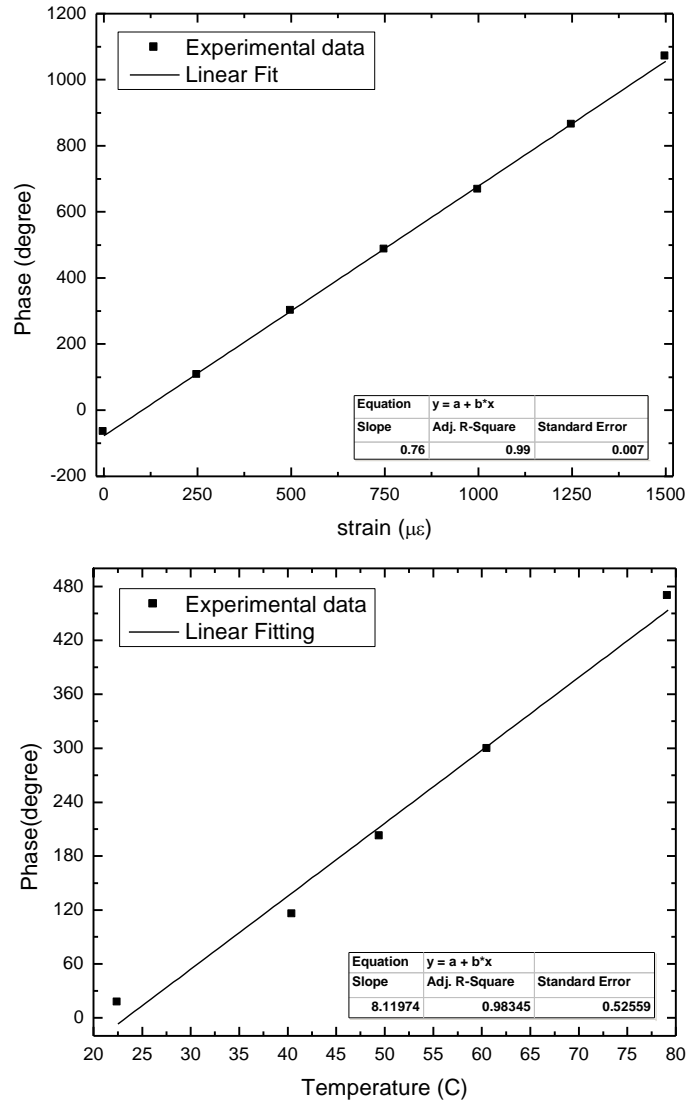
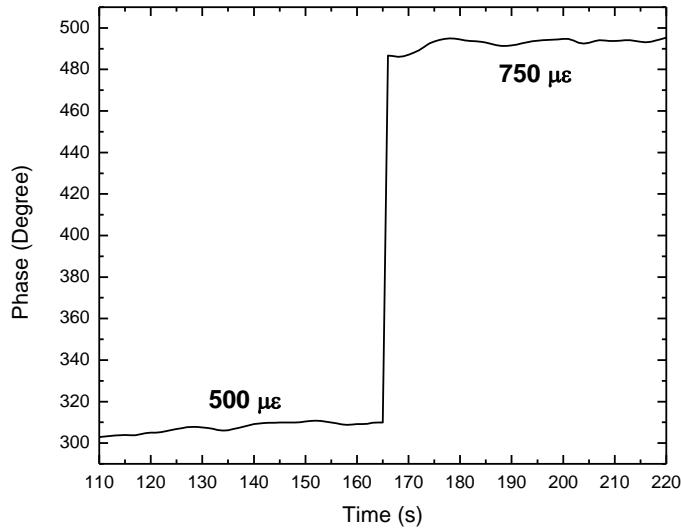


**Figure 68 - Phase changes induced by strain and temperature variations applied to the sensing head, respectively.**

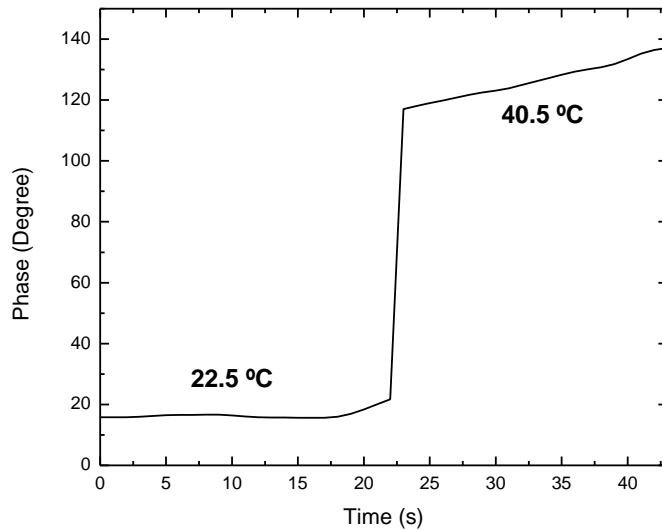
To evaluate the measurand resolutions achievable with this sensing head structure the step technique was used (Figure 69). If  $\delta\phi$  are the phase *r.m.s.* fluctuations during the periods of constant measurand values, and if a measurand step change  $\Delta X$  (being  $X$  the applied strain or temperature) originates a phase step change of  $\Delta\phi$ , then the measurand resolution,  $\delta X$  is given by

$$\delta X = \delta\phi \frac{\Delta X}{\Delta\phi} \quad (5.2)$$

For the case of temperature, in the determination of  $\delta\phi$  privileged the region corresponding to water at a stable temperature of 22.5 °C was selected, because it was difficult to stabilize the water temperature at 40.5°C after the step change, i.e., for some time the temperature of the water continued to increase at a slow rate. Following this approach, resolutions of  $\pm 1.4 \mu\epsilon$  and  $\pm 0.2 \text{ }^{\circ}\text{C}$  were obtained for strain and temperature, respectively.



(a)



(b)

**Figure 69 - Phase response of the sensing head implemented with an HC-MOF fiber for a step change in (a) strain and (b) temperature, respectively.**

The pseudo-heterodyne technique used to interrogate the interferometric system can be implemented with standard electronics (or using an approach relying on computer-based virtual instrumentation), which means that besides the demonstration of the proposed sensing structure, a step further was done towards the utilization of this configuration in field applications.

#### **5.4 Modal interferometers in Hi-Bi microstructured fibers**

In this section is demonstrated an in-line fiber intermodal interferometer fabricated with a boron-doped highly birefringent microstructured fiber. The boron doped region located in the middle of the core, decreases the effective index of the fundamental mode and facilitates coupling between the fundamental and the first order mode. The coupling regions have the form of tapers, fabricated using CO<sub>2</sub> lasers, and are distant by a few millimeters. Light from a broadband source is coupled into the fundamental LP<sub>01</sub> mode of the microstructured fiber. At the fiber output, the light confined mostly in the fundamental mode is delivered to the optical spectrum analyzer by the lead-out fiber. As a result, the spectral intensity at the sensor output is modulated only by intermodal interference produced by a short piece of fiber between the two coupling points. Moreover, as the fiber is highly birefringent, each pair of polarization modes produces its own intermodal fringes, which results in the contrast modulation of the overall interference signal observed at the fiber output. On the other hand, it provides an additional degree of freedom in interrogating the interference signal and makes it possible to measure simultaneously two physical parameters acting on the interferometer.

The typical limitations of MOF based interferometric sensors are related to the efficiency in optical power launching, difficulties in controlling light polarization, the need for unavailable MOFs based passive devices, and/or incompatibility with standard fibers. The proposed sensor deals with almost all of these impairments, except the difficulty in polarization control, which was overcome thanks to the high fiber birefringence, giving rise to contrast modulation of the intermodal interference fringes when the sensor is powered with depolarized light. This was, to the best of our knowledge, the first intermodal highly birefringent MOF based interferometric sensor

reported in literature. In comparison with fiber Bragg grating sensors, it shows two times greater sensitivity to strain and temperature. Moreover, the proposed sensor allows for simultaneous measurements of the two parameters, by interrogation of the visibility and the displacement of interference fringes.

#### 5.4.1 Sensor Fabrication and Operation Principle

For fabrication of the intermodal interferometer, the boron-doped birefringent microstructured fiber shown in Figure 70 was used, which was drawn at the Department of Optical Fibers Technology, University of Marie Curie-Sklodowska in Lublin, Poland. The birefringence in this fiber is induced by two large holes located symmetrically with respect to the core. Its geometrical parameters (see Table 3) averaged for the first two layers of holes surrounding the core are as follows: pitch distance 3.6  $\mu\text{m}$ , diameter of cladding holes 1.63  $\mu\text{m}$ , diameter of large holes 4.14  $\mu\text{m}$ , external diameter of the fiber 100  $\mu\text{m}$ , size of the boron doped inclusion  $0.46 \times 0.79$   $\mu\text{m}$ , and boron concentration in the inclusion 13 mol%. It is worth mentioning that fibers of similar construction, with properly optimized geometry, can be used as a wideband fiber optic polarizer [126].

**Table 3 - Geometrical parameters of the highly birefringent MOF.**

$A_F$ [ $\mu\text{m}$ ]	$D$ [ $\mu\text{m}$ ]	$d$ [ $\mu\text{m}$ ]	$\phi$ [ $\mu\text{m}$ ]
3.6	4.14	1.63	100

To better understand the behavior of the proposed sensor, in collaboration with the Fiber Optics Group of the Institute of Physics at the Wrocław University of Technology, the propagation characteristics of the boron doped fiber were modeled, using a fully vectorial mode solver, based on the hybrid edge-nodal finite-element method (FEM) with a perfectly matched layer [127]. As it can be seen in Figure 70, the cross section of the investigated fiber is not uniform due to technological imperfections. The edges of the holes in the cladding and the doped inclusion were automatically detected by post processing of the scanning electron microscope (SEM) image, which included the modification of the histogram, followed by thresholding and binarization. Using this tool, the mesh for FEM calculations could be generated, which reflected the actual shape and location of each hole with an accuracy of about

30 nm. A precise copying of the fiber geometry is a key requirement for accurate modeling of its propagation characteristics. Using such an approach, the spectral dependence of effective indices for the fundamental and the first order polarization modes, phase and group modal birefringence and the confinement losses for each mode were calculated.

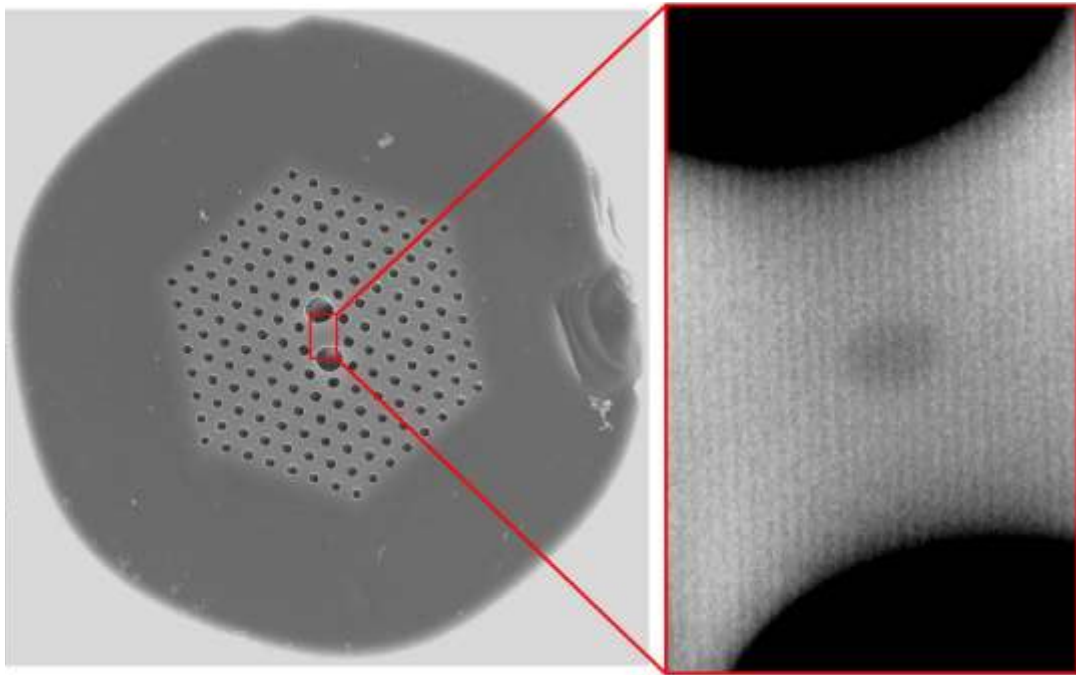


**Figure 70 - SEM image of the birefringent MOF with boron doped inclusion in the center of the core (darker spot) used for fabrication of the intermodal interferometer.**

Numerical calculations, presented in Figure 71, clearly prove that the boron doped inclusion diminishes the effective index of the fundamental mode, while the first order mode remains unaffected. This can be intuitively understood on the grounds of perturbation theory [128], which predicts that the change in the effective index squared for a specific mode can be expressed as the following overlap integral

$$\delta n_{eff}^2 = \int \delta n^2 |\Psi|^2 dA \quad (5.3)$$

where  $|\Psi|^2$  represents the normalized intensity distribution in the considered mode and  $\delta n^2$  stands for the change in the material refractive index squared introduced by the inclusion. As it is shown in Figure 71, the overlap integral between the first order mode and the inclusion is close to zero, while for the fundamental mode it takes the

highest value. This explains the difference in the impact of the inclusion on the fundamental and on the first order mode. Moreover, the lower effective index of the fundamental mode causes it to spread deeper into the microstructured cladding in the tapered regions, which facilitates its coupling to the  $LP_{11}$  mode.

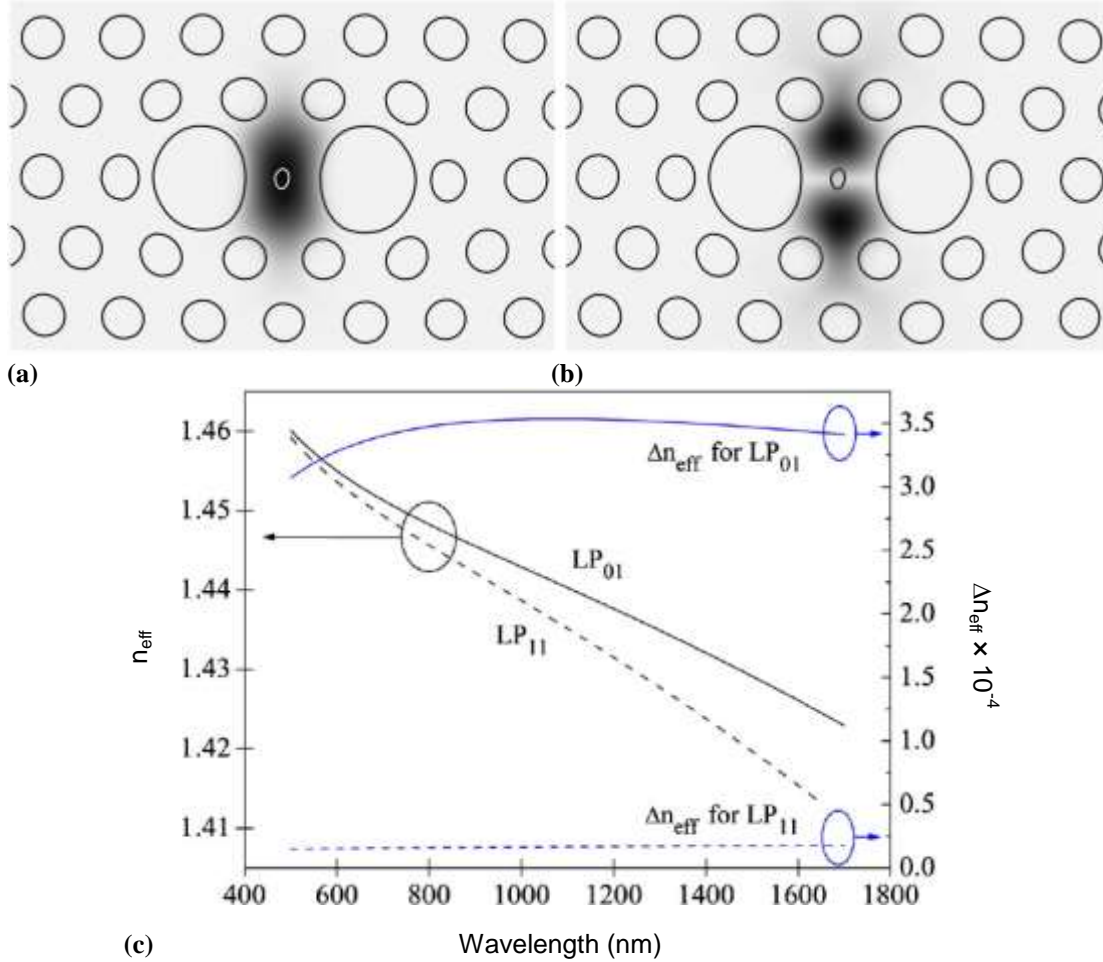


**Figure 71 - Field distribution calculated for the fundamental (a) and the first order mode (b) at  $\lambda = 1.55 \mu\text{m}$ . Spectral dependence of the effective indices in the fiber with boron doped inclusion for the fundamental and the first order modes and the effective index change introduced by the inclusion (c).**

The operation principle of the proposed interferometer is schematically illustrated in Figure 72 (a), while in Figure 72 (b) two tapered regions are shown formed by exposing the fiber to a  $\text{CO}_2$  laser beam and simultaneously stretching it when the glass becomes soft. The first taper causes coupling of the  $LP_{01}$  to the  $LP_{11}$  mode, and the two modes copropagate from this point onward. At the second taper the two modes are recombined producing the interference signal. The  $LP_{11}$  mode is partially filtered out at the splice between the boron doped two-mode microstructured fiber and the

endlessly single mode leading-out fiber (not shown in Figure 72). As a result, at the sensor output was observed only the interference signal carried in the fundamental mode. Such an inline fiber Mach–Zehnder interferometer is very compact and easy to fabricate. The splices have been made using a fusion arc splicer. Special care was taken to minimize the collapse of the microstructured regions. A typical loss of about 3 dB was achieved at each splice.

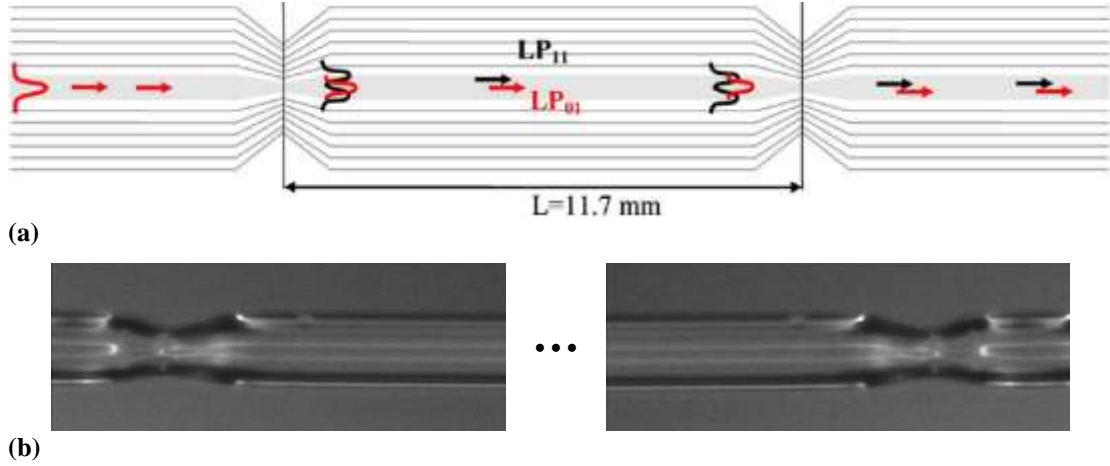


**Figure 72 - (a) Schematic configuration of the proposed intermodal interferometric sensor and the (b) microscope image of the microstructured fiber with the interferometer formed by two tapered regions.**

For a depolarized broadband input beam, at the fiber output was observed the superposition of two interference signals produced by two pairs of orthogonally polarized modes. Assuming that the coupling strength is the same for both polarizations, one obtains the following expressions for the interference signal produced by the modes  $LP_{01}^x$  and  $LP_{11}^x$

$$I_x(\lambda) = I_0 \left( 1 + \gamma \cos \frac{2\pi n_{01}^x - n_{11}^x L}{\lambda} \right) \quad (5.4)$$

and respectively by the modes  $LP_{01}^y$  and  $LP_{11}^y$

$$I_y(\lambda) = I_0 \left( 1 + \gamma \cos \frac{2\pi n_{01}^y - n_{11}^y L}{\lambda} \right) \quad (5.5)$$

where  $\gamma$  is the fringe contrast. In the output spectrogram, was observed the superposition of the two interference signals, which can be represented by the following formula

$$I(\lambda) = 2I_0 \left[ 1 + \gamma \cos \left( \frac{\pi (n_{01}^x + n_{01}^y - n_{11}^x - n_{11}^y) L}{\lambda} \right) \cos \left( \frac{\pi (n_{01}^x - n_{01}^y - n_{11}^x + n_{11}^y) L}{\lambda} \right) \right] \quad (5.6)$$

The above equation can be represented as

$$I(\lambda) = 2I_0 \left[ 1 + \gamma \cos \left( \frac{2\pi (n_{01}^a - n_{11}^a) L}{\lambda} \right) \cos \left( \frac{\pi (\Delta n_{01} - \Delta n_{11}) L}{\lambda} \right) \right] \quad (5.7)$$

where  $n_{01}^a$  and  $n_{11}^a$  stands respectively for the effective refractive index of the fundamental and the first order mode averaged with respect to polarization

$$n_{01}^a = \frac{n_{01}^x + n_{01}^y}{2}, \quad n_{11}^a = \frac{n_{11}^x + n_{11}^y}{2} \quad (5.8)$$

and  $\Delta n_{01}$  and  $\Delta n_{11}$  stands for the phase modal birefringence in the fundamental and the first order mode

$$\Delta n_{01} = n_{01}^x - n_{01}^y, \quad \Delta n_{11} = n_{11}^x - n_{11}^y \quad (5.9)$$

The first cosine term in equation (5.7) represents the intermodal interference fringes averaged with respect to polarization, while the second term constitutes the slowly varying envelope determined by the birefringence difference in the fundamental and first order mode. The corresponding terms are indicated by black and red lines in Figure 73, which shows the output interferogram produced by the 11.7 mm long interferometer.



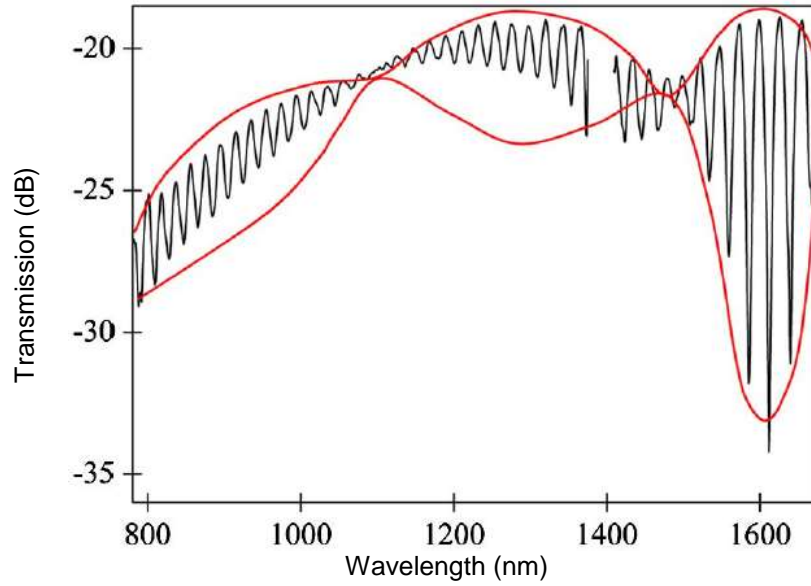


**Figure 73 - The interference spectrum at the output of an in-fiber Mach–Zehnder intermodal interferometer fabricated in the microstructured fiber.**

To confirm that the coupling indeed occurs between the fundamental and the first order mode, the calculated and measured difference in the group refractive indices for these modes, averaged with respect to polarization,  $N_{01}^a - N_{11}^a$ , were compared. It is well known [129] that the difference  $N_{01}^a - N_{11}^a$  can be determined from the spectral interference fringes shown in Figure 73

$$N_{01}^a - N_{11}^a = \frac{\lambda^2}{\Delta\lambda L} \quad (5.10)$$

where  $L = 11.7$  mm is the interferometer length and  $\Delta\lambda$  is the separation of successive interference fringes. The measured and calculated values of  $N_{01}^a - N_{11}^a$  presented in Figure 74 show very good agreement.

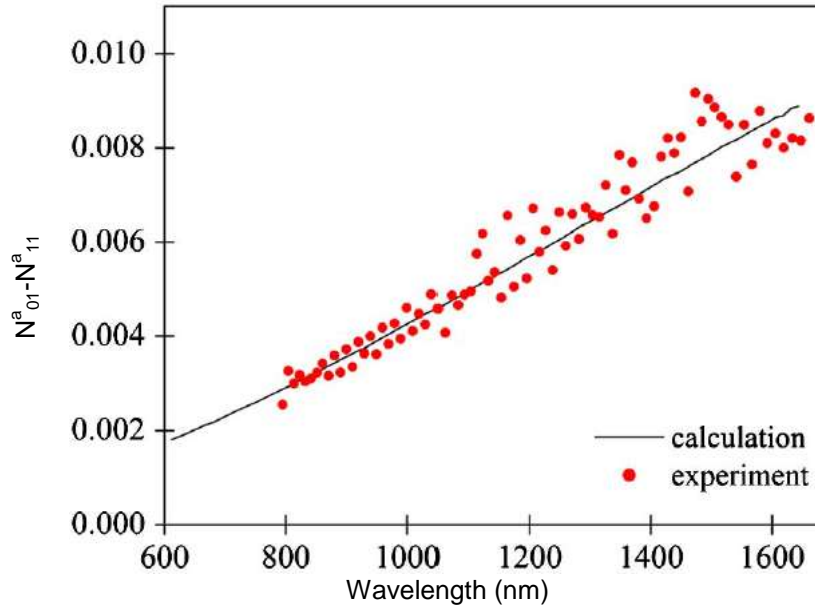


**Figure 74 - Calculated (solid line) and measured (dots) difference in group effective indices of the LP<sub>01</sub> and LP<sub>11</sub> modes averaged with respect to polarization.**

It was also compared the difference in group modal birefringence between the fundamental and the first order mode  $\Delta N_{01} - \Delta N_{11}$  calculated and estimated from the spectrogram shown in Figure 73. For experimental evaluation of the birefringence difference, the following relation was used

$$\Delta N_{01} - \Delta N_{11} = \frac{\lambda^2}{2\Delta\lambda L} \quad (5.11)$$

where  $\Delta\lambda$  indicates the separation of successive contrast extremes (maxima or minima). The numerical values of the group birefringence were obtained from FEM analysis. The positions of minima and maxima of the interference pattern envelope were approximated by a red curve shown in Figure 73 with a precision of about 15 nm. Figure 75 presents the calculated values of the birefringence difference  $\Delta N_{01} - \Delta N_{11}$  and compares them with the experimental values estimated from the spectrogram, with a precision of about 25%. Good agreement between the simulation results and measured values of  $\Delta N_{01} - \Delta N_{11}$  provides an additional argument that the observed fringes result from the interference between the LP<sub>01</sub> and LP<sub>11</sub> modes.

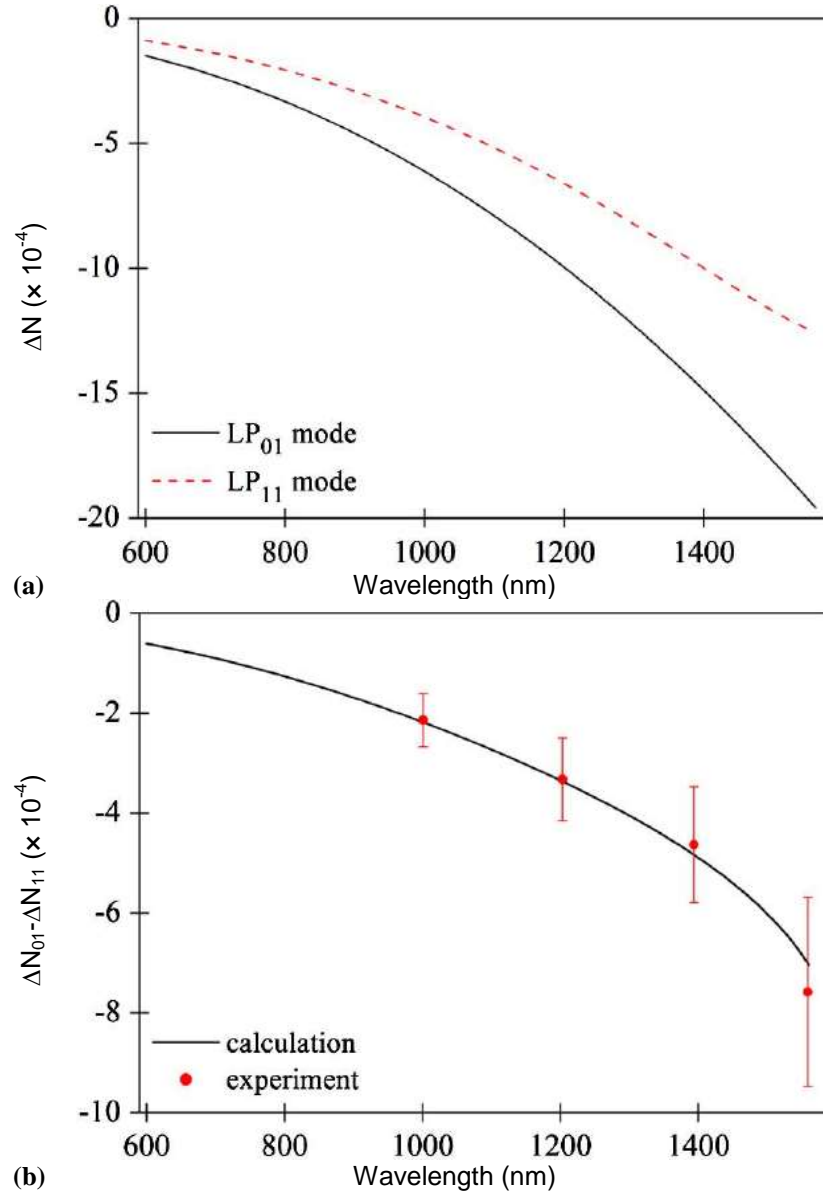


**Figure 75 - (a) Calculated group modal birefringence of the  $LP_{01}$  (solid line) and  $LP_{11}$  (dashed line) modes in the investigated fiber with boron doped inclusion and (b) comparison of the calculated (solid line) and measured (dots) birefringence difference.**

#### 5.4.2 Experimental Results and Discussion

The experimental setup for measurement of different physical parameters using the proposed interferometer is presented in Figure 76. As the light source, was used an amplified spontaneous emission source, with a central wavelength at 1570 nm. The transmission spectrum at the output of the interferometer was registered by an optical spectrum analyzer, with a resolution of 0.05 nm.

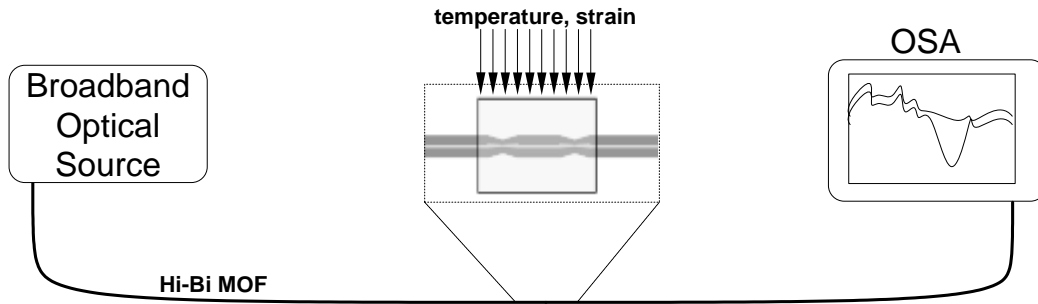


**Figure 76 - Experimental setup for strain and temperature measurements.**

As it is shown in Figure 77, the interference fringes, with the modulation depth increasing against the wavelength, were observed in the spectral range of 1520-1620 nm. Variation of both the modulation depth and the fringe displacement were observed in response to changes in temperature and strain applied to the interferometer.

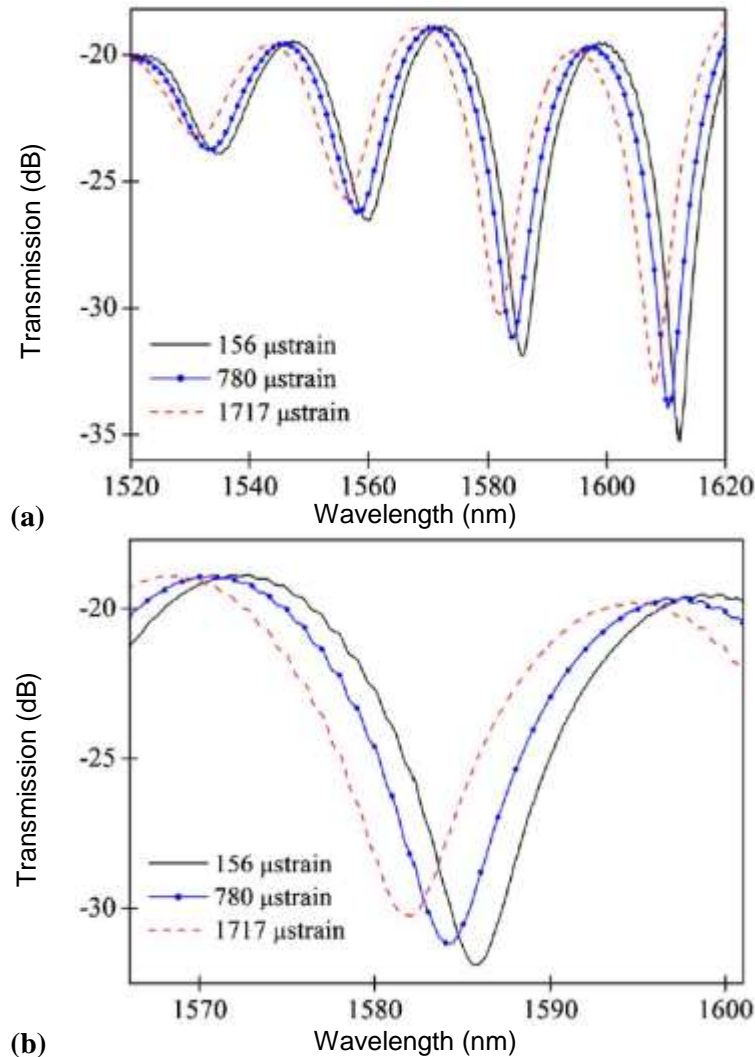


**Figure 77 - (a) Transmission characteristic registered in the full spectral range for selected values of applied strain and (b) variation of the modulation depth and displacement of the third fringe in response to applied strain.**

According to equation (5.6), the shift of the interference fringes is related to the variation of the effective refractive indices of the fundamental and the first order mode ( $n_{01}^a$  and  $n_{11}^a$ ) and the interferometer length  $L$ . The shift of the interference fringe  $\Delta\lambda$  induced by the measurand change  $\Delta X$  can be quantitatively represented by the following relation

$$\frac{\partial}{\partial \lambda} \left( \frac{n_{01}^a - n_{11}^a}{\lambda} L \right) \Delta\lambda + \frac{\partial}{\partial X} \left( \frac{n_{01}^a - n_{11}^a}{\lambda} L \right) \Delta X = 0 \quad (5.12)$$

After performing rather straightforward calculations, one can express the sensitivity of the proposed sensors in the following way

$$\frac{1}{\lambda} \frac{\Delta\lambda}{\Delta X} = \frac{n_{01}^a - n_{11}^a}{N_{01}^a - N_{11}^a} \left( \frac{1}{L} \frac{\partial L}{\partial X} + \frac{1}{n_{01}^a - n_{11}^a} \frac{\partial (n_{01}^a - n_{11}^a)}{\partial X} \right) \quad (5.13)$$

or more conveniently with relation to the phase intermodal sensitivity of the fiber

$$\frac{\Delta\lambda}{\Delta X} = \frac{\lambda^2 K_X}{2\pi (N_{01}^a - N_{11}^a)} \quad (5.14)$$

where

$$K_X = \frac{1}{L} \frac{\partial (\varphi_{01}^a - \varphi_{11}^a)}{\partial X} \quad (5.15)$$

and  $\varphi_{01}^a$  and  $\varphi_{11}^a$  are the phase shifts averaged with respect to polarization induced by the unit change in the measurand in the fiber of unit length. On the other hand, to avoid ambiguity, the measurand-induced displacement of the interference fringe must be lower than the separation of successive fringes defined by equation (5.10). This

leads to a simple relation between the maximum length of the sensor and its operation range

$$L_{\max} \Delta X_{\max} < \frac{2\pi}{K_X}. \quad (5.16)$$

For the sake of simplicity it was considered that the interferometer length is comprised between the narrowest points in the tapered regions. As the taper's length (about 150  $\mu\text{m}$ ) is relatively small compared to the interferometer length (10–20 mm), the effect of the transition regions on variations of  $K_X$  was disregarded and assumed that the fiber sensitivity is constant over the entire sensor length.

In strain measurements, the interferometer was elongated up to 1.7 m $\epsilon$ , while for temperature tests it was placed in an electrical oven, whose temperature was increased from 20  $^{\circ}\text{C}$  to 700  $^{\circ}\text{C}$ . The precision of temperature control in the oven was about 5  $^{\circ}\text{C}$ . In spite of a wide temperature range, it was not observed any change in the sensor's characteristics after several temperature cycles. A possible impact of the boron diffusion on the sensor performance is minimized by the fact that the boron doped inclusion is located in the center of the core. Therefore, a change in the boron concentration profile has little influence on the overlap coefficient with the fundamental and the first order modes, which according to the perturbation approach represent the impact of the diffusion process on the effective indices of both modes. It is however possible that in more demanding applications the boron diffusion may limit the maximum temperature range of the proposed sensor.

As it is shown in Figure 77, the interference fringes move toward shorter wavelengths and their visibility decreases in response to the applied strain. The displacement of the third fringe with the intensity minimum located at 1583 nm, is linear in the investigated range of strain 0–1.7 m $\epsilon$ , with no trace of hysteresis. The sensitivity coefficient for strain is  $-2.51 \text{ nm/m}\epsilon$ , as shown on Figure 78 (a). Moreover, the visibility of the third fringe (Figure 78 (b)) linearly decreases against the applied strain, with a rate of  $-0.0256 \text{ m}\epsilon^{-1}$ . The root mean square deviation of the

experimental data from a linear trend is equal, respectively, to 35 pm for the fringe displacement and  $1.4 \times 10^{-3}$  for the visibility change.

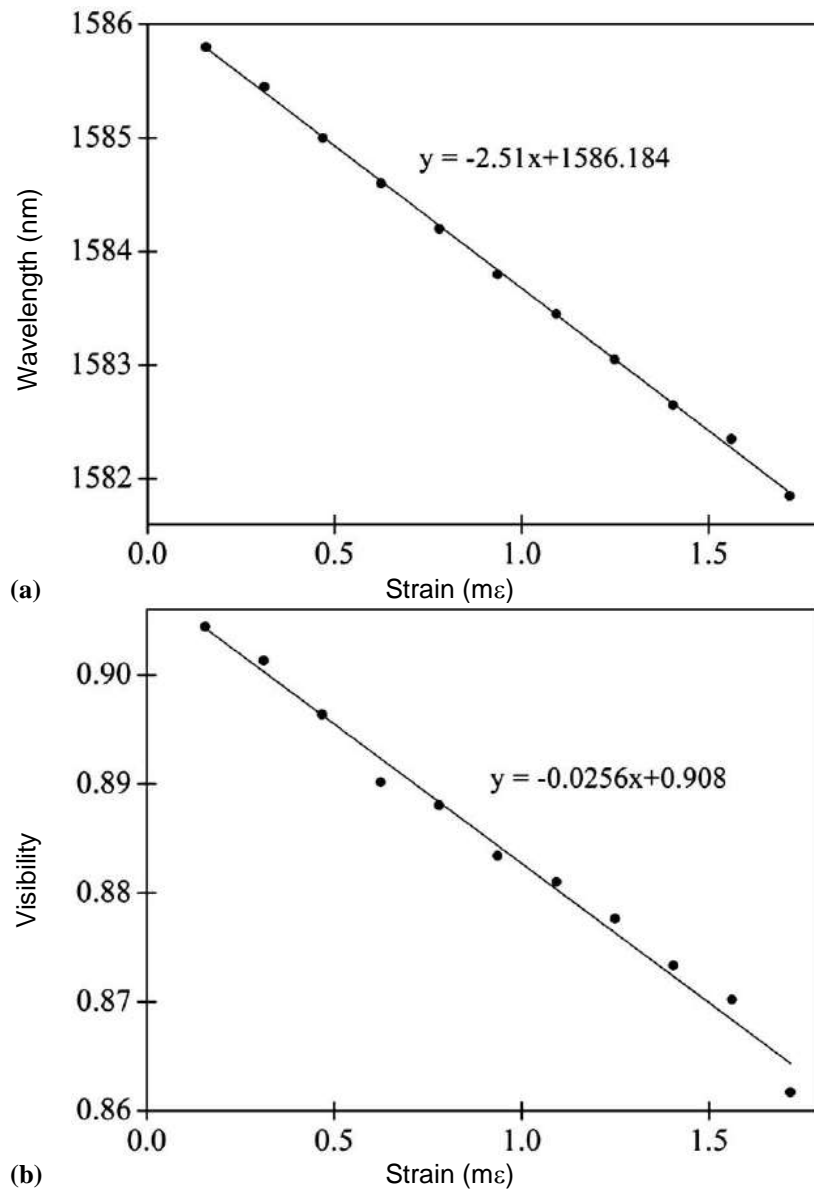


**Figure 78 - (a) Displacement of the third interference fringe against applied strain and (b) change in its visibility.**

In Figure 79 (a), is presented the measured linear dependence of the third fringe displacement induced by temperature change. The resulting sensitivity to temperature has a positive sign and equals  $16.7 \text{ pm}/^\circ\text{C}$ . The visibility of the third fringe linearly increases against temperature, which results in a sensitivity coefficient equal to  $5.74 \times 10^{-5} / ^\circ\text{C}$ . In this case the root mean square deviation of the experimental data from a linear trend is 76 pm for the fringe displacement and  $1.7 \times 10^{-3}$  for the visibility variation. As the sensitivity coefficients for strain and temperature have opposite signs

and are different in absolute values, the sensitivity matrix for these two parameters is well conditioned, thus providing the possibility of simultaneous measurements of strain and temperature by interrogating the position and the visibility of a selected fringe.

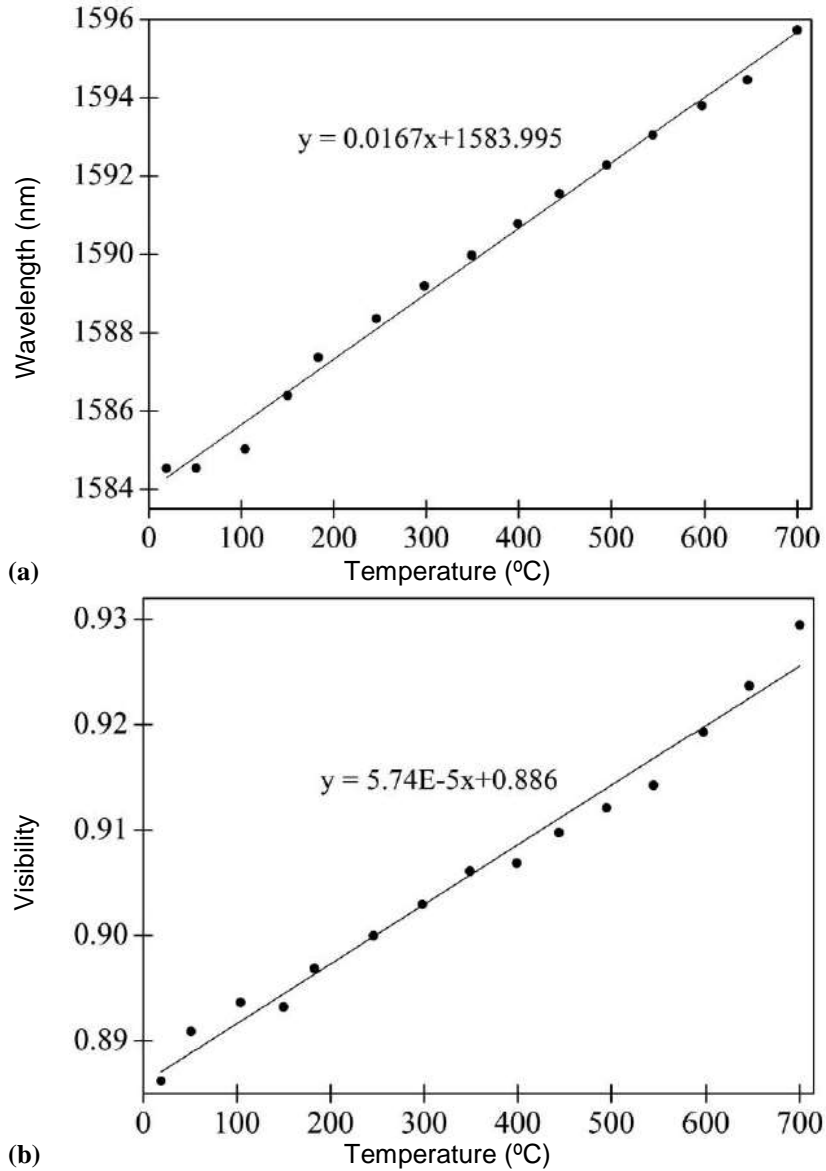


**Figure 79 - Displacement of the third interference fringe against temperature (a) and change of its visibility (b).**

In terms of interferometric sensitivity, the performance of the proposed sensor is similar to other intermodal MOF based sensors reported in literature [112, 123, 130]. For example, the sensitivity to strain reported for nonbirefringent MOF ranges from 2.28 pm/ $\mu$ strain [112] to 5.3 pm/ $\mu$ strain [130], while the sensitivity to temperature is 12 pm/ $^{\circ}$ C [130] and 3–5 pm/ $^{\circ}$ C [123]. These numbers do not differ significantly from



the interferometric sensitivity of the proposed sensors, which is equal to  $-2.51$  pm/ $\mu$ strain and  $16.7$  pm/ $^{\circ}$ C, respectively. However, the main advantage of the proposed sensor is that thanks to the high birefringence of the MOF one can interrogate simultaneously the displacement of the interference fringes and the visibility variations.

## 5.5 Summary

In section 5.3 a sensing head based on hollow-core photonic crystal fiber for measurement of strain and temperature has been presented. The sensor consists of a piece of 7-cell HC-MOF connected to SMF-28 in both ends. The interference occurs between the fundamental mode and higher order modes inside the HC-MOF. A white light interferometric technique for coherent phase reading was used. Resolutions of  $\pm 1.4$   $\mu\epsilon$  and  $\pm 0.2$   $^{\circ}$ C were obtained for strain and temperature, respectively. It was also found that the fiber structure was not sensitive to curvature.

Further, an in-line fiber Mach–Zehnder interferometer for strain and temperature measurements was demonstrated in section 5.4, fabricated in a highly birefringent boron doped microstructured fiber, using a CO<sub>2</sub> laser. The operation principle of the proposed sensor exploits the effect of intermodal interference arising between the fundamental LP<sub>01</sub> and the first order LP<sub>11</sub> mode. Boron doped inclusion facilitates coupling between the two modes, which takes place in the fiber tapers fabricated using a CO<sub>2</sub> laser. The origin of the interference fringes and visibility modulation has been confirmed by comparing the measured and calculated values of group effective indices and group birefringence for the LP<sub>01</sub> and the LP<sub>11</sub> modes. Because of the high fiber birefringence, the intermodal interference fringes are modulated in contrast when the sensor is powered with depolarized light. Sensitivity coefficients were determined for temperature and strain corresponding to fringe displacement and visibility variations. These coefficients are equal respectively for strain  $-2.51$  nm/ $\mu\epsilon$ ,  $-0.0256$  / $\mu\epsilon$  and for temperature  $16.7$  pm/ $^{\circ}$ C and  $5.74 \times 10^{-5}$  / $^{\circ}$ C. As the sensitivity matrix is well conditioned, the proposed sensor can be used for simultaneous measurements of temperature and strain.



## Chapter 6 – Dynamic Interrogation of Fiber Optic Sensors

---

### 6.1 Introduction

Due to their principle of operation and spectral characteristics, LPGs as sensing elements are mostly used to detect variations of quasi-static parameters. Their interrogation is normally achieved with optical spectrum analyzers or by detecting optical power changes at one or more wavelengths, located on the edges of the LPG transmission spectrum. If two wavelengths, one in each edge of the LPG, are selected (for example using selective filters, such as fiber Bragg gratings), and if the detected optical powers in these wavelengths are  $P_1$  and  $P_2$ , respectively, then processing of the type

$$P_{proc} = \frac{P_1 - P_2}{P_1 + P_2} \quad (6.1)$$

gives a signal proportional to the measurand induced LPG shift, and is independent of optical power fluctuations along the system [52, 131, 132]. Considering the associated photodetection, amplification and processing are, in most of the cases, in the DC or quasi-DC regime, the measurand readout resolution can be substantially affected by the  $1/f$  noise of the electronics. Therefore, it would be advantageous to set-up a LPG interrogation approach, compatible with signal photodetection and amplification at higher frequencies [132-135].

In this chapter, results are reported of a LPG interrogation technique based on modulation at different frequencies of the Bragg wavelengths of two FBGs, spectrally located in the edges of the LPG. The amplitudes at these modulating frequencies of the signals reflected by the FBGs are detected. These amplitudes are proportional to the slopes of the LPG spectral response at the FBG wavelengths, which change with the relative spectral movements of the LPG to the FBGs, permitting to generate an optical signal proportional to the LPG spectral shift, immune to optical power

fluctuations along the system. This technique was tested for the measurement of refractive index variations of the surrounding medium, as detailed in section 6.2. Also, the impact of introducing Erbium and Raman optical amplification is experimentally investigated and shown in section 6.3.

In section 6.4, a systematic description is presented addressing an experimental configuration with optimized characteristics focused on curvature measurement, the potential of this interrogation approach also being emphasized for the multiplexing of fiber optic sensors with spectral loss band characteristics.

Further, a progressed version of the LPG dynamic interrogation technique based on modulation at different frequencies of two Distributed-Feedback Lasers (DFB), spectrally located near the LPG resonance depth, is presented in section 6.5. This technique is tested in a multiplexing scheme to measure refractive index variations of two LPGs sensors working in reflection.

## 6.2 Electrical Dynamic Interrogation

The feasibility of the proposed interrogation approach is dependent on the level of slope variation along the LPG spectral resonance. To a good approximation the LPG transfer function can be represented by the following expression [136],

$$P_{out}(\lambda) = P_o \left[ 1 - m e^{\left[ -4 \ln 2 \left( \frac{\lambda - \lambda_{res}}{\Delta \lambda_{LPG}} \right)^2 \right]} \right], \quad (6.2)$$

where  $\lambda_{res}$  and  $\Delta \lambda_{LPG}$  are the LPG resonance wavelength and spectral width, respectively, and  $m$  indicates the resonance loss level. For a typical LPG with 20 dB of attenuation at  $\lambda_{res}$ ,  $m = 0.99$ .

Figure 80 shows  $P_{out}(\lambda)/P_0$  as well as  $dP_{out}/d\lambda / P_0$  versus  $\lambda$ . It can be observed that the magnitude of the normalized slope variation along the full LPG response is approximately one order of magnitude smaller than the normalized optical power variation, which means a corresponding factor for the signal variations associated with  $P_{out}(\lambda)/P_0$  or  $dP_{out}/d\lambda / P_0$ , with origin at a LPG spectral shift relative to fixed wavelength values (that can be defined by FBGs). Therefore, from this argument it seems that the preferable option should be to monitor  $P_{out}(\lambda)/P_0$ , i.e., following the standard approach. However, this is a DC reading, consequently affected by low-frequency noise, which usually has a  $1/f$  power spectral dependence. On the other hand, the slope approach is compatible with interrogation in a frequency range far from the  $1/f$  noise region, which means the signal-to-noise ratio can eventually be favored by the reduction of the noise level, compensating the disadvantage of the reduction in signal amplitude.

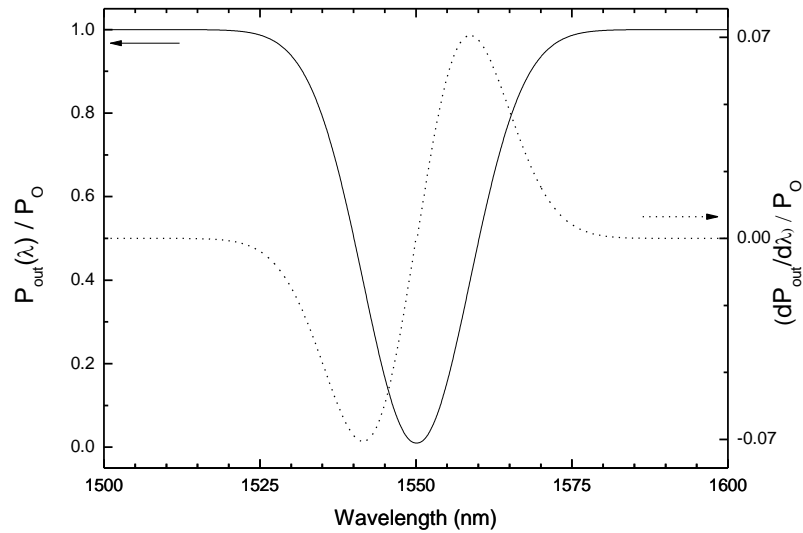


**Figure 80 -  $P_{out}(\lambda)/P_0$  in a typical LPG spectrum and  $(dP_{out}/d\lambda)/P_0$  versus wavelength**

The proposed interrogation approach is implemented using an LPG as an optical sensing device. The LPG is illuminated by means of an ASE broadband source and is adequate to quantify the desired physical parameter. The optical fiber at the LPG right side was mirrored with silver nitrate allowing the sensing head to operate in reflection. Two fiber Bragg gratings (FBG<sub>1</sub>, FBG<sub>2</sub>), designed to be spectrally located

on each edge of the LPG were added to the system and had their Bragg wavelengths  $(\lambda_1, \lambda_2)$  sinewave modulated, with a fixed amplitude, using two piezoelectric transducers (PZTs) driven by two independent signal generators  $(f_1, f_2)$ .

After photodetection of the optical signals reflected by the FBGs, the resultant electrical signals were added with an electrical circuit and visualized in an electrical spectrum analyzer (ESA), with adequate impedance matching. The modulation of the FBG resonance originates a relative spectral movement with reference to the LPG transfer function, with a consequent optical power modulation at the modulation frequencies. The amplitude of this power modulation for each FBG would be constant if the LPG response were linear, which is not the case. Therefore, this amplitude is function of the LPG spectral position, which changes due to the measurand variation.

The optical peaks observed in the ESA  $(f_1, f_2)$ , corresponds to the frequencies at which each FBG wavelength  $(\lambda_1, \lambda_2)$  is being modulated. Due to an adequate previous selection of the FBGs Bragg wavelengths, the corresponding reflected optical power amplitudes will change in phase opposition, a useful feature for readout sensitivity enhancement. The processing adopted was

$$V_{proc} = \frac{V_1 - V_2}{V_1 + V_2} \quad (6.3)$$

where  $V_1$  and  $V_2$  are the *rms* voltage amplitudes of the signals at frequencies  $f_1$  and  $f_2$ , respectively.

### 6.3 Dynamic Interrogation for Refractive Index Measurements

In order to evaluate the feasibility of the proposed interrogation approach for refractive index measurements the setup presented in Figure 81 was implemented. Figure 82 shows a LPG with a strong resonance centered at 1550 nm that was fabricated using the electric arc technique (period of the refractive index modulation:

$\Lambda = 395 \text{ } \mu\text{m}$ ; coupling to a 5<sup>th</sup> order cladding mode). The LPG was placed into a recipient with an aqueous solution of ethylene glycol and illuminated by means of an ASE broadband source. The optical fiber at the LPG right side was mirrored with silver nitrate allowing the sensing head to operate in reflection [131].

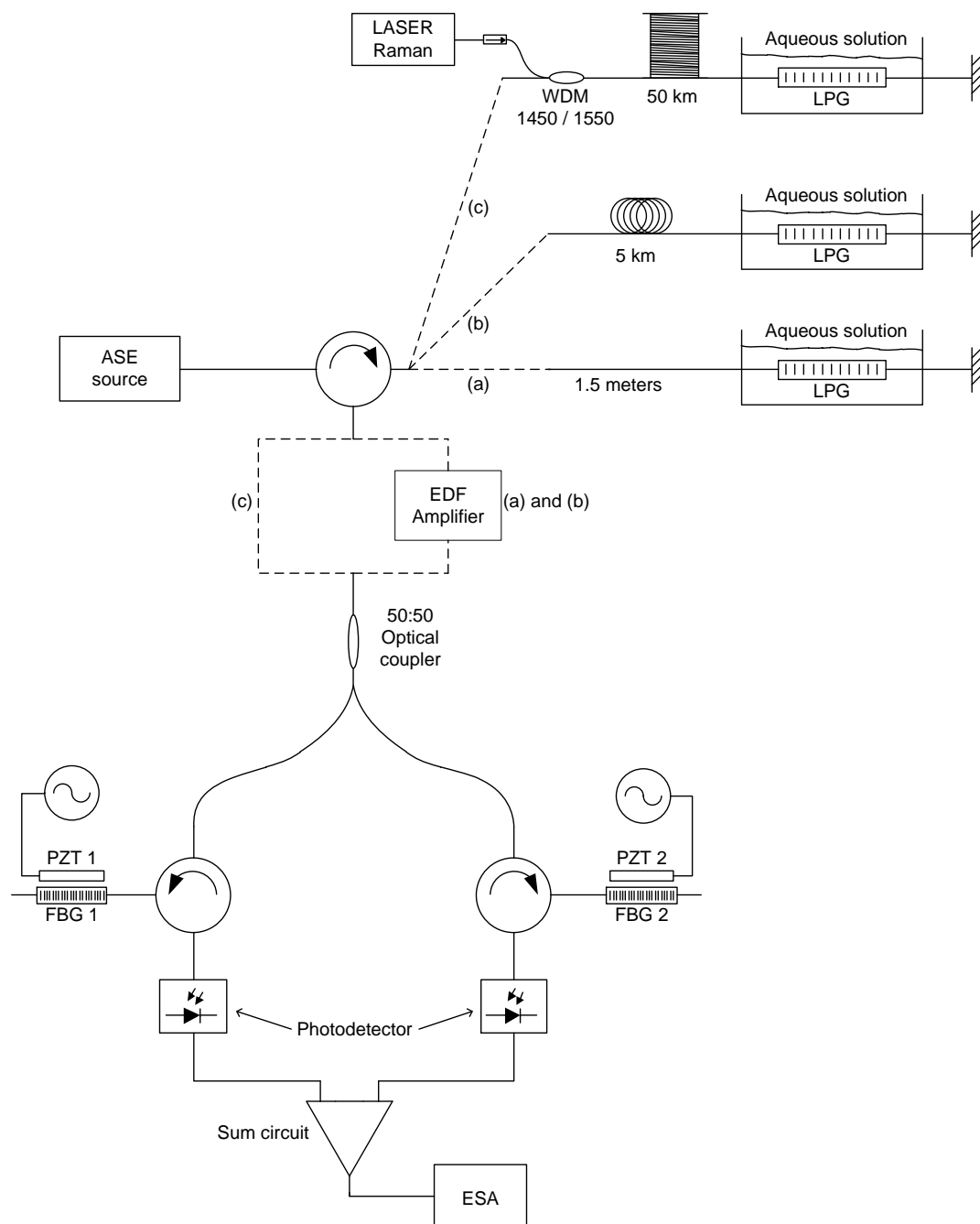


**Figure 81 - Experimental setup for different configurations: a) for 1.5 meters with and without EDF amplifier; b) for 5 km with and without EDF amplifier; c) for 50 km with and without Raman amplifier.**

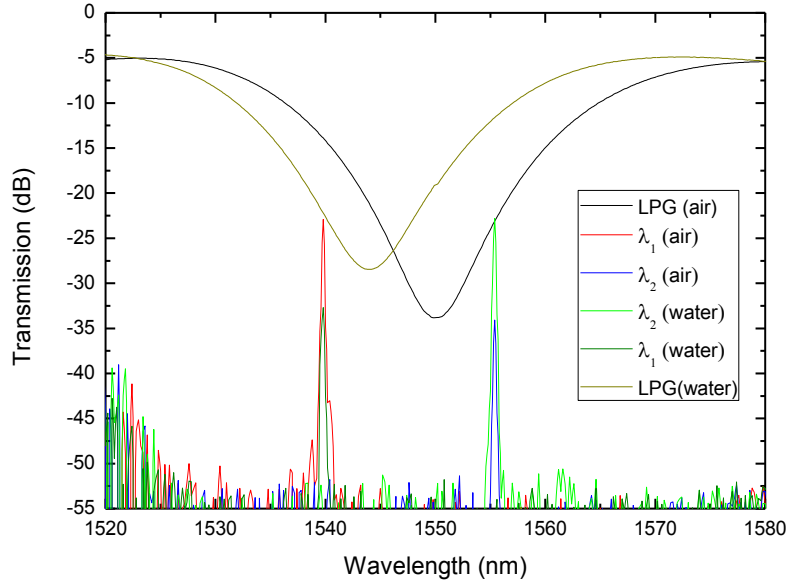


**Figure 82 - Optical spectra of the FBGs and LPG in air and immersed in water.**

FBG<sub>1</sub> was modulated at  $f_1 = 620$  Hz and FBG<sub>2</sub> at  $f_2 = 740$  Hz, both in a frequency region where the system noise level stabilized at approximately  $-90$  dBV<sub>rms</sub> (as can be seen in Figure 83). The modulation of the FBG resonance originates a relative spectral movement with reference to the LPG transfer function, with a consequent optical power modulation at the modulation frequencies. The amplitude of this power modulation for each FBG would be constant if the LPG response were linear, which is not the case. Therefore, this amplitude is function of the LPG spectral position, which changes due to the measurand variation. This effect can also be observed in Figure 82 for the LPG in air and in water, where it can be seen that the wavelength shift of the LPG resonance at 1550 nm is transformed into an amplitude variation of the two peaks observed in the ESA (as shown in Figure 84), each one corresponding to the frequency in which each FBG is being modulated. Once again, due to an adequate previous selection of the FBGs Bragg wavelengths, the corresponding reflected optical power amplitudes will change in phase opposition, a useful feature for readout sensitivity enhancement.



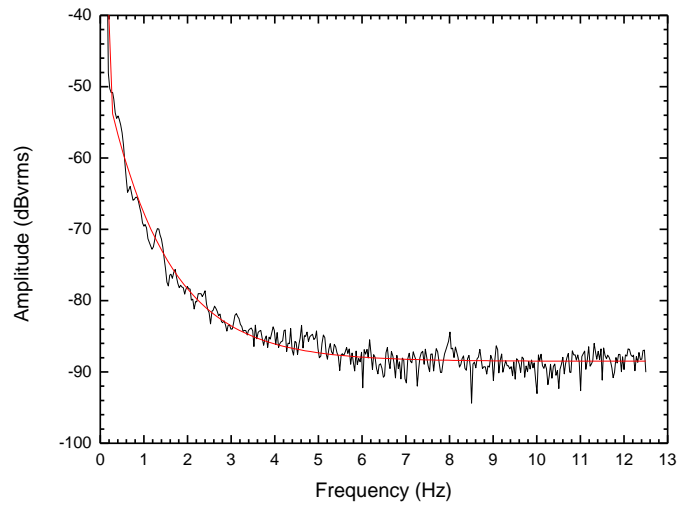


**Figure 83 - Noise level of the electronics at low frequencies.**

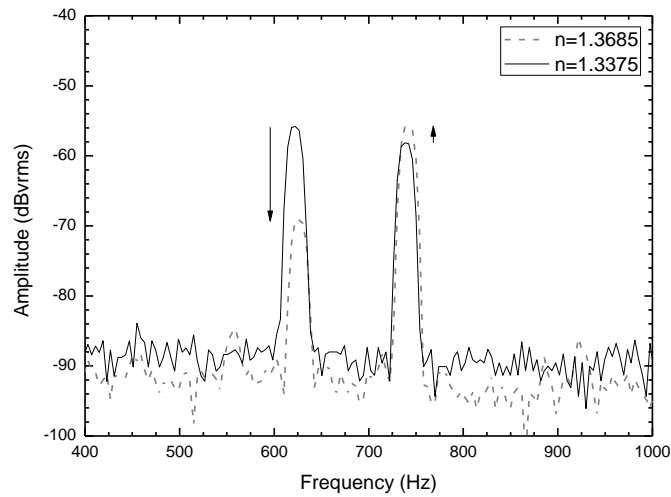


**Figure 84 - Electrical spectra when modulating FBG1 and FBG2 with  $f_1 = 620$  Hz and  $f_2 = 740$  Hz, respectively, for the LPG immersed in solutions with different refractive indexes.**

The dynamic electrical interrogation concept previously described was implemented with six different schemes that were presented in Figure 81. First, the system was tested with a fiber length of 1.5 m, with and without an EDFA amplifier with a flat optical power response for the C+L bands. Then, the process was repeated for lengths of 5 km and 50 km, simulating a remote detection system with and without amplification. In the 50 km remote detection scheme Raman amplification was applied instead of using EDF amplification.

### 6.3.1 Results for the Refractive Index Measurement

The setup depicted in Figure 81 was used to estimate  $V_{proc}$  in several situations: with and without optical amplification, considering local (Figure 81(a)) or remote sensing (Figure 81(b) and Figure 81(c)). The obtained responses with the dynamic interrogation approach are shown in Figure 85, Figure 86 and Figure 87 respectively to 1.5 m, 5.0 km and 50.0 km of fiber length, when the refractive index of the environment changes. It can be seen that the proposed interrogation scheme permits us to read refractive index variations, exhibiting  $V_{proc}$  versus refractive index with a linear relationship. Also, as can be observed in Figure 85 and Figure 86 the slopes are not substantially different, which is understandable in face of the way  $V_{proc}$  is defined. On the other hand, the amplification has real impact in the readout resolution when the sensing head is located far away.

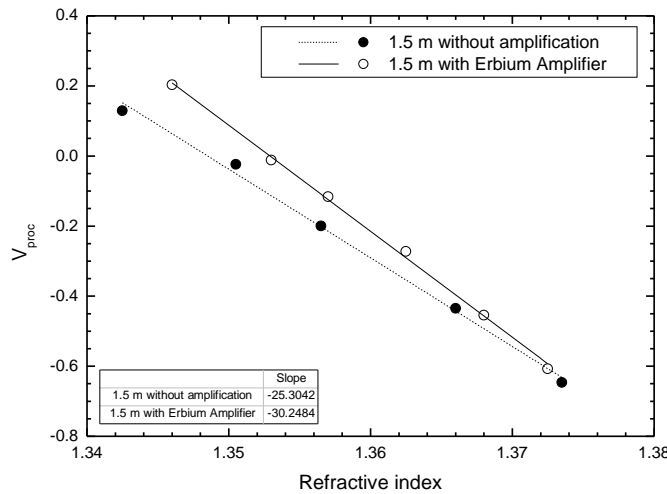


**Figure 85 - System output versus refractive index for the case of not using and using EDFA amplification. Fiber length to the sensing head: 1.5 m.**

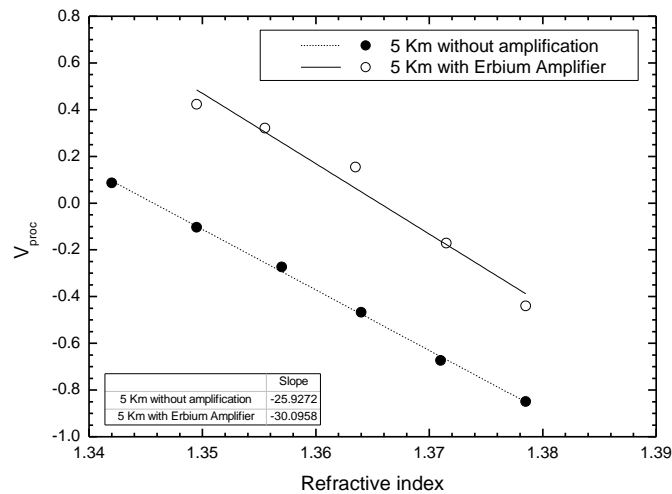


**Figure 86 - System output versus refractive index for the case of not using and using EDFA amplification. Fiber length to the sensing head: 5 km.**

For the case of 50 km of fiber, located between the sensing head and the processing region, simulating therefore the situation of a long haul remote sensor, the results are presented in the following graphic. In this case the Erbium amplification was replaced by a Raman amplification stage.

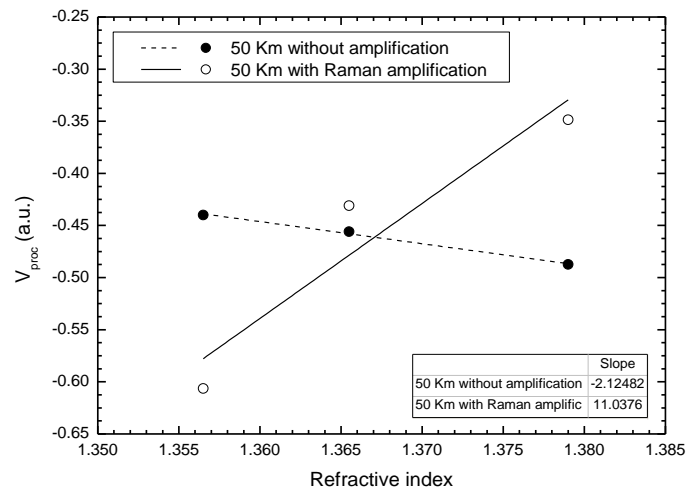


**Figure 87 - System output versus refractive index for the case of not using and using Raman amplification. Fiber length to the sensing head: 50 km.**

As it can be seen, Raman amplification enhances the sensing unit sensitivity. The system resolution with Raman amplification was also estimated by applying a

refractive index step change of 0.023 RIU, determining the corresponding signal change and *rms* noise fluctuations as well. It is interesting to observe that Raman amplification affects the behavior of  $V_{proc}$  versus refractive index as the output slope gets the opposite signal. Although it seems weird, it happens due to the fact that the Raman gain curve changes the reflected shape of the LPG that will be interrogated by the two modulated FBGs. Due to this effect on the signal inversion points of the LPG resonance slope,  $dP_{out}/d\lambda / P_0$  versus  $\lambda$  as can be seen in Figure 80, the FBGs will not be placed exactly in the same location and thus the processing adopted made  $V_{proc}$  get a different behavior.

Figure 88 shows the obtained refractive index step variation of the dynamic interrogation system for the three amplified setups previously described.

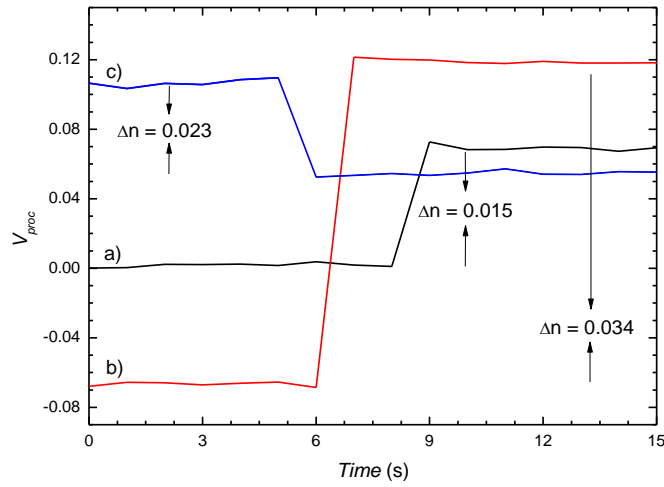


**Figure 88 - System output for a refractive index step variation for the different configurations: a) sensing head located 1.5 meters away with an EDF amplifier; b) sensing head located 5 km away with EDF amplifier; c) sensing head located 50 km away with Raman Amplification.**

From the refractive index step variation, the resolution of the interrogation system can be calculated. Table 4 summarizes the resolutions obtained with the proposed interrogation technique in all considered situations.

**Table 4 - Refractive index resolutions obtained with the dynamic interrogation technique for the studied configurations**

<i>Length of the Fiber to the Sensing Head</i>	<i>Configuration</i>	$\delta n_{\min}$
1.5 m	Without amplification	$2.5 \times 10^{-4}$
	Erbium amplification	$2.4 \times 10^{-4}$
5 km	Without amplification	$4.3 \times 10^{-4}$
	Erbium amplification	$2.2 \times 10^{-4}$
50 km	Without amplification	$4.5 \times 10^{-3}$
	Raman amplification	$7.4 \times 10^{-4}$

An interesting result is the one obtained for the long haul remote sensing head and from it comes a resolution of  $7.4 \times 10^{-4}$ , which is a factor of  $\sim 6$  better compared with the situation without amplification.

These results permit us to state that the technique proposed, based on signal reading outside the  $1/f$  noise level, is effective for refractive index measurement with a resolution that compares favorably with the obtained using the standard DC approach, which is typically around  $10^{-3}$  [131]. Moreover, the amplification associated with the processing employed provides a combination that permits us to get high resolutions when the sensing head is remotely located. These two characteristics route to the critical aspect of operating far from the low-frequency noise. Indeed, from Figure 83 it can be observed that the noise level present in these experiments was  $\sim 25$  dB lower than the one shown at 1 Hz, which far compensates the lower signal variations associated with the proposed slope readout technique.

#### 6.4 Dynamic Interrogation for Curvature Measurements

Refractive index measurements results obtained with the dynamic interrogation approach were presented in section 6.3. Here, a systematic description is presented addressing an experimental configuration with optimized characteristics focused on curvature measurement, being also emphasized the potential of this interrogation approach for the multiplexing of fiber optic sensors with spectral loss band characteristics.

The setup presented in Figure 89 was implemented. A LPG with a strong resonance centred at 1550 nm (Figure 90) was fabricated in standard Corning<sup>®</sup> SMF-28e<sup>®</sup> fiber, using the electric arc technique (period of the refractive index modulation:  $\Lambda = 395 \mu\text{m}$ ; coupling to a 5<sup>th</sup> order cladding mode). The LPG was placed between two holders - one of them adjustable by a translation stage - and illuminated by means of an amplified spontaneous emission (ASE) broadband source. The optical fiber end at the LPG right side was, once more, mirrored with silver nitrate, allowing the sensing head to operate in reflection [131], thus improving its behaviour once the light travels twice in the sensing head.

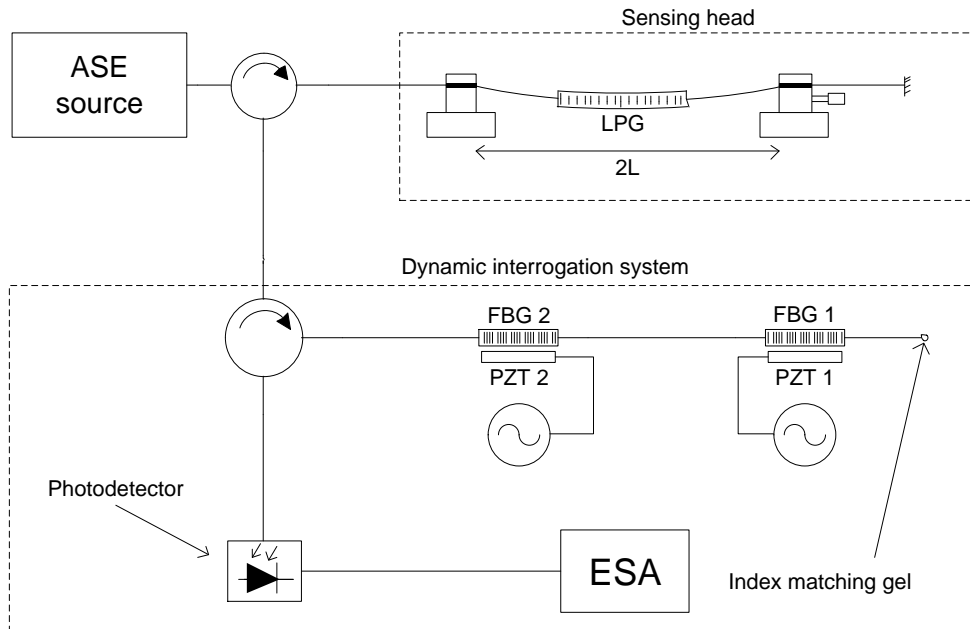


**Figure 89 - Experimental setup to test the LPG dynamic interrogation method for curvature measurement purposes.**

Two fiber Bragg gratings (FBG<sub>1</sub>, FBG<sub>2</sub>), designed to be spectrally located in each edge of the LPG ( $\lambda_1$ ,  $\lambda_2$ ) – as can be seen in Figure 90 – had their Bragg wavelengths sinewave modulated with a fixed amplitude, using two piezoelectric transducers driven by two independent signal generators ( $f_1$ ,  $f_2$ ).

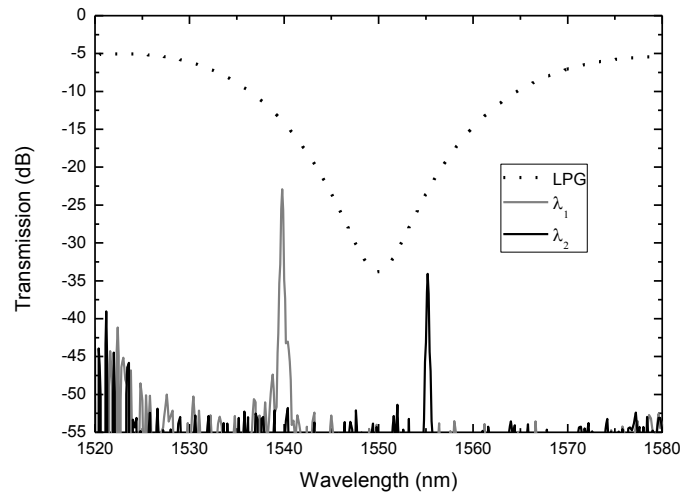


**Figure 90 - Optical spectra of the FBGs and LPG, both written in Corning® SMF-28e® fiber.**

After travelling through the optical circulator, the optical signal reflected by the FBGs, went to the photodetector and that signal was visualized in an electrical spectrum analyser (ESA), with adequate impedance matching.

As presented in section 6.2, the modulation of the FBG resonance originates a relative spectral movement with reference to the LPG transfer function, that creates a power modulation whose amplitude is a function of the LPG spectral position, and therefore changes with curvature variation. This effect can be observed in Figure 91 (a) for a curved LPG, where it can be seen that the wavelength shift of the LPG resonance at 1550 nm is transformed into an amplitude variation of the two peaks observed in the ESA, each one corresponding to the frequency at which each FBG is being modulated.

FBG<sub>1</sub> was modulated at  $f_1 = 900$  Hz and FBG<sub>2</sub> at  $f_2 = 1040$  Hz, both in a frequency region where the system noise level stabilized at  $\sim -90$  dBV<sub>rms</sub>, as can be observed in Figure 91 (b). The inset of this figure shows that the noise level at these frequencies is  $\sim 25$  dB lower than the one present at the quasi-DC region, with the corresponding positive implications on the achievable measurand resolution.

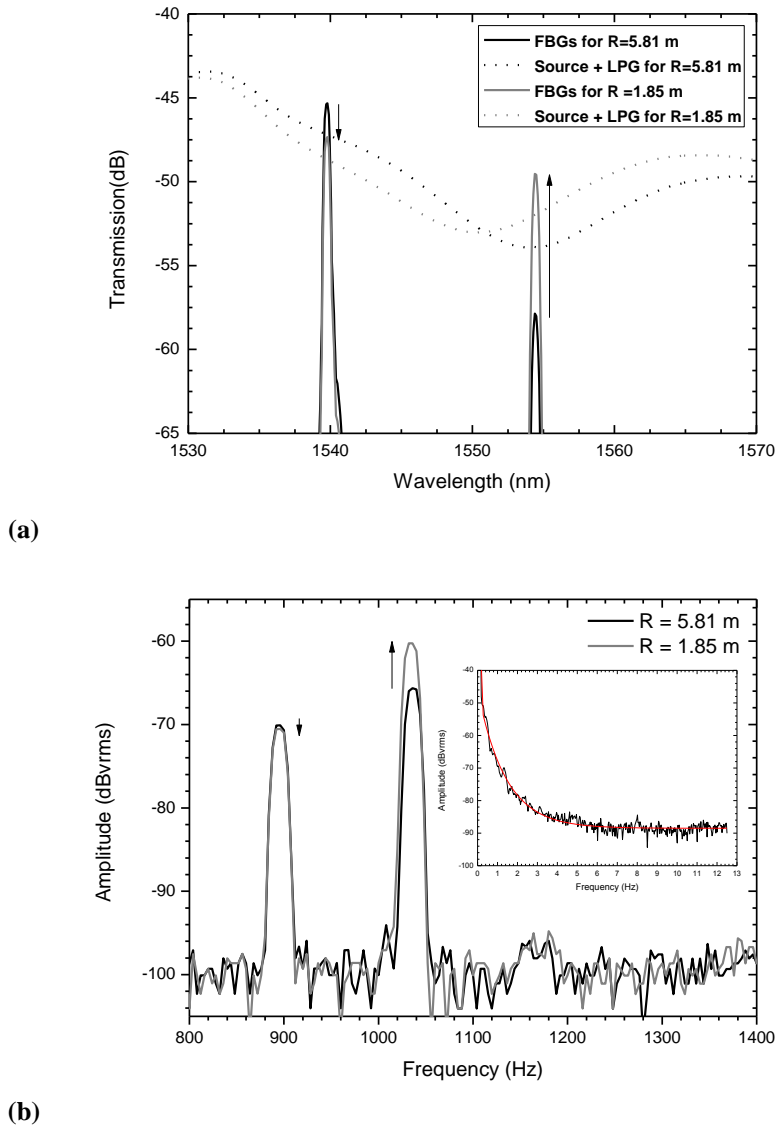


**Figure 91 - Optical (a) and electrical (b) spectra of the output signal for the LPG with a curvature radius of 5.81 m and 1.85 m, respectively (the spectral position of the FBG<sub>1</sub> and FBG<sub>2</sub> resonances are sinewave modulated, with frequencies  $f_1 = 900$  Hz and  $f_2 = 1040$  Hz, respectively). The inset of (b) shows the system electrical noise level at low frequencies.**

#### 6.4.1 Results for Curvature Measurement

The setup depicted in Figure 89 was used to estimate  $V_{proc}$ . The obtained response with the dynamic interrogation approach is shown in Figure 92.



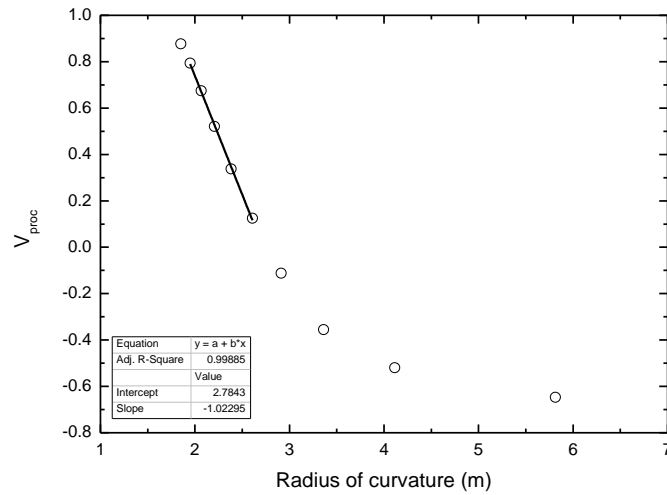


**Figure 92 - System output *versus* radius of curvature.**

Due to the type of processing adopted, based in the  $(dP_{out} / d\lambda) / P_0$  ratio, a linear system response was not expected. However, in the radius of curvature range from 1.95 m to 2.61 m, a clear linear behaviour can be observed with a sensitivity of  $-1.023 \text{ m}^{-1}$ .

To determine the measurand resolution achievable with this sensing head and interrogation approach, a curvature step change was applied and, from the associated output signal step change and *rms* noise fluctuations at the regions of constant curvature (Figure 93), it results a radius of curvature resolution of  $\sim 9.4 \text{ mm}$  in the linear region shown in Figure 92.

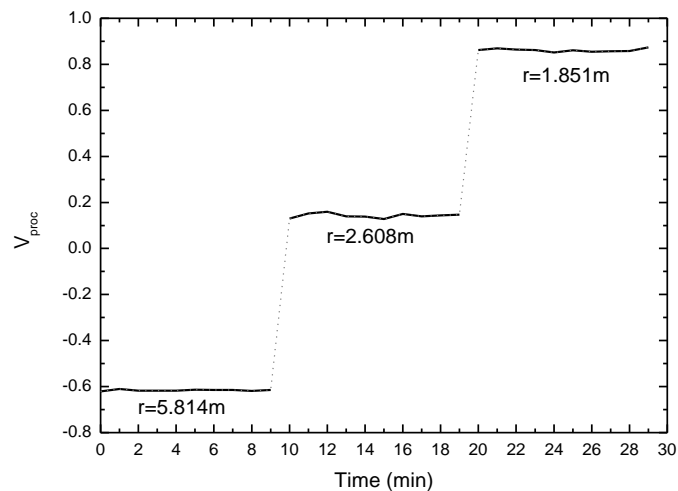


**Figure 93 - System output signal for step changes of the LPG curvature.**

These results permit us to state the following: first, the technique proposed based on signal reading outside the  $1/f$  noise level is effective for curvature measurements; second, the system noise reduction obtained by working outside the  $1/f$  noise region is larger than the reduction of the signal level (as can be observed in Figure 91) by operating with the derivative of the LPG transfer function.

It should also be emphasized that an important advantage of the proposed interrogation approach comes from its application in the multiplexing of spectral loss band fiber optic sensors, particularly LPGs. It is just required to place the sensors in series, in the sensing head branch, and increase the number of FBGs in the dynamic interrogation system branch. For scalability purposes, if  $N$  sensing heads are needed  $N+1$  FBGs will be used for its interrogation (one for referencing objectives the other  $N$  for interrogation purposes). The key point is the appropriate choice of the wavelengths of LPGs, and FBGs without the need of adding other optical components. Figure 94 presents the described concept.

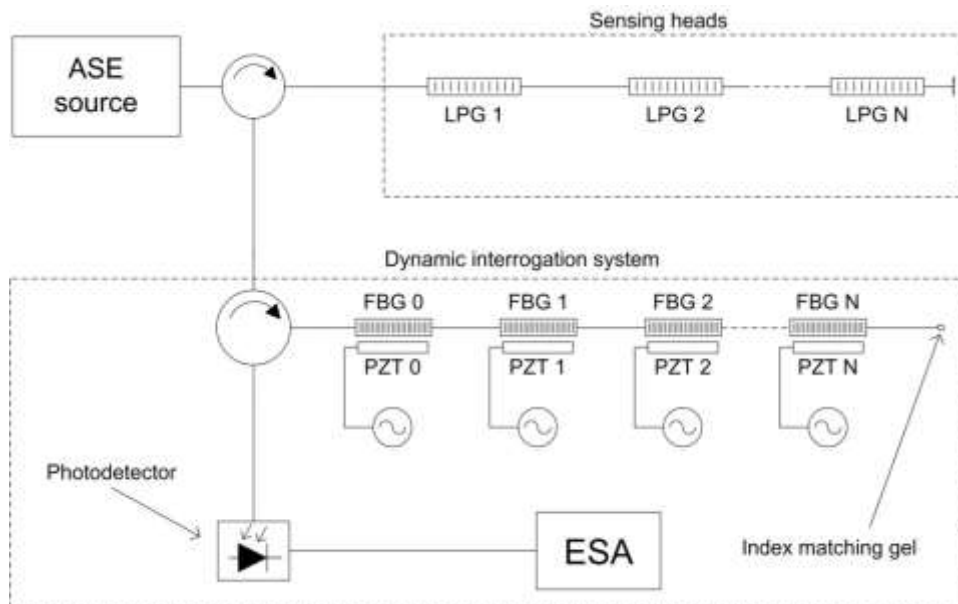


**Figure 94 - Electrical dynamic interrogation approach of a LPG based multiplexed scheme.**

An additional application of such an interrogation concept for fiber optic sensors is described in Appendix 2 where the preliminary results of an interferometric optical fiber inclinometer are presented.

## 6.5 Distributed Feedback Lasers Based Dynamic interrogation

In this section is presented a improved version of the LPG dynamic interrogation technique previously presented in sections 6.3 and 6.4, based on modulation, at different frequencies, of two Distributed-Feedback Lasers (DFB) spectrally located near the LPG resonance depth. The interrogation method relies on detecting with an electrical spectrum analyzer (ESA) the amplitude of the first and the second harmonic of the electrical signals that result from the optoelectronic conversion of the DFB laser spectrum. The amplitude of the first harmonic is proportional to the slope of the LPG spectral response at the DFB laser operating wavelengths, being the amplitude of the second harmonic also proportional to the second derivative of the LPG original spectrum. As mentioned before, both electrical amplitudes, of the first and second harmonic, change with the relative spectral movements between the LPG and the fixed operation wavelength of the DFB laser, permitting us to obtain a processed signal which is proportional to the LPG spectral shift and immune to optical power fluctuations along the system. This technique is tested in a multiplexing scheme to measure refractive index variations of two LPGs sensors working in reflection.

As stated in section 6.2 a good approximation to the LPG transfer function can be represented by equation (6.2). Figure 95, an upgraded version of Figure 78, shows  $P_{out}(\lambda)/P_0$ ,  $dP_{out}/d\lambda / P_0$  and  $d^2P_{out}/d\lambda^2 / P_0$  versus  $\lambda$ . It can be observed that the magnitude of the normalized slope variation along the full LPG response is approximately one order of magnitude smaller than the normalized optical power variation. It is also observed that the second derivative of the normalized FBG spectrum is approximately a factor of five smaller than the normalized slope variation. These factors translate into corresponding factors for the signal variations associated with  $P_{out}(\lambda)/P_0$ ,  $dP_{out}/d\lambda / P_0$  and  $d^2P_{out}/d\lambda^2 / P_0$ , with origin at a LPG spectral shift relative to fixed wavelength values defined by the DFB lasers.

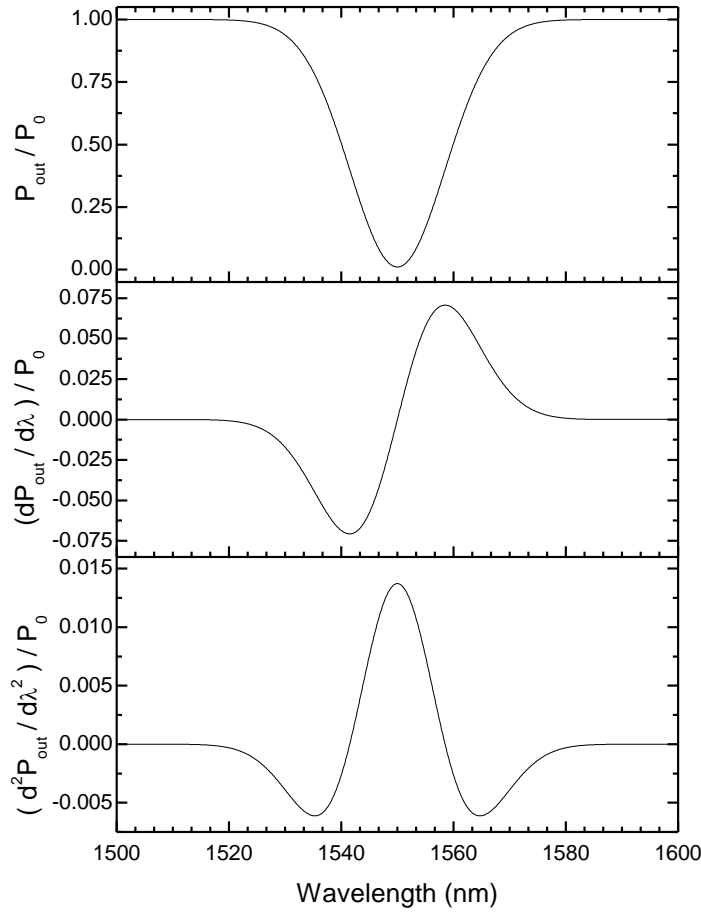


**Figure 95 -  $P_{out}(\lambda)/P_0$ ,  $(dP_{out}/d\lambda)/P_0$  and  $(d^2P_{out}/d\lambda^2)/P_0$  versus wavelength for a LPG.**

### 6.5.1 Experimental Setup for the DFB Laser Based Dynamic Interrogation

To evaluate the feasibility of the proposed interrogation approach, the setup presented in Figure 96 was implemented. Two LPGs with resonances centred at 1530 nm (LPG<sub>1</sub>) and 1565 nm (LPG<sub>2</sub>), presented in Figure 97, were fabricated using the electric arc technique (the periods of the refractive index modulation,  $\Lambda$ , are 391  $\mu\text{m}$  and 397  $\mu\text{m}$ , respectively; coupling to a 6<sup>th</sup> order cladding mode). Both LPGs were placed between fiber holders, inside a recipient with an aqueous sodium chloride (NaCl) solution.

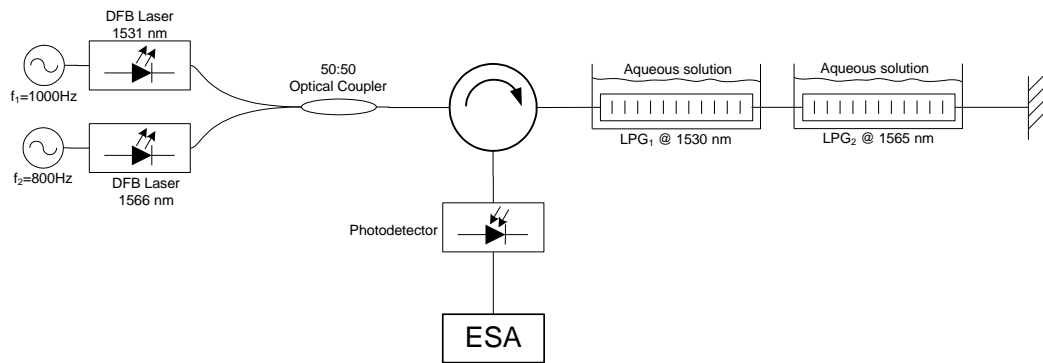


**Figure 96 - Experimental setup of the multiplexing layout for measuring refractive index variations using the electrical dynamic interrogation approach.**

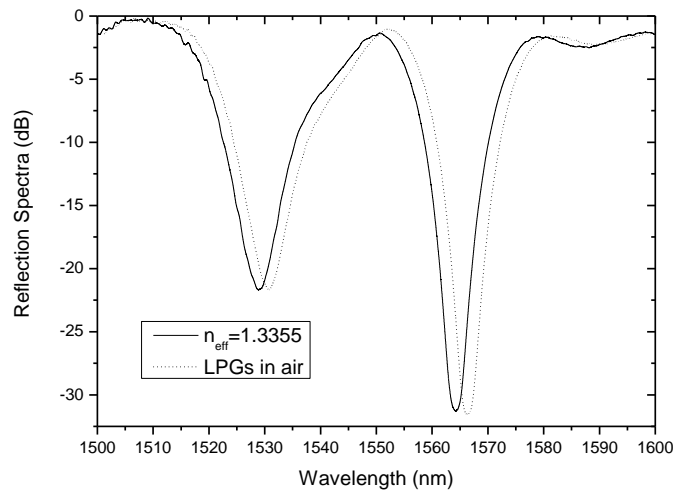


**Figure 97 - Optical reflection spectra of the LPGs multiplexing scheme for refractive index measurement. Spectrum of both structures immersed in distilled water (solid line); optical response of the multiplexed LPGs in air (dashed line).**

The experimental setup is illuminated by means of two DFB lasers emitting at 1531 nm ( $\lambda_1$ ) and 1566 nm ( $\lambda_2$ ), modulated by two independent signal generators with sine waves of ~300 mV of amplitude at the frequencies of 1000 Hz ( $f_1$ ) and 800 Hz ( $f_2$ ). These modulations induced corresponding modulations of the lasers injection currents around the DC bias values, with the consequent spectral shifts. The optical fiber end at the LPGs right side was mirrored with silver nitrate ( $\text{AgNO}_3$ ) allowing the sensing heads multiplexing scheme to operate in reflection.

The system noise level was stabilized at  $\sim -85$  dBV<sub>rms</sub> and the processing adopted was

$$V_{proc} = \frac{V_{\omega_1} - V_{\omega_2}}{V_{\omega_1} + V_{\omega_2}} \quad (6.4)$$

where  $V_{\omega_1}$  and  $V_{\omega_2}$  are the *rms* voltage amplitudes of the first and second harmonic signals relative to each DFB laser when modulated (DFB Laser @  $\lambda_1$ :  $\omega_1 = 1000$  Hz,  $\omega_2 = 2000$  Hz; DFB Laser @  $\lambda_2$ :  $\omega_1 = 800$  Hz,  $\omega_2 = 1600$  Hz) as shown in Figure 98. This processing eliminates the deleterious consequences of optical power fluctuations considering the amplitudes of these harmonics are both affected.

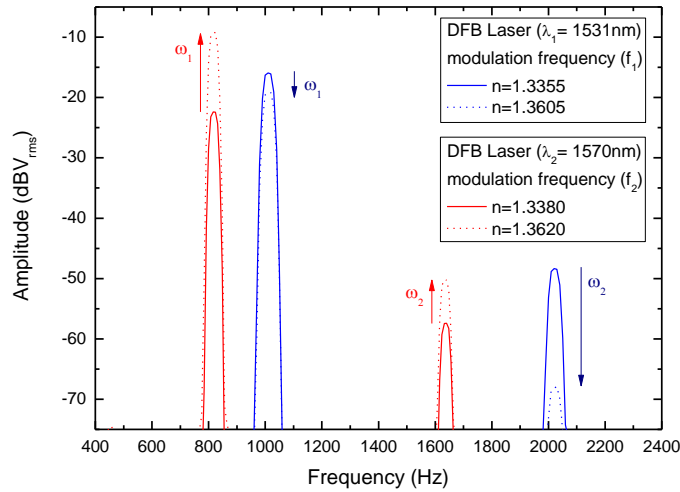


**Figure 98 - Electrical spectra of the multiplexed scheme, being (in red)  $\omega_1$  and  $\omega_2$ , the first and second harmonic of the DFB laser modulation frequency ( $f_1$ ), and (in blue)  $\omega_1$  and  $\omega_2$ , the first and second harmonic of the DFB Laser modulation frequency ( $f_2$ ).**

After photodetection of the optical signals reflected by the AgNO<sub>3</sub> mirror at the top of the sensing fiber, the resultant electrical signals were added with an electrical circuit and visualized in an HP 35660A electrical spectrum analyzer (ESA) with adequate impedance matching. The modulation of the injection current of each DFB lasers originates a relative spectral movement with respect to the LPG transfer function, with a consequent optical power modulation at the modulation frequencies and their second harmonics. The amplitude of this power modulation is a function of

the LPG spectral position, which changes due to the measurand variation. This effect can be observed in Figure 97 and Figure 98, where it can be seen that the wavelength shift of the LPGs resonances is transformed into an amplitude variation of the two harmonics ( $\omega_1$  and  $\omega_2$ ) observed in the ESA, corresponding to the frequency ( $f_1$  or  $f_2$ ) in which each DFB laser is being modulated.

### 6.5.2 Results for the DFB Laser Based Multiplexed Interrogation Scheme

The setup depicted in Figure 94 was used to estimate  $V_{\text{proc}}$  for each sensor, as shown in Figure 99.

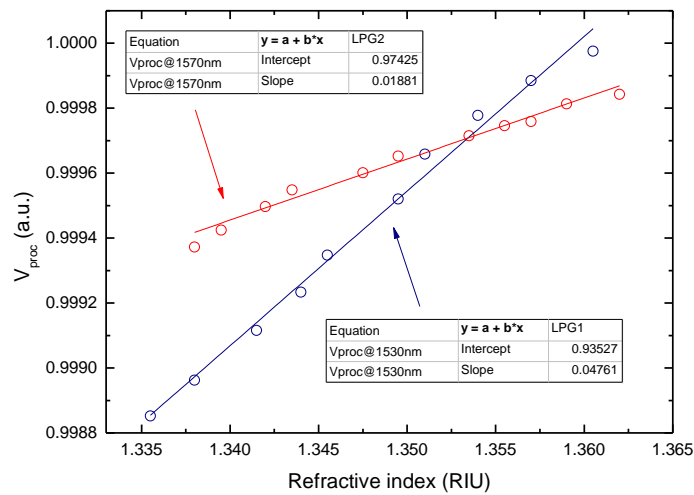
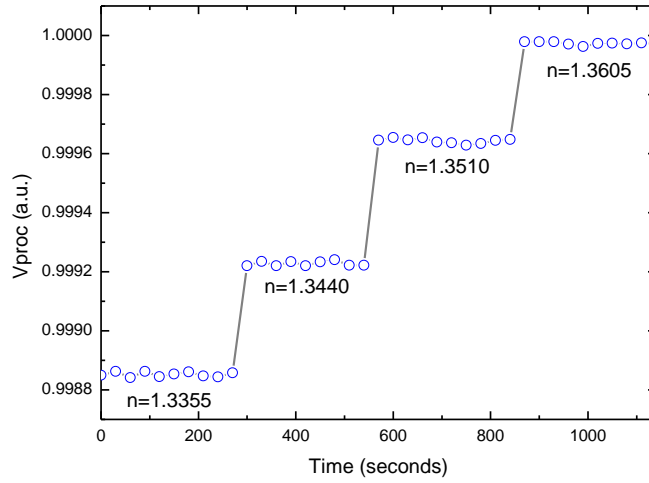
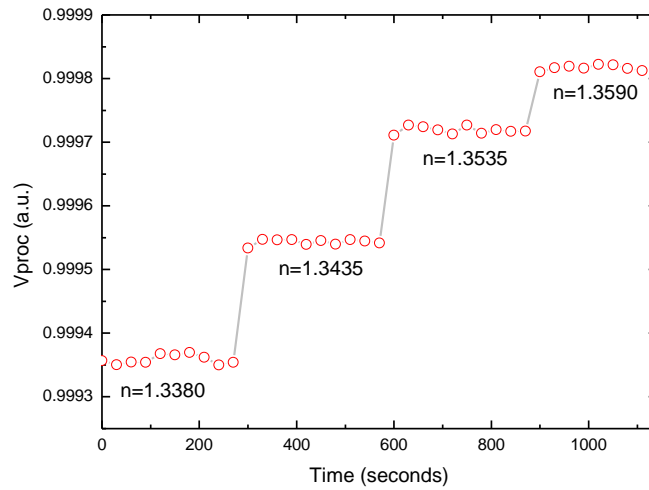


**Figure 99 - System output *versus* refractive index variations for each LPG: LPG<sub>1</sub> (in blue); LPG<sub>2</sub> (in red).**

As can be observed, a linear system response was obtained, as stated by the linear regression presented in Figure 99. Figure 100 shows the system step response for an induced NaCl concentration variation which corresponds to a refractive index change for both, LPG<sub>1</sub> and LPG<sub>2</sub>, cases.



(a)



(b)

**Figure 100 - Step response for induced refractive index variations of the aqueous solution of NaCl of LPG<sub>1</sub> (a) and of LPG<sub>2</sub> (b).**

From the amplitude of the step changes of the output signals induced by the refractive index step variations and the *rms* fluctuations of these signals in the situation of constant refractive index, a resolution of  $3.3 \times 10^{-4}$  RIU for LPG<sub>1</sub> and  $4.4 \times 10^{-4}$  RIU for LPG<sub>2</sub> was obtained. These results indicate that a refractive index resolution is expected to be improved with optimization of the configuration, particularly in what concerns the tuning of the relative spectral positions of the LPGs and DFB emission lines. Also, no crosstalk was observed between the two sensors of the structure.



## 6.6 Summary

In this chapter it was reported a LPG dynamic interrogation technique based on the modulation of fiber Bragg gratings located in the readout unit of the system. It permits the attenuation of the effect of the  $1/f$  noise of the electronics in the resolution of the LPG-based sensing head.

The concept was tested, as presented in section 6.3, to detect variations of the external refractive index and a resolution of  $2.0 \times 10^{-4}$  RIU was achieved without system optimization. Additionally, the effect on the sensor's resolution when introducing Erbium and Raman optical amplification was experimentally investigated.

In section 6.4 the proposed dynamic interrogation technique was tested for curvature measurements. The setup was simplified and a radius of curvature resolution of  $\sim 9.4$  mm was obtained. It was also proposed the application of such a technique for the multiplexing of spectral loss band fiber optic sensors, particularly LPGs.

Finally, a multiplexing scheme based in an upgraded approach of the electrical dynamic LPG interrogation technique was presented in section 6.5. It was based on the analysis of the electrical spectrum of two modulated DFB lasers located nearby a LPG resonance. A resolution value of  $10^{-4}$  RIU was achieved.

The developed interrogation architectures presented in this chapter easily allow multiplexing several sensing heads, as they are simple and also could be applied in several structures used for the measurement of DC or quasi-DC measurands, as is the case for multimode interferometers (MMI) or other sensing devices based on the phenomenon of surface plasmonic resonance (SPR).



## Chapter 7 – Optical Fiber Sensing Configurations for Remote Sensing

---

### 7.1 Introduction

A concept of long period gratings based optical fiber sensors, with broadband light illumination generated just after the sensing structure, is presented in section 7.2. This new approach allows the interrogation in transmission of the sensing head, while integrated in a reflective configuration, which means the LPG sensor is seen in transmission by the optical source but in reflection by the measurement system. Also, it is shown that with this illumination layout the optical power balance is more favorable when compared with the standard configurations, allowing better sensor performances particularly when the sensing head is located far away from the photodetection and processing unit. This is demonstrated for the case of an LPG structure applied to measure strain and using ratiometric interrogation based on the readout of the optical power reflected by two fiber Bragg gratings spectrally located in each side of the LPG resonance.

In section 7.3, a remote environmental sensing configuration is presented using a standard optical time domain reflectometer (OTDR). The measurement of environmental parameters using optical sensors is an expanding area of research with growing importance. Fiber optic sensors are an interesting solution for that due to their high sensitivity, small size, and capability for on-site or remote, real-time and distributed sensing capabilities. The suggested multiplexing sensing scheme approach uses transmissive filters (LPGs) interrogated by the OTDR return pulses. The loss induced at the resonance wavelengths varies with changes in the environment refractive index, temperature or other physical parameters. Experimental results show that the insertion of an erbium amplifier improves the measurement resolution in certain situations. Further analysis shows that a remote multiplexed sensing scheme allows us to perform simple and low cost real time measurement of refractive index and temperature over long distances.

Finally a remote optical fiber sensor system based on a long period grating, Raman amplification and electrical interrogation – described in chapter 6 – was investigated and a method to predict its behaviour was tested. The interrogation unit is composed by two fiber Bragg gratings modulated by two piezoelectrics transducers. Optical fiber sensor systems may be limited to operate at distances of only few kilometers due to attenuation effects and noise, that adversely affects the performance of the sensor interrogation process. Experimental and simulation results were obtained in the context of analysis of remote optical fiber sensors, and are shown in section 7.4. The simulation models use numerical methods to compute the Raman interaction between the pumps and the sensor signals and allow speeding up the analysis regarding the setup to be experimentally implemented to measure environmental temperature. The results obtained show that under Raman amplification the power ratio between the two central wavelengths of the FBGs has a linear relation with the change of the LPG resonance induced by temperature variation.

## 7.2 In-situ Optical Source for Remote Sensing Purposes

In optical fiber sensing, the measurement system can be configured to operate in reflection or in transmission mode. Usually, transmission measurement systems are used with specific sensing heads based on spectraly selective loss. Long period gratings are a paradigmatic example of such sensing schemes, in which the transmission spectrum has depths at wavelengths corresponding to resonance coupling to specific cladding modes, that change when the device is subjected to different physical interactions. In general, these sensing structures are located remotely and the broadband light that propagates in the downlead illuminating fiber has its spectrum modulated by the LPG in a way that depends on the measurand status. This light propagates back to the measurement unit using a dedicated return fiber, where interrogation is performed with a variety of techniques, such as those based on derivative spectroscopy [137-139]. The need of a return fiber can be avoided by mirroring the fiber end and operating the sensing head in reflection, a situation in which light crosses two times the LPG [140, 141]. This layout has advantages, but is prone to interference effects that induce modulation of the LPG spectral response,

conflicting with its interrogation when interferometric readout is not the objective. In both situations (light return using a second fiber or using the same input fiber due to the mirroring of the distal end face) the light in the spectral region of the LPG travels twice the distance between the LPG location and the optical source. Additionally, when the sensor is remote, the losses involved can be substantial, degrading its performance, particularly when dealing with sensing networks for multi-point measurement.

In field applications of LPG based sensors the relevance of this constraint comes to surface in an acute way, which motivated the search for possible solutions to overcome it. As a result of this, it turned out that an effective approach would be to generate the LPG illuminating light close to the location of the sensing element, using a length of erbium doped fiber just after the LPG, pumped by the light of a laser diode located remotely in the photodetection/processing system.

This section describes the investigation of such a sensing layout, where the LPG sensor is seen in transmission by the optical source, but in reflection by the measurement system. The presented study demonstrates, to the best of our knowledge and by the time it was done, the first approach of the concept of having a sensing head being illuminated in situ by an optical source just after the sensing structure. Comparison of the performance obtained in this situation relatively to the standard approach is provided for the case of a LPG-strain sensor with FBG based ratiometric interrogation.

### **7.2.1 In Situ Optical Source for Remote Sensing**

In order to characterize the performance of the new proposed configuration, the system depicted in Figure 101 was implemented. The new layout is based on an erbium doped fiber (EDF) optical source, with the active fiber located just after the sensing head. As represented, a 1480/1550 nm wavelength division multiplexer (WDM) is used which allows the laser pump light to propagate down to the 20 km of fiber up to the one meter length EDF, crossing the LPG that is transparent to this radiation. The pump laser optical power used was around 200 mW, guaranteeing the

saturation regime of the EDF. The EDF bidirectional emitted light illuminates the LPG via the direct path or via reflection in the mirrored fiber end.

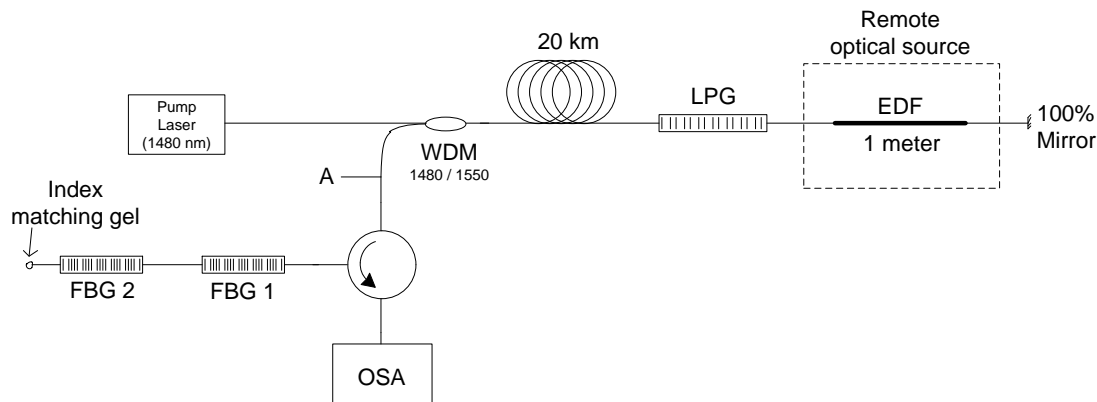


**Figure 101 - Experimental setup for the new LPG-sensor layout.**

Analysis of the layout in Figure 101 makes it clear that, from the view point of the illuminating source, the LPG operates in transmission, but the optical system is configured in reflection. The LPG encoded light is directed to the two interrogating FBGs and detected by an optical spectrum analyzer (OSA).

## 7.2.2 Standard Remote Sensing Approach

In order to compare the performance of the proposed new configuration, a standard interrogation scheme for a LPG-based sensing head was also implemented. As shown in Figure 102, a local optical source was built combining a pump laser diode emitting at 1480 nm, a WDM and a one meter EDF. The pump laser used in the configuration was the same used in the in situ optical source. In this configuration the EDF will be in the oversaturation regime. The light from the local optical source goes to the LPG sensor through an optical circulator. To simulate a remote sensing solution, 20 km of connecting optical fiber was added to the system. To get a reflective configuration, one of the leads of the fiber was mirrored, therefore the light in the relevant spectral region runs for 40 km of fiber. The returned light from the LPG circulates towards two fiber Bragg gratings (FBG) with resonance wavelengths located in each side of the LPG spectrum. The light reflected by the FBGs is detected by an OSA.

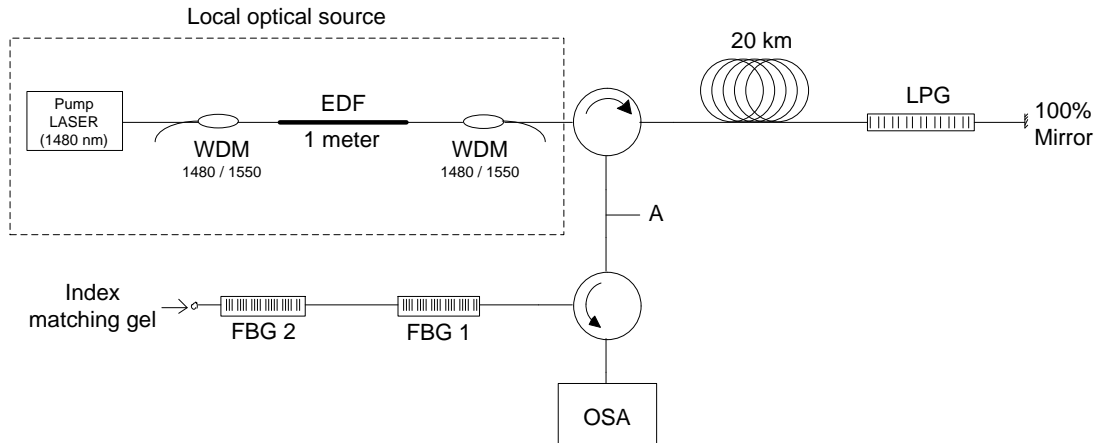


**Figure 102 - Experimental setup for the standard LPG-sensor layout.**

### 7.2.3 Results and Discussion

Figure 103 (a) shows the spectrum of the broadband light detected by the OSA at point A relative to the configurations shown in Figure 101 and Figure 102, respectively. As expected, the spectral shape is the same, but for the configuration here proposed the power spectral density is  $\sim 8$  dB higher than the value obtained with the standard layout in the spectral region of the LPG used as the sensing element for a wavelength of 1550 nm. This positive power difference is not constant along the erbium emission spectral window, ranging from  $\sim 10.5$  dB in the peak emission around 1530 nm to  $\sim 5$  dB in the emission spectral edges.

When the LPG is inserted in the system, the effect of its resonance loss band is well evident for the case of the new layout (Figure 103 (b)), but less pronounced for the case of the standard configuration, a result that can be attributed to the low power level that reaches the OSA in this situation. The signal in the standard configuration is close to the detection sensitivity limit of the instrument, as is evident from the noisiest spectral curve recorded by the OSA.

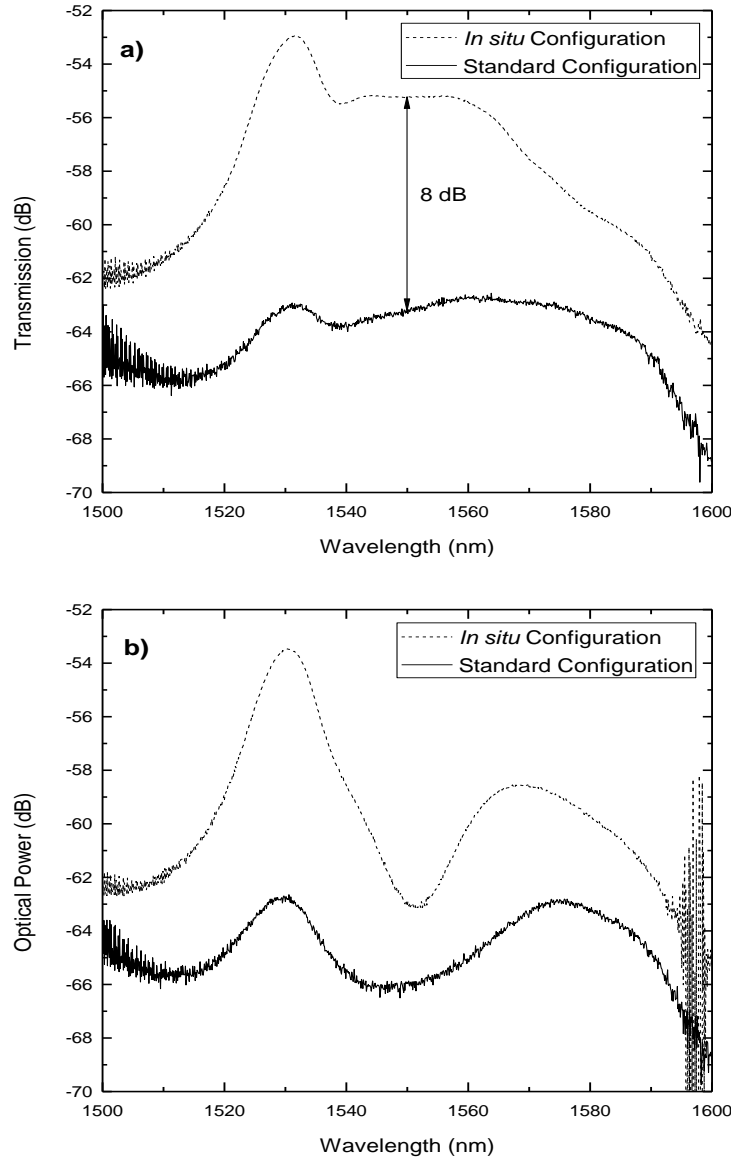


**Figure 103 - Optical spectra recorded by the OSA at point A of configurations depicted in Figure 101 and Figure 102 when: (a) the LPG is not present; (b) after the insertion of the LPG.**

Both configurations were tested when the LPG was configured to measure strain. The interrogation was performed using the ratiometric technique applied to the optical power reflected by the two FBGs with resonances located in the edges of the LPG spectrum. Figure 104 shows the relative spectral positions of the LPG/FBGs and associated optical powers, in the case of no strain applied to the LPG. Again, it can be observed the low power level present in the case of the standard configuration. The FBGs select two narrow spectral slices of the returned optical radiation modulated by the LPG attenuation band, with powers  $P_1$  and  $P_2$ .



The ratiometric processing [142] implemented was

$$P_{proc} = \frac{P_1 - P_2}{P_1 + P_2} \quad (7.1)$$

enabling referentiation to optical power fluctuations. The dependence of  $P_{proc}$  with strain applied to the LPG is shown in Figure 105.

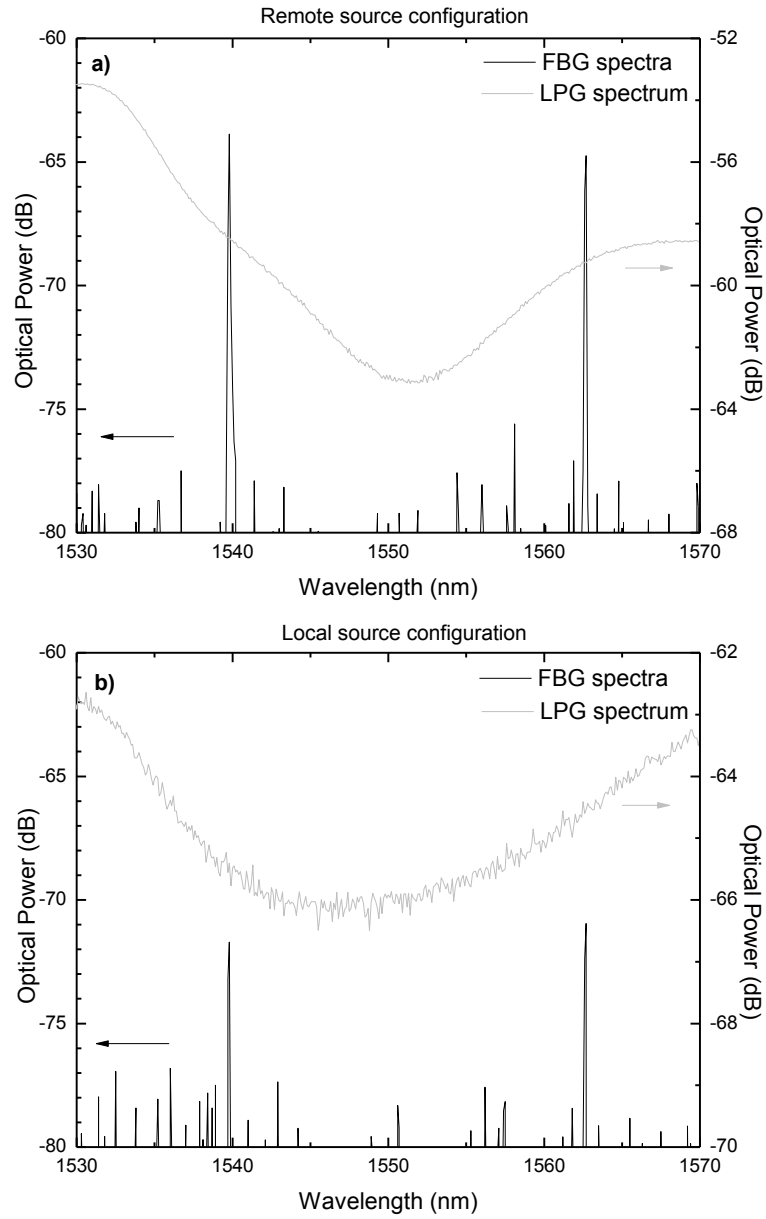


**Figure 104 - Relative spectral positions of the LPG/FBGs and associated optical powers for the cases (no strain applied to the LPG): (a) local source configuration; (b) remote source configuration.**

The data in Figure 105 clearly shows that with the same pump laser diode and the same length of erbium doped fiber, when the LPG sensor is located 20 km away from the photodetection/processing unit, with the standard configuration it is not possible to read the sensor status, since the weak signals are strongly corrupted by noise, originating a strong scatter of  $P_{\text{proc}}$ . However, the proposed approach enables the sensor readout with a sensitivity of  $\sim 100 \mu\epsilon^{-1}$ . This single result indicates the potential of the novel configuration when dealing with the remote interrogation of fiber optic sensors. Add to this, the fact that in several situations is not advantageous the double pass the light through the sensing elements, since the induced resonance loss bands can easily lead to excess attenuation, reducing the sensor resolution from the side of the signal strength compared to the noise level (a detrimental effect that overcomes the advantages of the double pass of the light by the measurement region). This condition is quite common in resonance plasmonic sensors, a reason why it is almost mandatory to work out in a transmission configuration when addressing such sensors, implying the requirement of a dedicated return fiber.

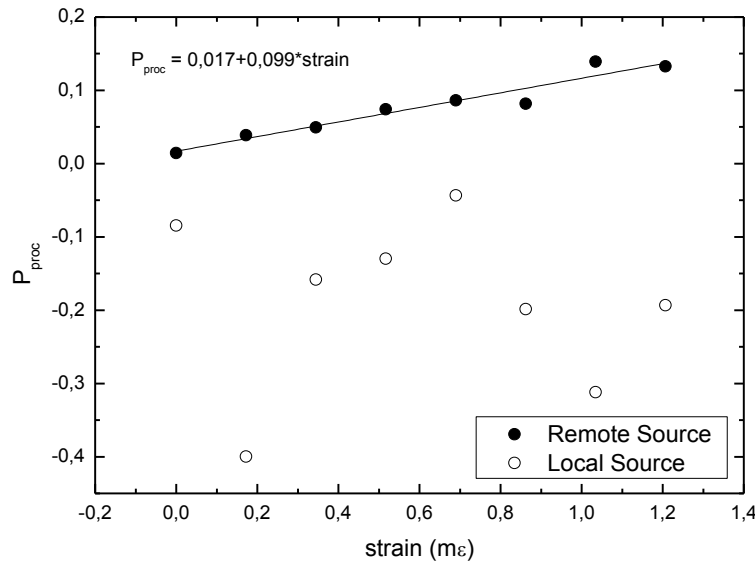


**Figure 105 - Variation of  $P_{\text{proc}}$  versus strain for the two configurations studied.**

With the innovative approach proposed here, this extra fiber is not needed in view of the circumstance that it is now possible to illuminate the sensor in transmission, while operating in a reflective layout from the viewpoint of the measurement system. This characteristic, together with the positive impact in the sensor power levels that reach the photodetection/processing unit, points out the advantages of using this approach to improve the performance levels of several types of optical fiber sensing

heads. The sensing concept and the architecture proposed in this work were patented, as can be seen in Appendix 3.

### **7.3 Remote Sensing of Refractive Index with an OTDR**

The measurement of chemical parameters using optical sensors is an expanding area of research with growing importance, especially in environmental applications. The refractive index measurement in liquids is an important mechanism for label-free chemical and biological sensing and fiber optic sensors are an interesting platform in this regard due to their high sensitivity, small size, and capability for on-site or remote, real-time and distributed sensing capabilities. Several schemes and interrogation methods for refractive index sensing using optical fibers have already been proposed [52, 143].

An optical time-domain reflectometer (OTDR) is an optical instrument that injects optical pulses into a fiber under test, extracting then from the same end of the fiber the amount of light that is scattered or reflected back along the fiber. Due to its intrinsic characteristics, the OTDR instrument has been also used to characterize fiber optic displacement sensors [144, 145]. Special types of fibers, grating structures and elaborated sensing heads schemes have already been proposed, for refractive index measurements with an OTDR [146, 147].

In this section, a remote refractive index measurement system using a standard OTDR is presented. This approach uses a LPG in which the resonant wavelengths can be interrogated by analyzing the strength of the OTDR return pulses that are plotted as a function of the fiber length. This is, to the best of our knowledge and by the time the study was done, the first refractive index sensor based on a LPG interrogated by an OTDR. The effect of optical amplification in the sensor's performance is also investigated. Finally, a multiplexing sensing scheme using two LPGs is also carried out to measure refractive index and temperature.

### 7.3.1 Sensing Scheme for Refractive Index Measurements

To implement the proposed sensing scheme, an experimental setup with an Ando AQ7250 OTDR and a LPG sensing head placed between two fiber rolls, of 1.3 km and 11 km, was prepared as depicted in Figure 106. The amplification scheme, comprehending two circulators and an Erbium Doped Fiber Amplifier (EDFA) was only introduced later in the experiment.

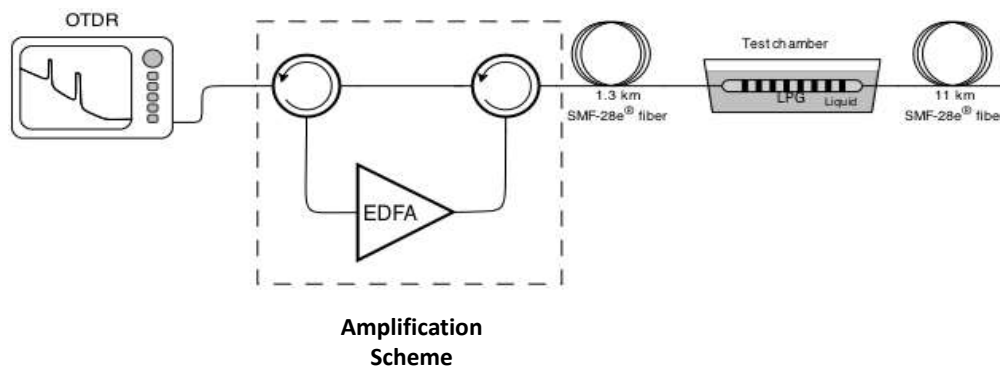


**Figure 106 - Experimental setup of the LPG based sensing head for refractive index measurements.**

The LPG was fabricated using the electric arc technique, with a period of the refractive index modulation ( $\Lambda$ ) of 395  $\mu\text{m}$ , with strong resonances at 1317 nm (coupling to a 5<sup>th</sup> order cladding mode) and at 1542 nm (coupling to a 6<sup>th</sup> order cladding mode). The OTDR multiwavelength lasers and the LPG spectrum in both regions (1310 and 1550 nm) are superimposed and depicted in Figure 107.

In Figure 108, it can be seen a detail of the signal retrieved by the OTDR in the vicinity of the 1.3 km fiber length, showing the precise position of the LPG sensing head. The resonant peak of the LPG shifts in wavelength in accordance with the variations of the refractive index of the surrounding medium. This perturbation thus changes the intensity of the 20 ns light pulses that will be backscattered at the position where the LPG is located.

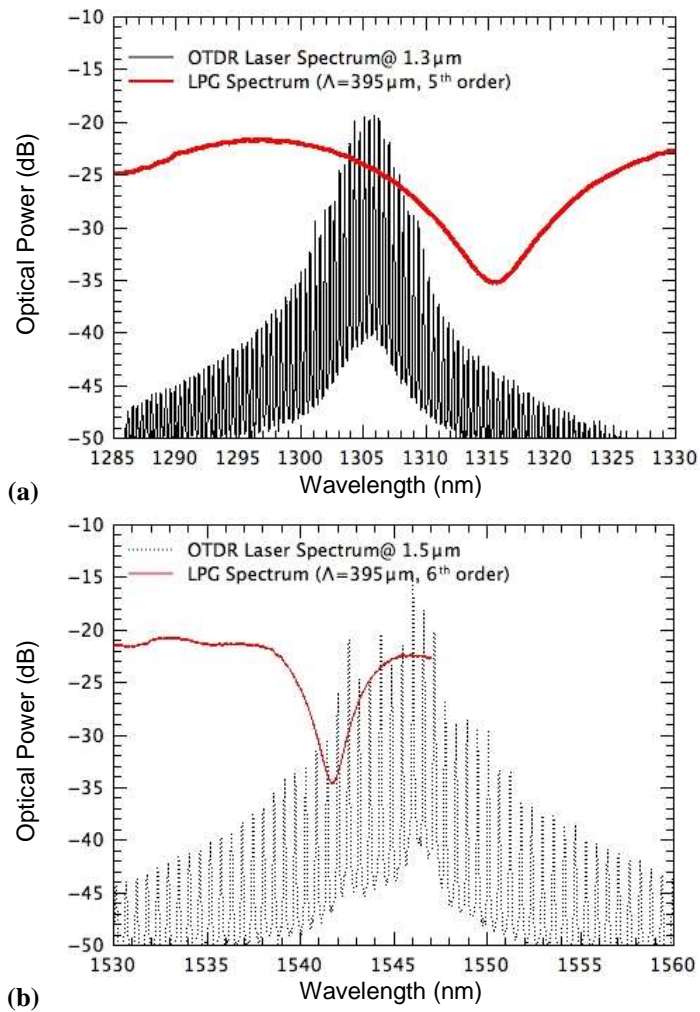


**Figure 107 - OTDR multiwavelength laser and LPG spectrum at (a) 1310 nm and (b) 1550 nm ranges.**

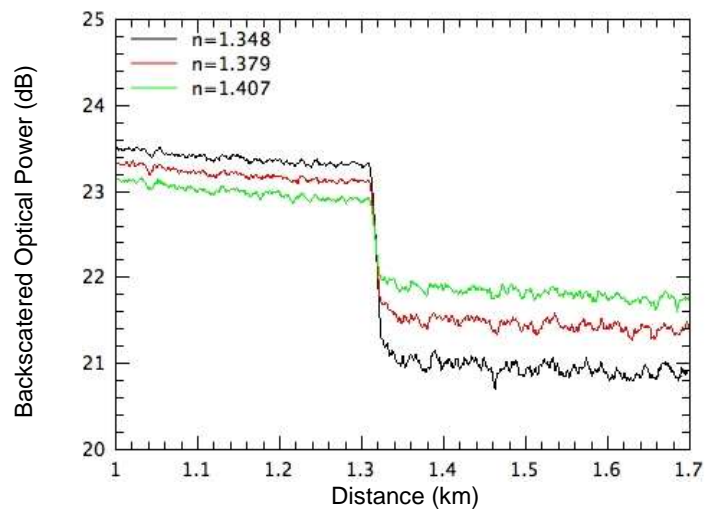


**Figure 108 - Detail of the OTDR obtained traces for different refractive index values, for the 1550 nm wavelength.**

As can be observed, with the increase of the refractive index value, a reduction of the backscattered optical power is obtained. Plotting the amplitude of such a step as function of the refractive index, for the 1300 nm and 1550 nm range, the data depicted in Figure 109 is obtained.

It is clear that in the 1550 nm range, the LPG resonance presents a larger evanescent field interaction. So, the amount of light lost in the refractive index measurements for this wavelength range will be higher than for the 1310 nm range. On the other hand, the more favorable relative position between the LPG resonance and the OTDR central wavelength, for the 1550 nm range, surely contributes for the achievement of higher sensibilities.

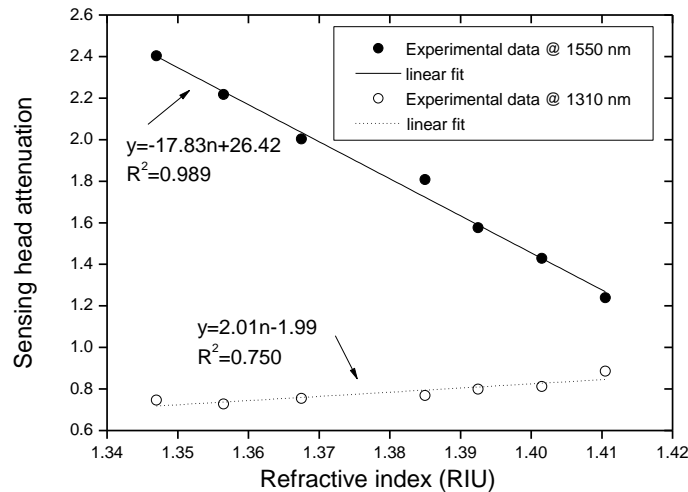


**Figure 109 - Comparison of the LPG ( $\Lambda=395\mu\text{m}$ ) attenuation observed in the 1310 nm and 1550 nm ranges of an OTDR as function of refractive index variation.**

At this point a new LPG was developed, with similar spectral characteristics to the previously used, and the experimental procedure was repeated for two different cases, without amplification and inserting the amplification scheme module. A Multiwave Photonics EDFA-C amplifier was used. The results are presented in Figure 110.

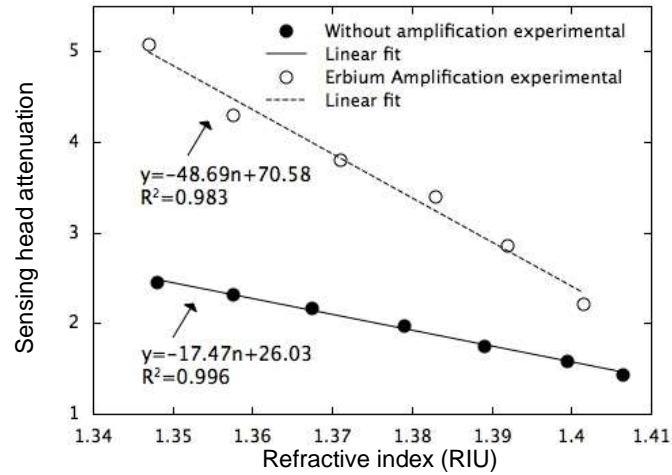


**Figure 110 - LPG ( $\Lambda=395\mu\text{m}$ ) based sensing head attenuation, obtained from the setup depicted in Figure 106, for the 1550nm OTDR range, as function of the refractive index variations with and without optical amplification, respectively.**

Similarly to the result obtained previously in Figure 109, the sensitivity of the sensing system is  $\sim 17$  dB/RIU. With the introduction of the amplification scheme this value is improved to  $\sim 48$  dB/RIU. Therefore, the sensitivity of the developed setup changes with the inclusion of the optical amplification scheme, improving by almost a factor of 3. Table 5 presents the refractive index resolutions, calculated considering a minimum detectable signal of two times the standard deviation, for the two configurations.

**Table 5 - Refractive index resolutions obtained for the traces depicted in Figure 110.**

Configuration	$\delta n$
Without amplification	$4.02 \times 10^{-3}$ RIU
Erbium amplification	$1.50 \times 10^{-4}$ RIU

As can be observed, the amplification scheme introduces an improvement on the system resolution and sensitivity. This happens because the erbium gain curve is superimposed on the LPG spectrum and enhances the system behavior. The sensitivity normally depends only on the sensing element, the LPG in this experiment, but in this case, it is highly dependent on the spectral position of the resonance relatively to the multimode laser source, meaning that the sensitivity depends also on the initial LPG resonance, and also on the optical source conditions. Therefore the additional gain improves both the sensitivity, by changing the spectral slope of the laser, and the resolution by improving the signal to noise ratio of the overall system.

### 7.3.2 Multiplexing Sensing Scheme for Refractive Index and Temperature Measurements

To implement the multiplexing sensing scheme, a new experimental setup was implemented using the same OTDR and two LPGs placed between three fiber rolls of 3 km, 1.2 km and 0.9 km, as depicted in Figure 111.

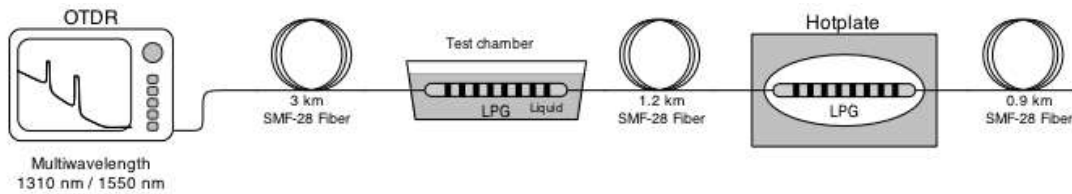


**Figure 111 - Experimental setup of the implemented multiplexing scheme for refractive index and temperature measurements based in two LPGs.**

Two new LPGs were fabricated, using the electric arc technique, with a period of refractive index modulation ( $\Lambda$ ) of 397  $\mu\text{m}$  and 398  $\mu\text{m}$ , with strong resonances at 1546 nm and 1552 nm (both coupling to 6<sup>th</sup> order cladding modes), respectively. The OTDR multiwavelength laser at 1550 nm and the LPGs spectrums are superimposed and depicted in Figure 112.

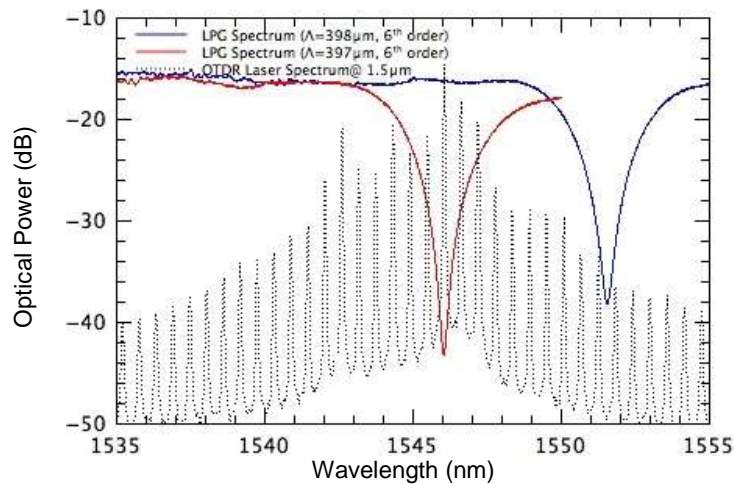


**Figure 112 - OTDR multiwavelength laser for the 1550 nm range superimposed with (in red) the LPG at 1546 nm ( $\Lambda=397 \mu\text{m}$ ) used for refractive index measurement, and (in blue) the LPG at 1552 nm ( $\Lambda=398 \mu\text{m}$ ) used for temperature discrimination.**

Plotting the amplitude of the obtained OTDR backscattered loss steps as a function of the refractive index (for the LPG at 1546 nm), and as a function of temperature (for the LPG at 1552 nm), the data depicted in Figure 113 is obtained.



From Figure 113 it can be observed that a dependence of 106 dB/RIU is obtained for the refractive index measurement and a sensitivity of 0.06 dB/°C is achieved. As previously stated, the sensitivity of the sensing head is a consequence of its spectral characteristics, i.e. it is highly dependent on the spectral position of the LPG resonance relatively to the OTDR multiwavelength laser source. Due to an appropriate LPG shape, the sensitivity for the refractive index change was improved by a factor of 5 in comparison with the initial experiment without amplification and by a factor of 2 considering the amplification case. Thus it is clear that the amplification scheme is not the only mechanism for improving system performance.

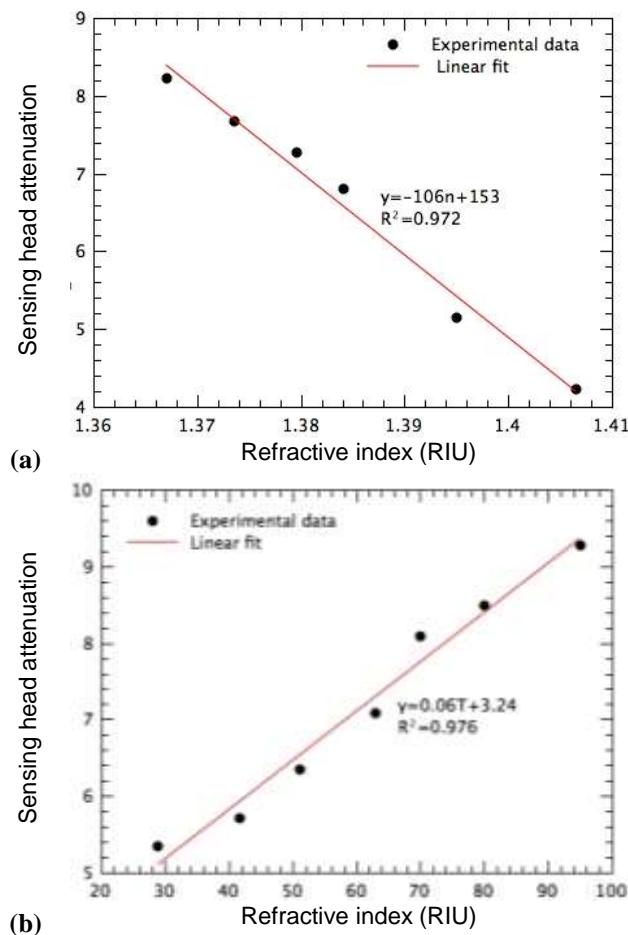


**Figure 113 - LPGs based sensing head attenuation, obtained from the setup depicted in Figure 111, for the 1550 nm OTDR range as function of (a) the refractive index (LPG at 1546 nm) and (b) temperature (LPG at 1552 nm) variations.**

The calculations of the resolutions obtained for the multiplexing sensing scheme were performed by considering a minimum detectable signal of two times the standard deviation, and are presented in Table 6.

**Table 6 - Resolutions obtained for the traces depicted in Figure 113**

Measurement	Resolution
Refractive Index	$\delta n = 3 \times 10^{-4}$ RIU
Temperature	$\delta T = 0.16$ °C

Considering the ratio between the refractive index and temperature sensitivities of the proposed scheme it is noticed that a deviation of 1 °C introduces an error to the index measurement of  $\sim 6 \times 10^{-4}$  RIU. Within this context a simultaneous measurement is not recommendable, because the cross sensitivity to temperature could induce an error of the same order of magnitude of the resolution of the refractive index measurement.

#### 7.4 Remote LPG Sensor with Electrical Interrogation Assisted by Raman Amplification

When compared with EDFAs, Raman amplifiers do not need doped or specialized fibers, therefore single mode fiber can be used as the gain medium. So, Raman amplification can occur in long fiber lengths which is a characteristic of distributed amplification. Distributed amplifiers improve the noise figure and reduce the nonlinear impairments in fiber optic systems [148]. Additionally, the amplification bandwidth size can be adjusted by changing parameters like the number of pump lasers, spectral and spatial position and their optical power.

Another important issue in LPG sensor systems is the interrogation technique that allows retrieving the wavelength encoded measurement after the propagation in the optical fiber. Optical interrogation can be realized, but this approach suffers with high cost and low time resolution. An electrical interrogation can offer a better time resolution with minimal costs.

Lee *et al.* [149] demonstrated a Raman amplifier-based long-distance sensing system for simultaneous measurement of temperature and strain using a combined

sensing probe formed by an erbium-doped fiber (EDF) and a FBG. This scheme allows the use of a recycling Raman pump to feed the EDFA, to act as a broadband source in the sensing head, achieving a distance of 50 km. Hu *et al.* [150] also reported the Raman amplification capability in remote sensing, combined with two EDFAs stages, to achieve an operation distance of 100 km to the FBG sensor head.

Alahabi *et al.* [151] reported an extended-range distributed temperature sensor based on coherent detection of the frequency shift of the spontaneous Brillouin backscatter combined with Raman amplification using a microwave detection system. Another work that applies Raman amplification in remote fiber sensing was presented by Lee *et al.* [149], that demonstrated a Raman amplifier-based long-distance sensing system with optical interrogation for simultaneous measurement of temperature and strain, using a combined sensing probe with an erbium-doped fiber (EDF) and a fiber Bragg grating. Bravo *et al.* [152] demonstrated a 253 km remote displacement sensor, based on a fiber loop mirror interrogated by a commercial optical time-domain reflectometer. All of them consider basically experimental analysis.

This work analyzes different remote sensor setups for temperature measurement using Raman amplification. Experiments and numerical simulations that describe the propagation, the spontaneous emission noise and the Raman interactions between the pumps and the sensor signals along the fiber are presented. The simulations allow the performance analysis of the setup to be experimentally implemented in order to measure/monitor environmental temperature, using the electric dynamic interrogation scheme presented in chapter 6 that shows improved performance. Different schemes were investigated and an optimal setup for a remote sensing system based on a LPG sensor head was developed, applied to the measurement of temperature.

#### **7.4.1 CW Raman Amplification Applied to Remote Sensing**

Raman amplifiers are based on the nonlinear effect of Stimulated Raman Scattering (SRS). This physical phenomenon is an inelastic scattering process based on the interaction between the incident photons and the silica molecules in the optical fibers.

Its main characteristic is the energy transfer from one or more pump wavelengths to the wavelength signals [148, 153].

A numerical model [154] was used to describe the spatial propagation and the interaction between the signal and pump lasers along the optical fiber, taking into account Raman amplification. Effects such as the single and double Rayleigh scattering (DRS), the amplifying spontaneous emission (ASE) noise, polarization effects and the interaction between signal and pumps, signal-signal and pump-pump are also considered. The main equation is

$$\begin{aligned} \frac{dP_{\nu}^{\pm}}{dz} = & \mp \alpha_{\nu} P_{\nu}^{\pm} \pm \varepsilon_{\nu} P_{\nu}^{\mp} \pm P_{\nu}^{\pm} \sum_{\mu > \nu} \frac{C_{R\mu\nu}}{\Gamma} (P_{\mu}^{+} + P_{\mu}^{-}) \\ & \pm 2\hbar\nu B_e \sum_{\mu > \nu} \frac{C_{R\mu\nu}}{\Gamma} P_{\mu}^{+} + P_{\mu}^{-} [1 + \eta(T)] P_{\nu}^{\pm} \sum_{\mu < \nu} \frac{\omega_{\nu}}{\omega_{\mu}} \frac{C_{R\nu\mu}}{\Gamma} P_{\mu}^{+} + P_{\mu}^{-} \\ & \mp P_{\nu}^{\pm} \sum_{\mu < \nu} \frac{\omega_{\nu}}{\omega_{\mu}} \frac{C_{R\nu\mu}}{\Gamma} [1 + \eta(T)] 4\hbar\mu B_e \end{aligned} \quad (7.2)$$

where  $\eta(T)$  is the thermal factor, which correspond to the phonon population, defined as

$$\eta(T) = \frac{1}{\left( \exp\left[ \frac{\hbar(\mu - \nu)}{K_B T} \right] - 1 \right)} \quad (7.3)$$

$P_{\mu}$ ,  $P_{\nu}$ ,  $\alpha_{\mu}$  and  $\alpha_{\nu}$  are the power and attenuation coefficients relative to frequencies  $\mu$  and  $\nu$  respectively. The superscripts + and – indicate, respectively, the forward and backward propagation in the  $z$  axis direction,  $C_{R\mu\nu}$  is the Raman gain efficiency between the frequencies  $\mu$  and  $\nu$ ,  $\Gamma$  is the polarization factor and takes a value 1 if the polarizations are preserved and 2 when the polarizations are not maintained,  $\varepsilon_{\nu}$  is the Rayleigh scattering coefficient,  $\hbar$  is the Planck constant,  $K_B$  is the Boltzman constant,  $T$  is the absolute temperature in the optical fiber and  $B_e$  is the considered noise bandwidth.

The first term in equation (7.2) corresponds to the optical fiber losses and the second term is related to the DRS. The third term refers to the Raman gain at frequency generated by higher frequencies. The fourth term gives the ASE at frequency, with the thermal factor contribution. The fifth term corresponds to the depletion at frequency, due to lower frequencies, and the sixth term is the loss at frequency originated by the noise emission at lower frequencies.

The coupled differential equations given by equation (7.2) can be solved with numerical methods using boundary conditions. In telecommunications applications, these boundary conditions are well known as illustrated in Figure 114. The intensity of the signal ( $P_{signal}$ ) and pump ( $P_{pump}$ ) are input parameters and the reflected signal and pump at the end of the fiber can be neglected.

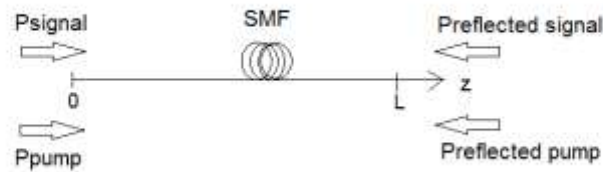


**Figure 114 - Boundary conditions in a co-propagating Raman amplifier, applied for telecommunications systems.**

Three main configurations for remote optical fiber sensors were analyzed in this work. One a Raman co-propagating amplifying mode, a second with a Raman counter-propagating amplifying mode, and the last one including a Raman co-propagating amplifying mode for the injected signal and a Raman counter-propagating amplifying mode for the received signal.

An amplified spontaneous emission (ASE) source, from the Erbium doped fiber amplifier, is used on each setup to provide an high power broadband source (BRS). 50 km of single mode fiber (SMF) serve as transmission and Raman amplification medium, and are used in the different configurations to connect the interrogation unit to the sensor head. An optical spectrum analyzer is included in the interrogation unit

to show the LPG received spectrum during the numerical and model validation procedure.

The setup showed at Figure 115 utilizes an optical circulator to connect the light source to the WDM coupler, which couples the pump laser and the BRS signal into the SMF optical fiber.

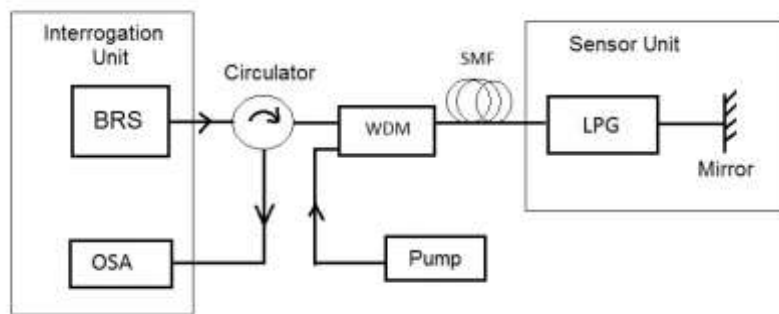


**Figure 115 - Co-propagating Raman amplifier remote LPG system.**

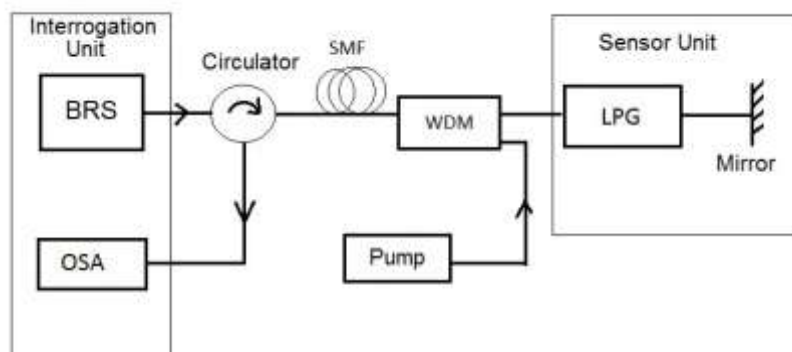


**Figure 116 - Counter-propagating Raman amplifier remote LPG system.**

Note that Figure 116 differs from Figure 115 due to the pump laser placed now at the fiber end. So, the pump wave will propagate to the opposite direction from the optical source signal.

The setup depicted at Figure 117 deploys two optical fibers that provide an additional path between the optical source and the sensor unit, allowing the detection of the reflected signal from the LPG sensor under lower noise levels. The power splitter (splitter X:Y) is responsible for dividing the pump power between the two

optical paths. So, this configuration allows the use of regular components and part of the Raman amplification into the broadband signal and the other part to amplify the processed signal delivered by the sensor head. One means no interference between the BRS and the reflected sensor signal.

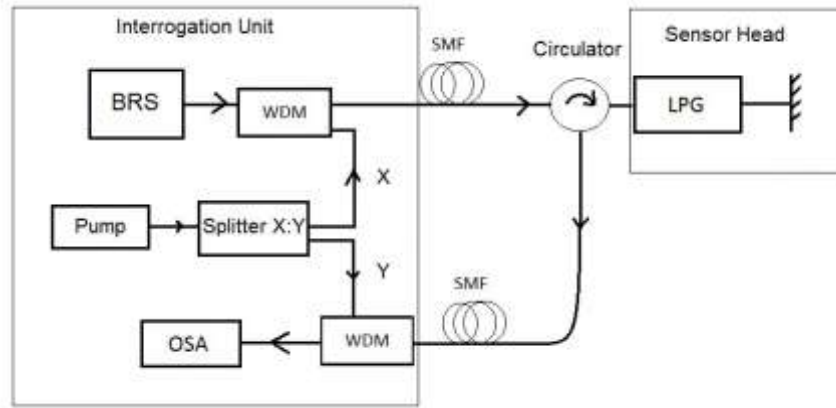


**Figure 117 - Raman amplifier remote LPG system using two optical fibers.**

As the reflected signal intensity, obtained from the sensor head in these setups, is not known *a priori*, the boundary conditions need to be set in order to compute such optical powers. The reflected signal intensity ( $P_S^{reflected}$ ) depends on the sensor head transfer function. The Raman pump power laser is also an input parameter. A method to calculate the Raman amplification and include the transmitted and reflected powers in the sensor system based in diffraction gratings was developed and consists of three steps, given as follow:

- i. As a first step, it is defined the initial and boundary conditions, where the intensity of the reflected signal ( $P_S^{reflected}$ ) and the reflected pump ( $P_P^{reflected}$ ) at the optical fiber output are null, and the signal intensity ( $P_S$ ) and pump power ( $P_P$ ) are input parameters given by the signal input and by the Raman pump laser, respectively;
- ii. After completing the first step, the reflected signal can be calculated using the reflection characteristics of the sensor head;
- iii. Finally, the first step is repeated, but now  $P_S^{reflected}$  at the fiber end is identical to the value obtained in step ii). Now, the signal reflected by the LPG that arrives at the OSA can be calculated.

Notice that the estimations performed by step *i*. provide a good approximated solution for the boundary conditions. It happens because in low power signal systems the depletion of the pumps by the signals can be neglected [155]. The pumps depletion occurs due to interactions among pumps in multi-pump schemes.

Numerical simulations and experimental work were considered in the analysis. The implemented numerical routines have been validated by measurements in the laboratory, that enabled a careful analysis of the three main configurations of remote optical fiber sensors proposed here (Figure 115 to Figure 117). Further numerical simulations generated results that allowed choosing the best remote fiber sensor setup.

#### 7.4.2 Validation of the Numerical Modeling Results

Simulations were validated with experimental results obtained for an optical fiber sensor system, with only one fiber and one LPG, as shown in Figure 116, which considers a counter-propagating pump scheme. Figure 118 shows the comparison between the model results (line) and the measured data (symbols) for a remote optical fiber sensor system with 50 km of fiber length.

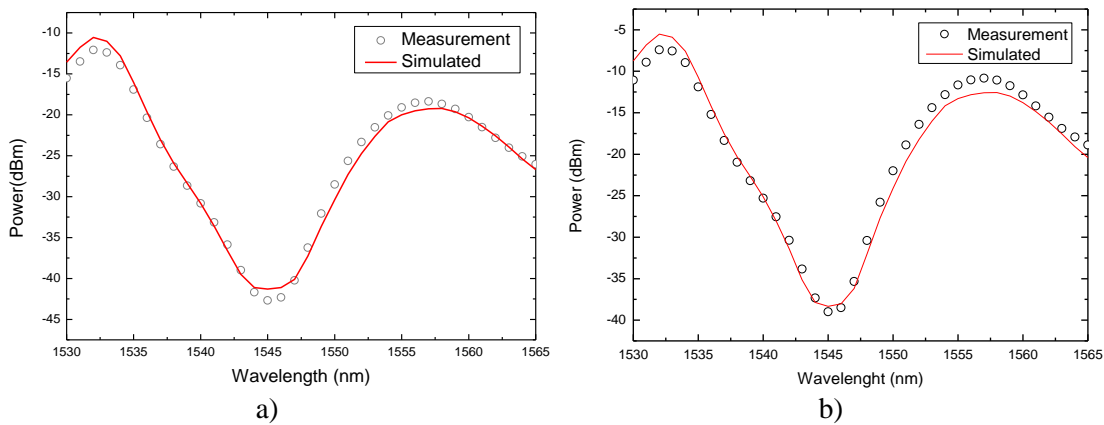


**Figure 118 - Experimental (symbols) and simulated optical spectrum (straight line) for a pump power of (a) 800 mW and (b) 1 W.**

Pump powers of 800 mW and 1 W were coupled to the fiber sensor, whose results are shown, respectively, in Figure 118 (a) and Figure 118 (b) with a pump wavelength of 1455.1 nm. Simulated and measured results show a good agreement. The higher deviation observed is  $\sim 1.5$  dB and occurs around 1557 nm when pump power of 1 W



is applied. The higher deviation observed to the lower pump power, i.e. 800 mW, is reduced and corresponds to ~1 dB.

The  $C_{R\mu\nu}$  considered in the calculations is a standard value for a singlemode type SMF-28 fiber, which is not the measured value to the singlemode fiber used in the experiments. The higher deviation between measured and simulated results for higher pumps can be attributed to this difference. Moreover, the Raman amplification is proportional to the  $C_{R\mu\nu}$  parameter or to the Raman gain efficiency between the signal at frequency  $\nu$  and the laser pump at frequency  $\mu$ , as observed in equation (7.2). Note that the pump power is multiplied by  $C_{R\mu\nu}$ .

So, the deviation observed around 1557 nm can be attributed to the  $C_{R\mu\nu}$  value difference, that is higher in this wavelength since the Raman gain peak occurs approximately 100 nm above 1455.1 nm, i.e. the Raman pump laser wavelength. As the pump power increases, this deviation is also accentuated due to the increase into the  $C_{R\mu\nu}(P_\mu)$  factor.

Therefore, these results validate the numerical model, so it can be applied in the different setups to analyze the performance of sensing systems of the type considered above.

### 7.4.3 Numerical Analysis

Numerical modeling was applied in the analysis for an appropriate choice of the best setup to be used in a remote sensing system to measure environmental temperature. Figure 119 shows some of the results obtained.

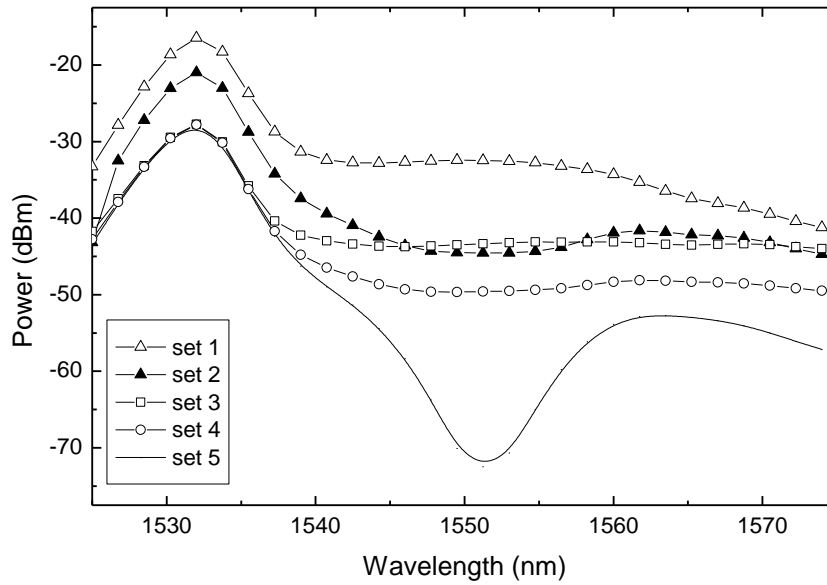


**Figure 119 - Optical spectrum at the receiver for the different setups calculated by the numerical modeling.**

In the first amplification configuration analyzed (set 1: Raman amplification in one fiber + co-propagating), with a single channel and co-propagating pump scheme, the spectrum of the LPG vanishes due to the presence of Rayleigh and ASE noise, that are higher than the signal intensity in the LPG resonance wavelength. The signal at the receiver is too weak to be detected.

The second amplification configuration (set 2: Raman amplification in one fiber + counter-propagating) considers one fiber span pumped by a Raman pump laser set in a counter-propagating scheme. Despite the lower signal gain, this configuration is more advantageous than the previous one, due to the lower noise figure and higher signal-to-noise ratio, as occurs in telecommunications systems. However, this configuration for some applications is not the best choice, since the pumps will be placed near to the sensor location and most of the times these locations are remote and of difficult access.

In the setup with two optical fibers and an optical power splitter (set 3: Raman amplification in two fibers and splitter, with a split ratio of 0:100), the amplification only occurs in the return fiber. In that case the signal arrives on the LPG with residual intensity, so the ASE noise due to amplification causes the resonance peak to vanish.

The case with two optical fibers and a 3-dB optical power splitter (set 4: Raman amplification in two fibers and splitter, with a split ratio of 50:50), the LPG resonance is slightly observed, although with a poor definition. It means an improvement in the spectrum response detection, but not with a resolution that allows the measure with good sensitivity.

The case with two optical fibers and the optical power splitter in the 100:0 position (set 5: Raman amplification in two fibers and splitter, with a split ratio of 100:0) presents the lowest power received, but the resolution of the resonance wavelength is the best observed. So, if the photodetector in the system has a sensitivity that can read this power levels, this setup is the best choice in terms of measurement sensitivity. Therefore, this setup was chosen for practical implementation. The setup with one fiber (set 1) was also implemented to be compared to the other four configurations.

#### 7.4.4 Experimental Analysis

After performing numerical simulations, which allowed the analysis and selection of the best setup, experimental evaluation of temperature sensing was developed. It is important to notice that refractive index measurement is also possible, by including small changes in the LPG sensor head, which means adding liquid samples to be analyzed.

Two remote optical fiber sensor systems were set with a broadband source (BRS) illuminating the temperature sensor, based on a mirrored LPG, placed 50 km away from the interrogation unit. A silver mirror spliced at the end of the grating permits the system to work in reflection and is responsible for the light signal traveling two times on the LPG. It increases the sensitivity of the sensing system. The measured mirrored LPG transfer function is shown in Figure 120. The resonance wavelength is placed around 1543.5 nm for 300 K. The LPG has been written in a single mode fiber (SMF-28) with a modulation period of 392  $\mu\text{m}$ . The presence of the silver mirror at the end of the grating is responsible by an asymmetry, around 2 dB, between the right and the left side of the grating.

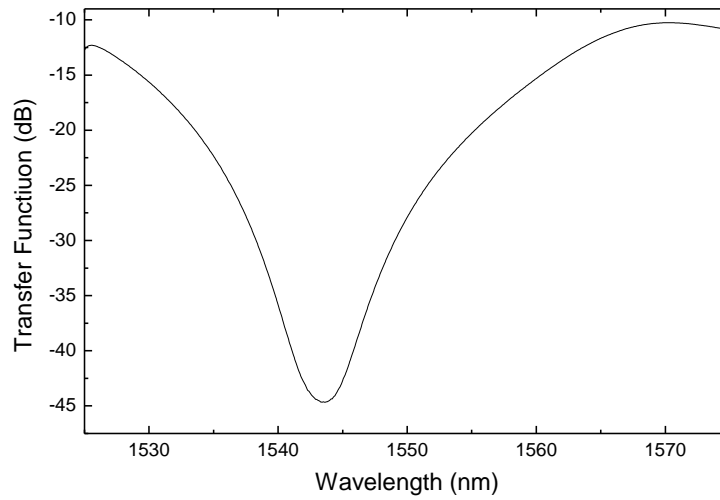


**Figure 120 - Mirrored LPG transfer function measured at 300 K written in a single mode fiber (SMF 28).**

The first setup is simpler and presents only one optical fiber, as observed in Figure 121 (a), while the second uses two optical fiber spans, as can be seen in Figure 121 (b), that is analogous to the scheme presented by [156].

The interrogation unit is formed by two FBGs, whose central wavelengths are respectively positioned just above ( $\lambda_1$ ) and below ( $\lambda_2$ ) the LPG resonance depth. Piezoelectric actuators (PZTs) are responsible for the electrical frequency modulation of the FBGs reflection spectrum. An electrical spectrum analyzer (ESA) was used to measure the amplitude power at the modulation frequencies of each FBG ( $f_1$  and  $f_2$ ) induced by the modulated PZTs and the temperature measurement was accomplished by a processing technique that relies in the analysis of the amplitude of the electrical powers which correspond to the PZTs modulations of  $\lambda_1$  and  $\lambda_2$ . Using the electrical dynamic interrogation approach, described in chapter 6, instead of the standard optical interrogation methods [52, 131, 157], a more effective cost solution was achieved with the benefit that the system operates in a frequency range far from the  $1/f$  noise region, which means the signal-to-noise ratio can be favored by the reduction of the noise level.

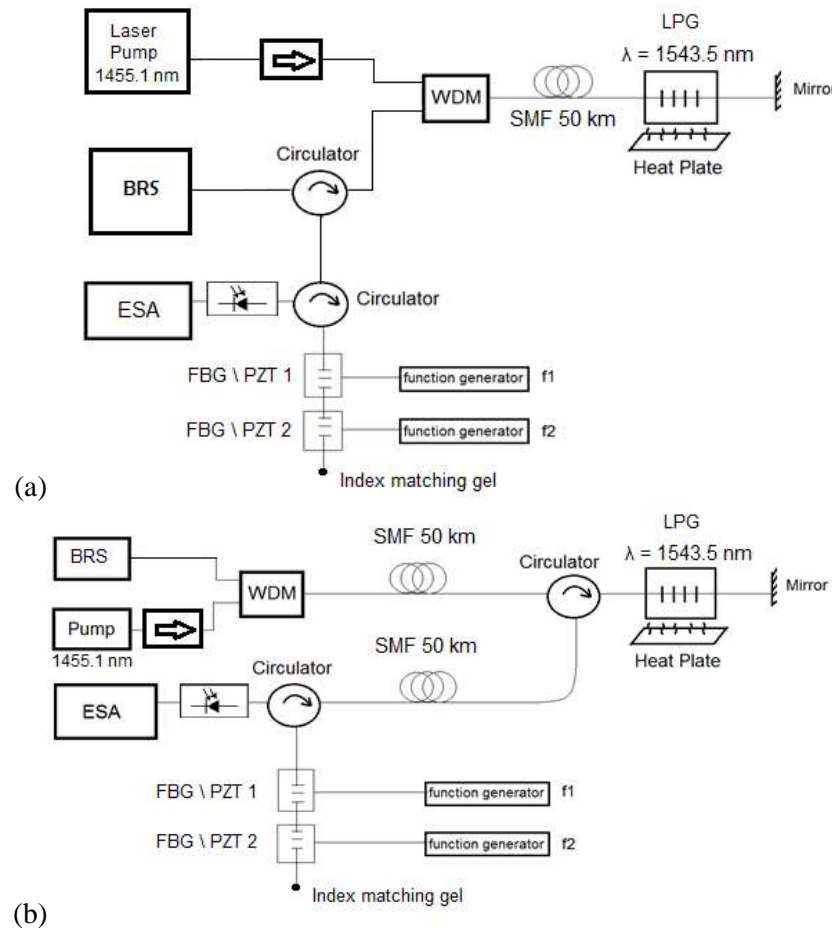


**Figure 121 - (a) Remote temperature optical fiber sensor system with one optical fiber and a co-propagating pump setup. (b) Remote temperature optical fiber sensor system with two optical fibers and the total pump power coupled to the feed optical fiber.**

The LPG resonance wavelength shift measurement is carried out by a ratiometric technique [142], applied to the signals derived from each FBG reflection in the interrogation system placed in the reception. The parameter  $P_{proc}$  is defined as

$$P_{proc} = \frac{P_1 - P_2}{P_1 + P_2} \quad (7.4)$$

where  $P_1$  and  $P_2$  are the optical powers reflected by the first and the second FBG, respectively, placed above and below the LPG resonance wavelength, modulated by the PZTs in the electrical frequencies  $f_1$  and  $f_2$ , respectively.

Figure 121 (a) shows the setup of the remote sensor system with one optical fiber, in this case a 50 km standard single mode optical fiber (SMF). Raman amplification is

provided by a pump laser with emission at 1455.1 nm, with 1.5 W coupled to the SMF through a WDM coupler.

The optical channel shared by the broadband signal and the signal processed by the optical sensor is affected by distortions caused by the Rayleigh noise and the amplified spontaneous emission (ASE) observed in the SMF and resulting from the pump laser. As a consequence, the LPG resonance depth disappears in the presence of the noise, as is shown in Figure 122.

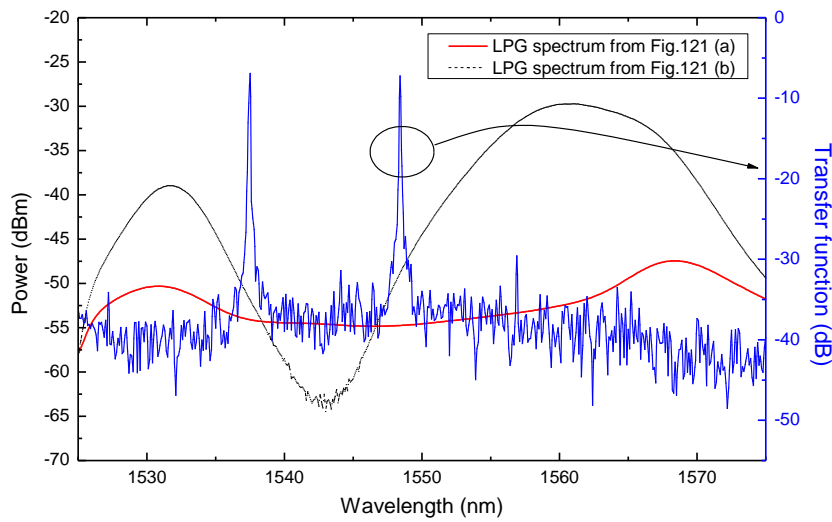


**Figure 122 - Spectrum of the signal processed by the LPG with resonance wavelength at 1544 nm measured at the input port of the interrogation unit for the two setups; it is also shown the transfer function of the FBGs at the interrogation unit.**

A simple way to increase the signal reflected by the sensor head and to overcome these drawbacks relies in a system with two different fibers, shown in Figure 121 (b). The first optical path is used to couple the broadband signal to the sensor and also acts as the Raman gain medium, since the pump laser is emitting co-propagating light with the broadband signal into the fiber. The second optical path receives the optical signal processed by the LPG sensor head and delivers it to the interrogation unit.

The transmission of the optical signal along two separated optical paths reduces both the ASE noise and the backward Rayleigh scattering in the return fiber, since these effects will be concentrated at the transmission channel and affect mainly the signals propagating from the sensor to the source.

The LPG works as the sensor element and is set at the SMF output. In this setup, the broadband signal used to feed the sensor head and the pumps are propagating together in the same single mode fiber. The LPG sensor head is placed in a metal surface that can be heated and maintained at a stabilized temperature, using a thermostat control circuit. The LPG with a period of 392  $\mu\text{m}$  is spliced to a fiber mirror that reflects part of the incident light. An optical isolator is positioned at the pump laser output to prevent back reflections. The number of pumps was chosen adequately to provide gain over the spectral response of the optical sensor and to compensate the losses over a fiber span of 50 km. In this case, just one pump laser was used. The spectral response of the sensor was measured with the dynamic interrogation approach described above.

Figure 122 shows the power spectrum measured at the input port of the interrogation unit for both schemes of Figure 121. The setup with only one optical channel presents poor resolution, since this scheme has an higher noise figure, due to the Rayleigh backscattering and ASE concentrated in only one fiber. Therefore, the resonance wavelength in this setup vanishes in the presence of the noise, as the previous simulations predicted in Figure 119.

As can be seen in Figure 122, the LPG spectrum received at the interrogation unit is unusual, i.e., the right side of the spectrum around 1561.0 nm shows higher amplification. Although it can appear not conventional, the measured spectrum is a result of the characteristics of the Raman amplification, due to the continuous wave (CW) high power laser pump centered at 1455.1 nm available in the laboratory. It should be noted that the Raman gain peak is around 106 nm far away from the pump laser wavelength.

The LPG temperature sensitivity is around 0.13 nm/ $^{\circ}\text{C}$ , which is similar to the one encountered in typical LPG sensors and one order greater than the typical value for FBG sensors [158]. The change in temperature shifts the resonance wavelength incrementally toward longer wavelengths. Therefore, the interrogation unit using the ratiometric technique can read this wavelength shifts and interpret these changes as temperature variations.

Piezoelectric actuators (PZTs) are responsible for the electrical frequency modulation of the power reflected by the FBGs. The spectral response of the sensor was measured at the interrogation unit composed by two FBGs, centered at 1537.5 nm and 1548.4 nm, respectively, and modulated by PZT<sub>1</sub> and PZT<sub>2</sub>. These PZTs are activated by two different function generators, set at frequencies  $f_1$  (756.6 Hz) and  $f_2$  (600.6 Hz), respectively. So, an electrical spectrum analyzer (ESA) can be used to measure power at these frequencies. The advantage of using an interrogation setup with electrical measurement instead of optical techniques is the better spectral resolution and the lower cost in comparison with optical interrogation methods [62].

Figure 123 shows the electrical spectra received at the ESA in the remote optical fiber sensor using Raman amplification due to a laser pump with power equal to 1.5 W, centered at 1455.1 nm. The power reflected by the first FBG ( $P_1$ ) was modulated with  $f_1$  and the power reflected by the second FBG ( $P_2$ ) was modulated with  $f_2$ . Notice that without the Distributed Raman Amplification, these electrical peaks ( $P_1$  and  $P_2$ ) generated by the modulation of the FBGs are vanished, so the electrical interrogation is not suitable anymore.

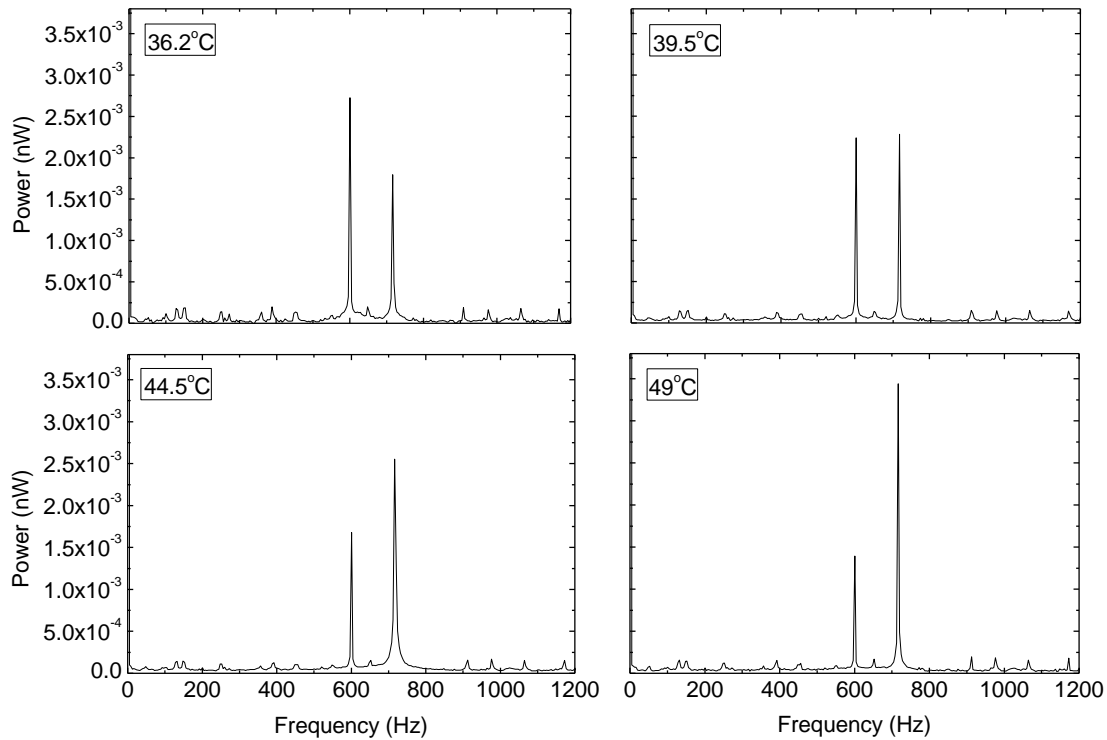


**Figure 123 - Electrical power spectrum of the signal received at the ESA for the temperatures of 36.2 °C, 39.5 °C, 44.50 °C and 49.00 °C, respectively.**



The relationship between the temperature and the parameter  $P_{proc}$ , derived from the measurements performed by the ESA and shown in Figure 123, is depicted in Figure 124. A linear relationship can be observed between temperature measured 50 km away and the output processed signal.

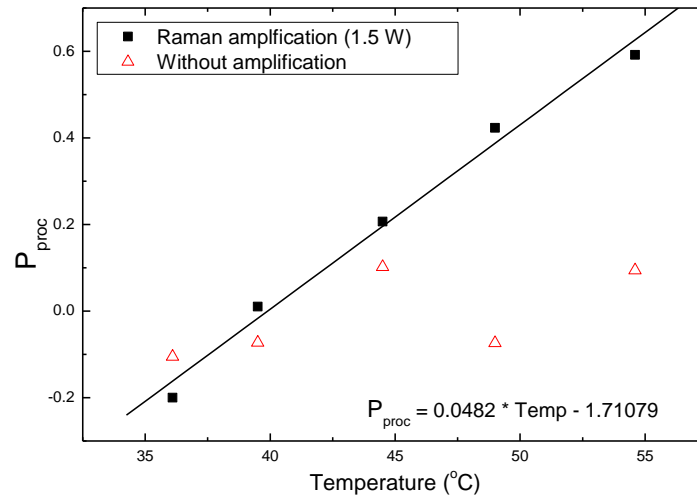


**Figure 124 -  $P_{proc}$  parameter as a function of temperature for the setup depicted in Figure 121 (b) (laser pump at 1455.1 nm and launched power of 1.5 W).**

Without amplification the signal levels were too low and the amplitude modulated electrical frequencies of both FBGs were in the same level of the noise floor, degrading the sensor sensitivity. The Raman amplification is responsible for mitigating the attenuation of these signals and raising the level of the electrical power peaks, resulting in a temperature sensitivity of  $0.05\text{ }^{\circ}\text{C}^{-1}$ .

The maximum temperature measurement range is a function of the LPG bandwidth. As it increases, it enables a larger measurement range, surely with the penalty of a reduced sensitivity due to the decreasing of the linear slope in the LPG optical spectrum. Also, the LPG depth strongly affects the electrical interrogation sensitivity. Therefore, a compromise is observed among sensitivity and measurement range. An evaluation of Raman amplification on the optimal sensing system dramatically improves the resolution of the electrical interrogation technique when the noise levels of the systems are mitigated. The measurement range shown in Figure 124 can be

increased if the device used to control the temperature enables temperature reduction of the metallic plate where the grating is deployed.

## 7.5 Summary

An optical fiber sensing layout in which the sensing head (in this case, a LPG sensor) is seen in transmission by the optical source, but in reflection by the processing unit was demonstrated in section 7.2. The results obtained indicate that for a 20km lead fiber, the sensor modulated optical power that reaches the detector is ~8 dB higher than the value associated with the standard configuration, allowing the sensor readout when located far away. Insights about the potential of this new approach were presented considering other important merit factors that need to be addressed when dealing with specific sensor types, such as resonance plasmonic sensors.

In the study presented in section 7.3, a LPG was used in conjunction with an OTDR for remote refractive index measurement. A comparison between the system responses at the OTDR laser ranges of 1310nm and 1550nm was carried out. Moreover its behavior was also assessed with and without Erbium doped fiber amplification. The experimental results show that the first setup has a good performance and a resolution of  $1.5 \times 10^{-4}$  RIU was obtained without any kind of optimization. The obtained results show that the scheme presented is a simple, low cost solution for environmental remote monitoring. The multiplexing ability was also tested. Refractive index and temperature were measured with two different fiber gratings. The measured sensitivities were 106 dB/RIU and 0.06 dB/°C respectively and resolutions of  $3 \times 10^{-4}$  and 0.16 °C were estimated. The presented configurations show high potential for remote sensing, with multiplexing capability, allowing the possibility of multiparameter or quasi-distributed sensing for environmental purposes.

The work presented in section 7.4 addressed the importance of optical amplification in the operation of optical fiber sensors for remote sensing, showing the relevance of Raman amplification to increase the sensing distances and realize environmental monitoring in distances of several kilometers. This technology allows the use of the

same infrastructure of the optical fiber system using the SMF optical fiber as a gain medium. The scalability of the gain bandwidth can be optimized by changing the number and characteristics of the pump lasers. The flexibility and possibility of incorporating optical sensors directly in already installed systems, strongly suggests that Raman amplification can be considered the best choice for remote optical fiber systems, mainly when sensor multiplexing is considered due to the tuning capability of the Raman gain bandwidth. A numerical model was developed in this work that permits us to analyze the performance of the remote optical fiber sensor system based on diffraction gratings, mainly LPGs and FBGs. It was based on the differential equations that describe spatial propagation and interaction between signal and pumps. The model succeed to predict the LPG response and permits us to consider the best setup to be used to perform the remote measurement with the best resolution on the LPG wavelength. Different setup configurations can be analyzed with the developed model. In particular, a remote (50 km) optical fiber system for environmental temperature measurement was demonstrated. An electrical interrogation unit was used, providing operational performance at a reduced cost.



## **Chapter 8 – Conclusions and further work**

---

Optical sensing, more specifically fiber based sensing heads and the interrogation techniques developed to understand what is happening in the sensing medium are nowadays a hot topic of research, looking for developments suitable for specific applications in a variety of fields. A brief overview on this thesis content, the contributions achieved within its topics and the actual contextualization of such work was given in Chapter 1.

Chapter 2 presented a general state of the art in the optical fiber sensors area, with particular emphasis in the technologies that were involved in the developments presented in the further chapters.

Chapter 3 highlighted a few developments related with microstructured fibers. Achievements in coupling light and splicing special types of fibers were described. Further sensing capabilities, with the inscription of fiber Bragg gratings, long period gratings and rocking filters in microstructured fibers were carried out. The standard types of fibers gratings studied will continue to find adequate sensing applications once new designs of microstructured optical fibers provide new opportunities that bring them up to date.

The state of the art in optical fiber sensors for gas detection and an optical fiber sensing system for detecting low-levels of methane was developed and presented in Chapter 4. The properties of hollow-core photonic crystal fibers were explored to create a sensing head with favourable characteristics for gas sensing, particularly in what concerns intrinsic readout sensitivity and gas diffusion time in the sensing structure. The sensor interrogation was performed by applying the wavelength modulation spectroscopy technique and the results in terms of the system resolution were improved using a new optical sensing head. The research involved in the developments and achievements described in Chapter 4 will allow improved investigation and appropriate technology development for constructing versatile

prototypes, able to discriminate and measure simultaneously environmental gaseous parameters, of different gas species, using multi-point and/or distributed interrogation systems. Underlying this general direction is the purpose of combining with advantage for the development of science and technology, area of optical fiber sensors with the emerging concepts of biochemistry, biotechnology and biosensors.

Chapter 5 explains how modal interferometry can be used with different kinds of microstructured fibers to sense strain, temperature, curvature and torsion. Multimode interference sensing presents also interesting solutions, because they can be easily fabricated and applied in different situations. Though, multiplexing multimode interference sensors for refractive index measurement is still a challenge and this topic will certainly be object of intense research in the near future.

The principle of operation of a new concept for measuring quasi-static parameters, the electrical dynamic interrogation, was shown in Chapter 6. The analysis of the detected first harmonic generated by the electrical modulation of fiber gratings, allows generating a signal proportional to the LPG spectral shift and resilient to optical power fluctuations along the system. This concept permits the attenuation of the effect of the  $1/f$  noise of the photodetection, amplification and processing electronics on the sensing head resolution. A variation of this technique, using modulated distributed feedback lasers, was also employed in a multiplexing sensing scheme for refractive index measurements. The dynamical electrical interrogation concept will certainly find an interesting niche for environmental sensing applications. The advantages of this technique have to be combined with adequate signal processing techniques in order to achieve higher resolution measurements, which will be a topic of intense research in the near future. This interrogation method can be applied not only to LPGs but also to other band rejection filters based or not in microstructured fibers used for the measurement of DC or quasi-DC measurands, like multimode interferometers and surface plasmonic resonance devices.

Finally, Chapter 7 presented three different optical fiber based configurations for remote sensing of physical parameters. First, an *in situ* optical source for remote detection of refractive index variations was presented. Further an OTDR based scheme was also used to perform refractive index interrogation. By last a Raman

amplified system was numerically simulated and experimentally tested for remote detection of temperature.





## Appendix 1

---

### **Methane Detection with Non-PCF Based Solutions**

As observed in section 4.4.2, the presence of a deleterious phenomenon associated with intermodal interferences effects that unfortunately will reduce the signal-to-noise ratio was noticed. Open path gas cells were tested together with the developed interrogation system, in order to understand if a better signal-to-noise ratio would be obtained, leading to a lower methane detection limit.

### **Methane Measurements with the U-bench**

Using the U-bench, a sensing head with 30 mm of open path, presented in Figure 125, inside the gas chamber of the optoelectronic system described in section 4.3.1, was tested.

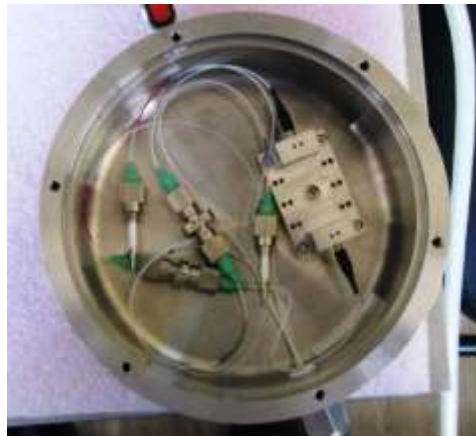


**Figure 125 - Detail of the U-bench, for methane measurements, inside the gas chamber.**

This sensing head behavior was characterized in transmission, as depicted in Figure 126.

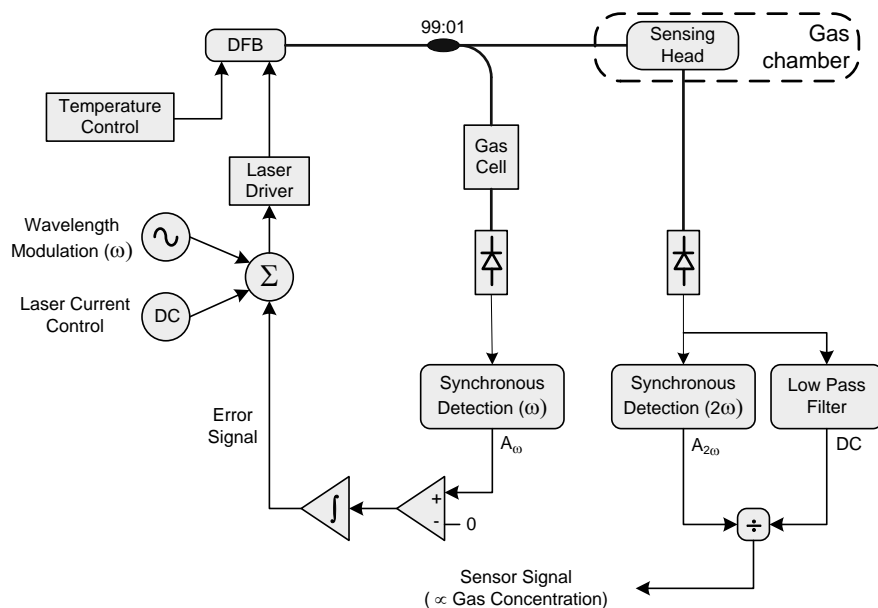


**Figure 126 - Experimental setup of the detection scheme using the U-bench as a sensing head.**

The experimental results obtained for the second harmonic amplitude, which is directly proportional to methane concentration, are shown in Figure 127.

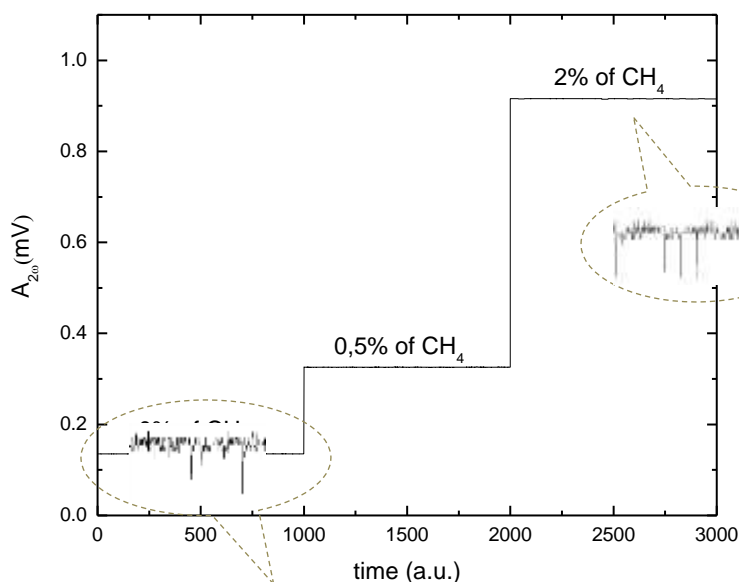


**Figure 127 - System response for three methane concentration changes.**

From Figure 127 a linear S/N value of 3041 was obtained, giving rise to a SNR of 69.7 dB. Thus, for the sensing head with 30 mm tested in transmission, a value of

7 ppm was reached, which is the methane detection limit for the U-bench sensing head.

### **Methane Measurements with a Developed Open-Path Gas-Cell**

Another non-PCF-based solution for the sensing head was evaluated as well. This alternative solution was based on a reflective open-path gas-cell with a GRIN lens on one side and a mirror on the other side. It was designed to be robust and compact, in order to be used in real field applications and at the same time a ppm-sized resolution was targeted.



**Figure 128 - Graphical representation of the open path gas cell and expanded view revealing the different components of which it is made up.**

The reflective open-path gas-cell was placed inside the gas chamber (Figure 129) and connected to the detection scheme as depicted in Figure 130.

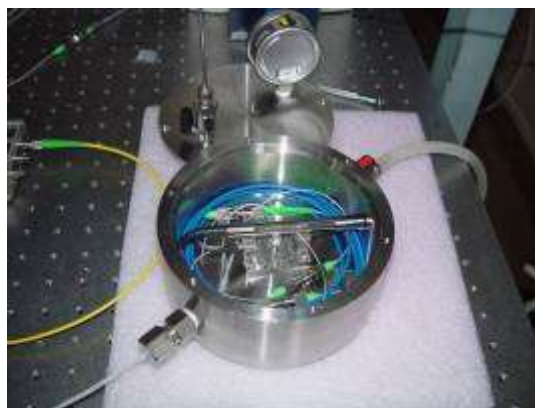


**Figure 129 - Detail of 80 mm open path sensing head inside the gas chamber.**

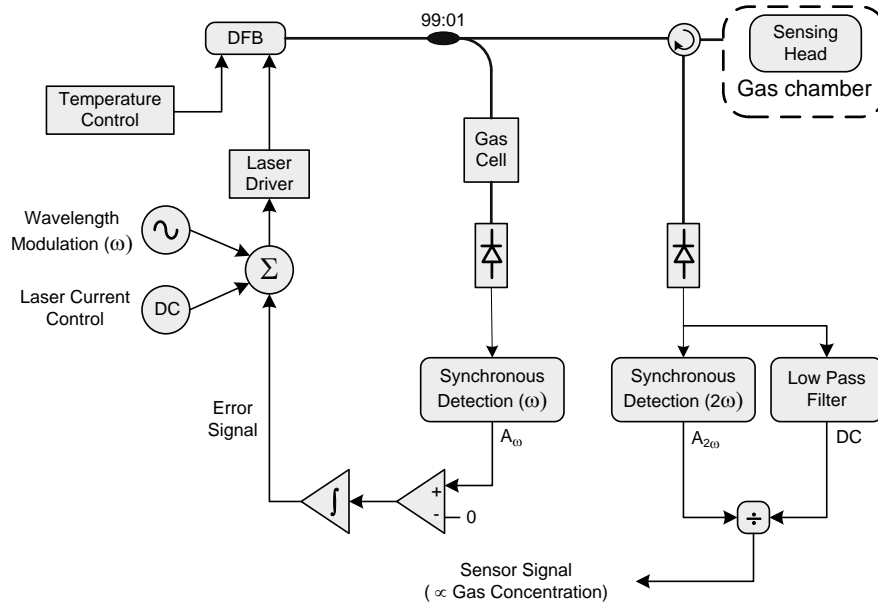


**Figure 130 - Experimental setup of the detection scheme using the developed reflective open-path gas-cell.**

The experimental result obtained for the behaviour of the second harmonic amplitude, which is directly proportional to the gas concentration, using the open-path reflective gas cell is shown in Figure 131.

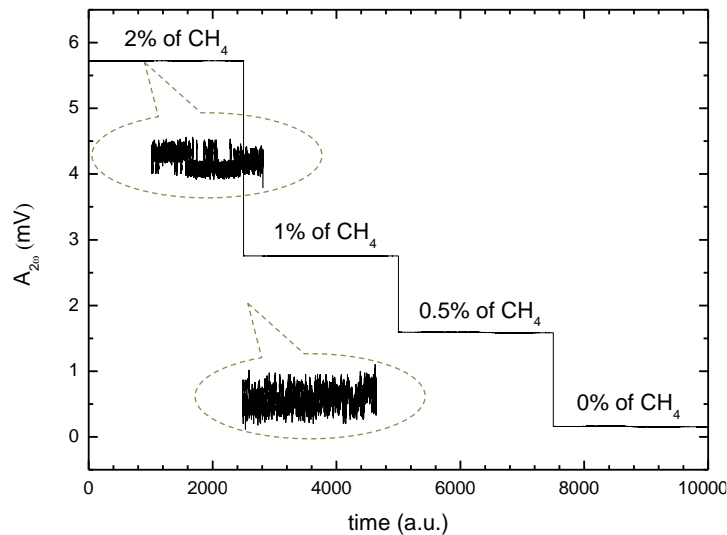


**Figure 131 - Measured amplitude of the second harmonic for four different methane concentrations.**

Once more, the sensitivity of the system is determined by the voltage change per change of gas concentration that, for the open-path gas-cell of 8 cm operating in

reflection, gives rise to a 4 ppm methane detection limit, which is a quite satisfactory result.

As could be seen in both experiments, the signal remains very stable during the periods of constant gas concentrations. This is an indication that the developed detection system has a high repeatability.



## Appendix 2

---

### **Interferometric Optical Fiber Inclinometer with Dynamic FBG Based Interrogation**

This work aims to achieve an interferometric optical inclinometer sensor for application in the electric power industry. The earliest application of optical fiber sensors in such context dates probably from 1977, where electric current measurement using optical fiber sensors was reported [159, 160]. More recently, loading of power transmission lines, winding temperature of electrical power transformers, and large electrical currents have been measured with FBG based sensors [160].

The goal is to analyze the possibility of using an optical inclinometer to measure the bending angle of the catenary of high voltage transmission cables as they are subject to overcurrent. Tilt sensors (also known as inclinometers) are required for measuring the angular deflection of an object against a reference plane or line. They are frequently used in the field of aviation (e.g., monitoring the aircraft landing) and civil engineering (e.g., monitoring the inclination of towers and bridge holders) [161]. They can also be applied to platform leveling, boom angle indication, slope angle measurement, etc. Most conventional tilt sensors are realized by transforming the inclination into electric signals through a magnetic effect [162, 163] or capacitive effect [164]. A significant number of optical inclinometers reported so far are based on fiber Bragg gratings (FBGs) coupled to a vertical pendulum. The sensor proposed here is based on a tapered fiber Michelson interferometer. A preliminary study of the inclinometer spectral behavior is assessed through experimental measurements and its computational analysis, aiming to characterize and improve the sensor response. An electric interrogation technique was tested, that is based on modulation at different electrical frequencies, of the Bragg wavelengths of two FBGs, spectrally located in strategic points of the interference pattern, and detection of the amplitude at these frequencies of the signals reflected by the FBGs. These amplitudes are proportional to the slopes of the fiber-taper Michelson interferometer spectral response at the FBG

wavelengths, which change with the relative amplitude changes of the interferometer and FBGs modulation movements. This processing allows the generation of a signal proportional to the interferometer visibility or wavelength shifts and is immune to optical power fluctuations along the system. The performance of this technique was tested for measurement of small angle variations. Preliminary results obtained with this interrogation technique are reported.

## Principle and Discussion

Michelson interferometers based in tapered optical fibers have been intensively studied in recent years. This device is used as a sensor to measure a multitude of physical parameters as temperature, refractive index and tilt [165]. In this appendix it is discussed the use of this kind of interferometer as an optical inclinometer, with the intention to analyze the possibility of its use to measure catenary bending in power systems cables which suffer elongation due to overcurrent as well as other applications in the power system industry. The fiber-taper Michelson interferometer, shown in Figure 132, consists of a section of the fiber between a taper, i.e., a small region of the fiber with the cladding diameter reduced, and its cleaved end. The taper couples a fraction of the core light to the cladding modes which are propagating along the cavity, until the tip end. Then they are reflected by the cleaved end, which acts as a partial mirror (4% reflection coefficient due to Fresnel reflection on a glass-air interface), and coupled back on the taper.

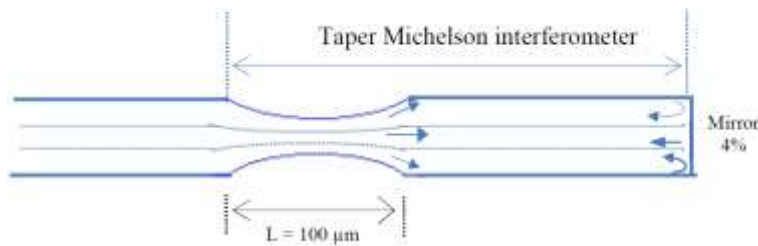


**Figure 132 - Schematic representation of the fiber-taper Michelson interferometer**

The phase difference between the cladding mode ( $LP_{nm}$ ) and the core mode ( $LP_{01}$ ) traveling in the taper length  $L$  is approximately expressed as,



$$\Delta\phi = \frac{4\pi\Delta n_{nm}L}{\lambda} \quad (\text{A2.1})$$

where  $\Delta n_{nm}$  is the effective refractive index difference between the two modes and  $\lambda$  is the wavelength of the traveling light. When the axis of the taper of the Michelson interferometer is bended the effective length of the taper is varied, resulting in phase and amplitude variations between the fundamental and cladding modes. This kind of inclinometer presents some advantages such as its ease of fabrication by the arc-discharge technique, operation in a reflective mode (allowing remote interrogation) and possibility of miniaturization and compactness.

There are some methods to fabricate tapers on fiber such as flame [166, 167], a focused CO<sub>2</sub> laser beam [168, 169], a micro furnace and an electronic arc formed between a pair of electrodes, such as a in fusion splicer [165]. The fabricated fiber-taper was done through a built-in program in a standard fusion splicer. The length of the taper was configured to be 100  $\mu\text{m}$ . After some preliminary tests the sensor selected for testing had an interferometer length of about 21 cm. Figure 133 presents the spectrum of the signal received from this interferometer, obtained with a broadband source illumination and detection with an optical spectrum analyzer.

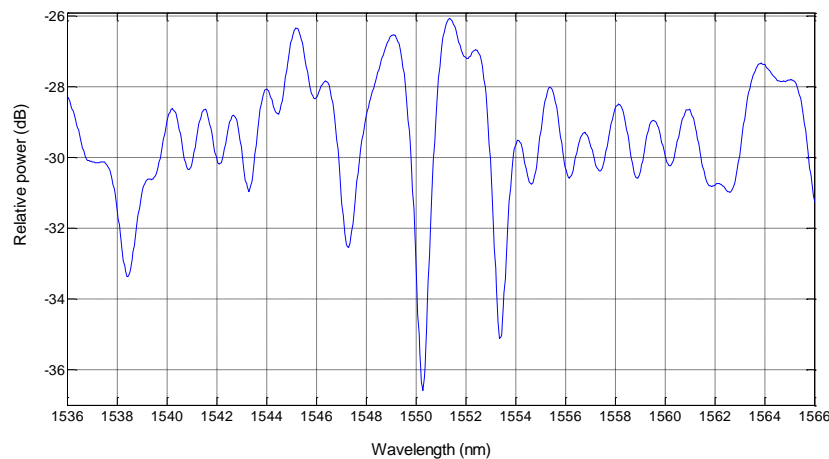


**Figure 133 - Optical spectrum of the optical inclinometer based on tapered optical fiber and a 21 cm cavity length (obtained at zero tilt angle).**

The first analysis of the optical inclinometer was performed using an optical spectrum analyzer (OSA) and acquiring the data to observe the behavior of the

interference fringes as the tilt angle was varied in the range from 1 to 15 degrees, with steps of 1 degree. The sensor response was then analyzed in terms of fringe visibility and peak spectral position. The fringe visibility refers to the contrast between a peak and a valley of an interference fringe. The fringe chosen for closer analysis was the one with greater visibility, which is located in the spectral range between 1548 nm and 1551 nm, as can be seen in the Figure 133. The fringe visibility,  $\nu$ , could be calculated using the following expression

$$\nu = \frac{I_{\max} - I_{\min}}{I_{\max} + I_{\min}} \quad (\text{A2.2})$$

where  $I_{\max}$  and  $I_{\min}$  are the maximum and minimum optical intensity of adjacent peaks and valleys of the interference fringe pattern, respectively. The results obtained for the visibility in the range studied can be observed in Figure 134 (a). Monitoring the spectral position of the interferometric peak was also performed in the same angular and spectral ranges and the results are shown in Figure 134 (b).

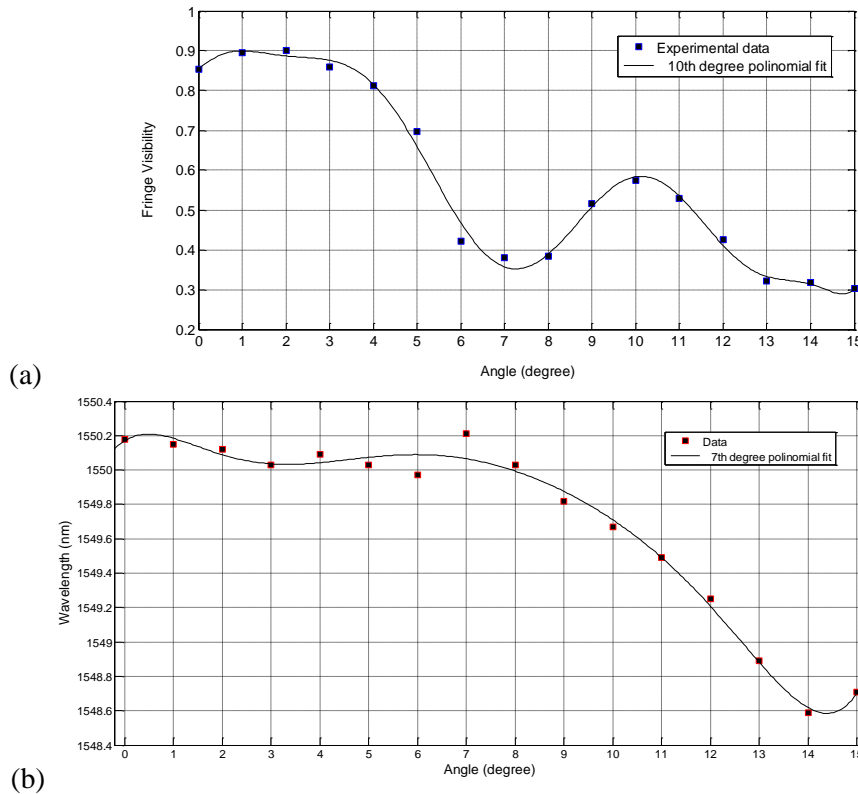


**Figure 134 - Behavior of the optical inclinometer for the angular range between 0 and 15 degrees with steps of 1 degree. (a) response of fringe visibility; (b) response of peak wavelength position.**

The results clearly show that the angular range with greater variation of visibility is found between 3 to 6 degrees. Therefore, a more detailed analysis was performed within this range making measurements with steps of 0.2 degrees. When using FBG based interrogation systems, the behavior of optical power intensity at different spectral positions can be analyzed and processed into a meaningful measurement. In this particular case two FBGs should be selected in spectral regions providing a response to angular changes with sensitivity and linearity as large as possible. In order to analyze the response of the inclinometer and choose the best positions for the interrogation FBGs, based in the aforementioned principles, numerical simulations were carried out using Matlab® software. With the developed software it was possible to simulate the response of the FBG interrogation system with the “virtual FBG” placed at any position of the spectrum. Using the least squares methods, the slope and correlation coefficient ( $R^2$ ) of the estimated linear fit for the sensor response was computed. The wavelength ranges presenting higher slope in consonance with a value of correlation coefficient of at least 0.9 ( $R^2 \geq 0.9$ ) were considered as appropriate for the spectral localization of the FBGs. In Figure 135 curves of the angular coefficient and  $R^2$  related to tilt variations between 3 and 6 degrees are shown. It can be seen that the best spectral locations for the FBGs are around 1549.2 nm and 1550.3 nm with values of  $R^2 = 0.994$  and  $R^2 = 0.982$ , respectively.

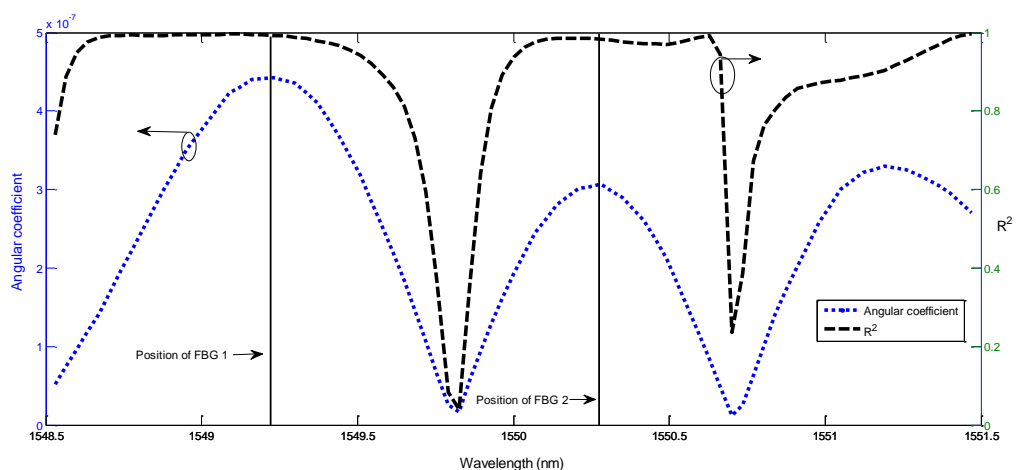


**Figure 135 - Plots of the angular coefficient and correlation coefficient ( $R^2$ ) referring to the changes observed in optical power as a function of wavelength obtained for tilt variations between 3 and 6 degrees. The wavelengths with higher sensitivity and linearity are 1549.2 nm ( $R^2 = 0.994$ ) and 1550.3 nm ( $R^2 = 0.982$ ) and are signaled by the vertical lines.**

Considering these optimum wavelengths the following operation was computed to obtain the sensor output response,

$$\text{Normalized output} = \frac{I_1 - I_2}{I_1 + I_2} \quad (\text{A2.3})$$

where  $I_1$  and  $I_2$  are the optical intensities reflected by FBG<sub>1</sub> and FBG<sub>2</sub>, respectively. It is interesting to note that the wavelength of 1551.3 nm could also have been chosen, since it presents an angular coefficient even greater and its  $R^2$  is satisfactory. However, since the sensor response is based on comparing of optical intensities between two spectral points, it is necessary to take into account the behavior of the fringes for the tilt range under consideration. For tilt angles within the range of 3 to 6 degrees, the main characteristic of the fringes is a variation of their visibility, as can be confirmed by comparison of Figure 134 (a) and (b). Therefore, in this particular case, the best response is achieved if one of the spectral points is located in the vicinity of a peak and the second one in a valley. Figure 136 shows the detailed spectral behavior of the fringe under study for tilt variations in the aforementioned range, and the optimized position for the FBGs signaled by vertical lines.

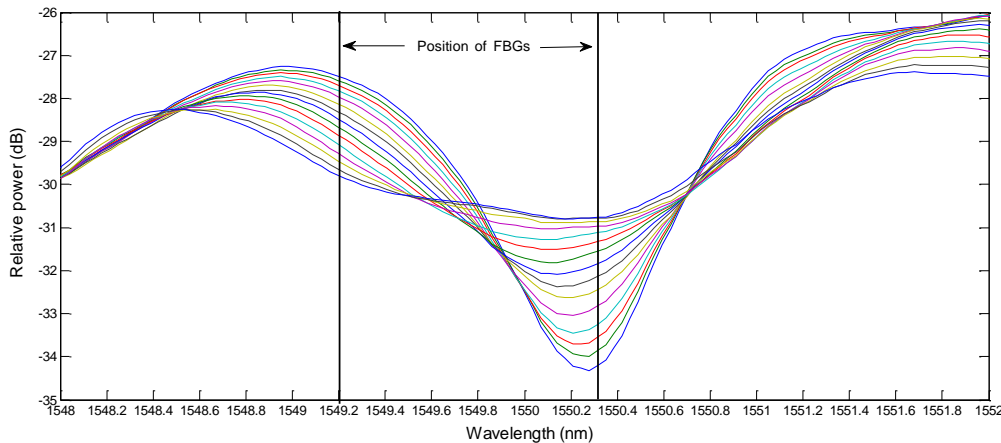


**Figure 136 - Interferometric fringes and spectral locations of the interrogation FBGs represented by vertical lines.**

Following this analysis for the selection of the FBGs, equation (A2.3) was used, considering these optimized spectral positions, to evaluate the sensor response. As can

be seen in the Figure 137 the optical inclinometer presents a good linear response within the range of 3.2 to 6 degrees.

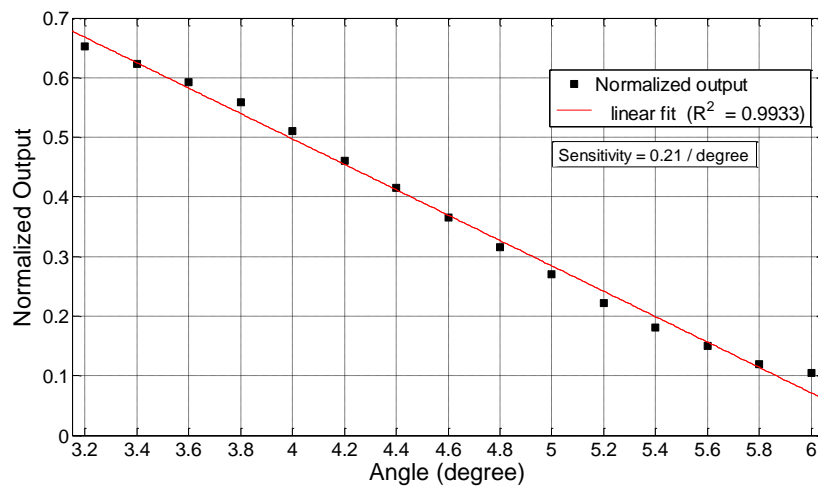


**Figure 137 - Normalized response of the sensor obtained through simulations.**

The angular range between 10 and 14 degrees was also analyzed. This angular range presents as its main characteristic a predominant wavelength shift of the spectral peak as can be seen in Figure 134 (b).

Similar criteria were used to select the FBG wavelength points for better performance. The spectral positions of the FBGs according to higher slope and correlation coefficient, were found to be 1549.6 nm and 1551.6 nm, with  $R^2 = 0.969$  and  $R^2 = 0.956$ , respectively. The response of the sensor was then calculated by equation **Error! Reference source not found.** within the range of 10 to 14 degrees. Figure 138 shows the curve of the sensor response for angular variation between 10 and 14 degrees. As can be noted, the sensor response presents a similar linearity and a better sensitivity (0.3 /degree) when compared with the previously studied angular range (0.21 /degree). Considering that the ratiometric technique allows for a small variation in visibility or wavelength shift to be measured, from this data it can be estimated that the sensor will be able to discriminate angular changes in the  $10^{-2}$  degree range.

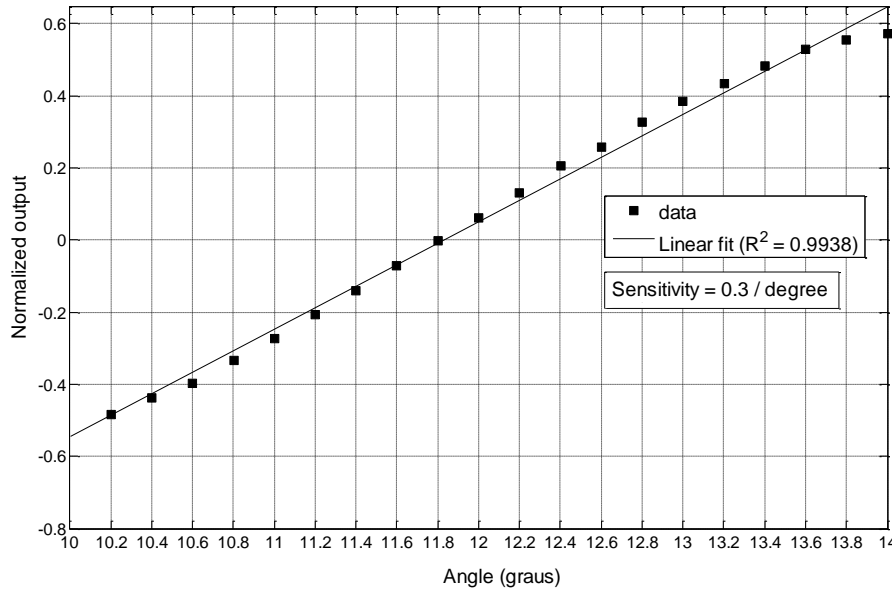


**Figure 138 - Normalized response of the inclinometer optical for the range of 10 to 14 degrees.**

Measurements by means of the dynamic interrogation technique described in chapter 5 were also performed. This approach can be an interesting low cost alternative to interrogate optical sensors in real systems. In this dynamic electrical interrogation approach  $P_{out}(\lambda) / P_0$  is not being monitored, i.e., it was not applied the standard DC reading approach consequently affected by low-frequency noise, which usually has a  $1 / f$  power spectral dependence. On the other hand, what is being monitored  $(dP_{out} / d\lambda) / P_0$ , i.e., the slope approach, which performs an interrogation that is compatible with a frequency range far from the  $1 / f$  noise region, which also means that the signal-to-noise ratio can eventually be favoured by the reduction of the noise level, eventually compensating, with advantage, the reduction in signal amplitude. The schematic diagram of the interrogation technique is showed in Figure 139.

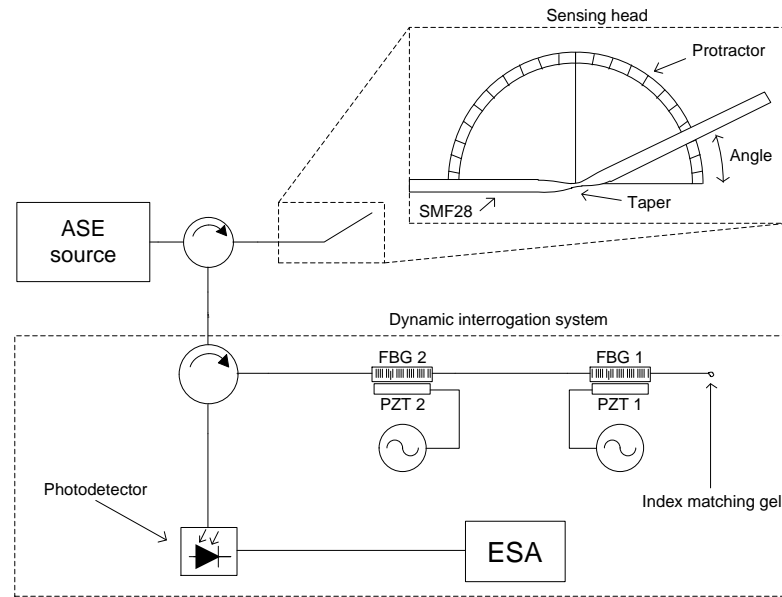


**Figure 139 - Setup of the interferometric optical fiber inclinometer with dynamic FBG based interrogation.**

A broadband source (ASE) was used to illuminate the sensor head. The light is reflected back in the cleaved tip of the interferometer and is injected again in the optical circulator, propagating towards the two interrogating fiber Bragg gratings (FBG<sub>1</sub> and FBG<sub>2</sub>). These FBGs are placed on piezoelectric transducers (PZT<sub>1</sub> and PZT<sub>2</sub>) driven by two independent signal generators at different frequencies. The optical signals are reflected from the electrically modulated FBGs and are injected into a photodiode for detection and conversion into an electrical signal. The detected electrical signal may be visualized by means of an electrical spectrum analyzer (ESA), where the signals coming from each grating can be identified by their corresponding modulation frequency. Then with the voltage values corresponding to each of the modulating frequencies the normalized sensor response can be obtained by computing

$$V_{proc} = \frac{V_1 - V_2}{V_1 + V_2} \quad (A2.4)$$

where  $V_1$  and  $V_2$  are the voltages corresponding to each of the modulating frequencies. In this particular experiment, FBG<sub>1</sub> and FBG<sub>2</sub> were modulated at frequencies of 1544 Hz and 1752 Hz, respectively.

Preliminary experiments were made with the electric interrogation technique. The experiments were carried out in the angular range between 3 and 6 degrees. The FBGs available at the time had wavelength peaks of 1549.5 nm and 1551.5 nm, which were not at the optimum calculated positions. Although the experiment was carried out with the FBGs deviated from their optimum spectral positions, the results obtained matched closely the results predicted by the simulations for the range of 3 to 6 degrees. Figure 140 shows the linear calibration curve obtained with the electrical interrogation setup demonstrating its viability (sensitivity of 0.35 /degree).

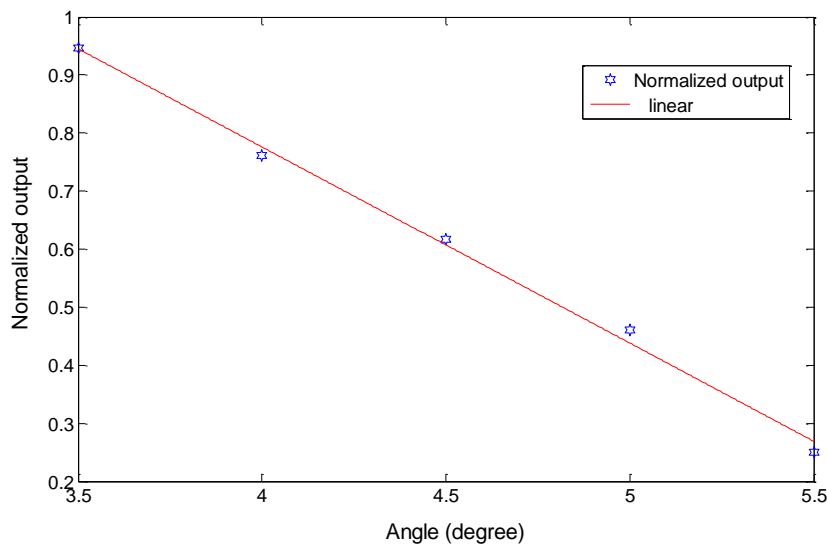


**Figure 140 - Normalized output of the electric interrogation system as a function of inclination angle of fiber-taper Michelson interferometer for 3.5 to 5.5 degrees.**

## Conclusions

An optimization study of an optical inclinometer based on a fiber-taper Michelson interferometer was presented. An evaluation by means of experimental measurements and numerical analysis of the experimental data was done. The numerical results indicated a sensor response with good sensitivity and linearity in the range of 3.2 to 6 degrees and 10 to 14 degrees. In the first range the predominant effect of tilting was a change in interferometric visibility. On the other hand, in the higher angular range, the predominant effect was a spectral shift of the fringe peak wavelengths. Both mechanisms are suitable for interrogation using spectral scanning or strategically placed FBGs, in a fashion that is independent of optical power fluctuations. A low cost strategy to interrogate the response of sensors using electrically modulated fiber



Bragg gratings, a photodetector and frequency analysis was described. Preliminary results were obtained with the electrical dynamic interrogation method showing good linearity and sensitivity in the range around 3.5 to 5.5 degrees. At this stage temperature was kept constant for simplification of the analysis. Further studies are underway to assess the possibility of compensating or simultaneously measure temperature and inclination. Also reproducibility, long term stability and packaging will be the subject of further experiments.

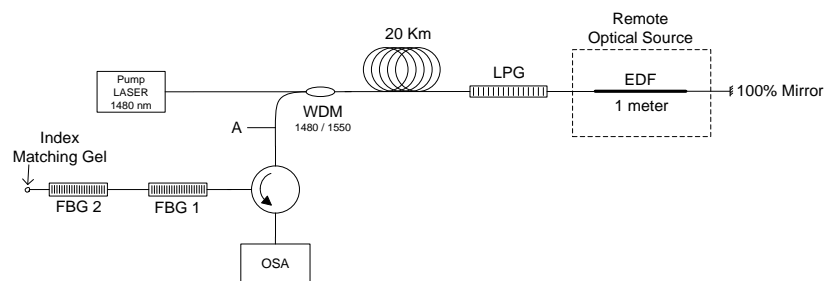


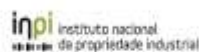
---

## Orlando Frazão, Diana Viegas, Luis Coelho, Joel Carvalho

## Resumo

É apresentado um sistema de interrogação para detecção remota de sensores óptico de rejeição de banda monitorizados em reflexão usando assim uma única fibra que ler o sensor óptico. A nova configuração remota consiste em acoplar uma fonte de espectro largo ao sensor óptico. A fonte de espectro largo está localizada depois do sensor óptico e o sensor é interrogado em transmissão pela fonte remota. A fonte de espectro largo consiste numa fibra dopada com terras-raras em que é bombeada com um laser de bombagem que se encontra perto do sistema de processamento de sinal. Esta técnica apresenta uma grande vantagem quando comparada com o sistema tradicional em que se necessita de duas fibras para interrogar o sensor óptico. Uma para iluminar o sensor óptico e outra para levar a informação do sensor ao sistema de processamento de sinal.





Campos dos Gólgotes - 1149-035 Lisboa - Portugal  
Tel: +351 218921000 / Linha Azul 800 200699 / Fax: +351 218925308 / Fax: +351 218920066 / E-mail: [atm@inpi.pt](mailto:atm@inpi.pt) / [www.inpi.pt](http://www.inpi.pt)

Nº	CÓDIGO	DATA E HORA DE RECEPÇÃO	MODALIDADE	PROCESSO RELACIONADO
20101000062014	0198	2010/08/09-13:03:34	PAT	

### PEDIDO DE PATENTE, MODELO DE UTILIDADE OU DE TOPOGRAFIA DE PRODUTOS SEMICONDUTORES

<b>1 REQUERENTE</b>	
<b>Código</b>	<b>Nacionalidade PORTUGUESA</b>
<b>Nome</b> INESC PORTO - INSTITUTO DE ENGENHARIA DE SISTEMAS E COMPUTADORES DO PORTO	
<b>Endereço</b> CAMPUS DA FACULDADE DE ENGENHARIA DA UNIVERSIDADE DO PORTO, RUA DR. ROBERTO FRIAS, N.º 378	
<b>Localidade</b> PORTO	<b>Código Postal</b> 4200-465
<b>Telefone</b> +351 22 209 40 00	<b>Telemóvel</b>
	<b>Fax</b> + 351 22 209 40 50
<b>E-mail</b> TERESA.R.ANTUNES@INESCPORTO.PT	
<b>Actividade (CAE)</b> 72190	
<b>NIF</b> 504441361	<b>Cód. Certidão Permanente</b> 3686-8098-3247
<b>Tipo de Representação</b> Representante legal da entidade	
<b>Nome</b> JOSÉ CARLOS CALDEIRA PINTO DE SOUSA	<b>Código</b>
<b>Endereço</b> TRAVESSA DE SANTIAGO, N.º 185, CUSTÓIAS	
<b>Localidade</b> CUSTÓIAS MTS	<b>Código Postal</b> 4460-811
<b>Telefone</b> + 351 22 209 40 00	<b>Telemóvel</b>
	<b>Fax</b> + 351 22 209 40 50
<b>E-mail</b> teresa.r.antunes@inescporto.pt	
<b>2 MODALIDADE / TIPO DE PEDIDO</b>	
Modalidade: PEDIDO PROVISÓRIO DE PATENTE	
Realização de pesquisa pelo INPI: SIM	
<b>3 EPIGRAFE OU TÍTULO</b>	
SISTEMA DE INTERROGAÇÃO REMOTO COM FONTE ÓPTICA ACOPLADA À CABEÇA SENSORA	
<b>4 RESUMO</b>	
<b>5 FIGURAS</b>	
<b>6 INVENTORES</b>	
<b>Nacionalidade</b> PORTUGUESA	
<b>Nome</b> ORLANDO JOSÉ DOS REIS FRAZÃO	
<b>Endereço</b> PRACETA DA RUA DA REPUBLICA, N.º 9, 2F	
<b>Localidade</b> AVEIRO	<b>Código Postal</b> 3810-495
<b>Telefone</b> + 351 220 402 301	<b>Telemóvel</b> + 351 914509897
	<b>Fax</b> 351 220 402 437
<b>E-mail</b> OFRAZAO@INESCPORTO.PT	
<b>NIF</b> 208225676	

20101000062014 - 2010/08/09-13:03:34

1/3

<b>Nome</b> LUIS CARLOS COSTA COELHO <b>Endereço</b> RUA ALBERTO SERPA Nº 179 5º HAB. 1 <b>Localidade</b> PORTO <b>Telefone</b> + 351 220 402 301 <b>Telemóvel</b> + 351 914275776 <b>E-mail</b> LCCOELHO@GMAIL.COM <b>NIF</b> 209928360		<b>Nacionalidade</b> PORTUGUESA  <b>Código Postal</b> 4100 - 010 <b>Fax</b> + 351 220 402 437
<b>Nome</b> JOEL PEDRO PEIXOTO DE CARVALHO <b>Endereço</b> RUA 5 DE OUTUBRO 5482, 3º ANDAR - FRACÇÃO S, S. MAMEDE DE INFESTA <b>Localidade</b> SÃO MAMEDE DE INFESTA <b>Telefone</b> + 351 220 402 301 <b>Telemóvel</b> + 351 914 835 867 <b>E-mail</b> JPC@INESCPORTO.PT <b>NIF</b> 224931229		<b>Nacionalidade</b> PORTUGUESA  <b>Código Postal</b> 4465-080 <b>Fax</b> + 351 220 402 437
<b>Nome</b> DIANA CATARINO DAS NEVES VIEGAS <b>Endereço</b> AVENIDA DR. FRANCISCO SÁ CARNEIRO 709/A HABITAÇÃO 103, MARCO DE CANAVEZES <b>Localidade</b> MARCO DE CANAVESES <b>Telefone</b> + 351 220 402 301 <b>Telemóvel</b> + 351 964 426 545 <b>E-mail</b> DVIEGAS@INESCPORTO.PT <b>NIF</b> 219137064		<b>Nacionalidade</b> PORTUGUESA  <b>Código Postal</b> 4630-205 <b>Fax</b> + 351 220 402 437
<b>7 REIVINDICAÇÃO DE PRIORIDADE</b>		
<b>8 DOCUMENTOS ANEXOS</b> DOCUMENTO DO PEDIDO PROVISÓRIO DE PATENTE DOCUMENTO DO PEDIDO PROVISÓRIO DE PATENTE OUTROS		
<b>9 OBSERVAÇÕES</b> O Requerente e o INPI acordam em submeter a Tribunal Arbitral eventuais litígios emergentes do presente acto, nos termos e condições especificados em Anexo. Esta cláusula vincula as partes que a subscrevem, apenas podendo ser revogada, por comum acordo, até à pronúncia da decisão arbitral.		
<b>10 TAXAS</b>		
Taxa	Importância	
PEDIDO PROVISÓRIO DE PATENTE	10,00 €	
PESQUISA EM PEDIDO PROVISÓRIO DE PATENTE	20,00 €	
Total:	30,00 €	
Por Extenso:	TRINTA EUROS	

11 PAGAMENTO	
Tipo de Pagamento	Multibanco/Homebanking
Entidade	10587
Referência	017 391 626
Montante	30,00 €
Data Limite de Pagamento	12-08-2010
	<p>Poderá efectuar o pagamento em qualquer Caixa Multibanco (opção pagamento de serviços/compras) ou serviço de Homebanking (opção Pagamento de Compras).</p> <p>Se, ao efectuar o pagamento, for necessária a selecção de "pagamentos de compra" e o respectivo pagamento não for possível, deverá contactar a sua entidade bancária no sentido de verificar se o cartão bancário que está a utilizar tem essa função activa.</p> <p>Nos termos da alínea a) do n.º 1 do artigo 24.º do Código da Propriedade Industrial, fica por este meio notificado para proceder ao pagamento do acto solicitado no prazo de três dias. Findo este prazo, e na ausência de pagamento, o acto solicitado poderá ser alvo de recusa/indeferimento.</p>
12 ASSINATURA DO REQUERENTE OU MANDATÁRIO/REPRESENTANTE LEGAL	
Assinatura/Nome José Carlos Caldeira Pinto de Sousa	
Nº B.I. 06578407 3 ZZ6	Data 2010/08/09

## Bibliography

---

1. López-Higuera, J.M., *Handbook of Optical Fibre Sensing Technology*2002: Wiley.
2. Dakin, J., *The distributed fibre optic sensing handbook*1990: IFS Publications.
3. Hill, K.O., et al., *Photosensitivity in Optical Fiber Waveguides - Application to Reflection Filter Fabrication*. Applied Physics Letters, 1978. **32**(10): p. 647-649.
4. Meltz, G., W.W. Morey, and W.H. Glenn, *Formation of Bragg Gratings in Optical Fibers by a Transverse Holographic Method*. Optics Letters, 1989. **14**(15): p. 823-825.
5. Kashyap, R., et al., *All-Fiber Narrow-Band Reflection Gratings at 1500 nm*. Electronics Letters, 1990. **26**(11): p. 730-732.
6. Kashyap, R., *Fiber Bragg Gratings*1999: Elsevier. 458.
7. Othonos, A. and K. Kalli, *Fiber Bragg Gratings: Fundamentals and Applications in Telecommunications and Sensing*1999: Artech House Publishers. 433.
8. Carvalho, J.P., *Optical Switching Techniques: Device Development and Implementation in Fibre Optic Technology*, in *Electrical and Computers Engineering Department*2007, University of Porto: Faculty of Engineering.
9. Kashyap, R., *Fiber bragg gratings*1999: Access Online via Elsevier.
10. Othonos, A., *Fiber Bragg Gratings*. Review of Scientific Instruments, 1997. **68**(12): p. 4309-4341.
11. Vengsarkar, A.M., et al., *Long-period fiber gratings as band-rejection filters*. Journal of Lightwave Technology, 1996. **14**(1): p. 58-65.
12. Brakel, A.V., *Sensing Characteristics Of An Optical Fibre Long-Period Grating Michelson Refractometer*, in *Faculty Of Engieenering*2004, Rand Afrikaans University.
13. Bhatia, V., *Applications of long-period gratings to single and multi-parameter sensing*. Opt. Express, 1999. **4**(11): p. 457-466.
14. Shu, X., et al., *Thermally tunable optical fiber loss filter with wide tuning range*, in *Lasers and Electro-optics*2001.
15. Khaliq S., J.S.W., Tatam R. P, *Enhanced sensitivity fibre optic long period grating temperature sensor*. Meas. Sci. Technology, 2002. **13**.
16. James, S.W. and R.P. Tatam, *Optical fibre long-period grating sensors: Characteristics and application*. Measurement Science & Technology, 2003. **14**(5): p. R49-R61.
17. Kakarantzas, G., et al. *Rocking Filter Formation in Non-Photosensitive Highly Birefringent Photonic Crystal Fibres*. in *Optical Communication, 2002. ECOC 2002. 28th European Conference on*. 2002.
18. Stolen, R.H., et al., *In-line fiber-polarization-rocking rotator and filter*. Opt. Lett., 1984. **9**(7): p. 300-302.
19. Yariv, A. and P. Yeh, *Optical Waves in Crystals: Propagation and Control of Laser Radiation*2002: John Wiley & Sons.

20. Rego, G., et al., *High-temperature stability of long-period fiber gratings produced using an electric arc*. Lightwave Technology, Journal of, 2001. **19**(10): p. 1574-1579.
21. Knight, J.C., et al., *All-silica single-mode optical fiber with photonic crystal cladding*. Opt. Lett., 1996. **21**(19): p. 1547-1549.
22. Knight, J.C., *Photonic crystal fibres*. Nature, 2003. **424**(6950): p. 847-851.
23. Russell, P., *Photonic crystal fibers*. Science, 2003. **299**(5605): p. 358-362.
24. Monro, T.M., et al., *Sensing with microstructured optical fibres*. Measurement Science & Technology, 2001. **12**(7): p. 854-858.
25. Fini, J.M., *Microstructure fibres for optical sensing in gases and liquids*. Measurement Science & Technology, 2004. **15**(6): p. 1120-1128.
26. Birks, T.A., et al., *Full 2-D Photonic Bandgaps in Silica/Air Structures*. Electronics Letters, 1995. **31**(22): p. 1941-1943.
27. Knight, J.C., et al., *Photonic Band Gap Guidance in Optical Fibers*. Science, 1998. **282**(5393): p. 1476-1478.
28. Cregan, R.F., et al., *Single-mode photonic band gap guidance of light in air*. Science, 1999. **285**(5433): p. 1537-1539.
29. Eggleton, B.J., et al., *Microstructured optical fiber devices*. Optics Express, 2001. **9**(13): p. 698-713.
30. Dobb, H., K. Kalli, and D.J. Webb, *Temperature-insensitive long period grating sensors in photonic crystal fibre*. Electronics Letters, 2004. **40**(11): p. 657-658.
31. Kakarantzas, G., et al., *Structural rocking filters in highly birefringent photonic crystal fiber*. Opt. Lett., 2003. **28**(3): p. 158-160.
32. Statkiewicz-Barabach, G., et al., *Sensing characteristics of rocking filter fabricated in microstructured birefringent fiber using fusion arc splicer*. Opt. Express, 2008. **16**(22): p. 17249-17257.
33. Ju, J., et al., *A simple method for estimating the splice loss of photonic-crystal fiber/single-mode fiber*. Microwave and Optical Technology Letters, 2004. **42**(2): p. 171-173.
34. Bennett, P.J., T.M. Monro, and D.J. Richardson, *Toward practical holey fiber technology: fabrication, splicing, modeling, and characterization*. Opt. Lett., 1999. **24**(17): p. 1203-1205.
35. Chong, J.H. and M. Rao, *Development of a system for laser splicing photonic crystal fiber*. Opt. Express, 2003. **11**(12): p. 1365-1370.
36. Bourliaguet, B., et al., *Microstructured fiber splicing*. Optics Express, 2003. **11**(25): p. 3412-3417.
37. Bisbee, D.L., *Splicing Silica Fibers with an Electric-Arc*. Applied Optics, 1976. **15**(3): p. 796-798.
38. Kato, Y., S. Seikai, and M. Tateda, *Arc-Fusion Splicing of Single-Mode Fibers .I. Optimum Splice Conditions*. Applied Optics, 1982. **21**(7): p. 1332-1336.
39. Lizard, J.T. and G.E. Town, *Splice losses in holey optical fibers*. IEEE Photonics Technology Letters, 2001. **13**(8): p. 794-796.
40. Hansen, K.P., et al. *Highly nonlinear photonic crystal fiber with zero-dispersion at 1.55  $\mu\text{m}$* . in *Optical Fiber Communication Conference and Exhibit, 2002. OFC 2002*. 2002.
41. Mortensen, N.A., *Effective area of photonic crystal fibers*. Optics Express, 2002. **10**(7): p. 341-348.



42. Hansen, T.P., et al., *Air-guiding photonic bandgap fibers: Spectral properties, macrobending loss, and practical handling*. Journal of Lightwave Technology, 2004. **22**(1): p. 11-15.
43. Thapa, R., et al., *Arc fusion splicing of hollow-core photonic bandgap fibers for gas-filled fiber cells*. Opt. Express, 2006. **14**(21): p. 9576-9583.
44. Xiao, L., et al., *Fusion Splicing Photonic Crystal Fibers and Conventional Single-Mode Fibers: Microhole Collapse Effect*. J. Lightwave Technol., 2007. **25**(11): p. 3563-3574.
45. Frazao, O., J.P. Carvalho, and H.M. Salgado, *Low-loss splice in a microstructured fibre using a conventional fusion splicer*. Microwave and Optical Technology Letters, 2005. **46**(2): p. 172-174.
46. Ferreira, L.A., et al., *Simultaneous measurement of strain and temperature using interferometrically interrogated fiber Bragg grating sensors*. Optical Engineering, 2000. **39**(8): p. 2226-2234.
47. Frazão, O. and J.L. Santos, *Simultaneous measurement of strain and temperature using a Bragg grating structure written in germanosilicate fibres*. Journal of Optics A: Pure and Applied Optics, 2004. **6**(6): p. 553.
48. Kotynski, R., et al., *Sensitivity of holey fiber based sensors*. Icton 2003: 5th International Conference on Transparent Optical Networks, Vol 1, Proceedings, 2003: p. 340-343.
49. Martelli, C., et al., *Strain and temperature characterization of photonic crystal fiber Bragg gratings*. Opt. Lett., 2005. **30**(14): p. 1785-1787.
50. Jin, W., et al., *Simultaneous measurement of strain and temperature: Error analysis*. Optical Engineering, 1997. **36**(2): p. 598-609.
51. Kersey, A.D., T.A. Berkoff, and W.W. Morey, *High-Resolution Fiber-Grating Based Strain Sensor with Interferometric Wavelength-Shift Detection*. Electronics Letters, 1992. **28**(3): p. 236-238.
52. Jesus, C., et al., *Simultaneous Measurement of Refractive Index and Temperature Using a Hybrid Fiber Bragg Grating/Long-Period Fiber Grating Configuration*. Fiber and Integrated Optics, 2009. **28**(6): p. 440-449.
53. Benabid, F., *Hollow-core photonic bandgap fibre: new light guidance for new science and technology*. Philosophical Transactions of the Royal Society a-Mathematical Physical and Engineering Sciences, 2006. **364**(1849): p. 3439-3462.
54. West, J., et al., *Surface modes in air-core photonic band-gap fibers*. Opt. Express, 2004. **12**(8): p. 1485-1496.
55. Couny, F., et al., *Visualizing the photonic band gap in hollow core photonic crystal fibers*. Optics Express, 2005. **13**(2): p. 558-563.
56. Antonopoulos, G., et al., *Experimental demonstration of the frequency shift of bandgaps in photonic crystal fibers due to refractive index scaling*. Opt. Express, 2006. **14**(7): p. 3000-3006.
57. Birks, T., et al., *Scaling laws and vector effects in bandgap-guiding fibres*. Opt. Express, 2004. **12**(1): p. 69-74.
58. Sun, J. and C.C. Chan, *Photonic bandgap fiber for refractive index measurement*. Sensors and Actuators B-Chemical, 2007. **128**(1): p. 46-50.
59. Ferreira, L.A., et al., *Frequency-modulated multimode laser diode for fiber Bragg grating sensors*. Journal of Lightwave Technology, 1998. **16**(9): p. 1620-1630.
60. Humbert, G., et al., *Electric arc-induced long-period gratings in Ge-free air-silica microstructure fibres*. Electronics Letters, 2003. **39**(4): p. 349-350.

61. Dobb, H., K. Kalli, and D.J. Webb, *Measured sensitivity of arc-induced long-period grating sensors in photonic crystal fibre*. Optics Communications, 2006. **260**(1): p. 184-191.
62. Petrovic, J.S., et al., *Sensitivity of LPGs in PCFs Fabricated by an Electric Arc to Temperature, Strain, and External Refractive Index*. J. Lightwave Technol., 2007. **25**(5): p. 1306-1312.
63. Bock, W.J., et al., *Pressure sensing using periodically tapered long-period gratings written in photonic crystal fibres*. Measurement Science and Technology, 2007. **18**(10): p. 3098.
64. Kaul, R., *Pressure Sensitivity of Rocking Filters Fabricated in an Elliptic-Core Optical-Fiber*. Optics Letters, 1995. **20**(9): p. 1000-1001.
65. Moore, C.B., *Gas-Laser Frequency Selection by Molecular Absorption*. Appl. Opt., 1965. **4**(2): p. 252-253.
66. Grant, W.B., *He-Ne and cw CO<sub>2</sub> laser long-path systems for gas detection*. Appl. Opt., 1986. **25**(5): p. 709-719.
67. Culshaw, B., et al., *Fibre optic techniques for remote spectroscopic methane detection-from concept to system realisation*. Sensors and Actuators B: Chemical, 1998. **51**(1): p. 25-37.
68. Uehara, K. and H. Tai, *Remote detection of methane with a 1.66- $\mu$ m diode laser*. Appl. Opt., 1992. **31**(6): p. 809-814.
69. Silveira, J.P. and F. Grasdepot, *CH<sub>4</sub> optical sensor using a 1.31  $\mu$ m DFB laser diode*. Sensors and Actuators B: Chemical, 1995. **25**(1-3): p. 603-606.
70. Stewart, G., et al., *Interferometric Signals in Fiber Optic Methane Sensors with Wavelength Modulation of the DFB Laser Source*. J. Lightwave Technol., 1998. **16**(1): p. 43.
71. Takaya, I., T. Hideo, and K. Kiyoshi, *A portable remote methane sensor using a tunable diode laser*. Measurement Science and Technology, 2000. **11**(6): p. 594.
72. Chan, K., et al., *10 km-long fibre-optic remote sensing of CH<sub>4</sub> gas by near infrared absorption*. Applied Physics B: Lasers and Optics, 1985. **38**(1): p. 11-15.
73. Chan, K., H. Ito, and H. Inaba, *Remote-Sensing System for near-Infrared Differential Absorption of CH<sub>4</sub> Gas-Using Low-Loss Optical Fiber Link*. Applied Optics, 1984. **23**(19): p. 3415-3420.
74. Gillian, W., et al., *Optical fibre instrumentation for environmental monitoring applications*. Journal of Optics A: Pure and Applied Optics, 2003. **5**(5): p. S140.
75. Kosterev, A.A., Y.A. Bakhirkin, and F.K. Tittel, *Ultrasensitive gas detection by quartz-enhanced photoacoustic spectroscopy in the fundamental molecular absorption bands region*. Applied Physics B, 2005. **80**(1): p. 133-138.
76. Charlton, C.M. and B. Mizaikoff, *Sensing Trace Gases with Quantum Cascade Lasers*, in *Photonics Spectra* 2006, Laurin Publishing.
77. McManus, J.B., P.L. Kebabian, and M.S. Zahniser, *Astigmatic mirror multipass absorption cells for long-path-length spectroscopy*. Appl. Opt., 1995. **34**(18): p. 3336-3348.
78. Culshaw, B., et al., *Evanescent wave methane detection using optical fibres*. Electronics Letters, 1992. **28**(24): p. 2232-2234.
79. Stewart, G., W. Jin, and B. Culshaw, *Prospects for fibre-optic evanescent-field gas sensors using absorption in the near-infrared*. Sensors and Actuators B: Chemical, 1997. **38**(1-3): p. 42-47.

80. Muhammad, F.A., G. Stewart, and W. Jin, *Sensitivity enhancement of D-fibre methane gas sensor using high-index overlay*. Optoelectronics, IEE Proceedings J, 1993. **140**(2): p. 115-118.
81. Benounis, M., et al., *Study of a new evanescent wave optical fibre sensor for methane detection based on cryptophane molecules*. Sensors and Actuators B: Chemical, 2005. **107**(1): p. 32-39.
82. Roy, R.K., M.P. Chowdhury, and A.K. Pal, *Room temperature sensor based on carbon nanotubes and nanofibres for methane detection*. Vacuum, 2005. **77**(3): p. 223-229.
83. Magalhães, F., *Development of gas detection systems based on microstructured optical fibres*, in *Electrical and Computers Engineering Department* 2008, University of Porto: Faculty of Engineering.
84. Monro, T.M., D.J. Richardson, and P.J. Bennett, *Developing holey fibres for evanescent field devices*. Electronics Letters, 1999. **35**(14): p. 1188-1189.
85. Pickrell, G., W. Peng, and A. Wang, *Random-hole optical fiber evanescent-wave gas sensing*. Optics Letters, 2004. **29**(13): p. 1476-1478.
86. Hoo, Y.L., et al., *Evanescent-wave gas sensing using microstructure fiber*. Optical Engineering, 2002. **41**(1): p. 8-9.
87. Hoo, Y.L., et al., *Design and modeling of a photonic crystal fiber gas sensor*. Applied Optics, 2003. **42**(18): p. 3509-3515.
88. Ritari, T., et al., *Gas sensing using air-guiding photonic bandgap fibers*. Optics Express, 2004. **12**(17): p. 4080-4087.
89. Cubillas, A.M., et al., *Methane detection at 1670-nm band using a hollow-core photonic bandgap fiber and a multiline algorithm*. Optics Express, 2007. **15**(26): p. 17570-17576.
90. Cubillas, A.M., et al., *Methane sensing at 1300 nm band with hollow-core photonic bandgap fibre as gas cell*. Electronics Letters, 2008. **44**(6): p. 403-405.
91. Cordeiro, C.M.B., et al., *Lateral access to the holes of photonic crystal fibers - selective filling and sensing applications*. Optics Express, 2006. **14**(18): p. 8403-8412.
92. Cordeiro, C.M.B., et al., *Microstructured-core optical fibre for evanescent sensing applications*. Optics Express, 2006. **14**(26): p. 13056-13066.
93. Li, S.G., et al., *Study of the sensitivity of gas sensing by use of index-guiding photonic crystal fibers*. Applied Optics, 2007. **46**(22): p. 5183-5188.
94. van Brakel, A., et al., *Micro-channels machined in microstructured optical fibers by femtosecond laser*. Opt. Express, 2007. **15**(14): p. 8731-8736.
95. Skucha, K., et al., *Palladium/silicon nanowire Schottky barrier-based hydrogen sensors*. Sensors and Actuators B: Chemical, 2010. **145**(1): p. 232-238.
96. Korotcenkov, G., S.D. Han, and J.R. Stetter, *Review of Electrochemical Hydrogen Sensors*. Chemical Reviews, 2009. **109**(3): p. 1402-1433.
97. Nishibori, M., et al., *Robust hydrogen detection system with a thermoelectric hydrogen sensor for hydrogen station application*. International Journal of Hydrogen Energy, 2009. **34**(6): p. 2834-2841.
98. Ya-Shan, H., C. Yung-Yu, and W. Tsung-Tsong, *A passive wireless hydrogen surface acoustic wave sensor based on Pt-coated ZnO nanorods*. Nanotechnology, 2010. **21**(9): p. 095503.
99. Lin, K., et al., *Surface plasmon resonance hydrogen sensor based on metallic grating with high sensitivity*. Opt. Express, 2008. **16**(23): p. 18599-18604.

100. Silva, S.F., et al., *A Review of Palladium-Based Fiber-Optic Sensors for Molecular Hydrogen Detection*. Sensors Journal, IEEE, 2012. **12**(1): p. 93-102.
101. Carvalho, J.P., et al., *Evaluation of coupling losses in hollow-core photonic crystal fibres*. Third European Workshop on Optical Fibre Sensors, 2007. **6619**: p. 66191V1-66191V4.
102. Crank, J., *The mathematics of diffusion*. 2d ed1975, Oxford, Eng: Clarendon Press. viii, 414 p.
103. Lide, D.R. and H.P.R. Frederikse, *CRC handbook of chemistry and physics : a ready-reference book of chemical and physical data*. 78th ed. / editor-in-chief David R. Lide, associate editor H. P. R. Frederikse. ed1997, Boca Raton, Fla.: CRC.
104. Silver, J.A., *Frequency-Modulation Spectroscopy for Trace Species Detection - Theory and Comparison among Experimental Methods*. Applied Optics, 1992. **31**(6): p. 707-717.
105. Ingle, J.D. and S.R. Crouch, *Spectrochemical analysis*1988: Prentice-Hall International.
106. Rothman, L.S., et al., *The HITRAN 2004 molecular spectroscopic database*. Journal of Quantitative Spectroscopy and Radiative Transfer, 2005. **96**(2): p. 139-204.
107. Rothman, L.S., et al., *The HITRAN 2004 molecular spectroscopic database*. Journal of Quantitative Spectroscopy and Radiative Transfer, 2005. **96**(2): p. 139-204.
108. Bock, W.J., et al., *Novel Fiber Optic Sensor Based on in-Line Core-Cladding Intermodal Interferometer and Photonic Crystal Fiber*. Xix Imeko World Congress: Fundamental and Applied Metrology, Proceedings, 2009: p. 65-68.
109. Jung, Y.M., et al., *Ultracompact in-line broadband Mach-Zehnder interferometer using a composite leaky hollow-optical-fiber waveguide*. Optics Letters, 2008. **33**(24): p. 2934-2936.
110. Minkovich, V.P., et al., *Holey fiber tapers with resonance transmission for high-resolution refractive index sensing*. Optics Express, 2005. **13**(19): p. 7609-7614.
111. Villatoro, J., et al., *Highly Sensitive Sensors Based on Photonic Crystal Fiber Modal Interferometers*. Journal of Sensors, 2009. **2009**.
112. Choi, H.Y., M.J. Kim, and B.H. Lee, *All-fiber Mach-Zehnder type interferometers formed in photonic crystal fiber*. Opt. Express, 2007. **15**(9): p. 5711-5720.
113. Villatoro, J., et al., *Simple all-microstructured-optical-fiber interferometer built via fusion splicing*. Optics Express, 2007. **15**(4): p. 1491-1496.
114. Donlagic, D. and M. Zavrsnik, *Fiber-optic microbend sensor structure*. Optics Letters, 1997. **22**(11): p. 837-839.
115. Li, E.B., *Sensitivity-enhanced fiber-optic strain sensor based on interference of higher order modes in circular fibers*. Ieee Photonics Technology Letters, 2007. **19**(13-16): p. 1266-1268.
116. Tripathi, S.M., et al., *Strain and Temperature Sensing Characteristics of Single-Mode-Multimode-Single-Mode Structures*. Journal of Lightwave Technology, 2009. **27**(13): p. 2348-2356.
117. Li, E.B., X.L. Wang, and C. Zhang, *Fiber-optic temperature sensor based on interference of selective higher-order modes*. Applied Physics Letters, 2006. **89**(9).

118. Li, Q., et al., *Demonstration of high extinction ratio modal interference in a two-mode fiber and its applications for all-fiber comb filter and high-temperature sensor*. Optics Communications, 2005. **250**(4-6): p. 280-285.
119. Villatoro, J., V.P. Minkovich, and D. Monzon-Hernandez, *Compact modal interferometer built with tapered microstructured optical fiber*. Ieee Photonics Technology Letters, 2006. **18**(9-12): p. 1258-1260.
120. Villatoro, J., et al., *Simple all-microstructured-optical-fiber interferometer built via fusion splicing*. Opt. Express, 2007. **15**(4): p. 1491-1496.
121. Choi, H.Y., M.J. Kim, and B.H. Lee, *All-fiber Mach-Zehnder type interferometers formed in photonic crystal fiber*. Optics Express, 2007. **15**(9): p. 5711-5720.
122. Yong-min, J., et al. *Ultra-Compact Mach-Zehnder Interferometer Using Hollow Optical Fiber for High Temperature Sensing*. 2008. Optical Society of America.
123. Villatoro, J., et al., *Temperature-insensitive photonic crystal fiber interferometer for absolute strain sensing*. Applied Physics Letters, 2007. **91**(9).
124. Rao, Y.J. and D.A. Jackson, *Recent progress in fibre optic low-coherence interferometry*. Measurement Science & Technology, 1996. **7**(7): p. 981-999.
125. Caldas, P., et al., *Fiber modal Michelson interferometers with coherence addressing and heterodyne interrogation*. Optical Engineering, 2008. **47**(4).
126. Statkiewicz-Barabach, G., et al., *Polarizing photonic crystal fiber with low index inclusion in the core*. Journal of Optics, 2010. **12**(7).
127. Szpulak, M., et al., *Comparison of different methods for rigorous modeling of photonic crystal fibers*. Optics Express, 2006. **14**(12): p. 5699-5714.
128. Snyder, A.W. and J.D. Love, *Optical waveguide theory*. Science paperbacks 1983, London ; New York: Chapman and Hall. viii, 734 p.
129. Hlubina, P., *White-light spectral interferometry to measure intermodal dispersion in two-mode elliptical-core optical fibres*. Optics Communications, 2003. **218**(4-6): p. 283-289.
130. Villatoro, J., V.P. Minkovich, and D. Monzon-Hernandez, *Temperature-independent strain sensor made from tapered holey optical fiber*. Optics Letters, 2006. **31**(3): p. 305-307.
131. Falate, R., et al., *Refractometric sensor based on a phase-shifted long-period fiber grating*. Appl. Opt., 2006. **45**(21): p. 5066-5072.
132. Ferreira, L.A., et al., *Frequency-modulated multimode laser diode for fiber Bragg grating sensors*. Lightwave Technology, Journal of, 1998. **16**(9): p. 1620-1630.
133. Fallon, R.W., et al., *All-fibre optical sensing system: Bragg grating sensor interrogated by a long-period grating*. Measurement Science & Technology, 1998. **9**(12): p. 1969-1973.
134. Kersey, A.D., T.A. Berkoff, and W.W. Morey, *Multiplexed Fiber Bragg Grating Strain-Sensor System with a Fiber Fabry-Perot Wavelength Filter*. Optics Letters, 1993. **18**(16): p. 1370-1372.
135. Volanthen, M., et al., *Simultaneous monitoring of multiple fibre gratings with a single acousto-optic tunable filter*. Electronics Letters, 1996. **32**(13): p. 1228-1229.
136. Ferreira, L., *Interrogação de Sensores de Bragg em Fibra Óptica*, in *Fisica* 2000, Porto: Porto.

137. Allsop, T., et al., *The interrogation and multiplexing of long period grating curvature sensors using a Bragg grating based, derivative spectroscopy technique*. Measurement Science & Technology, 2004. **15**(1): p. 44-48.
138. Brady, G.P., et al., *Demultiplexing of Fiber Bragg Grating Temperature and Strain Sensors*. Optics Communications, 1994. **111**(1-2): p. 51-54.
139. Ferreira, L.A., et al., *Demodulation of fiber Bragg grating sensors based on dynamic tuning of a multimode laser diode*. Applied Optics, 1999. **38**(22): p. 4751-4759.
140. Falate, R., et al., *Refractometric sensor based on a phase-shifted long-period fiber grating*. Applied Optics, 2006. **45**(21): p. 5066-5072.
141. Swart, P.L., *Long-period grating Michelson refractometric sensor*. Measurement Science & Technology, 2004. **15**(8): p. 1576-1580.
142. Kersey, A.D., et al., *Fiber grating sensors*. Journal of Lightwave Technology, 1997. **15**(8): p. 1442-1463.
143. Meeten, G.H. and A.N. North, *Refractive index measurement of turbid colloidal fluids by transmission near the critical angle*. Measurement Science and Technology, 1991. **2**(5): p. 441.
144. Sienkiewicz, F. and A. Shukla, *A simple fiber-optic sensor for use over a large displacement range*. Optics and Lasers in Engineering, 1997. **28**(4): p. 293-304.
145. Pinto, N.M.P., et al., *Quasi-distributed displacement sensor for structural monitoring using a commercial OTDR*. Optics and Lasers in Engineering, 2006. **44**(8): p. 771-778.
146. Caucheteur, C., et al. *Multi-point in-line refractometry using tilted fiber Bragg gratings*. in *IEEE/LEOS Winter Topicals Meeting Series*, 2009. 2009.
147. Yun, C.-Y., et al., *Design of multiplexed fiber optic chemical sensing system using clad-removable optical fibers*. Optics & Laser Technology, 2012. **44**(1): p. 269-280.
148. Islam, M.N., *Raman amplifiers for telecommunications*. Selected Topics in Quantum Electronics, IEEE Journal of, 2002. **8**(3): p. 548-559.
149. Lee, J.H., et al., *Raman amplifier-based long-distance remote, strain and temperature sensing system using an erbium-doped fiber and a fiber Bragg grating*. Opt. Express, 2004. **12**(15): p. 3515-3520.
150. Junhao, H., et al., *100-km Long Distance Fiber Bragg Grating Sensor System Based on Erbium-Doped Fiber and Raman Amplification*. Photonics Technology Letters, IEEE, 2010. **22**(19): p. 1422-1424.
151. Alahbabi, M.N., Y.T. Cho, and T.P. Newson, *150-km-range distributed temperature sensor based on coherent detection of spontaneous Brillouin backscatter and in-line Raman amplification*. J. Opt. Soc. Am. B, 2005. **22**(6): p. 1321-1324.
152. Bravo, M., et al., *Ultralong 250 km remote sensor system based on a fiber loop mirror interrogated by an optical time-domain reflectometer*. Opt. Lett., 2011. **36**(20): p. 4059-4061.
153. Achtenhagen, M., et al., *Analysis of a multiple-pump Raman amplifier*. Applied Physics Letters, 2001. **78**(10): p. 1322-1324.
154. Cani, S.P.N., et al., *An Analytical Approximated Solution for the Gain of Broadband Raman Amplifiers With Multiple Counter-Pumps*. J. Lightwave Technol., 2009. **27**(7): p. 944-951.

155. Xiang, Z., et al., *A simplified model and optimal design of a multiwavelength backward-pumped fiber Raman amplifier*. Photonics Technology Letters, IEEE, 2001. **13**(9): p. 945-947.
156. Fernandez-Vallejo, M., S. Rota-Rodrigo, and M. Lopez-Amo, *Remote (250 km) Fiber Bragg Grating Multiplexing System*. Sensors, 2011. **11**(9): p. 8711-8720.
157. Patrick, H.J., et al., *Hybrid fiber Bragg grating/long period fiber grating sensor for strain/temperature discrimination*. Ieee Photonics Technology Letters, 1996. **8**(9): p. 1223-1225.
158. Sharma, T., et al., *Experimental Characterization of Optical Fiber Long Period Grating with Reduced Temperature Sensitivity*. International Journal of Computer and Electrical Engineering, 2011. **3**(5): p. 711-713.
159. Rogers, A.J., *Optical Fibre Current Measurement*. 1983: p. 196-201.
160. Yin, S., P.B. Ruffin, and F.T.S. Yu, *Fiber optic sensors*. 2nd ed. Optical science and engineering 2008, Boca Raton, FL: CRC Press. xiii, 477 p.
161. Ni, K., et al. *Temperature-Independent Inclination Management with Fiber Bragg Grating sensor*. 2009. Optical Society of America.
162. Berkoff, T.A. and A.D. Kersey, *Experimental demonstration of a fiber Bragg grating accelerometer*. Photonics Technology Letters, IEEE, 1996. **8**(12): p. 1677-1679.
163. Bai-Ou, G., T. Hwa-Yaw, and L. Shun-ye, *Temperature-independent fiber Bragg grating tilt sensor*. Photonics Technology Letters, IEEE, 2004. **16**(1): p. 224-226.
164. Olaru, R. and C. Cota, *Tilt sensor with magnetic liquid*. Sensors and Actuators A: Physical, 1997. **59**(1-3): p. 133-135.
165. Amaral, L.M.N., et al., *Optical inclinometer based on fibre-taper-modal Michelson interferometer*. 2010: p. 76530J-76530J.
166. Zibaii, M.I., et al., *Non-adiabatic tapered optical fiber sensor for measuring the interaction between  $\alpha$ -amino acids in aqueous carbohydrate solution*. Measurement Science and Technology, 2010. **21**(10): p. 105801.
167. Kieu, K.Q. and M. Mansuripur, *Biconical Fiber Taper Sensors*. Photonics Technology Letters, IEEE, 2006. **18**(21): p. 2239-2241.
168. Kakarantzas, G., et al., *Miniature all-fiber devices based on CO<sub>2</sub> laser microstructuring of tapered fibers*. Opt. Lett., 2001. **26**(15): p. 1137-1139.
169. Zibaii, M.I., et al., *Non-adiabatic tapered optical fiber sensor for measuring the interaction between alpha-amino acids in aqueous carbohydrate solution*. Measurement Science & Technology, 2010. **21**(10).